AD-767 288

FUNDAMENTAL STUDIES OF SEMICONDUCTOR HETEROEPITAXY

PART II

ROCKWELL INTERNATIONAL CORP.

PREPARED FOR
ARMY MISSILE COMMAND
ADVANCED RESEARCH PROJECTS AGENCY

AUGUST 1973

FUNDAMENTAL STUDIES OF SEMICONDUCTOR HETEROEPITAXY

FINAL REPORT

PART II

ARPA Support Office
Research, Development, Engineering and Missile Systems Laboratory
United States Army Missile Command AMSMI RND
Redstone Arsenal
Huntsville, Alabama

Contract No. DAAH01-70-C-1311

Distribution of this document
is unlimited.

Sponsored by:
Advanced Research Projects Agency
ARPA Order No. 1585

AD

FUNDAMENTAL STUDIES OF SEMICONDUCTOR HETEROEPITAXY

FINAL REPORT

PART II

R. P. Ruth, A. J. Hughes, J. L. Kenty, H. M. Manasevit,
D Medellin, A. C. Thorsen, Y. T. Chan, C. R. Viswanathan, and M. A. Ring

Research and Technology Division
Electronics Group
Rockwell International
August 1973

ARPA Support Office
Research, Development, Engineering and Missile Systems Laboratory
United States Army Missile Command AMSMI RND
Redstone Arsenal
Huntsville, Alabama
Contract No. DAAH01-70-C-1311

Sponsored by:
Advanced Research Projects Agency
ARPA Order No. 1585

Security Classification

DOCUMENT CONTROL DATA - R & D

(Security classification of title, body of abstract and indexing annotation must be entered when the overall report is classified)

1. ORIGINATING ACTIVITY (Corporate author) Rockwell International Corp., Electronics Group Electronics Research Division Anaheim, California	2a. REPORT SECURITY CLASSIFICATION Unclassified 2b. GROUP

3. REPORT TITLE

Fundamental Studies of Semiconductor Heteroepitaxy, Part II

4. DESCRIPTIVE NOTES (Type of report and inclusive dates)

Final Report, June 1970 through June 1973

5. AUTHOR(S) (First name, middle initial, last name)

Ralph P. Ruth, A. James Hughes, Joseph L. Kenty, Harold M. Manasevit, Arthur C. Thorsen, Y. T. Chan, C. R. Viswanathan, Morey A. Ring

6. REPORT DATE August 1973	7a. TOTAL NO. OF PAGES 216	7b. NO. OF REFS 49
8a. CONTRACT OR GRANT NO. DAAH01-70-C-1311 b. PROJECT NO. c. d.	9a. ORIGINATOR'S REPORT NUMBER(S) C71-86/501 9b. OTHER REPORT NO(S) (Any other numbers that may be assigned this report)	

10. DISTRIBUTION STATEMENT

Distribution of this document is unlimited.

11. SUPPLEMENTARY NOTES	12. SPONSORING MILITARY ACTIVITY Advanced Research Projects Agency ARPA Order No. 1585 Washington, D.C.

13. ABSTRACT

The results of a three-year research program are described. The overall objective of the program was to carry out a fundamental study of nucleation and film growth mechanisms in heteroepitaxial semiconductor thin films. The specific technical objectives were 1) investigation of various aspects of the mechanisms of heteroepitaxial film growth, to establish technical guidelines for the preparation of better films; 2) preparation of improved, high-quality, device-grade heteroepitaxial films of Si and GaAs on insulating substrates by chemical vapor deposition (CVD) methods; 3) development of new or improved methods of characterizing heteroepitaxial semiconductor films; and 4) design and fabrication of selected thin-film devices taking advantage of the unique properties of heteroepitaxial films. The program involved both theoretical and experimental investigations of nucleation and growth mechanisms and development of improved techniques for film and substrate preparation and characterization. The CVD method of growing semiconductor films was emphasized because of its importance in the semiconductor device industry. Main emphasis was on the Si-on-Al_2O_3 system, with attention also given to the Si-on-$MgAl_2O_4$ and GaAs-on-Al_2O_3 systems. The work was divided among seven subtasks: 1) theory of epitaxy and heteroepitaxial interfaces; 2) deposition studies and film growth; 3) analysis and purification of CVD reactants; 4) preparation and characterization of substrates; 5) studies of *in situ* CVD film growth in the electron microscope; 6) evaluation of film properties; and 7) design and fabrication of special devices.

DD FORM 1 NOV 68 1473

Security Classification

Security Classification

14 KEY WORDS	LINK A		LINK B		LINK C	
	ROLE	WT	ROLE	WT	ROLE	WT
Epitaxy						
GaAs						
Si						
Al_2O_3 (sapphire)						
$MgAl_2O_4$ (spinel)						
Chemical vapor deposition (CVD)						
In situ film growth						
Electron microscopy						
Epitaxy theory						
Heteroepitaxy						
Thin-film devices						
Semiconductors						
Film nucleation						
Transport properties						
Metalorganic compounds						
Physical vapor deposition (PVD)						
Substrate						
Polishing						
Gas-phase etching						
Anisotropy						
Thermally induced stress						
Piezoresistance						

Principal technical accomplishments include 1) experimental discovery and empirical characterization of significant anisotropy in the electrical properties of Si/Al_2O_3 films of several crystallographic orientations, and theoretical explanation of the effects in terms of a model that combines thermally-induced stresses due to expansion coefficient differences with the piezoresistance effect in Si; 2) delineation of preferred substrate orientations, deposition temperatures, film growth rates, and carrier gas atmosphere for optimized film properties in the Si/Al_2O_3 and $Si/MgAl_2O_4$ systems; 3) identification of the influence of surface-state conduction on measured electrical properties in Si films with carrier concentrations $<10^{16}cm^{-3}$; 4) identification of the role of the Al_2O_3 surface as a catalyst for the pyrolytic decomposition of SiH_4 in the formation of Si films by CVD; 5) development of gas-phase etching and improved mechanical polishing techniques for preparing surfaces of Al_2O_3 and $MgAl_2O_4$ substrates for the heteroepitaxial growth of semiconductor films; 6) development of an ion-beam sputtering technique for preparing ultrathin (<500Å) regions in Al_2O_3 substrates for transmission electron microscopy; 7) observation of the in situ growth of Si by physical vapor deposition (PVD) and CVD on Al_2O_3 and amosphous carbon substrates in the electron microscope; 8) observation and characterization of the transport of photoinjected electrons through single-crystal Al_2O_3; 9) measurement of carrier lifetimes in Si heteroepitaxial films on Al_2O_3 and correlation of lifetimes with various experimental parameters; 10) determination of surface-state density distributions in Si heteroepitaxial films on Al_2O_3; and 11) the successful fabrication in Si/Al_2O_3 of charge-coupled devices exhibiting good charge-transfer efficiency at high frequencies. Details of these and other results and investigations are given by means of data tabulations, graphs, photographs, and narrative. An extensive bibliography of electron microscope in situ film nucleation and growth studies is also included. The report is bound in three separate parts.

Security Classification

ABSTRACT

The results of a three-year research program are described. The overall objective of the program was to carry out a fundamental study of nucleation and film growth mechanisms in heteroepitaxial semiconductor thin films. The specific technical objectives were 1) investigation of various aspects of the mechanisms of heteroepitaxial film growth, to establish technical guidelines for the preparation of better films; 2) preparation of improved, high-quality, device-grade heteroepitaxial films of Si and GaAs on insulating substrates by chemical vapor deposition (CVD) methods; 3) development of new or improved methods of characterizing heteroepitaxial semiconductor films; and 4) design and fabrication of selected thin-film devices taking advantage of the unique properties of heteroepitaxial films.

The program involved both theoretical and experimental investigations of nucleation and growth mechanisms and development of improved techniques for film and substrate preparation and characterization. The CVD method of growing semiconductor films was emphasized because of its importance in the semiconductor device industry. Main emphasis was on the Si-on-Al_2O_3 system, with attention also given to the Si-on-$MgAl_2O_4$ and GaAs-on-Al_2O_3 systems. The work was divided among seven subtasks: 1) theory of epitaxy and heteroepitaxial interfaces; 2) deposition studies and film growth; 3) analysis and purification of CVD reactants; 4) preparation and characterization of substrates; 5) studies of *in situ* CVD film growth in the electron microscope; 6) evaluation of film properties; and 7) design and fabrication of special devices.

Principal technical accomplishments include 1) experimental discovery and empirical characterization of significant anisotropy in the electrical properties of Si/Al_2O_3 films of several crystallographic orientations, and theoretical explanation of the effects in terms of a model that combines thermally-induced stresses due to expansion coefficient differences with the piezoresistance effect in Si; 2) delineation of preferred substrate orientations, deposition temperatures, film growth rates, and carrier gas atmosphere for optimized film properties in the Si/Al_2O_3 and Si/$MgAl_2O_4$ systems; 3) identification of the influence of surface-state conduction on measured electrical properties in Si films with carrier concentrations $<10^{16}cm^{-3}$; 4) identification of the role of the Al_2O_3 surface as a catalyst for the pyrolytic decomposition of SiH_4 in the formation of Si films by CVD; 5) development of gas-phase etching and improved mechanical polishing techniques for preparing surfaces of Al_2O_3 and $MgAl_2O_4$ substrates for the heteroepitaxial growth of semiconductor films; 6) development of an ion-beam sputtering technique for preparing ultrathin (<500Å) regions in Al_2O_3 substrates for transmission electron microscopy; 7) observation of the *in situ* growth of Si by physical vapor deposition (PVD) and CVD on Al_2O_3 and amorphous carbon substrates in the electron microscope; 8) observation and characterization of the transport of photoinjected electrons through single-crystal Al_2O_3; 9) measurement of carrier lifetimes in Si heteroepitaxial films on Al_2O_3 and

correlation of lifetimes with various experimental parameters; 10) determination of surface-state density distributions in Si heteroepitaxial films on Al_2O_3; and 11) the successful fabrication in Si/Al_2O_3 of charge-coupled devices exhibiting good charge-transfer efficiency at high frequencies.

Details of these and other results and investigations are given by means of data tabulations, graphs, photographs, and narrative. An extensive bibliography of electron microscope in situ film nucleation and growth studies is also included. The report is bound in three separate parts.

PROGRAM SUMMARY

The overall objective of this three-year program was to carry out a fundamental study of nucleation and film growth mechanisms in heteroepitaxial semiconductor thin-film systems which would lead to new knowledge and understanding of these processes, and then to apply the results to the preparation of improved semiconductor thin films and thin-film devices on insulating substrates.

The specific technical objectives were the following: 1) investigation of various aspects of the mechanisms of heteroepitaxial film growth, to establish technical guidelines for the preparation of better films which could be applied to real situations; 2) preparation of improved, high-quality, device-grade heteroepitaxial films of Si and GaAs on insulating substrates by chemical vapor deposition (CVD) methods; 3) development of methods of characterizing heteroepitaxial films as to their suitability for subsequent device fabrication; and 4) design and fabrication of selected thin-film devices which take advantage of the unique properties of such films.

The plan for accomplishing these objectives involved the study of the fundamentals of heteroepitaxial semiconductor film growth on insulating substrates as the primary activity, with specialized device fabrication used as a means both of evaluating film properties and of exploiting certain unique properties of heteroepitaxial semiconductor-insulator systems. Both theoretical and experimental investigations were involved. The theoretical studies consisted of two types: 1) direct interaction with the experimental program, involving data analyses, suggestion of definitive experiments, and postulation of specific models to explain experimental observations; 2) development of original contributions to the theory of heteroepitaxial growth. The experimental investigations were also of two types: 1) fundamental explorations to delineate mechanisms and general empirical principles of the heteroepitaxial growth process; 2) practical device studies accompanying the fundamental investigations, so that new developments could be applied to the improvement of films and thin-film devices.

The chemical vapor deposition (CVD) method of growing semiconductor films was emphasized because of its importance in the semiconductor device industry. Main emphasis was on the Si-on-Al_2O_3 system, with attention also given to the Si-on-$MgAl_2O_4$ and GaAs-on-Al_2O_3 systems. The work was divided among seven subtasks: 1) theory of epitaxy and heteroepitaxial interfaces; 2) deposition studies and film growth; 3) analysis and purification of CVD reactants; 4) preparation and characterization of substrates; 5) studies of <u>in situ</u> CVD film growth in the electron microscope; 6) evaluation of film properties; and 7) design and fabrication of special devices.

The program was carried out primarily at facilities of the Electronics Group of the Rockwell International Corporation, by Rockwell personnel. Parts of three of the specific subtasks were performed by personnel of the University of California at Los Angeles (UCLA), in the Department of Electrical Sciences and Engineering and the Chemistry Department. Work on another subtask was done in part in the Department of Chemistry of California State University, San Diego (CSUSD). Both the UCLA and the CSUSD programs were supported by subcontracts from Rockwell.

The principal technical accomplishments of the program include the following: 1) experimental discovery and extensive characterization of significant anisotropy in the electrical properties of Si/Al_2O_3 films, and theoretical explanation of the effect in terms of a model that combines thermally-induced stresses with the piezoresistance effect in Si; 2) delineation of preferred substrate orientations, deposition temperatures, film growth rates, and carrier gas atmospheres for optimized film properties in the Si/Al_2O_3 and $Si/MgAl_2O_4$ systems; 3) identification of the influence of surface-state conduction on measured electrical properties in Si films with carrier concentrations $<10^{16}cm^{-3}$; 4) identification of the catalytic role of the Al_2O_3 surface in the heterogeneous pyrolytic decomposition of SiH_4 to form Si films by CVD; 5) development of gas-phase etching and improved mechanical polishing techniques for preparing surfaces of Al_2O_3 and $MgAl_2O_4$ for the heteroepitaxial growth of semiconductor films; 6) development of an ion-beam sputtering technique for preparing ultrathin (<500Å) regions in Al_2O_3 substrates for transmission electron microscopy; 7) observation of the in situ growth of Si by physical vapor deposition (PVD) and by CVD on Al_2O_3 and amorphous carbon substrates in the electron microscope; 8) observation and characterization of the transport of photoinjected electrons through single-crystal Al_2O_3; 9) measurement of carrier lifetimes in Si heteroepitaxial films on Al_2O_3; 10) determination of surface-state density distributions in Si heteroepitaxial films on Al_2O_3; and 11) the successful fabrication in Si/Al_2O_3 of charge-coupled devices exhibiting good charge-transfer efficiency at high frequencies.

A summary of the work of the contract program by subtask follows:

Subtask 1: Theory of Epitaxy and Heteroepitaxial Interfaces. Several separate investigations were carried out in attempts to model heteroepitaxial systems. An extension of the island alignment model using a Gaussian-atom Fourier-transform technique, the Frank-van der Merwe model, a Green's-function/Wannier-function approach, a contrived potential-energy model, and a molecular-orbital method for developing the heteroepitaxial interface were all critically reviewed for the purpose, and all were found inadequate for application to the real systems of interest. A two-body interatomic potential method, although also initially rejected, was finally adopted for modeling the Al_2O_3 lattice with Morse potentials and a suitable computer program; mechanical stability and surface reconstruction phenomena in Al_2O_3 were treated successfully by this method, involving relaxation of the several atomic planes nearest the Al_2O_3 surface. An electron-on-network method was also considered for determination of surface atom configurations and interfacial binding energies in situations where the surface structure is allowed to relax, but was also eventually found inadequate for realistic calculations in heteroepitaxial systems.

Extension of the modeling to the Si/Al_2O_3 composite was interrupted by the theoretical investigation of the effects on electrical properties of stresses in the Si films resulting from differential thermal contraction of substrate and film, prompted by the experimental observation of ~10% anisotropy in the carrier mobility in (001)Si/Al_2O_3 and ~40% anisotropy in (221)Si/Al_2O_3. A model combining thermal expansion stress and the piezoresistance effect, incorporating the anisotropies in substrate thermal expansion, Si elastic constants, and Si piezoresistance coefficients, was developed and applied to (001), (221) and (111)Si

films on Al_2O_3. Excellent agreement was obtained between theory and experiment in the first two cases; the amount of anisotropy and the directions (in the plane of the film) of maximum and minimum carrier mobility were correctly predicted. In (111)Si (on two different Al_2O_3 substrate orientations), however, the theoretically predicted effects were too small to account for the experimental observations, indicating that other (not yet identified) phenomena are more important in determining anisotropy in the (111)Si/Al_2O_3 system.

Extensive calculations were made for the general (xxl)Si orientation ($0 \leq x \leq \infty$), which defines all Si orientations along the zone that includes (001), (111), (221), and (110)Si and thus all of the Si/Al_2O_3 epitaxy modes of major interest. For n-type Si/Al_2O_3, the predicted stress effects ranged from a ~30% reduction for (001)Si to a ~25% enhancement in maximum mobility near (110)Si. For p-type Si films, the predicted stress effect is always a mobility enhancement, with the maximum mobility ranging from ~1.07μ_o for (001)Si to ~2.4μ_o for (110)Si, where μ_o is the zero-stress mobility. It is significant that the Si film orientation most used in commercial devices - (001) - is the one showing the lowest mobilities of all those investigated. Thus, considerable improvement in performance of certain types of devices could be realized by exploiting these predicted effects, which have major significance for heteroepitaxial device technology.

Subtask 2: Deposition Studies and Film Preparation. A major part of the work of this subtask consisted of preparing a variety of Si and GaAs heteroepitaxial film samples for use in other parts of the program. Experimental investigations of the effects of various deposition parameters upon the properties of Si and GaAs films continued throughout the program, including examination of the following: 1) dependence of electrical properties on growth temperature, growth rate, and crystallographic orientation of substrate (including the $(11\bar{2}0)$ orientation, not previously used for heteroepitaxy studies); 2) variations in Si film properties with thickness; 3) formation and properties of p-type Si/Al_2O_3 films; 4) effects of autodoping (at temperatures above ~1050C) in Si films on Al_2O_3 and $MgAl_2O_4$; 5) effects of reactor configuration on film properties; 6) characteristics of early-stage growth of Si films on Al_2O_3; 7) growth of Si films by SiH_4 pyrolysis at reduced pressures (1 to 10 torr); 8) growth of Si films in gaseous atmospheres other than pure H_2; 9) effects of annealing during growth on properties of Si films (no significant improvement in film properties observed); and 10) growth of GaAs films on Al_2O_3 and $MgAl_2O_4$. These studies revealed the strong interrelationships that exist among the various parameters involved in optimizing Si growth on insulators. Evaluation of the electrical properties of Si films on Al_2O_3 demonstrated that growth conditions (1) must be optimized for the particular substrate orientation chosen; (2) differ for those Al_2O_3 orientations which produce the same Si orientation; (3) are dependent upon reactor geometry and gaseous atmosphere; and (4) must be optimized for the particular film thickness desired.

Based on electrical properties of the films grown, the preferred substrate for Si heteroepitaxy was identified as one that produces (111)Si growth rather than (100)Si growth, namely ~$(11\bar{2}0)Al_2O_3$ or $(111)MgAl_2O_4$, the highest mobilities being obtained on $(111)MgAl_2O_4$. Optimum growth temperatures varied with substrate orientation: (100)Si on $(01\bar{1}2)Al_2O_3$, 1050-1075C; (111)Si on $(10\bar{1}4)Al_2O_3$, 1075-1100C; (111)Si on ~$(11\bar{2}0)Al_2O_3$, 1075-1100C; and (111)Si on $(111)MgAl_2O_4$, ~1025C. The preferred growth atmosphere appeared to be either H_2 or a $He-H_2$

mixture for growth on $(01\bar{1}2)Al_2O_3$ or $\sim(11\bar{2}0)Al_2O_3$, but both $(10\bar{1}4)Al_2O_3$ and $(111)MgAl_2O_4$ apparently need a He-rich atmosphere (~90% He-10% H_2) for obtaining high quality films. For essentially every orientation studied, growth rates from ~2μm/min to ~4μm/min were found sufficient, although good growth was also achieved on $(01\bar{1}2)Al_2O_3$ at lower rates. These growth conditions are optimum for the reactor system used, but should be useful guides for CVD film growth in systems with other reactor geometries. These observations should lead to definite improvements in Si/Al_2O_3 film properties and thus to improved performance and reliability in Si/Al_2O_3 devices and circuits.

Subtask 3: Analysis and Purification of CVD Reactants. Since the impurity content of the various reactants used for CVD of Si and GaAs heteroepitaxial films probably provides the real limitation on the achievable impurity levels in the films themselves, a study was undertaken to attempt to identify and establish the concentrations of the principal impurities in the reactants that might influence the film properties if they were to become incorporated into the films during growth. During the first year, techniques of gas chromatography were developed for analysis of the reactants used for Si and GaAs heteroepitaxy by CVD, with silicone oil and polymer columns used for the chromatography. Several extraneous impurity peaks were observed in the chromatograms of SiH_4 samples, and diborane (B_2H_6) was tentatively identified as a significant impurity (~10 ppm), although not confirmed by mass spectrometer techniques. Small quantities of purified SiH_4, free of diborane, were prepared by successive injections in the chromatograph, but the quantities were too small for use in laboratory CVD experiments. Beginning in the second year of the program, samples of SiH_4 and of trimethylgallium (TMG) used for Si and GaAs CVD experiments were analyzed for impurity content by sensitive mass spectrometric techniques. Disilane and trimethylsilane, together with several other impurities of less concern, were found in the SiH_4 samples.

Significant impurity concentrations in some of the reactants (especially SiH_4) at times limited the accuracy of the study of the effects of deposition parameters on Si film properties. Cooperative efforts with vendors for preparation of improved-purity reactants continued throughout the program, as did analyses of reactants by mass spectrometer techniques. It was made clear that significant differences occurred in the purity of reactant materials; not only did they vary from supplier to supplier but also different tanks of the same material from the same supplier were not consistent in purity. Another problem was the lack of agreement in the analyses supplied by different analytical laboratories for the same tank of reactant and the differences in detection limits for the same element or compound that different laboratories possessed, making it difficult to determine which results were the most reliable and which supplier of gases was best. A "use test" still appears to be the most reasonable way of evaluating materials for the intended application. The analyses demonstrated the ultimate lack of understanding of the role of impurities in epitaxial film growth and the minimum requirements for the analytical methods that should be used in detecting these impurities. An extensive collaborative study involving the reactant supplier, the analytical laboratory, and the ultimate user is needed.

To examine some of the fundamentals of the chemistry and reaction kinetics of the CVD processes used for growing heteroepitaxial films of Si and GaAs, investigations of the reactions involved in the formation of Si by SiH_4 pyrolysis and of GaAs by the trimethylgallium (TMG)-AsH_3 reaction were undertaken. The influence of the Al_2O_3 surface on the mechanism of decomposition of SiH_4 as a function of temperature, and the decomposition modes and reaction products of TMG and

AsH_3 as functions of temperature, concentration ratio, and H_2 partial pressure (to attempt to determine the requirements for formation of optimum-quality GaAs) were examined. It was found that the surface of single-crystal Al_2O_3 does catalyze the thermal decomposition of SiH_4, whereas the pyrolysis is homogeneous over a Si surface. No effect of preheating the Al_2O_3 to temperatures as high as 1200C was found. A variety of observations made on the TMG-AsH_3 system included the following, among others: 1) GaAs does result from the reaction of TMG with AsH_3, and an excess of AsH_3 should be used in any application of the process; and 2) both CH_4 (methane) and H_2 are produced in the series of stepwise reactions leading to the final product. Further study of the reaction at high temperatures is recommended.

Subtask 4: Preparation and Characterization of Substrates. It was demonstrated that Al_2O_3 surfaces prepared by mechanical polishing techniques and used routinely for semiconductor heteroepitaxy typically had severe surface and subsurface damage, with many scratches often several microns deep yet often rendered invisible to close inspection because of amorphous or fine-grained debris embedded in the scratches in the final polishing stages. Early in the second year a much improved technique for mechanical polishing of $(10\bar{1}4)Al_2O_3$ was developed, and very good surfaces in this previously troublesome orientation were then obtained. Gas-phase etching/polishing procedures using SF_6 and various fluorinated halocarbons in the 1350 to 1500C temperature range were found to produce essentially scratch-free surfaces on $(01\bar{1}2)$ and near-$(11\bar{2}0)Al_2O_3$ substrates. Extensive gas-phase etch-rate data were obtained as a function of crystallographic orientation in this temperature range. The technique was further developed for (1) thinning Al_2O_3 substrates; (2) evaluating the effects of prolonged etching on $(01\bar{1}2)$, (0001), and ~$(11\bar{2}0)Al_2O_3$; and (3) assessing the subsurface damage caused by various mechanical polishing procedures. Evaluation of mechanical polishing methods for $MgAl_2O_4$ surfaces indicated that surface fill-in occurs for this material, just as for Al_2O_3. Some exploratory gas-phase etching experiments with $MgAl_2O_4$ surfaces were also carried out during the second year of the program.

Ion-beam sputtering techniques were developed for preparing ultra-thin (~200Å)Al_2O_3 wafers for use as substrates in the in situ CVD experiments with Si. Wafers successfully thinned to ~50μm or less by mechanical polishing techniques were subsequently thinned by ion etching to the point of perforation in some areas, resulting in adjoining regions of thicknesses suitable for transmission electron microscopy as applied in the in situ experiments. Three different Al_2O_3 orientations were successfully thinned by this method - (0001), $(10\bar{1}4)$, and $(01\bar{1}2)$. Considerable study of properties of the resulting thinned substrates was carried out, and improvements in the ion-thinning process were realized during the final year of the program, when the thinned substrates were used in the in situ CVD experiments (Subtask 5).

Mechanical lapping and polishing methods that produce good quality surfaces suitable for use as substrates for epitaxy were developed during the contract for several orientations of Al_2O_3 - (0001), $(01\bar{1}2)$, $(10\bar{1}4)$, $(11\bar{2}0)$, ~6 deg off $(11\bar{2}0)$ and $(11\bar{2}2)$. By means of etch-rate techniques developed for this

material it was possible to determine the apparent depth of damage in Al_2O_3 substrate wafers at various stages of preparation. At a given stage in the processing, the damage depth was found to increase for various orientations in the following order: $(10\bar{1}4)$, $(11\bar{2}0)$, $(01\bar{1}2)$, and (0001).

A technique utilizing the photoelectric process in a metal-insulator-semiconductor structure, consisting of an Al_2O_3 substrate with a Si or GaAs film grown on one surface and a semitransparent Al film on the other, demonstrated that photoexcited electrons from either the semiconductor or the metal film can be transported through single-crystal Al_2O_3 of several mils thickness. Further study of the charge transport process also established that (1) the Al_2O_3 used for substrates for growth of heteroepitaxial semiconductor films has trap levels approximately 0.18 eV below the conduction band; (2) the transport of photoinjected electrons occurs through the Poole-Frenkel conduction mechanism; and (3) the quantum efficiency for the photoelectric process is quite low, approximately 10^{-5}.

Routine characterization of substrate surfaces at various stages of preparation continued throughout the program, utilizing various standard techniques of x-ray and electron diffraction analysis and optical and electron (including scanning) microscopy.

Subtask 5: Studies of <u>in situ</u> Film Growth in the Electron Microscope.

In the first year of the program many of the modifications required in the transmission electron microscope for <u>in situ</u> observation of the nucleation and early-stage growth of CVD semiconductor films on insulating substrates were completed. Early in the second year a series of electron microscope modifications and tests was finished, culminating in the first series of successful PVD experiments inside the electron microscope. Al was deposited onto a heated carbon substrate and a sequence of micrographs was taken during the growth process, demonstrating the feasibility of performing <u>in situ</u> nucleation and growth studies in the equipment. Additional <u>in situ</u> PVD experiments were carried out in the second year, with both Al and Au deposited onto amorphous carbon substrates to delineate further the required techniques and experimental problems to be encountered in the later CVD experiments. Calculations and design for the CVD microchamber were also completed during the second year, and the fabrication of the microchamber and associated hardware was begun.

During the final year of the program the fabrication of the CVD microchamber and its mounting flange was completed, and a gas-handling manifold was installed on the electron microscope. Gas flow experiments were performed to determine the flow rate of gas through the microchamber as a function of pressure and to determine the maximum pressure attainable in the microchamber.

In addition, a number of <u>in situ</u> Si CVD experiments were performed resulting in the successful growth of Si films in the electron microscope by the pyrolysis of SiH_4. The nucleation and early growth of Si on both amorphous carbon and single-crystal Al_2O_3 substrates was observed, leading to the following conclusions: 1) the pyrolysis of SiH_4 to form Si films by CVD inside the electron microscope is feasible; 2) the <u>in situ</u> study by trans-

mission electron microscopy of the post-nucleation and early growth stages of a semiconductor film grown by CVD is feasible; 3) the nucleation and early growth processes for CVD Si are fundamentally similar to those of metal films grown by PVD, although some specific differences exist; 4) single-crystal Si growth on $(01\bar{1}2)Al_2O_3$ results primarily from the growth of nuclei of a preferred orientation at the expense of randomly oriented nuclei, and not from the large nucleation rate of these favorably oriented nuclei; 5) the ion-beam sputtering process can produce electron-transparent Al_2O_3 suitable for use as substrates for in situ CVD film growth experiments.

Subtask 6: Evaluation of Film Properties. From the beginning of the program, routine evaluation of film properties was carried out by established methods of x-ray and electron diffraction analysis, metallographic analysis, and electrical measurements of transport properties. A new technique for evaluating the characteristics of the interfacial region of heteroepitaxial films was developed, involving measurements of photoelectron emission from monochromatically-illuminated films in the MIS configuration on insulating substrates (see Subtask 4). Photocurrents due to electron transport through the single-crystal Al_2O_3 substrates were measured as a function of photon energy, permitting determination of various parameters in the Si/Al_2O_3 and $GaAs/Al_2O_3$ systems. These measurements gave values of 1.0eV for the electron affinity of Al_2O_3, 3.15eV for the barrier height at an Al_2O_3-Al interface, 4.50eV for the $Si-Al_2O_3$ interface barrier height, ~0.37eV for the band-bending in Si near the $Si-Al_2O_3$ interface, ~0.10eV for the band-bending in GaAs films near the Al_2O_3 interface, and electron escape lengths of at least 12μm in Si and 23μm in GaAs. Values for the work function of various metals were also determined by these measurements.

Determination of the energy spectrum of back-scattered proton or alpha-particle beams injected in channeling directions in heteroepitaxial semiconductor films was investigated as a means of measuring the density and the location of structural defects in the films. Experiments indicated that Si/insulator films have less imperfect interfacial regions than do GaAs/insulator films. The best structures of those examined were found in (100)Si films on $(01\bar{1}2)Al_2O_3$ substrates and in (111)Si films grown on near-$(11\bar{2}0)Al_2O_3$ substrates. Information on the early growth stages of Si on Al_2O_3 was also obtained by conventional transmission electron microscopy of very thin Si films grown on ion-thinned Al_2O_3 substrates in a conventional (atmospheric-pressure) vertical-flow CVD reactor. These experiments showed that the growth of a single-crystal Si film by CVD is the result of coalescence processes in the early growth stages and not of nucleation phenomena alone, producing films with a relatively higher incidence of defects and relatively lower carrier mobilities.

Rapid acquisition of data on electrical properties of the films was very important to the conduct of film growth experiments, especially in the second and third years; measurements of film conductivity type, resistivity, carrier concentration, and carrier mobility were made routinely on a majority of the epitaxial samples prepared on the program, utilizing either the van der Pauw method or the more accurate and conventional Hall-effect bridge method. These data were essential for the study of the effects of changes in deposition parameters on Si/Al_2O_3 and $Si/MgAl_2O_4$ film properties, and provided

considerable insight into the factors which most strongly influence film quality so that identification of the conditions for optimized film growth could be made.

It was determined that the electrical properties of undoped n-type heteroepitaxial Si films grown on various orientations of Al_2O_3 (and also $MgAl_2O_4$) by the pyrolysis of SiH_4 are dominated by surface-state conduction for carrier concentrations of $\sim 10^{16} cm^{-3}$ or below. It was found that there were inhomogeneities in the donor concentration of typical CVD Si/Al_2O_3 films over the film area, and that a concentration gradient existed from the center of the susceptor radially outward; films reflected this variation depending upon the placement of the substrate on the susceptor during CVD growth. Gas flow characteristics or a non-uniform temperature of the rf-heated pedestal (susceptor) were thought to account for the effect. Measurements were made of the variation of electrical properties of Si/Al_2O_3 with temperature, and some of the observed effects were attributed to high defect densities (e.g., deep-lying donor levels) or inhomogeneous strains in the films.

The most significant development to come from the film evaluation procedures was the observation of the anisotropy in electrical properties in Si/Al_2O_3 films. Mobility measurements as a function of azimuthal direction (every 18 deg) in the film plane indicated a maximum mobility in two directions and a minimum mobility in two directions, the latter displaced by 90 deg from the former. The mobility anisotropy factor A, defined as the ratio of the difference between the maximum and minimum values of mobility in the plane of the film to the average value of the mobility in that plane, was found to be about 40% for $(221)Si/(11\bar{2}2)Al_2O_3$ and about 9% for $(001)Si/01\bar{1}2)Al_2O_3$. Results of theoretical calculations (Subtask 1) agreed well with the experimental data. The calculations and the experimental results indicated that (221)Si exhibits higher electron mobilities than other more commonly used orientations. Measurements of anisotropy at 77K were also consistent with the corresponding increases in piezoresistance coefficients at that temperature. Data analyses predicted zero-stress mobilities significantly below bulk crystal values, however, indicating mechanisms other than thermally-induced stresses were dominant in reducing carrier mobilities in heteroepitaxial films. Extensive studies of $(111)Si$ on $(11\bar{2}0)Al_2O_3$ and on $(10\bar{1}4)Al_2O_3$ gave experimental anisotropies averaging 16% and 30%, respectively, much larger than theoretical predictions, again indicating the presence of other major influencing factors. There appeared to be an inverse relationship between anisotropy in (111)Si and the minimum or the average mobility, higher anisotropy corresponding to lower mobility. Attempts were made to correlate these results with reactor configuration (i.e., horizontal or vertical) and various deposition conditions. Measurements were also begun to examine the possibility of mobility anisotropy being present in the $Si/MgAl_2O_4$ system.

The surface-state density of thermally oxidized Si films on Al_2O_3 was determined late in the program using the MOS C-V technique. Evidence of both donor- and acceptor-type surface states was found; a peak in the acceptor-state density appeared at ~0.16eV below the conduction band, but the exact

location of the donor-state density peak could not be determined. Measurements of high-field transport properties of Si and GaAs heteroepitaxial films on Al_2O_3 were also undertaken, early in the program, to obtain drift mobility data for some of the films.

Subtask 7: Design and Fabrication of Devices. In the first year of the contract apparatus for determining minority carrier lifetime by pulsed C-V measurements in MOS structures was designed and constructed and tests were begun. A special MOS structure was designed for measurement of channel conductance, high- and low-field transport properties, and various interface characteristics of heteroepitaxial films. Initial attempts to fabricate Schottky-barrier diodes in Si/Al_2O_3 films as a means of evaluating their electrical properties were not successful and were not pursued further. In the second year the design of a Schottky-barrier type of FET was completed for use in fabricating experimental FET structures in GaAs/insulator films for operation at 1 GHz. Most of the device-oriented effort centered about the determination of carrier lifetimes using the MOS pulsed C-V technique (work which extended to the end of the program) and attempts to fabricate Schottky-barrier FET's in $GaAs/Al_2O_3$.

Recent device efforts produced Schottky-barrier diodes (in n-type Si/Al_2O_3 samples) having good reverse but unsatisfactory forward characteristics. The Schottky-barrier FET structures were still not satisfactory. Preliminary work on fabricating and evaluating Schottky-barrier photovoltaic cells using illumination from the back side was begun, and charge-coupled devices (CCD's) in Si/Al_2O_3 composites were successfully designed, fabricated, and tested.

The lifetime measurement method used has the important advantage that the actual carrier lifetime is magnified by the factor N/n_i, where N is the impurity concentration in the semiconductor and n_i is the intrinsic concentration, so that very short lifetimes typical of heteroepitaxial systems (10^{-10}–10^{-9}sec) could be measured. Carrier lifetimes and values of surface recombination velocity were obtained for As-doped n-type Si/Al_2O_3 samples and for As-doped n/n^+-type Si/Al_2O_3 samples grown by CVD on this contract, as well as for some commercially-obtained Si/Al_2O_3 samples that were P-doped. Lifetimes for As-doped (100)-oriented Si varied from $\sim 10^{-10}$ sec for films 1-3μm thick to $\sim 5 \times 10^{-9}$ sec for films ~10μm thick; the particular P-doped films measured exhibited lifetimes nearly an order of magnitude longer. No clear dependence of lifetime on As doping concentration or on Si orientation ((100) and (111) were studied) was detected. It was found that an underlying n^+ layer ($\sim 3 \times 10^{18} cm^{-3}$) significantly enhanced the lifetime in a 3μm top layer of As-doped ($\sim 10^{16} cm^{-3}$) Si for a given total film thickness, the enhancement being greater the greater the n^+ layer thickness ($\tau \sim 1\mu sec$ for 18μm total thickness); the n^+ sublayer evidently acts as a "getter" for the trapping centers that tend to lower the lifetime in the n-type material.

Since CCD's had previously been fabricated in Si and showed good charge transfer and since other Si/Al_2O_3 devices had exhibited good high-frequency and radiation-resistant characteristics it was determined that fabrication of CCD's should be undertaken in Si/Al_2O_3. The devices were successful, with good transfer

efficiency at high frequencies; four-phase 8-mil-per-cell CCD's were operated at 2MHz with 0.99 efficiency. Low-frequency operation, however, was found to be limited by the short carrier lifetime which allowed charge-up of the potential well.

CONTENTS

PART III

ILLUSTRATIONS

TABLES

PART II

SECTION 8

STUDIES OF IN SITU FILM GROWTH IN THE ELECTRON MICROSCOPE *

Observation of Si film growth on Al_2O_3 substrates while it is occurring was considered to be an important part of the fundamental heteroepitaxy studies of this contract. The post-nucleation growth of islands and island clusters has been observed in situ in an electron microscope for several systems of metal species deposited on dielectric or other suitable substrates (Refs 68-70) by physical vapor deposition (PVD). However, observation of in situ growth of CVD films (or other configurations) in the electron microscope has occurred in only a very limited number of cases (Refs 71-74), and not at all in the semiconductor/insulator heteroepitaxial system prior to this contract work.

Considerable effort was expended in this program to prepare and carry out such experiments, specifically in the Si/Al_2O_3 system because of its general importance in the semiconductor industry and because of its role as the system of primary attention in this contract. These studies are described in detail in this section.

In the first year of the program many of the modifications required in the electron microscope for in situ observation of the nucleation and early-stage growth of CVD semiconductor films on insulating substrates were completed. Provision for motion-picture recording of film growth was assembled and tested, and the heated specimen stage was installed and tested. The first exploratory in situ PVD experiments were also carried out near the end of the first year.

Early in the second year a series of electron microscope modifications and tests was completed, culminating in the first series of successful PVD experiments inside the electron microscope. Al was deposited onto a heated carbon substrate and a sequence of micrographs was taken during the growth process, demonstrating the feasibility of performing in situ nucleation and growth studies in the equipment. A transmission phosphor screen (for the motion picture camera) was installed, permitting motion picture photography which does not interfere with the normal still photography. The auxiliary vacuum

---

* See Appendix 5 for extensive bibliography.

pumping system for the specimen chamber was fabricated, installed and tested. The basic vacuum system of the microscope itself was improved, and a PVD source assembly was fabricated, installed and used in conjunction with the specimen heater to perform further PVD experiments.

Calculations and design for the CVD microchamber were completed during the second year, and the fabrication of the microchamber and associated hardware was begun. Additional in situ PVD experiments were carried out, with both Al and Au deposited onto amorphous carbon substrates to delineate further the required techniques and experimental problems to be encountered in the CVD experiments.

During the final year the fabrication of the CVD microchamber and its mounting flange was completed, and a gas-handling manifold was installed on the electron microscope. Gas flow experiments were performed to determine the flow rate of gas through the microchamber as a function of pressure and to determine the maximum pressure attainable in the microchamber.

In addition, a number of in situ Si CVD experiments were performed, resulting in the successful growth of Si films in the electron microscope by the pyrolysis of SiH_4. The nucleation and early growth of Si on both amorphous carbon and single-crystal Al_2O_3 substrates has been observed, leading to the following conclusions:

(1) The pyrolysis of SiH_4 to form Si films by CVD inside the electron microscope is feasible.

(2) The in situ study by transmission electron microscopy of the post-nucleation and early growth stages of a semiconductor film grown by CVD is feasible.

(3) The nucleation and early growth processes for CVD Si are fundamentally similar to those of metal films grown by PVD, although some specific differences exist.

(4) Single-crystal Si growth on $(01\bar{1}2)Al_2O_3$ results primarily from the growth of nuclei of a preferred orientation at the expense of randomly oriented nuclei and not from the large nucleation rate of these favorably oriented nuclei.

(5) The ion-beam sputtering process (Section 6-3) can produce electron-transparent Al_2O_3 suitable for use as substrates for in situ CVD film growth experiments.

Specific aspects of these investigations are described below.

1. ELECTRON MICROSCOPE MODIFICATIONS FOR IN SITU EXPERIMENTS

The basic instrument used for these investigations was an AEI Model EM6 transmission electron microscope. An overall view is shown in Figure 83 with the in situ modifications in place. Although the instrument operated well as a conventional 100 KV electron microscope, some modifications were considered necessary to meet the severe operating conditions of in situ CVD experiments. The basic modifications included upgrading the vacuum system and increasing the photographic capabilities.

Considerable effort was expended in improving the vacuum performance over that of the original design. The primary objective was to reduce the contamination rate, shown by some of the PVD experiments to be extremely detrimental to the nucleation and growth processes. The typical result of a high contamination rate is a deposit formed from residual hydrocarbon vapors in the microscope striking the substrate and becoming polymerized by the incident electron beam. The carbonaceous deposit thus formed gradually builds up, eventually obscuring the sample being examined. Hydrocarbon vapors which strike the sample outside the area irradiated by the electron beam will reevaporate without effect. These residual hydrocarbon vapors, present to a varying extent in all electron microscopes, originate from the vacuum oils and greases used in the pumping system, sealing gaskets, organic insulation on interior electrical wires, fingerprints, and residues of cleaning solvents.

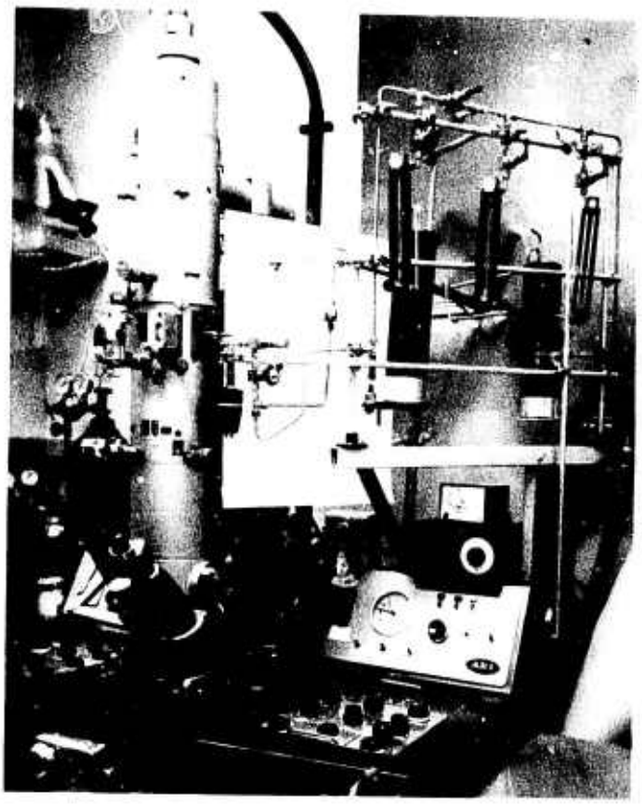

Figure 83. Electron Microscope and Gas Handling Manifold for In Situ CVD Experiments.

The vacuum performance was improved primarily by improving the polished finish on the O-ring sealing surfaces and by scrupulously cleaning all parts of the interior of the microscope to remove all traces of hydrocarbon condensates from prior usage. All of the approximately 150 neoprene O-rings in the microscope were replaced with Viton-A O-rings, which have a lower air permeation rate, lower hydrocarbon vapor pressure and lower retention of organic solvent vapors. The O-ring grooves were carefully inspected (most were adequate only for the normal operating vacuum of 5×10^{-5} torr) and were polished to better than a 16-microinch finish. An Edwards Model DCB-2 thermoelectrically-cooled baffle was installed between the diffusion pump and the microscope column. Cooling the chevron-type baffle to -15C reduced the diffusion-pump oil backstreaming to a near-negligible rate. A simple low-cost adapter was required, but no other modification to the microscope or its framework was necessary.

As anticipated, there was a slight improvement in ultimate vacuum and a slight increase in pumpdown time resulting from these changes. The important improvement from these modifications came in the form of a routinely lower operating pressure (5×10^{-6} torr compared with 5×10^{-5} torr previously) and a reduced contamination rate. The contamination rate was determined by measuring the rate of decrease in diameter of a hole in a carbon film at 103,000X magnification. The rate observed prior to the modifications was 240Å/min, typical of most microscopes. After the changes, the rate was less than 100Å/min.

A number of microscope modifications were made to improve the basic still-photograph capability and to add a motion-picture capability. The former was improved by installation of a commercially available 24-plate camera rather than the standard 6-plate camera. An automatic shutter was installed to permit accurate timing of exposures from 0.01 to 128 sec.

A transmission phosphor screen and motion-picture camera were also installed. The transmission phosphor screen consisted of a glass plate coated with a thin layer of suitable phosphor; it was mounted directly on and underneath the still-photograph plate camera. When the microscope shutter is opened, the electron beam impinges on the phosphor which fluoresces and is photographed

from below by a 16mm motion-picture camera. The motion-picture setup is independent of the still plate camera and does not interfere in any manner with its normal operation.

The first two phosphor screens were of P-11 phosphor, coated with a thin (~500Å) layer of Al to prevent charging. However, both the resolution and the brightness were less than desired, so a better screen was obtained from another manufacturer (Ladd Research Industries, Burlington, VT). This screen was of F-2S2 (green) fine-grained phosphor coated with a thin conductive layer of evaporated carbon. The resolution on this screen was excellent and the brightness acceptable for the purpose.

A Bolex H-16 motion-picture camera was mounted 6-1/2 in below the transmission phosphor screen. With a Switar 10mm f/1.6 lens with a 0.030 in spacer, Kodak RAR 2475 or 2479 film was underexposed at the normal frame rate of 12 frames/sec and exposure time of 1/33 sec, even with forced developing. The microscope was operated at maximum electron beam intensity and a saturation current of 300μa for these experiments. Satisfactorily exposed motion pictures could be obtained with normal development in Versamat developer, however, if the frame rate was reduced to 5.6 frames/sec and the exposure time increased to 1/15 sec.

An auxiliary pumping system was fabricated for the specimen chamber.* It consisted of a diffusion pump, liquid nitrogen trap, and isolation valve, and was connected to the specimen chamber through a vacuum tee and a special flexible metal bellows and adapter. An ionization gauge was mounted on the other side of the tee to record the pressure near the sample chamber. The design maintained the specimen airlock-exchange mechanism, so the microscope could also be used for routine electron microscopy with no time loss (if the CVD micro-

*The term "specimen chamber" refers to the relatively large portion of the electron microscope column containing the specimen holder (or CVD microchamber when installed), the specimen holder exchange and airlock mechanism, and the specimen holder stage with its associated control mechanisms for specimen rotation, tilt and translation.

chamber was not in place). A second ionization gauge was installed on a specially machined flange which temporarily replaced the right-hand side of the specimen-exchange air lock. The base pressure of the auxiliary system was $<1 \times 10^{-7}$ torr, but the best operating pressure obtained was 2×10^{-6} torr, limited by the organic vapor contaminants present in the insulation and coil windings of the objective lens and beam deflector stage of the microscope.

It was originally presumed that the auxiliary pumping system would be a vital requirement for removing the excess SiH_4 and H_2 from the CVD experiments. However, pressure tests and gas-flow tests with the microchamber installed showed only a slightly improved vacuum performance. Furthermore, the pumpdown procedure for the specimen chamber was more involved using the auxiliary pumping system. Accordingly, it was decided not to use the auxiliary system for the CVD experiments undertaken later.

2. IN SITU PVD EXPERIMENTS

Physical vapor deposition (PVD) experiments were performed early in the contract period to establish operational procedures with the modified electron microscope and to identify some of the technical problems to be encountered later in the CVD investigations. In these experiments a metal, usually Al but sometimes Au, was evaporated in situ from a small heated filament onto a heated substrate.

The accomplishments of the PVD experiments were two-fold: (1) they demonstrated the feasibility of in situ nucleation and growth studies in the microscope and (2) they provided a test mechanism whereby the effectiveness of various microscope modifications and procedures common to both PVD and CVD in situ studies was determined. The PVD experiments provided considerable important information of this type during the design and construction stage of the CVD microchamber.

The substrate heater for the PVD experiments was a standard EM6 electron microscope heating stage. The heating grid was made by cutting off opposite sides of a circular 200-mesh stainless-steel microscope specimen grid, leaving only the central 15 grid bars. This heater was capable of achieving a substrate

temperature of 1450C (the melting point of stainless steel) with a battery-supplied dc current of 1.9a.

A flange containing the source filament for the PVD experiment was fabricated and installed on the microscope specimen chamber, replacing the right-hand side of the air lock. A single V-shaped 0.020-in dia W wire filament heated the evaporant material. Al, for example, could be evaporated at a satisfactory rate with a current of 23a supplied by a well-regulated dc power supply. A shield surrounding the source filament provided adequate thermal protection for the microscope and confined the depositing material to the substrate and a small area of the specimen holder.

a. Al Deposition Experiments

The Al PVD experiments were normally performed by evaporating Al onto an amorphous carbon film heated to ~300C. A sequence of electron micrographs taken during the course of one such in situ experiment is shown in Figure 84. The first photograph in the series is that of the original substrate prior to nucleation; the particles visible are dust particles, not Al nuclei. They act as convenient reference points so that the same area can be located in the subsequent photographs.

Several important aspects of thin-film growth can be observed in these micrographs. Locations A and B in Figures 84b and c illustrate the formation of a grain boundary in a large crystal formed from several smaller crystals. Various contrasts visible at A in Figure 84b indicate that a number of differently oriented crystals are present. (The loss of resolution in reproducing the original photographs here may make discrimination of individual nuclei difficult, but they are readily discernible in the original micrographs.) Only three of the orientations survived the coalescence process; the remainder not visible in Figure 84c were absorbed, atom by atom, by their neighbors. Note that at A both orientations have apparently grown at approximately the same rate.

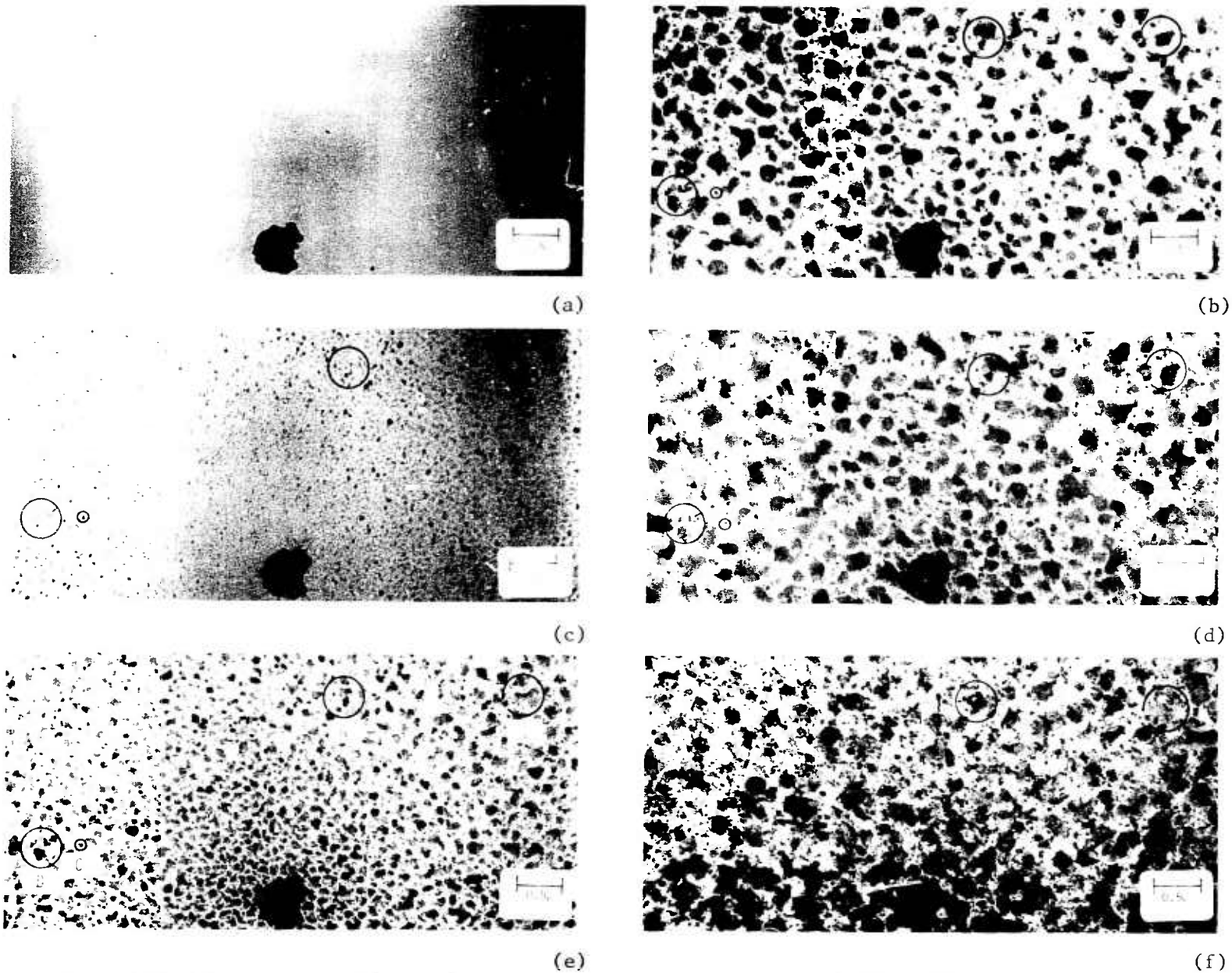

Figure 84. Sequence of Electron Micrographs Recorded during Al PVD at Times of (a) 0 sec, (b) 110 sec, (c) 130 sec, (d) 150 sec, (e) 190 sec, (f) 10 min

At B, it is seen that the original crystals grew at different rates, resulting in one orientation becoming dominant. The dark portion of the top crystal in Figure 84c is almost completely developed in Figure 84b and no further growth has occurred except in the light portion. The bottom crystal, however, shows the reverse behavior. (All four crystals are of different orientations.) Note at location C that not all crystals have grown at the same rate. At location D, the large extent to which rearrangement occurs during film growth is visible.

Some areas of the substrate originally covered with Al may become bare when several islands coalesce, and secondary nucleation will then occur in these bare areas. Such an area can be seen immediately outside and to the upper left of location B in Figures 84c and 84d. The presence of secondary nuclei causes some of the apparent "clutter" in the photographs; the remainder is caused by oxidation of the Al.

Al deposition was stopped after 190 sec in this particular experiment, but the substrate and deposited film were permitted to remain at an elevated temperature for an additional 10 min. Almost total oxidation of the Al occurred, completely changing the character of the film. All the O_2 required for the reaction was supplied by the residual O_2 and water vapor present in the electron microscope vacuum of $<1 \times 10^{-5}$ torr. Much of the water vapor originates in the photographic plates used for still pictures, a problem which could not be entirely eliminated but could be considerably reduced by extensive pre-pumping of the plates.

b. PVD Experiments with other Materials

A few PVD experiments were conducted using Au as the evaporant. An interesting effect was noted during several such experiments: The Au film was extremely fine-grained on the amorphous carbon substrate region irradiated by the 100 KV electron beam, but quite large-grained elsewhere. At first it was thought that pronounced enhancement of the nucleation rate had been induced by the electron beam. However, it was later shown to be caused by contamination altering the nucleation and growth processes.

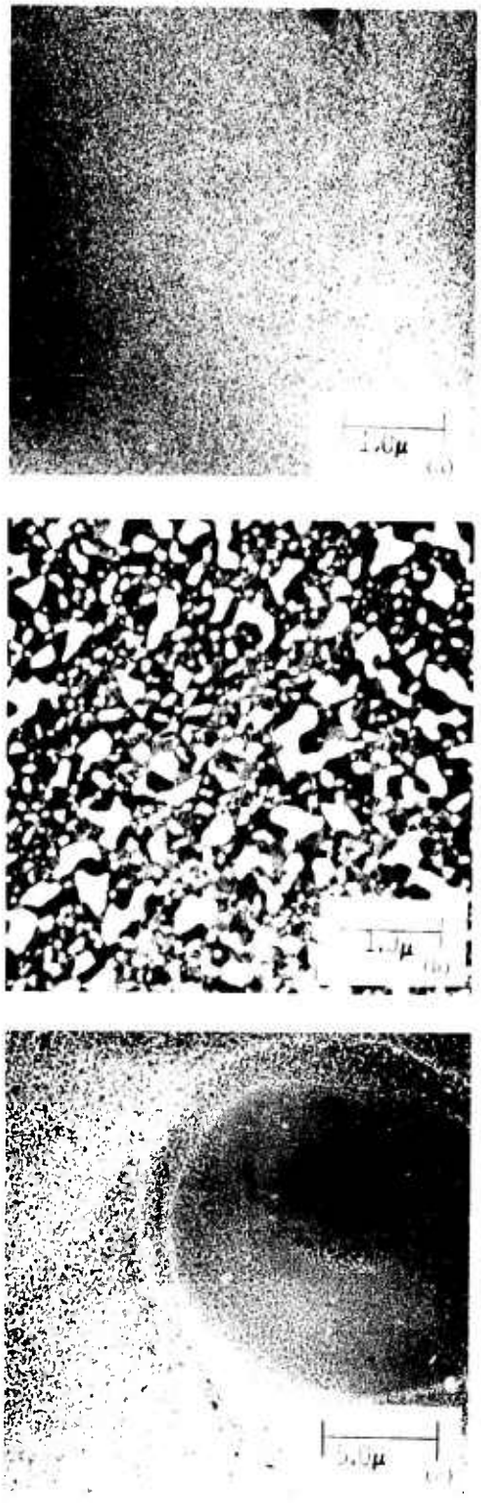

Figure 85. Au Film Grown in Electron Microscope by PVD. (a) Region Observed during Growth; (b) Adjoining Region not Irradiated by Electron Beam; (c) Lower Magnification View of Regions (a) and (b).

Figure 85a shows the region that was observed, and hence continuously irradiated by 100 KV electrons, during one such experiment. Figure 85b taken after completion, shows an adjacent area which had been outside of the field of view and not struck by the electron beam during the deposition experiment. The relatively large-grained character of the continuous lace-like network is typical of this stage in the normal growth of thin films. Figure 85c is a lower magnification view taken with the electron beam expanded to include both of the areas shown in a and b.

From the appearance of Figure 85c coupled with a gradual buildup of contamination on the specimen during the post-experiment examination of the deposit, it was concluded that a heavy contamination layer had probably formed during the experiment, becoming intermixed with the Au film during growth. Normal diffusion of the Au atoms became impossible and a fine-grained structure resulted. These observations of sample contamination during growth of PVD films were actually the motivating factors for the microscope cleaning and vacuum-system improvements discussed previously.

An excellent example of the nucleation and growth of Cr on $(01\bar{1}2)Al_2O_3$ was obtained in another PVD experiment. The Cr was supplied by thermal evaporation from the stainless steel of the substrate heater grid, inadvertently heated to above 1000C. The growth sequence is shown in Figure 86. The first micrograph was taken prior to the start of the experiment and represents a typical clean electron-transparent ion-thinned Al_2O_3 substrate. Two holes are visible in the substrate - a "large" one ~0.5μm dia and another ~0.03μm dia located ~0.8μm below it. The dark curved bands are extinction contours, discussed in Section 6-3. The typical development of numerous islands and island clusters can be followed through the sequence of micrographs.

3. IN SITU CVD EXPERIMENTS

The overall objective of these investigations was to examine the nucleation and early-stage growth of Si on Al_2O_3 directly and in real time, i.e., in situ in a transmission electron microscope. The reaction of interest was the pyrolysis

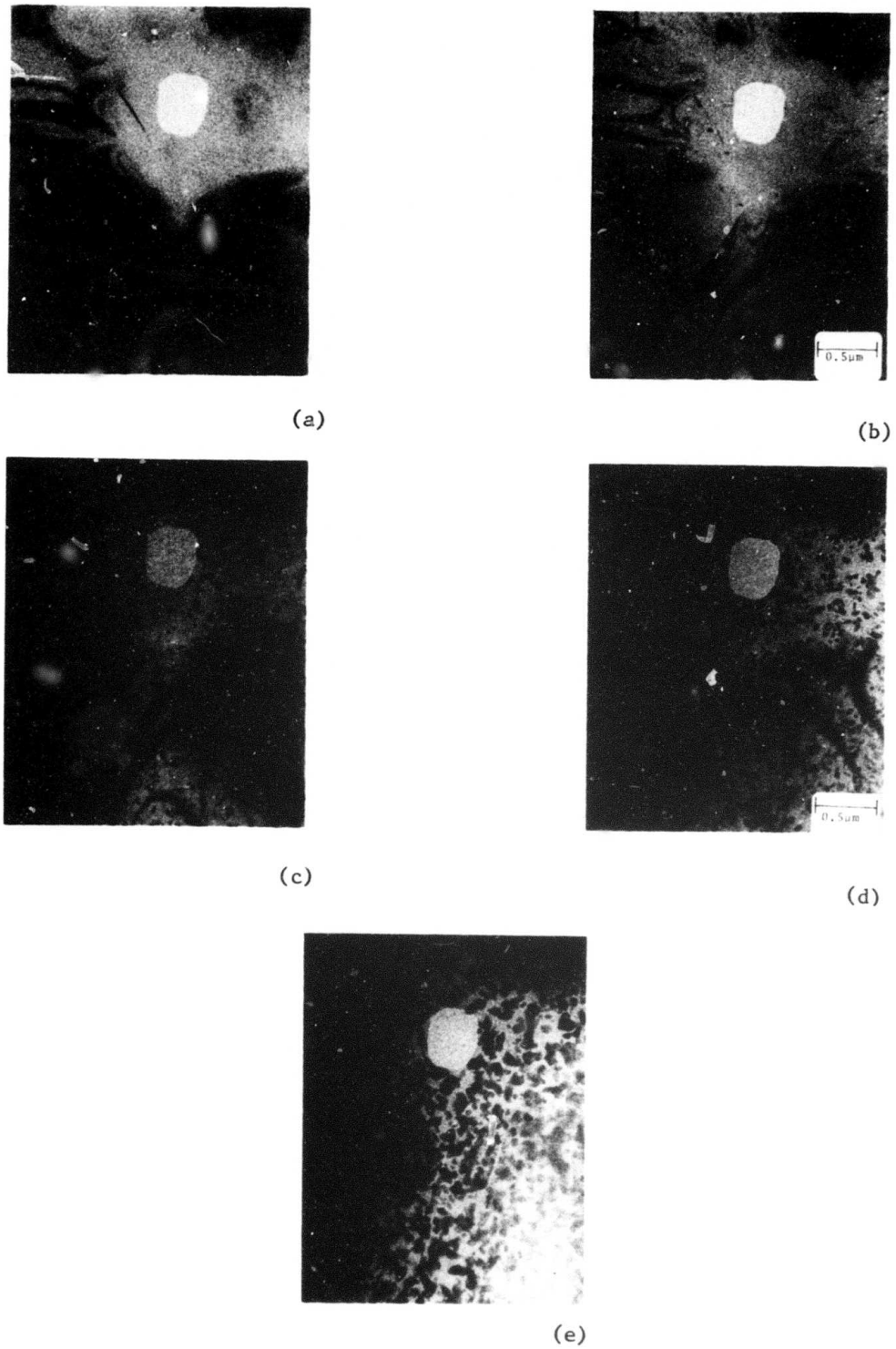

Figure 86. In Situ Nucleation and Growth of Cr on $(01\bar{1}2)Al_2O_3$ after (a) 0 min, (b) 8 min, (c) 14 min, (d) 16 min, (e) 18 min.

of SiH_4 to form Si and H_2, which typically takes place at 1000-1200C at ~1 atmosphere pressure. The transmission electron microscope typically is operated at room temperature in a vacuum of $\sim 10^{-5}$ torr. The magnitude of the task involved becomes clear when it is realized that the normal electron microscope specimen fits into a volume that is 1/4 in in diameter and 1/4 in high.

During the initial planning for these investigations an extensive literature review was conducted. A bibliography of papers related to in situ electron microscopy studies of nucleation and growth was compiled and is included in this report as Appendix 3. This bibliography was kept updated as the program progressed. Despite the large number of references, only a few are directly pertinent to the CVD studies involved here. In particular, the excellent works of Pashley et al (C1 to C3) and Poppa (C4 to C8) refer specifically to PVD, not CVD, but are illustrative of the information obtainable by the in situ technique. Several in situ CVD experiments have been performed (B4, B7, B10, and B14), but they involved low temperatures and relatively simple film-substrate systems. None involved pyrolysis of a gaseous phase to form a solid phase on an electron transparent substrate. Together with the other references in the bibliography they are valuable chiefly for the collective wealth of experimental ideas and techniques which may be applied to similar research.

Two distinctly different experimental approaches were considered for these investigations. The first - and preferred - plan was to conduct the in situ growth experiments under modified gas flow conditions which were to be as close as possible to those normally encountered in the conventional laboratory growth of Si from SiH_4. This plan was implemented with the construction and eventual use of a CVD microchamber which heated an electron-transparent Al_2O_3 substrate in a small volume of flowing SiH_4 and H_2.

The second (alternate) plan was to conduct a molecular-beam type of experiment, in which a directed beam of SiH_4 and H_2 in appropriate proportions would be made to impinge on a heated electron-transparent Al_2O_3 substrate in high vacuum.

The latter approach was rejected, primarily because it was less likely to provide information directly applicable to conventional growth of Si films for semiconductor device applications.

In addition, the physical mechanism of a CVD experiment conducted in a molecular-beam system is significantly different from that in a conventional laboratory flow system or in the modified flow system eventually used in these studies. The difference lies primarily in the effective supersaturation, i.e., the number of molecules/cm^2-sec striking the substrate surface. In a molecular-beam system all of those H_2 or SiH_4 molecules adsorbed on the substrate surface which reevaporate (desorb) are irretrievably lost from the system. Thus, the impingement rate is only that due to the flux from the directed beam. In a conventional flow system, however, all molecules on the surface which desorb have a high probability, through gaseous collisions, of subsequently returning to the surface. The effective supersaturation is thus considerably greater in the conventional system.

Numerical comparisons show the supersaturation difference clearly. At atmospheric pressure and room temperature the H_2 impingement rate is approximately 1.1×10^{24} molecules/cm^2-sec. At a reduced pressure of 10 torr the impingement rate is 1.4×10^{21} molecules/cm^2-sec. This should be compared with the rate available from a molecular beam, typically 1×10^{14} to 1×10^{16} molecules/cm^2-sec. The ratio of impingement rates for a conventional laboratory system and the in situ system used for these studies is thus about 76, whereas the same ratio for a conventional versus a molecular beam system is 1×10^8 to 1×10^{10}.

Two other differences may also be significant. First, the energy of the impinging molecules is absolutely determined in a molecular-beam arrangement, following the Maxwell-Boltzmann distribution corresponding to the source temperature. In the case of a flow system the gas molecules are heated to varying extents by collision as they approach the heated substrate. Second, a molecular-beam experiment always yields a heterogeneous reaction, whereas there is always the possibility of a homogeneous component being present in the hot layer of gas surrounding the substrate in a conventional flow system.

If the homogeneous reaction postulated by Givargizov (Ref 75) and indicated by the results described in Section 5 are correct, then indeed molecular-beam experiments would not give results readily relatable to those observed in conventional laboratory deposition of Si films by SiH_4 pyrolysis.

In view of these differences and an overriding desire to produce in situ CVD results which would directly assist in conventional laboratory growth of Si on Al_2O_3 the modified flow system was selected.

a. CVD Microchamber Design, Construction and Test

Selection of a modified flow system required that a microchamber be fabricated to minimize the volume of gas surrounding the specimen so that there would not be excessive scattering of the electron beam. Such scattering would result in both an intensity loss in the primary electron beam and an information loss, i.e., lower resolution in the resulting image. Electrons scattered at angles greater than the objective aperture semi-angle reduce the intensity of the beam; electrons scattered, then rescattered, such that the net scattering angle is less than this reduce the information content of the transmitted electron image.

The magnitude of these effects may be calculated to a first approximation by considering only the intensity loss of the electron beam as it passes through a gas layer. This loss is a function of the electron scattering cross-section (determined by the specific gas composition) and is directly proportional to the product of the gas pressure and the gas layer thickness. The latter two variables determine the dimensions of the specimen chamber; the thinner the microchamber in the direction of beam travel, the greater the maximum permissible gas pressure.

The electron beam intensity loss was calculated for SiH_4 and O_2 by the method described in Appendix 6. Specific results are presented in Table 31, based on the actual gas layer thickness of 1.6mm for the CVD microchamber finally constructed. Additional results are given in Appendix 6.

Table 31. Maximum Permissible Pressure-time (Pt) Product for SiH_4 and O_2 for Various Electron Beam Intensity Losses

Intensity Loss $\frac{I_o - I}{I_o} \times 100$ (%)	SiH_4		O_2	
	Pt Product (torr-mm)	Maximum Pressure P for t = 1.6 mm (torr)	Pt Product (torr-mm)	Maximum Pressure P for t = 1.6 mm (torr)
1	0.54	0.34	0.62	0.39
2	1.09	0.68	1.24	0.77
5	2.77	1.74	3.15	1.98
10	5.69	3.56	6.46	4.03
20	12.0	7.57	13.7	8.55
50	37.4	23.4	42.5	26.6

(1) Design and Construction

The design of the CVD microchamber* is shown in a cutaway drawing in Figure 87 and in photographs in Figures 88 and 89. The substrate is mounted on a resistively heated grid which is held by screws in contact with inner and outer electrodes. The sample and the grid are totally enclosed in a thin cylindrical region, vacuum-tight except for the gas inlet and two apertures (for the electron beam entrance and exit). The SiH_4 gas enters the microchamber through a coiled gas inlet tube, surrounds the sample, and exits via the two apertures. The microchamber has a gas layer thickness of 1.6mm through which the electron beam must pass.

Certain constructional details (Figure87) of the CVD microchamber are of interest. The center electrode contains a 100μm drilled hole to permit the electron beam to enter and a limited amount of gas to exit. A raised projection contains a tapped hole for the No. 40 National Miniature (NM) screw (0.016-in dia, 254 threads per in) which holds one end of the heating grid. The center electrode is brazed into a base which is an extensively modified AEI-EM6 electron microscope specimen holder.

One end of a coiled Cu gas inlet tube is brazed into the center electrode base, and the other end is joined to the CVD flange by a "Swagelok" tubing connector. The flat portion of the base is slotted to permit gas to flow from the inlet tube to the annular space between the inner and outer electrodes and then to the specimen. The center electrode is Be-Cu, selected for its superior machining characteristics over those of pure Cu,which is unsuitable for drilling and tapping the miniature holes required.

The outer electrode is attached, by means of three No. 80 NM flat-head screws (0.032-in dia, 127 threads per in), to the lava insulator which in turn is fastened to the base with four No. 80 NM fillister-head screws. The lava

*Constructional details of the microchamber were described in a brief technical paper (Ref 76), included in this report as Appendix 7.

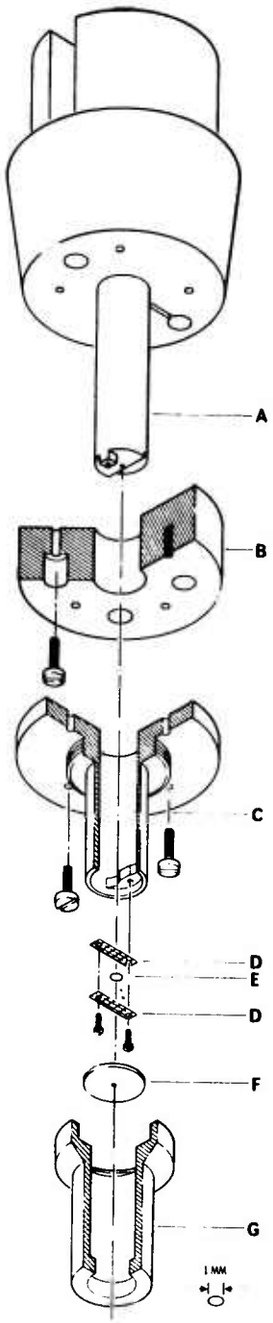

Figure 87. In Situ Chemical Vapor Deposition Microchamber. (A, center electrode and gas limiting aperture; B, lava insulator; C, outer electrode; D, heating grid; E, sample; F, removable aperture; G, aperture cap.)

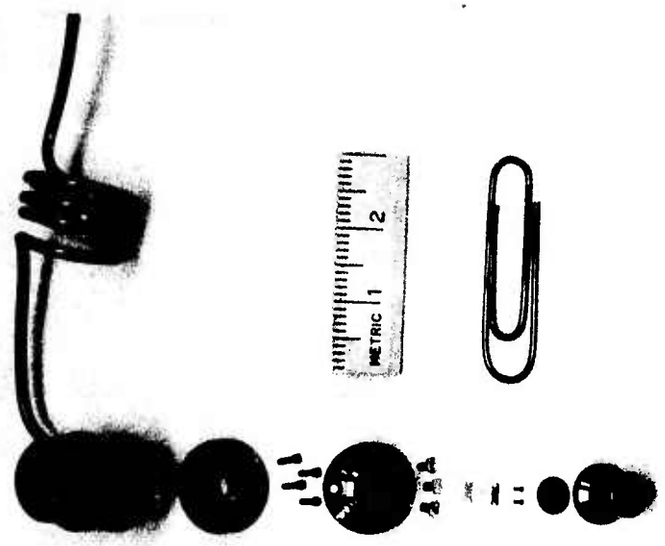

Figure 88. CVD Microchamber, Disassembled

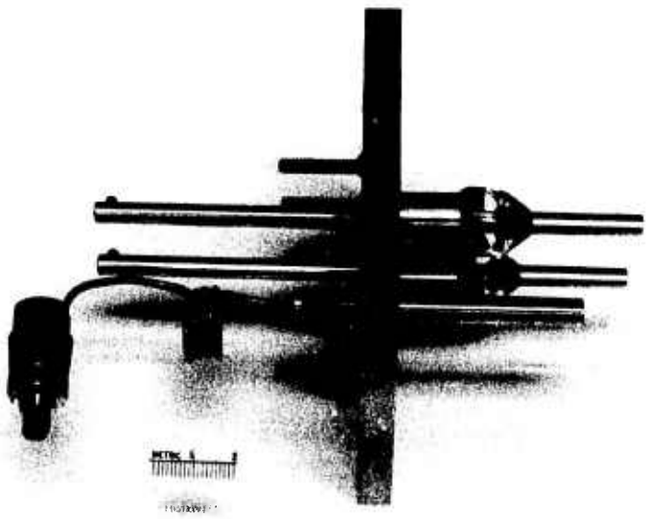

Figure 89. CVD Flange for Electron Microscope, with Assembled Microchamber Mounted in Place.

insulator was machined somewhat oversize in the unfired, soft condition, then fired, ground flat, and lapped to a 2-microinch surface finish. The bottom of the outer electrode and the flat portion of the center electrode base were also lapped to a 2-microinch surface finish so that the assembly is gas tight at these joints when assembled. This portion of the microchamber need not be disassembled to load or unload specimens.

The outer electrode has a projection containing a small tapped hole which accepts the No. 40 NM screw holding the other end of the heating grid. A threaded cap over the outer electrode holds a thin removable copper aperture disk in place. This aperture also contains a 100μm hole to permit the electron beam to exit. The outer electrode and cap are made of Ti, selected for its machinability, nonmagnetic properties, and low vapor pressure at elevated temperatures.

It was originally anticipated that stainless-steel screws would be used to attach the heating grid to the electrodes. However, use of similar screws in the PVD experiments revealed a small trace of ferromagnetic material in the essentially nonmagnetic screws; this created a distorted magnetic field in the vicinity of the specimen and prevented attainment of maximum resolution of the electron microscope above 20,000X. Various heat treatments failed to reduce the ferromagnetic content of the stainless-steel screws, so specially machined Ti screws were made.

Electrical and gas inlet connections to the microchamber were made through the vacuum region of the electron microscope by means of the CVD flange (Figure 89) attached to the specimen chamber* where the right-hand side of the air lock was normally installed. The microchamber gas inlet was a coiled, soft Cu tube which had to be attached to the flange for each experiment with a tube fitting. The coiled-tube design permitted some translational motion of the microchamber, thus allowing centering with respect to the electron beam.

---

*See footnote on p. 241 regarding the specimen chamber.

A gas-handling manifold and metering system was installed on the microscope and is shown in the photograph in Figure 83 and schematically in Figure 90. The manifold is of stainless-steel tubing (1/4 in dia) connected to the microchamber through the CVD flange. Gas was bled into the microchamber through a Whitey 22RS4-A metering valve, and the microchamber pressure was measured with a Leybold-Heraeus TM202 thermocouple gauge. The SiH_4:H_2 ratio was adjusted in the gas manifold at atmospheric pressure and then a small fraction was bled into the microchamber at reduced pressure. The remaining gas was exhausted and burned off. The entire gas-handling manifold could be evacuated to a pressure of <10 torr.

(2) Gas Flow Tests

The gas flow tests conducted with the microchamber and gas-handling manifold were of two types: (1) the gas pressure in the electron microscope was measured as a function of the microchamber gas pressure, and (2) the flow rate of gas through the microchamber was measured as a function of pressure. The gas pressure in the electron microscope was measured by an ionization gauge mounted on the side of the specimen chamber; the microchamber pressure was measured by the thermocouple gauge mounted between the microchamber and the metering valve, so the measured pressure could be somewhat greater than the actual pressure in the substrate region. Both apertures were 100μm in diameter.

Results of the pressure tests with only the normal microscope pumping system in operation are shown in Figure 91. The maximum pressure permissible in the electron microscope was 1×10^{-4} torr, which corresponds to a maximum permissible microchamber pressure of approximately 1500 millitorr. The maximum permissible microchamber pressure varied slightly from one run to another, as shown by the four tests of Figure 91, presumably dependent upon how tightly the removable aperture was reinstalled.

Pressure tests with the auxiliary pumping system installed showed only a slightly higher maximum permissible microchamber pressure. It thus appeared that a larger pumping capacity would be required for the auxiliary system to

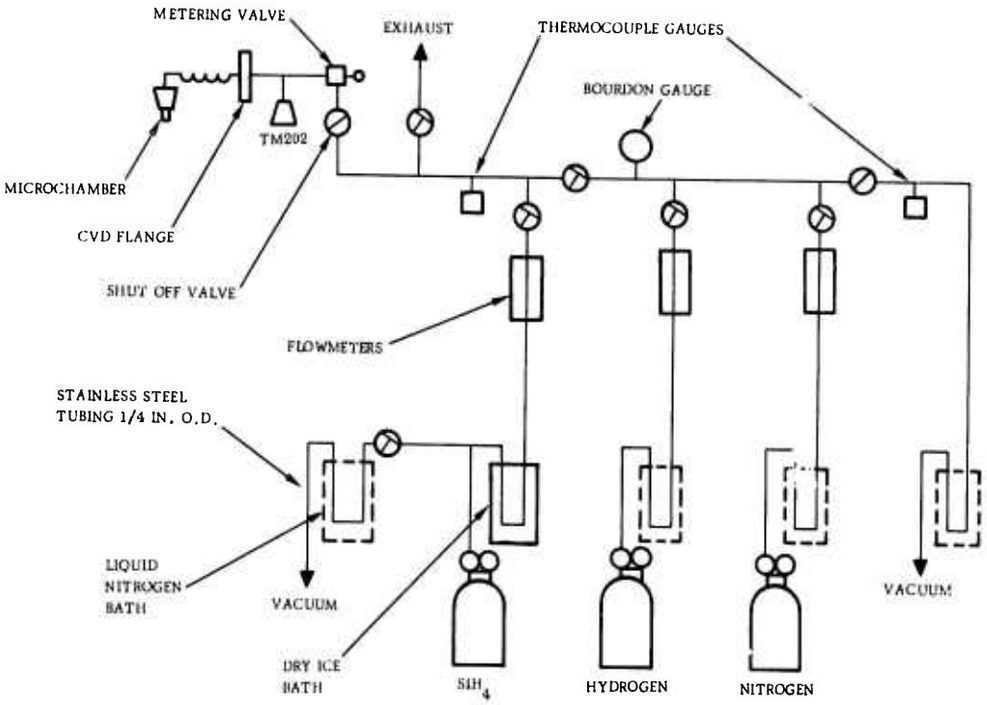

Figure 90. Schematic Diagram of Gas-handling Manifold for In Situ Studies

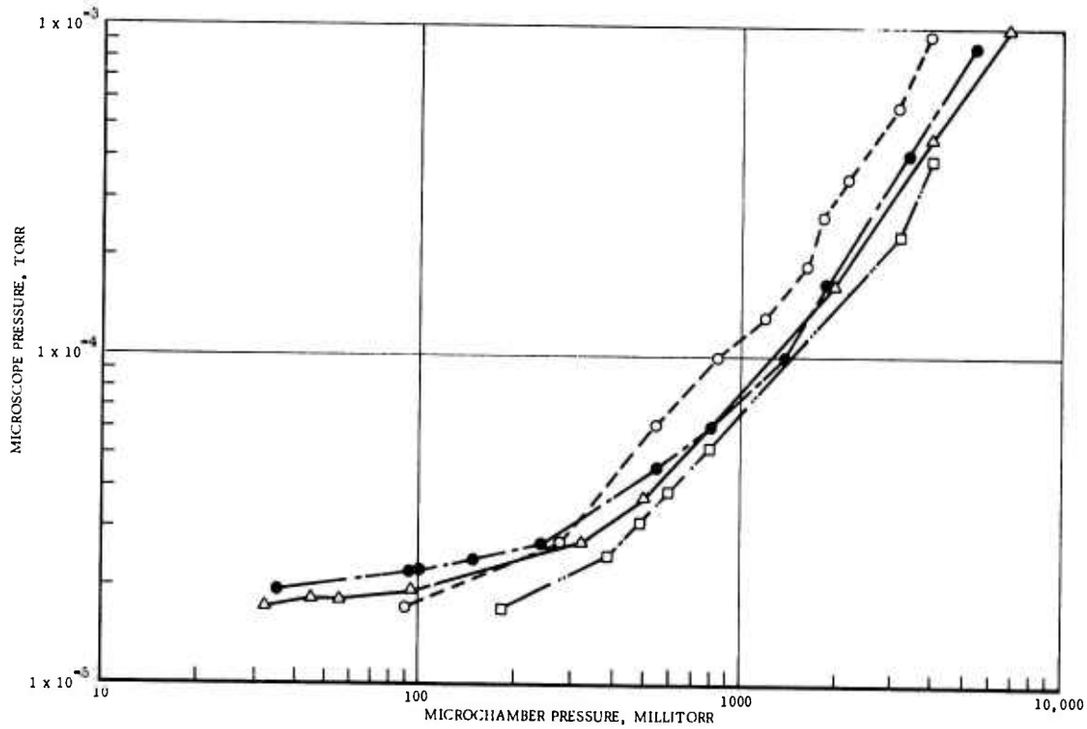

Figure 91. Measured Pressure in Electron Microscope as Function of Microchamber Pressure

be of significant value. The SiH_4 pressures attainable in the microchamber were found adequate, so only the normal microscope pumping system was utilized for the CVD experiments, as indicated previously.

The gas flow rate through the microchamber was determined by measuring the pressure decay when the metering valve was suddenly closed and then calculating the flow in cm^3/min corrected to standard temperature and pressure. The gas flow was found to vary with pressure as shown in Figure 92.

The presence of gas in the microchamber causes unwanted multiple scattering of many electrons in the electron beam, which consequently damages the image quality. Earlier estimates of the magnitude of this effect were shown to be correct, as only a slight change in image quality is noticeable in Figures 93a and 93b. These micrographs, taken under otherwise identical conditions, illustrate the loss of image quality visible in a network of cellulose acetate (a processing residue) on an amorphous carbon substrate with the microchamber containing 50% SiH_4 and 50% H_2 at a pressure of 3.5 torr.

With the removable aperture and aperture cap of the microchamber in place, the normal objective aperture of the electron microscope must be removed. The removable aperture is used in its place, with the resulting image quality a function of the aperture size, being better the smaller the aperture size. A 100μm dia removable aperture was used in place of the normal 25μm objective aperture, with a consequent slight reduction in image quality. This appeared as a slight loss in contrast and an increase in overall background intensity, which is visible to the experienced observer in Figure 93b. It was intended that as more experience was gained in aligning the removable aperture, a smaller aperture size would be used; however, the difficulty of sample loading and alignment precluded this.

After completion of the gas flow tests, a number of trial experiments were performed with SiH_4 to ensure that the gas handling procedures used were completely safe. A liquid N_2 trap had to be installed between the vacuum pump and the manifold, since otherwise a minor explosion/reaction would occur

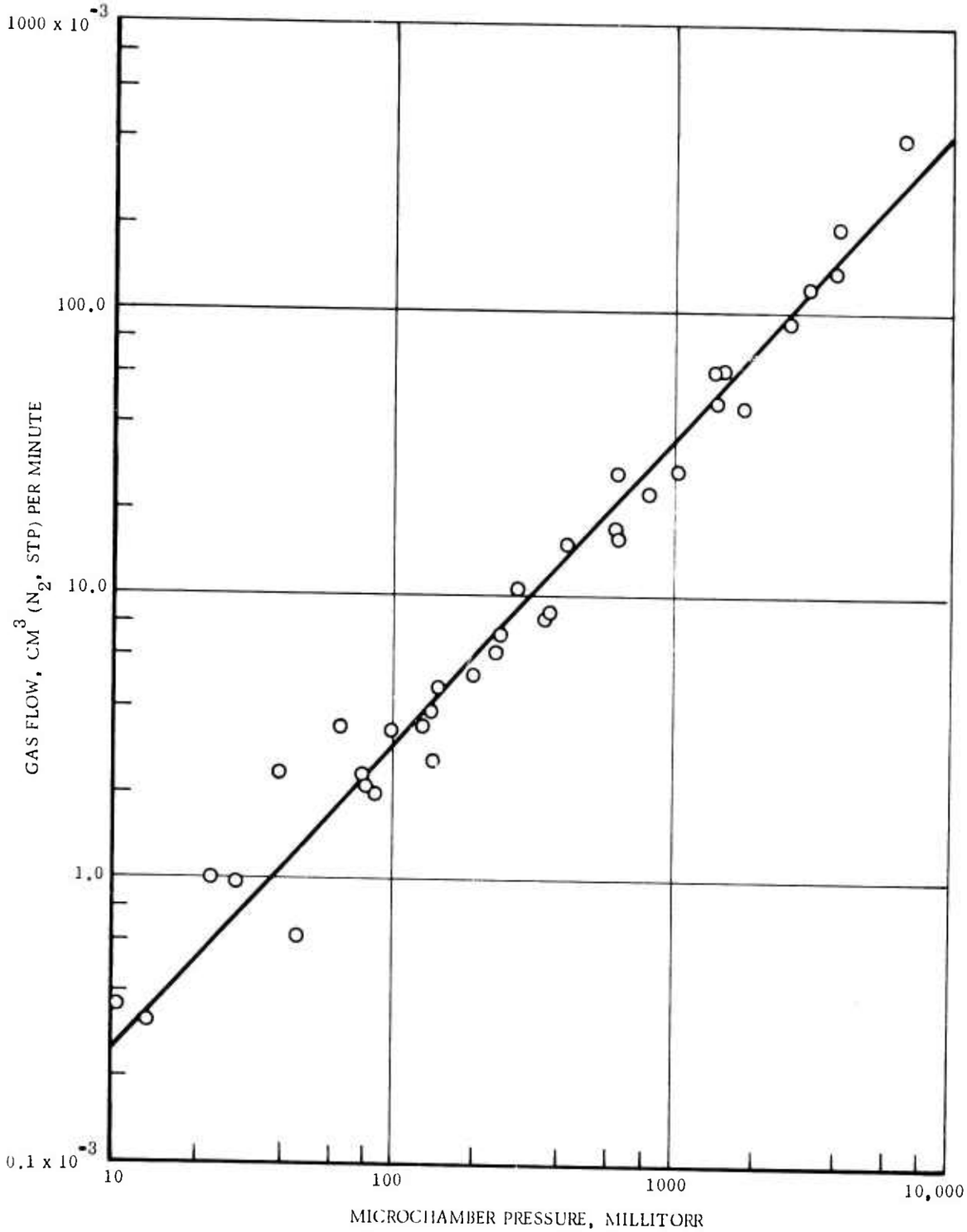

Figure 92. Measured Gas Flow through Microchamber as Function of Pressure

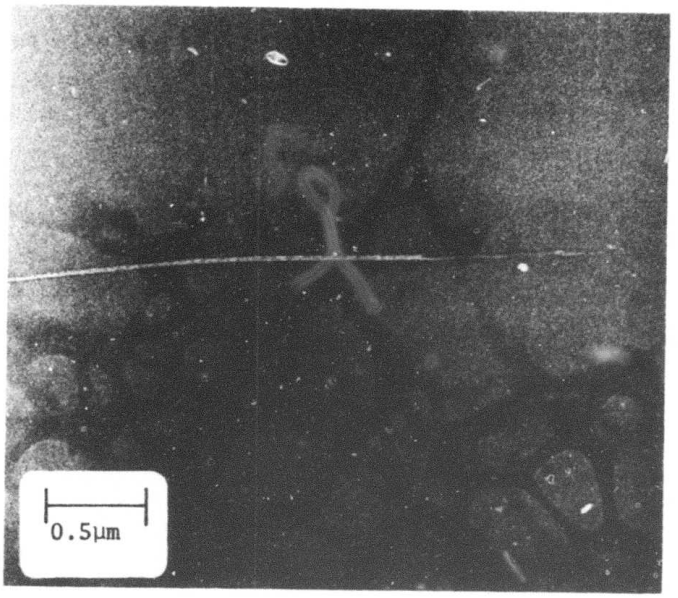

(a)

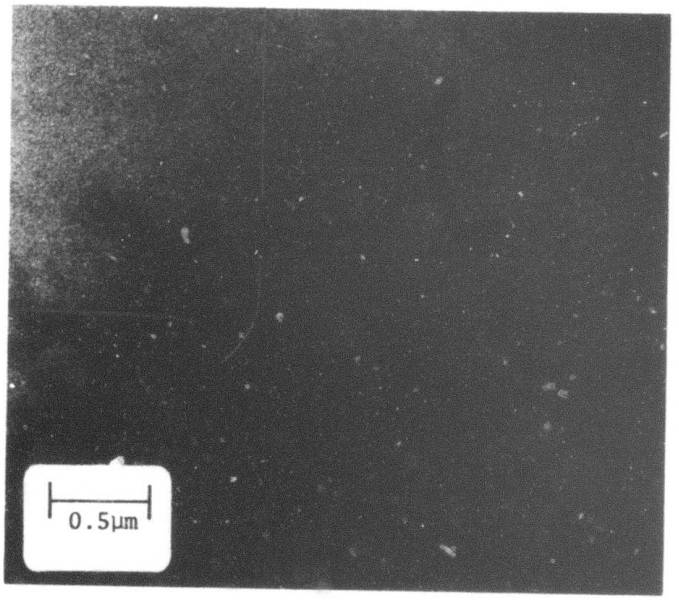

(b)

Figure 93. Electron Micrographs Showing Image Quality in CVD Microchamber at (a) $1x10^{-4}$ torr (normal microscope vacuum) and (b) 3.5 torr (50% SiH_4 and 50% H_2). (Image is cellulose acetate network on amorphous carbon substrate.)

in the pump exhaust due to the behavior of SiH_4 upon exposure to air. Warming the liquid N_2 trap slowly permitted the condensed SiH_4 to evaporate sufficiently slowly to prevent any serious difficulties.

b. Si Film Growth on Amorphous Carbon Substrates

The first in situ Si nucleation and growth experiments were conducted with electron-transparent amorphous carbon substrates, to define the operational parameters involved in Si growth in the CVD microchamber without the difficulty of loading and aligning attendant upon such experiments with Al_2O_3 substrates.

Although intended as a preliminary to deposition on Al_2O_3, these experiments are significant in themselves for they represent the first successful chemical vapor deposition of Si films inside an electron microscope. It was thus shown that it is indeed feasible to study the nucleation and early growth of a semiconductor film deposited by CVD by in situ transmission electron microscopy.

The following important features of this growth system were demonstrated:

(1) The in situ pyrolysis of SiH_4 to form Si is possible without adverse effects on the electron microscope.
(2) The study of CVD nucleation and early growth stages by in situ transmission electron microscopy is feasible.
(3) Crystalline Si can be grown in situ on amorphous carbon substrates, apparently without the formation of SiC.
(4) The Si islands formed on amorphous carbon are three-dimensional, angular in nature, and do not change significantly during coalescence.

The amorphous carbon substrates used for the in situ experiments were mounted, using standard techniques (Ref 77), onto a specially-cut heating grid. After the manifold and microchamber were H_2-purged at the desired pressures, the sample was heated and SiH_4 was then added to the H_2 in the desired proportion. Although specific experiments varied somewhat, the most suitable reactant concentration was 6% SiH_4 in H_2 at a total pressure of 1.3 torr in the microchamber.

The results of the initial depositions were disappointing in that a foreign material frequently deposited on the carbon substrate prior to Si deposition. The stainless-steel heating grid itself was found to be one source of contamination, as Cr was preferentially evaporated above 1000C and condensed on the substrate. Normally, the contamination was visible as a faint collection of small nuclei which moved about the surface leaving irregular trails somewhat similar to those shown in Figure 94 (which, however, are from a different origin). The appearance was similar to that observed in the catalytic oxidation of graphite (Ref 78), although the origin must be different.

In an effort to avoid contamination from the stainless-steel grid, other grids of W, Pt, and Ti were tested. All have a low vapor pressure at elevated temperatures so could be heated to at least 1200C before contamination from the grid itself would become noticeable. Both W and Pt have a low resistivity, requiring a very high heater current to reach the desired temperatures. Despite this, several in situ deposition experiments were performed with W heating grids, especially since a temperature-current calibration had been established.

An unidentified source of contamination appeared to be present if W grids were used with excessive heater power. Figure 94 illustrates one such experiment, showing the way in which this contamination confused the observation of Si growth. The first micrograph was taken prior to heating the substrate; the objects shown are dust particles originally present on the film. They serve as reference markers so that exactly the same areas can be compared in the series of micrographs. In Figure 94b small particles (or droplets) have nucleated and moved about the surface, leaving an irregular trail. They continued to move about the surface as the experiment proceeded, as shown in Figures 94b-d The contaminant was almost certainly not W evaporated from the heating grid (the vapor pressure of W is too low), so it was probably material evaporated from another part of the microchamber - most likely Cu from the aperture plates. Si islands are not visible until Figure 94e (44 min. of "growth"), at which time rapid growth began.

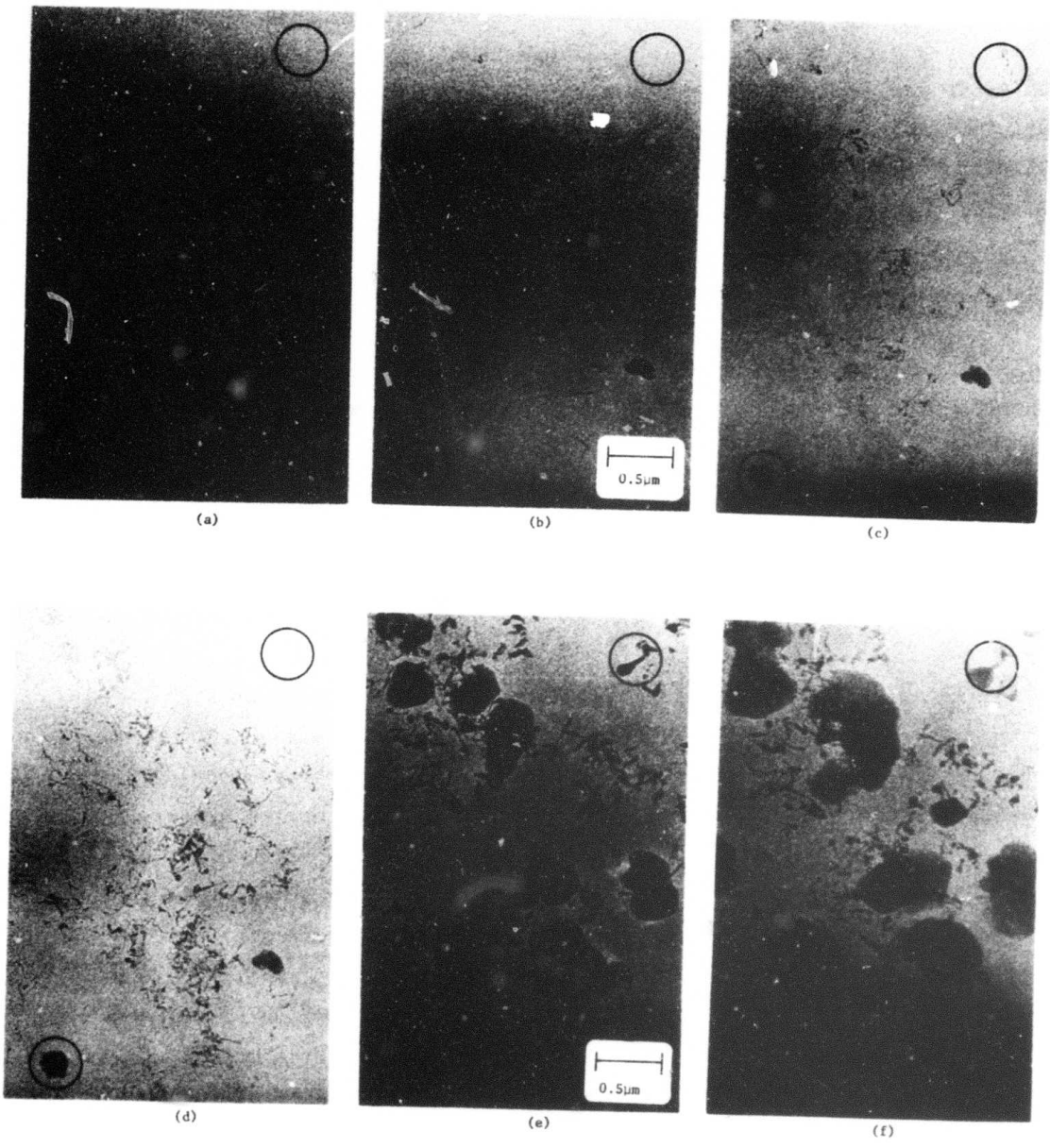

Figure 94. In Situ Nucleation on Amorphous Carbon Substrate at (a) zero time, (b) 4 min, (c) 10 min, (d) 37 min, (e) 44 min, (f) 45 min

When Ti grids became available they were found to be the most satisfactory of all those tested; specifically, a heater 4 meshes wide and 15μm thick was best. Ti was used for all of the in situ experiments on Al_2O_3 substrates, and no contamination was observed in subsequent experiments provided the heater power was kept below 0.3 w.

The growth sequence most representative of in situ Si growth on amorphous carbon substrates is shown in Figure 95. The substrate temperature was ~800C, as determined by the established method based on knowledge of the heater power, gas pressure, and specific location of the area examined. There is a temperature gradient of ~2.5 deg C/μm from the top of the micrographs to the bottom, which accounts for the variation in nucleation density and island size. The substrate region nearest the heating grid (not shown) was slightly hotter, so Si nucleation appeared in that region first. Figure 95a was taken 12 min after SiH_4 introduction. It should be noted that nucleation occurred on both sides of the substrate in this experiment, so the true nucleation density is one-half the apparent density as seen in the micrographs.

The most significant conclusion to be drawn by examination of Figure 95 is that the Si CVD nucleation and growth process is "normal", i.e., very similar to that of PVD growth. The islands are three dimensional and grow both by the addition of freshly deposited material and by coalescence with neighboring Si islands. Many of the growth features found in Figure 95 are also seen in Figure 84. Thus, it appears that the presence of additional gaseous and/or adsorbed phases associated with the CVD process does not significantly alter the essential growth features. Most of the conclusions drawn by Pashley et al (Ref 79) for PVD growth appear to be applicable to CVD growth as well.*

One feature of Si CVD growth which differs from the PVD growth reported in the literature concerns the Si island morphology. The CVD Si islands appear

---

*See other related references in Appendix 5.

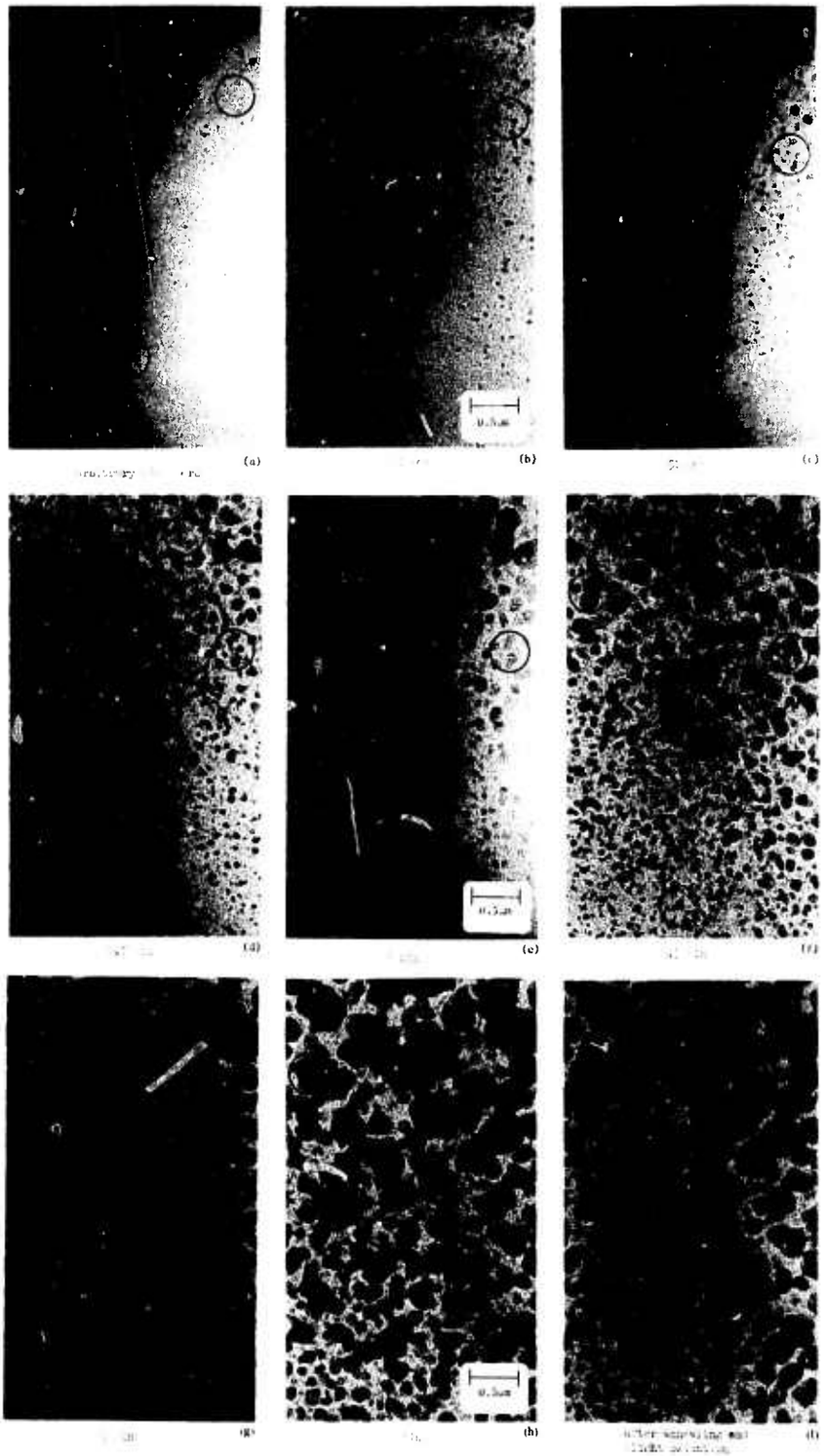

Figure 95. In Situ Growth of Si on Amorphous Carbon Substrate

more angular in nature and do not seem to change their character during further growth and coalescence. In contrast, in situ PVD experiments with Au and Ag (Ref 79) show considerable "smoothing" of the island surface as growth proceeds.

The difference could be attributed to differences in surface free energy; thus, if Si has a more anisotropic surface free energy then growth facets are more likely to remain. The difference could also be attributed to surface diffusion; if Si surface diffusion on the substrate has a greater activation energy than that of Au or Ag then less diffusion, and hence less smoothing, would result. Both factors are known to be sensitive functions of adsorbed surface contamination. This phenomenon was not further investigated because of time limitations in the program, but it might prove to be significant when CVD growth is compared with PVD growth in finer detail.

c. Si Film Growth on Thinned Single-crystal Al_2O_3 Substrates

Si was successfully grown on Al_2O_3 inside the electron microscope, confirming that the pyrolysis of SiH_4 to form Si inside the electron microscope is feasible and demonstrating that in situ studies of the nucleation and early growth stages of Si on Al_2O_3 also is possible. Based on the completed experiments, several conclusions were formed which supplemented those based on the study of thin samples grown in a conventional CVD flow system.

Only polycrystalline Si was formed in the experiments conducted to date, but there is no reason to presume that single-crystal Si can not be grown in situ. As a result of the problems outlined in a subsequent section it proved difficult to photograph nucleation and growth sequences of the quality anticipated. However, micrographs documenting the in situ growth of Si on Al_2O_3 were obtained.

The in situ experiments utilizing Al_2O_3 substrates were conducted as follows. The substrates were disks 0.030 in in diameter which had been ion-thinned to give an electron-transparent region around the periphery of a perforation.

A suitably thin region was selected, and the sample was mounted onto the heating mesh with the thin "target" region aligned over the fixed gas-limiting aperture. The removable gas-limiting aperture was also aligned, and the microchamber installed in the microscope.

The microchamber was rough-pumped through the gas inlet to $<1 \times 10^{-3}$ torr. The gas inlet valve was then closed and the microchamber pumped through the gas-limiting aperture by the microscope diffusion pump until the pressure dropped below 1×10^{-4} torr (generally overnight).

An experiment was begun by first purging the gas manifold with H_2 at atmospheric pressure, then opening the metering valve to purge the microchamber with H_2 at a pressure of ~1.3 torr. The electron beam was turned on after ~1 hour and the specimen was rapidly examined. If a suitable thin region was in view the heater power was rapidly increased to the desired power, typically 0.24-0.28w. SiH_4 was then added to the H_2 flow, and the nucleation and growth of Si that began thereafter was observed. If no nucleation was observed, the SiH_4 flow was shut off, the microchamber purged for ~15 min, the heater power increased, and the $SiH_4 + H_2$ flow restarted. The gas mixture was generally 6% SiH_4 in H_2, set by mixing 60 cc/min of SiH_4 in 1000 cc/min of H_2 at atmospheric pressure. Only a small fraction of the total mixture was admitted to the microchamber at 1.3 torr; the remainder was burned off.

Loading of the small Al_2O_3 samples was difficult. Originally the entire 0.030 in disk was loaded between two heating grids which were 0.020 in wide. It proved difficult to align the thin area of the sample and the open areas of both grids, so this technique was abandoned. Another method attempted involved a single grid and a semicircular sample held down by a thin carbon film at each end. This approach was also abandoned because of the inherently large risk of contaminating the deposition surface.

The technique ultimately found most satisfactory involved cutting a single Ti heating grid so as to leave several mounting arms in the center, as in Figure 96a. A sector was broken from a 0.030 in Al_2O_3 disk and attached

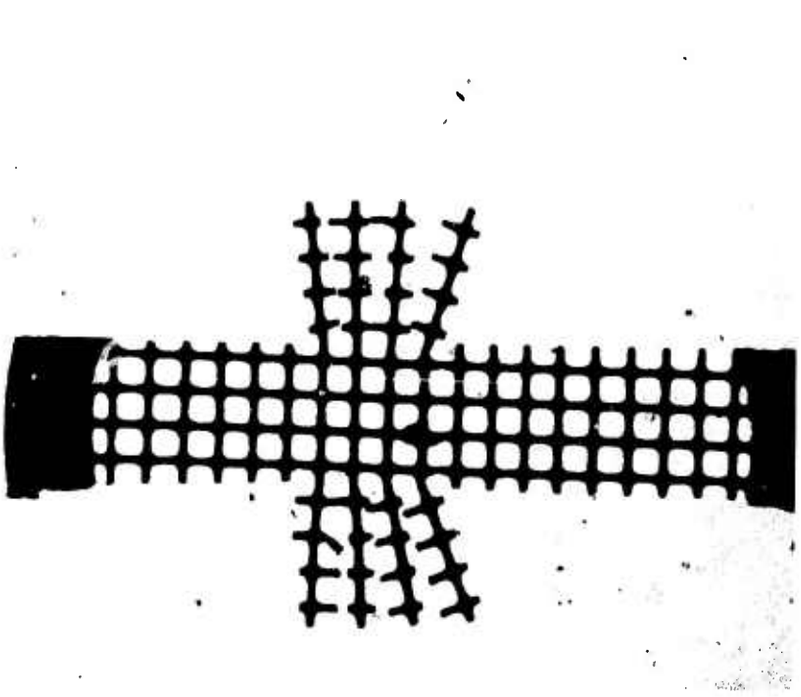

(a) 45X

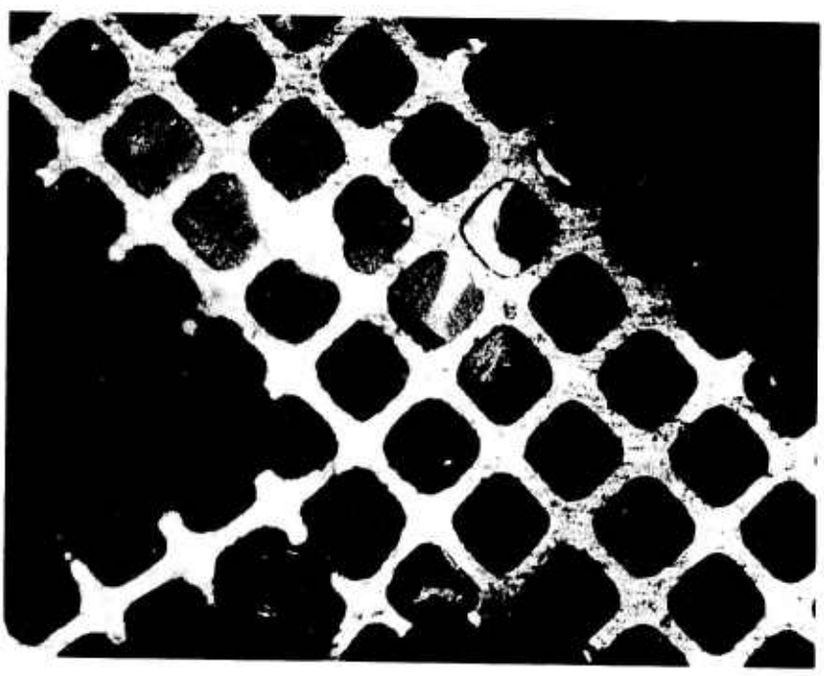

(b) 110X

Figure 96. CVD Microchamber Heating Grid (a) before and (b) after Loading Al_2O_3 Substrate

to the grid by wrapping one or two of the mounting arms around the sample. The electron-transparent region was at the point of the sector, and was placed centrally in the heating grid, as in Figure 96b. The assembly of grid plus sample was fastened onto the electrodes of the microchamber and checked for alignment using an optical microscope. The removable aperture was also centered in this manner. It proved difficult to verify the alignment because of the poor depth of focus of the optical microscope, so electron microscope examination was required. In many cases the sample either shifted position or never had been aligned, so removal of the microchamber from the electron microscope and complete reloading was required.

A total of 26 in situ Si deposition experiments was attempted on this program. Nine were successful in depositing Si on Al_2O_3, but in only six of those did the deposition occur on that portion of the Al_2O_3 visible in the microscope.

Due to various unfortunate experimental difficulties, a sequence of growth micrographs of the quality desired was not obtained. However, all samples were examined after deposition in a conventional electron microscope sample holder, so that conclusive evidence of Si growth was obtained for these samples. The growth sequences which were photographed took place on Al_2O_3 substrates thicker than optimum, so excessive electron scattering through the substrate reduced the information content of the image considerably. The problems inherent in the experiments are discussed in a later section.

The Si island growth and coalescence process was visible during the in situ experiments to varying degrees. In two cases it was clear to the observer that individual Si nuclei had formed and were growing. However, the overly thick Al_2O_3 made photography of the low-contrast image difficult, at best. In one experiment the nucleation and growth process was so rapid that the Si film grew to >1000Å, and hence became nontransparent to electrons, in one minute - less than the time required for adequate microscope focusing and photography. In another experiment the Al_2O_3 was far too thick. In two experiments a Si film was formed, but the nucleation and coalescence occurred on

such an extremely fine scale that a continuous film was formed before individual islands became visible in the electron microscope.

The most suitable micrographs taken during in situ Si growth on Al_2O_3 were on sample #19, shown in Figure 97. At the initial heater power of 0.21 w no Si growth was visible. After the SiH_4 was shut off the heater power was increased to 0.26 w. A few whiskers and irregular Si forms slowly grew at the edges, appearing as in Figure 97a after 10 min. The SiH_4 was again shut off, and the heater power increased to 0.28 w. A Si film rapidly formed on the surface, appearing as in Figure 97b after 1.5 min and Figure 97c after 2.5 min. The deposit was positively identified as polycrystalline Si by indexing the diffraction pattern shown in Figure 97d, also taken during growth.

These micrographs are of lower quality than it is possible to achieve in this in situ system, mainly because the Al_2O_3 was thicker than optimum and the reaction was overly rapid. However, some conclusions may be drawn by combining the information of the micrographs with that from visual observation during growth. The primary conclusion to be so reached is that the growth of Si on single-crystal Al_2O_3 by CVD is also generally similar to the growth of other materials by PVD methods (Ref 79), as was the case for CVD Si on amorphous carbon. That is, small nuclei are formed which grow to three-dimensional islands which then coalesce and continue to grow into a continuous thin film. A continuous film is not formed by growth of a monolayer at a time over the entire substrate area. This conclusion was based on the observations of other samples as well as of that of Figure 97.

Examination of Figure 97 also indicates that (1) the nucleation density was relatively high ($>6.4 \times 10^6/cm^2$) and (2) a continuous film is attained at a relatively small average thickness. (The poor resolution in these micrographs is due to the excessively thick Al_2O_3 and the fine-grained Si, not to a thick Si layer.) Both facts imply that little opportunity for coalescence was present. If the overall orientation of a Si film improves considerably during coalescence, then lack of a coalescence stage would cause the film to remain polycrystalline, as indeed was observed.

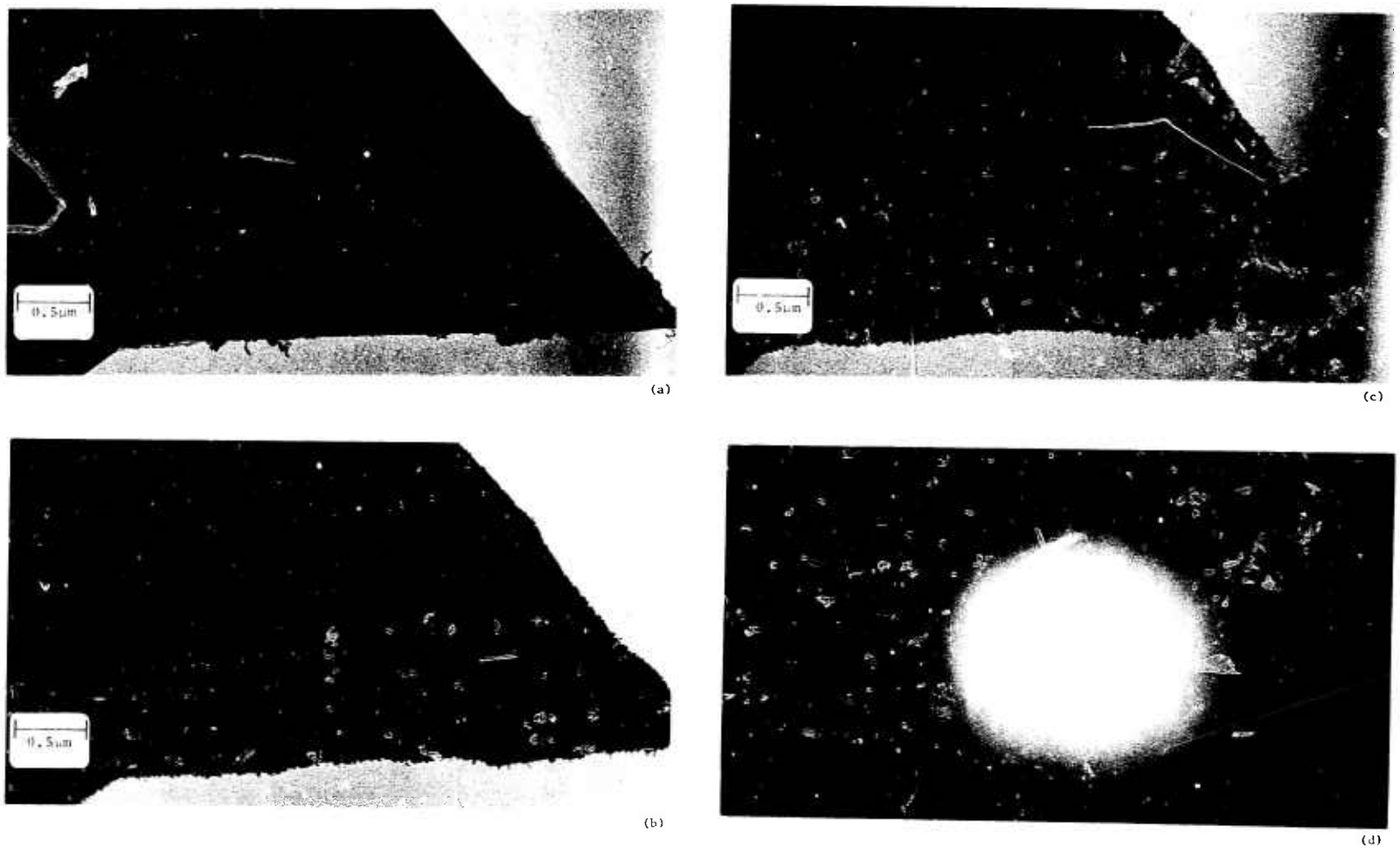

Figure 97. In Situ Nucleation of Si on Al_2O_3 (Sample #19)

The progress of Si nucleation and early growth was also visible in experiment #16, but again the Al_2O_3 was much too thick and the resulting excessive inelastic electron scattering produced low-contrast micrographs (Figure 98). The film was fine-grained and polycrystalline during the major portion of growth. However, after the SiH_4 was shut off, but with H_2 still flowing, Si whisker growth was noticed. Figure 98c was made with the microchamber pressurized with H_2 at 1.3 torr; Figure 98d was taken afterward, with pressure back to normal.

Sample #16 was the only one on which large numbers of whiskers appeared, although occasional Si whiskers were noticed in several other experiments, particularly on or near the grid bars. The reason for the whisker growth was not ascertained, but typically it is the result of a low supersaturation, frequently coupled with traces of contamination.

Several other Si-on-Al_2O_3 samples examined after growth were also fine-grained and polycrystalline, so their nucleation rates were also high compared with the growth and coalescence rate. One such sample (#22) is shown in Figure 99. This thin area of Al_2O_3 containing Si nuclei was, unfortunately, not in the field of view during the experiment. The Al_2O_3 which had been visible did not experience Si nucleation, so that region was presumably below the SiH_4 pyrolysis temperature. The corresponding diffraction pattern, Figure 99b, shows no trace of preferred orientation (the spots are from the Al_2O_3 substrate).

Another film, #17, examined after <u>in situ</u> growth was so fine-grained that no Si features were discernible. The film was not amorphous, however, as a crystalline diffraction pattern was obtained (Figure 100); note there are polycrystalline rings containing strong (111) spots (especially visible in the innermost ring). This observation was unique to this sample. No explanation is available as to why a relatively large number of (111)-oriented grains were present on a $(01\bar{1}2)Al_2O_3$ surface normally yielding (100)Si growth.

In numerous instances no Si growth was observed on the Al_2O_3 surface visible during the course of the experiment. A variety of factors was probably

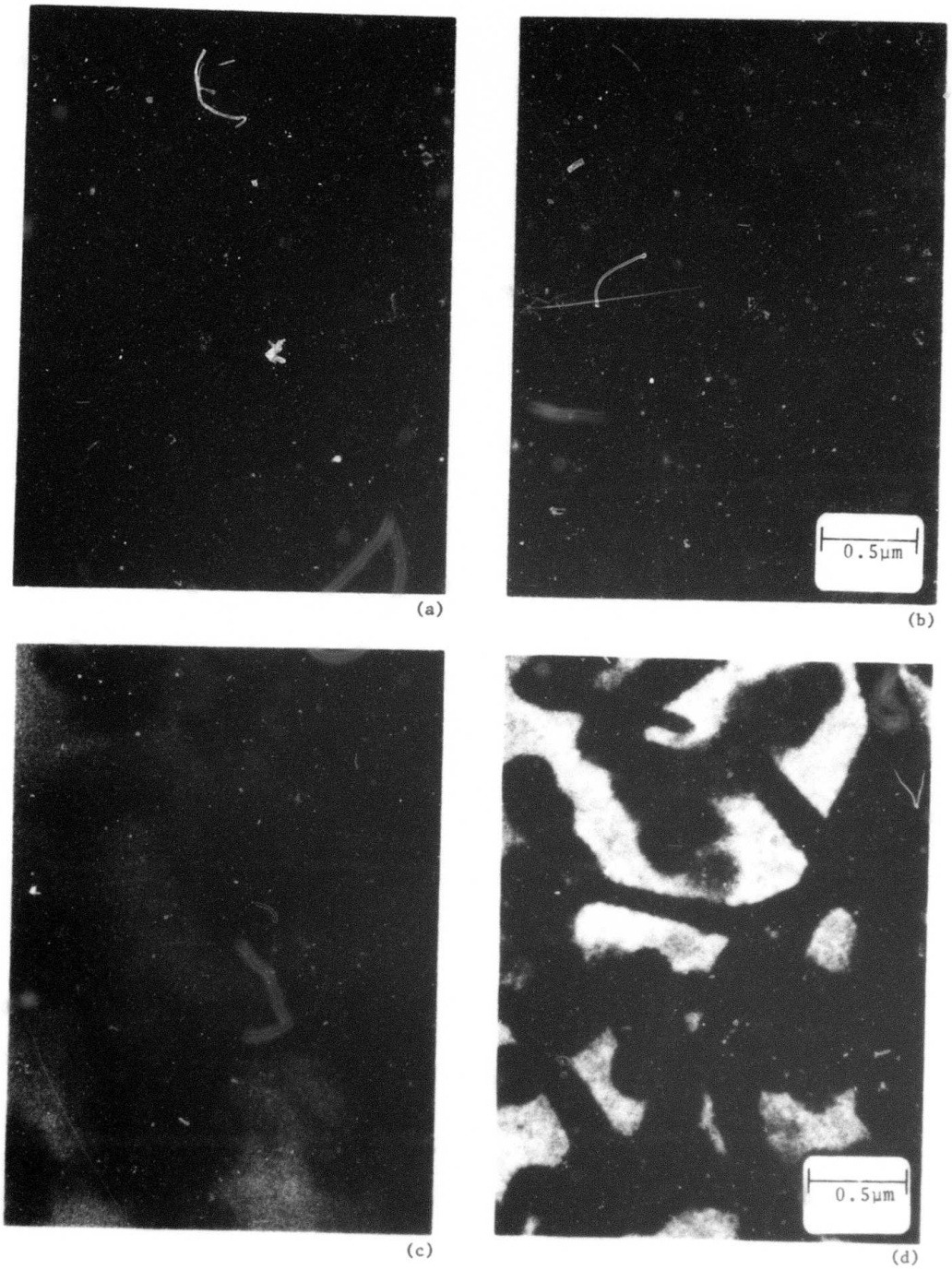

Figure 98. In Situ Nucleation of Si on Al_2O_3 (Sample #16)

(a)

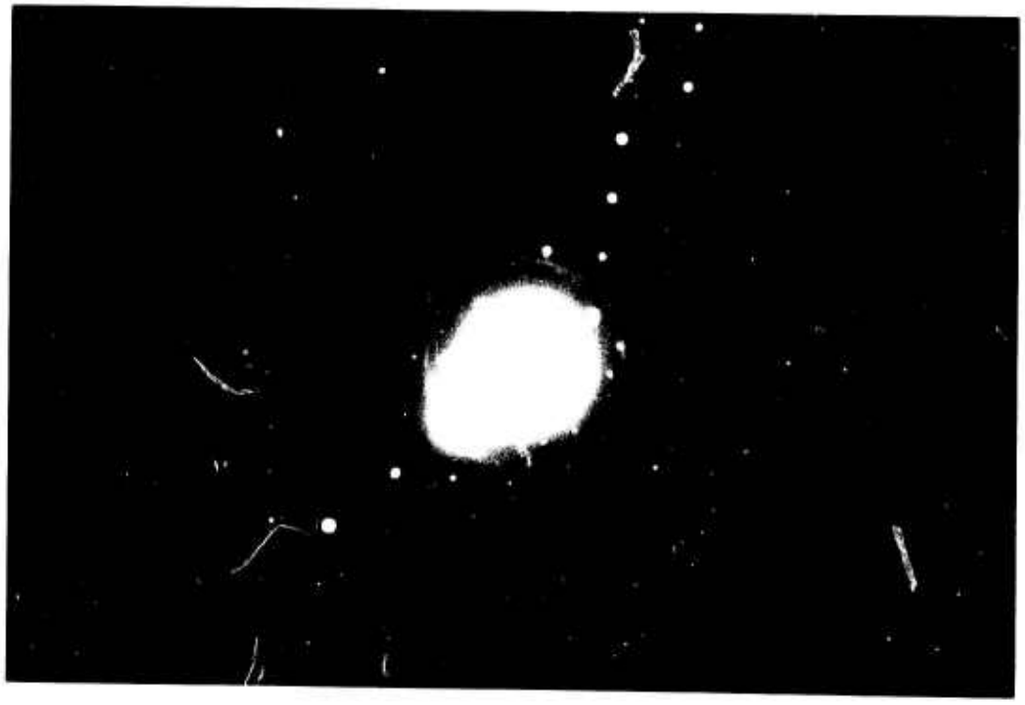

(b)

Figure 99. Nucleation of Si on Al_2O_3 after In Situ Growth (Sample #22); (a) Micrograph, (b) Diffraction Pattern.

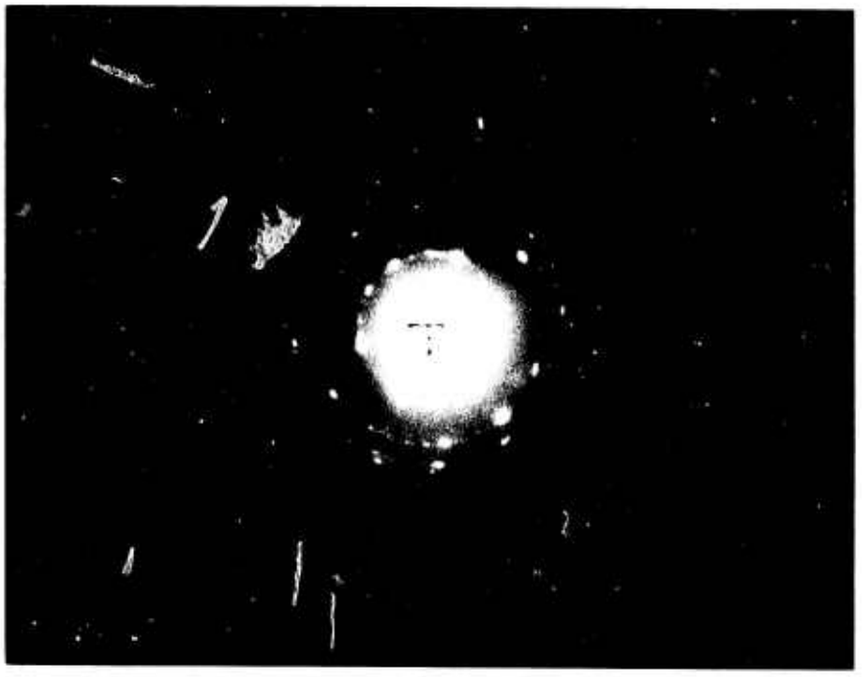

Figure 100. Diffraction Pattern of Si Film on $(01\bar{1}2)Al_2O_3$ Substrate, Showing Strong (111) Spots on Polycrystalline Rings

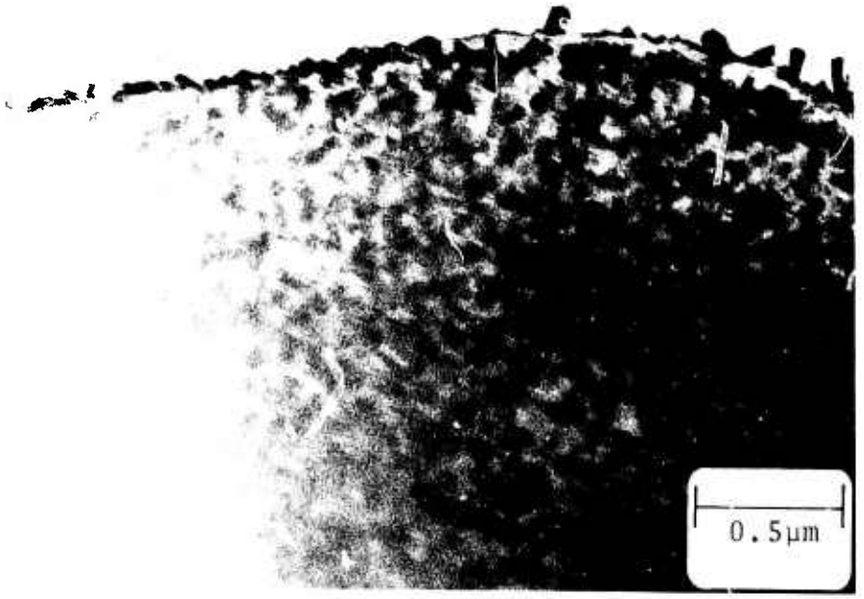

Figure 101. Contamination Observed during In Situ Experiment with Sample #18

Figure 102. Reaction of Ti Heating Grid with Al_2O_3

Figure 103. Reaction of Si with Al_2O_3 during <u>In Situ</u> Growth

responsible. Most common was failure of the Al_2O_3, or at least of the electron-transparent region, to become sufficiently hot to cause SiH_4 pyrolysis. If no Si growth was visible at the predetermined heater power the SiH_4 was turned off, the heater power increased, and the SiH_4 flow restarted. The heater power was increased stepwise in this manner until a reaction was visible; failing this, the increments were continued until the maximum feasible heater power was obtained. In all such cases in which no reaction was visible, except one, disassembly and examination afterward always revealed Si deposition on the heater grid and usually on the nearby Al_2O_3.

Two experiments were terminated prior to SiH_4 introduction because of contamination which became visible on the Al_2O_3. A severe example of this is shown in Figure 101. From these experiments it was concluded that the upper limit of heater power was ~0.3 w for a Ti heating grid. Above this point excessive evaporation of the Ti took place, contaminating and reacting with the substrate. Some contamination of the substrate by Cu from the apertures may also have occurred at the high power levels. The Ti grid temperature was estimated to be 1200C during the higher-power experiments.

In an attempt to form Si nuclei larger than had been seen previously, several more experiments were run at high heater powers. In one experiment, there was a severe reaction between the Ti grid and the Al_2O_3, as shown in Figure 102. Note the holes etched into the Al_2O_3. No other sample exhibited such a reaction. In another experiment, a severe reaction occurred between the Si and the Al_2O_3 during the final SiH_4 admission, as shown in Figure 103. The deposit was indeed Si, as confirmed by electron diffraction analysis. The similarity between Figure 103 and Figure 138 suggests that - for this experiment, at least - the Al_2O_3 temperature must have reached nearly 1200C.

Unintentional shifting of the thinned region of the Al_2O_3 out of the microscope field of view was a common event during <u>in situ</u> experiments. There were two alternatives, both undesirable, that were then available: either continue the experiment, trying to deposit a small amount of Si without monitoring

the deposition process, or disassemble the microchamber and either realign the Al_2O_3 or install a new Al_2O_3 sample. The former was attempted several times, but no deposit was noted afterward in any of the attempts. The reason for the shift was either movement of the Al_2O_3 in gradually working its way loose from the grid or a shift of the heater grid as a result of uneven heating. In nearly all cases it was not possible to identify which applied.

4. DISCUSSION AND RECOMMENDATIONS

There were two major problems which limited the success of the in situ growth experiments. One was the difficulty and complexity of the overall experiment, and especially the Al_2O_3 substrate loading and alignment procedure. The other was a lack of reproducibility in the temperature of the Al_2O_3 substrate.

The former was a practical limitation in the sense that the long preparation time per experiment, typically about five days, permitted only a small number of experiments in the available time. The heating problem, however, was a fundamental limitation that prevented precise quantitative experiments. Additional minor problems, by themselves soluble, combined with the above to prevent the full attainment of the initial objectives of these experiments by the end of the contract. Many of the practical problems actually encountered had been anticipated earlier but their magnitudes were not fully appreciated until later.

a. Substrate Alignment

The substrate loading and alignment problem was the chief reason for the long time required for each in situ CVD experiment. An appreciation of the difficulty involved can be gained by considering the size of the sample and microchamber components. The sample was typically twice as wide as the diameter of a human hair, held by supports one-third the diameter of a human hair. The screws which held the heating mesh to the electrodes were smaller than most watchmaker's screws now in use. Consequently, the loading was performed under a 12-50X stereomicroscope.

The Al_2O_3 substrates were attached to the heating mesh, as previously described, which then had to be fastened to the electrodes with the electron-transparent region of the Al_2O_3 directly aligned with the 100μm-dia fixed aperture of the microchamber. Repeated adjustments were required, even when the assembly was done with the assistance of a 100X transmitted-light optical microscope. The removable aperture, also 100μm in diameter, then had to be aligned with the

sample, again a tedious task. It was impossible to determine with the optical microscope if the desired 200Å-thick Al_2O_3 substrate region had broken off as the result of handling - a frequent occurrence. If it had, a CVD experiment was usually still attempted, provided at least a portion of the Al_2O_3 was visible, even if thicker than optimum. Unfortunately, more than half of the loading attempts resulted in failure to achieve placement of any Al_2O_3 whatever that was visible in the field of view.

A related problem was that the electron-transparent regions on the Al_2O_3 were small, comprising generally only 1-2% of the total sample area. Consequently, it was difficult to align a suitably thin region of the Al_2O_3 with the 75μm x 75μm open area of the heating mesh. As indicated earlier, considerable effort was expended in increasing the area and uniformity of the thinned regions for the specific purpose of facilitating this alignment procedure.

b. Temperature Calibration

The most serious problem was the lack of reproducibility in heating the Al_2O_3 substrates. The grid itself and (when due account was taken of factors discussed below) the amorphous carbon substrates used in some of the in situ experiments could be heated reproducibly.

To determine the temperature of the amorphous carbon substrates, it was necessary to obtain a temperature-power calibration for the grid-film composite. To accomplish this a thin non-continuous film of a suitable metal was vacuum-deposited onto the amorphous carbon substrate, which was in turn placed on the heater mesh and installed into the microchamber. The heater power was gradually increased until the melting point of the metal was obtained, as indicated by the sudden loss of the electron diffraction pattern characteristic of the solid phase. A series of such experiments was performed with Sn (m.p. 232C), Zn (m.p. 419C) and Al (m.p. 661C), but the latter two did not yield satisfactory results. The current required to attain the melting temperature of Sn was readily reproducible within ±0.01a for given operating conditions.

The heater current required to reach 232C was found to be a strong function of the microchamber gas pressure, electron-beam intensity, physical condition of the carbon substrate, and location of the substrate area of interest relative to the nearest mesh of the heater. The introduction of a gas flow into the microchamber at pressures of 1-10 torr had a large cooling effect on the substrate, requiring a greater heater power to reach a given temperature (e.g., 0.01w at 0.1 torr versus 0.03w at 1.0 torr). This effect is not linear, as the mechanism of gaseous thermal conduction changes in this pressure range; at the normal operating pressure of 1.3 torr the gradient is about 0.45 w/torr.

The variation in the required heater power with distance of the immediate area of interest (typically 1μm dia) from the nearest mesh in the heating grid was ~0.6×10^{-3} w/μm, which is equivalent to ~2.5 deg C/μm. The electron beam had a heating effect on the substrate, with ~15% less power required at maximum intensity than at 1/8 of maximum intensity. However, all experiments were conducted at maximum beam intensity so this never became a problem. Another obvious factor was emphasized during the calibration experiments: carbon films which became torn or were only partially attached to the heating grid yielded highly erratic results.

The combination of all of the variables resulted in the empirical temperature-versus-power relationship. For example, with a gas pressure of 1.3 torr and for a location 20μm from the grid, 0.052w was sufficient power to reach 232C; this corresponds to 4 deg C/mw for a W heater grid 4 meshes (0.020 in) wide.

Unfortunately, the Al_2O_3 substrates heated non-uniformly and irreproducibly, as judged by the widely differing behavior observed during <u>in situ</u> Si growth on Al_2O_3. One experiment might give almost instantaneous growth at 0.24w heater power, but the next might produce no visible growth whatever at 0.3w.

The difference was probably due to the Al_2O_3 making better or poorer contact with the grid from region to region and from experiment to experiment. Even

with the same macroscopic surface contour on two different Al_2O_3 substrates - a very unlikely situation to achieve - it is virtually impossible for the microscopic contour, hence the contact points to the grid, to be alike in the two cases. The thermal conductivity of Al_2O_3 is lower than that of carbon, so the temperature gradient from the sample center to the area near the heater mesh will be greater. The latter may be compensated by more elaborate temperature calibrations, but no mounting method is likely to eliminate erratic results with this substrate heating arrangement.

c. Recommendations for Further Work

These investigations have clearly shown that it is feasible to study in situ the nucleation and early growth of Si films formed by the pyrolysis of SiH_4. They have further shown that although many characteristics of PVD and CVD films are similar, there are differences which may be of major significance, including the morphology of the islands, the orientation changes occurring during the coalescence process, and the mechanism of defect incorporation into growing films.

Additional in situ studies of Si CVD growth should now be undertaken, with emphasis placed on those areas of fundamental uniqueness to the CVD process. It is also recommended that the experimental technique utilize a directed, molecular beam of SiH_4 and a furnace-type substrate heater rather than a flow system of the type used in these investigations.

The advantages and disadvantages of the present microchamber and modified flow system should be compared carefully with those of other alternatives relative to future studies of in situ CVD growth of Si. One such alternative would be to retain the flow characteristics but enclose the entire microchamber in a small furnace. While this would solve the problem of temperature reproducibility and uneven substrate heating, it would leave unchanged the problem of loading and aligning samples with the apertures. Additionally, it would create two other problems: (1) It would become extremely difficult to define the degree of supersaturation in the system due to excessive SiH_4

decomposition at the hot walls of the microchamber. (2) A significant loss of magnification would occur, as the furnace plus microchamber would of dimensional necessity be placed farther away from the focal point of the objective lens.

However, the use of a furnace-type heater for the substrate has certain real advantages for in situ experiments if a directed molecular beam is used as the source of SiH_4. The advantages of this type of arrangement are as follows: (1) substrate heating is uniform; (2) no gas-limiting apertures are required, so sample alignment is easier; (3) the sample may be moved freely to search for a thin region, making substrate preparation less critical, and (4) the reaction would be purely heterogeneous, with essentially no possibility of a homogeneous reaction.

The disadvantages of such an arrangement are as follows, (1) The physical mechanism of the reaction is unrelated to that commonly employed in the laboratory. (At 1 atm pressure any molecule adsorbed on the surface and then desorbed has an extremely high probability, through gaseous collisions, of subsequently returning to the surface. The effective supersaturation is thus considerably greater than that attainable with a molecular beam, in which a reevaporated atom is lost from the system.) (2) Extensive calibration of the molecular beam flux is required to determine the supersaturation. (3) The experimental setup is more elaborate, more costly, and requires greater electron microscope modification. (4) There is a somewhat greater probability of damaging the electron microscope during experimentation.

When the experiments of this contract program were designed it appeared that the disadvantages of a molecular beam system (particularly 1 above) considerably outweighed the advantages. Accordingly, a modified flow system was selected. In retrospect, it appears that a molecular beam system might well be more suitable for electron microscope in situ nucleation and growth studies of CVD films, despite the specified differences from conventional CVD Si film growth for device applications.

SECTION 9

ELECTRICAL PROPERTIES OF HETEROEPITAXIAL FILMS *

Evaluation of the electrical properties of the heteroepitaxial films prepared throughout the course of this contract constituted one of the most essential parts of the investigations. The results of these measurements were used both to determine the status of the film growth capabilities at a given time and to help determine the direction to be followed in subsequent experiments.

Rapid acquisition of data on electrical properties became very important to the daily conduct of film growth experiments; measurements of film conductivity type, resistivity, carrier concentration, and carrier mobility were made routinely on a majority of the epitaxial samples prepared on this program, utilizing either the van der Pauw method (Ref 41) or the more accurate and conventional Hall-effect bridge method.

Various experimentally measured quantities are required for determination of the electrical characteristics of thin semiconductor films. These include voltages, currents, magnetic field strengths, and geometrical properties (i.e., dimensions) of the semiconductor film samples. The accuracy of the values obtained for resistivity (ρ), carrier concentration (n) and mobility (μ) can therefore be estimated, based on estimates of the errors in the measured quantities.

Typically, for Si/Al_2O_3 films the largest source of error in the determination of ρ and n was the film thickness, leading to relative errors of approximately $\pm$5%, with an absolute error estimated to be about $\pm$ 10%. Since the other important parameters (width of the Hall bridge, voltage, current) were each known to approximately $\pm$0.5% or better, the overall relative error in ρ and n was estimated to be $\pm$7%. The mobility (μ) is independent of thickness as a measured parameter and was therefore measured to an accuracy of approximately $\pm$2-3%.

---

* Many of the results of the electrical measurements on semiconductor film samples are discussed separately in Sections 3 and 10 of this report.

However, there were other factors which could influence the accuracy of the measured values of electrical properties of the heteroepitaxial films. The influence of surface conduction was minimized by intentional doping of films to carrier concentrations of $\sim 10^{16} cm^{-3}$ or higher, but even in this range surface effects can lead to errors in all electrical parameters of approximately $\pm$10%. This error was, of course, much smaller for higher carrier concentrations and was probably insignificant compared with measurement errors for values of $n > 10^{17} cm^{-3}$.

Considering all of the above sources of error, the values of ρ and n typically reported in these studies are estimated to be accurate to approximately $\pm$15% (for samples with n in the low and middle $10^{16} cm^{-3}$ range), and the corresponding mobilities have approximately $\pm$10% accuracy.

The van der Pauw method, which was occasionally used for measuring the electrical properties of the semiconductor films, was examined to determine the accuracy of the technique when applied to the evaluation of Si/Al_2O_3 films. Several samples were measured by this technique by applying contacts at the periphery of films approximately 1/2 in in diameter. The electrical data obtained were compared with those found with the standard Hall bridge-type samples subsequently etched into each of the films. In most cases the resistivity found by the two methods differed at most by less than 6%, with the bridge method always yielding the smaller value. The carrier concentrations had a wider range of variation, with the bridge value being an average of 12% smaller. The largest variation occurred in the Hall mobility; the bridge values were an average of 16% larger than those found by the van der Pauw technique.

These differences between the two methods are similar to those previously established in the $GaAs/Al_2O_3$ system (Ref 80). As a consequence of these differences, the van der Pauw technique was not ordinarily used for data; if the method was used out of some necessity the results so obtained were clearly identified.

1. HOMOGENEITY OF ELECTRICAL PROPERTIES OF HETEROEPITAXIAL FILMS

The question of the homogeneity of the properties of the heteroepitaxial semiconductor films prepared on this program (or elsewhere) is one of major significance both to the contract investigations and to the semiconductor device industry in general.

Unfortunately, it is a problem that remains unsolved in detail at the conclusion of this program. It is known that the properties of Si films grown on Al_2O_3 substrates by SiH_4 pyrolysis in the vertical reactor system described in Section 3-1 are not completely uniform over the area of the film, irrespective of the position of the sample on the horizontal pedestal during film growth and despite rotation of the pedestal during deposition. (See Section 3-5 for discussion.) It is also known that Si/Al_2O_3 samples prepared in a commercial-type horizontal reactor system generally exhibit greater uniformity of electrical properties on a given sample, although there can be considerable spread in the Si properties obtained in films grown simultaneously but in widely separated parts of the reactor chamber. Furthermore, considerable effort has been expended by some commercial suppliers of Si/Al_2O_3 composites to design vertical reactor systems with multiple-substrate capacity yet only a limited range of film thickness and electrical properties in a given sample batch.

The problem remains unsolved in the sense that sample inhomogeneities still exist in each type of CVD reactor system. The extent of the inhomogeneities is a sensitive function of the overall reactor geometry, the gas flow rates and patterns, the type and design of substrate heating employed, substrate surface conditions, and other factors not all of which are known. On the other hand, the problem might be considered adequately under control when the epitaxial samples of interest can be prepared with structural and electrical properties that are sufficient for the particular application involved. (Cf Section 3-5).

Inhomogeneous donor concentrations observed in various regions of the Si/Al_2O_3 composites prepared in the vertical CVD reactor (Figure 3) had noticeably complicated the analysis of electrical properties as a function of direction of current flow in the plane of the film during the second year of the contract. In an attempt to produce films with more uniform doping impurity distributions, a number of films were grown with only one substrate in the reactor for each run. (Most often, two or three substrates were employed simultaneously.)

Anisotropy measurements on these samples generally did not show enough of an improvement in homogeneity for this technique to be considered a solution. For example, two $(221)Si/(11\bar{2}2)Al_2O_3$ samples still showed an average of 29% variation in carrier concentration in different regions of the film, compared with an average of 35% obtained on nine previous samples. (See Section 9-3 and Section 10.)

To quantify the extent of dopant variation across a given Si film, carrier concentration data from anisotropy samples formed in films grown simultaneously were correlated with their position on the rf-heated susceptor (pedestal) during growth. Since the exact positioning of the samples on the susceptor was not known, it was assumed that there was a radial gradient of carrier concentration such that the maximum concentration in the films would be obtained in the region grown at the center of the susceptor. The position of each leg of the anisotropy pattern (see Figure 128) on the susceptor could then be deduced so that a plot of the carrier concentration N_D versus distance from the center of the susceptor could be made.

Such a plot is shown in Figure104; the carrier concentration has been normalized to the value of carrier concentration at the center of the susceptor (N_D^C). Each curve represents data for two samples grown at the same time; each sample produced 10 data points corresponding to the 10 legs of the anisotropy bridge pattern.

The results of three runs are plotted in the figure; one shows a minimum

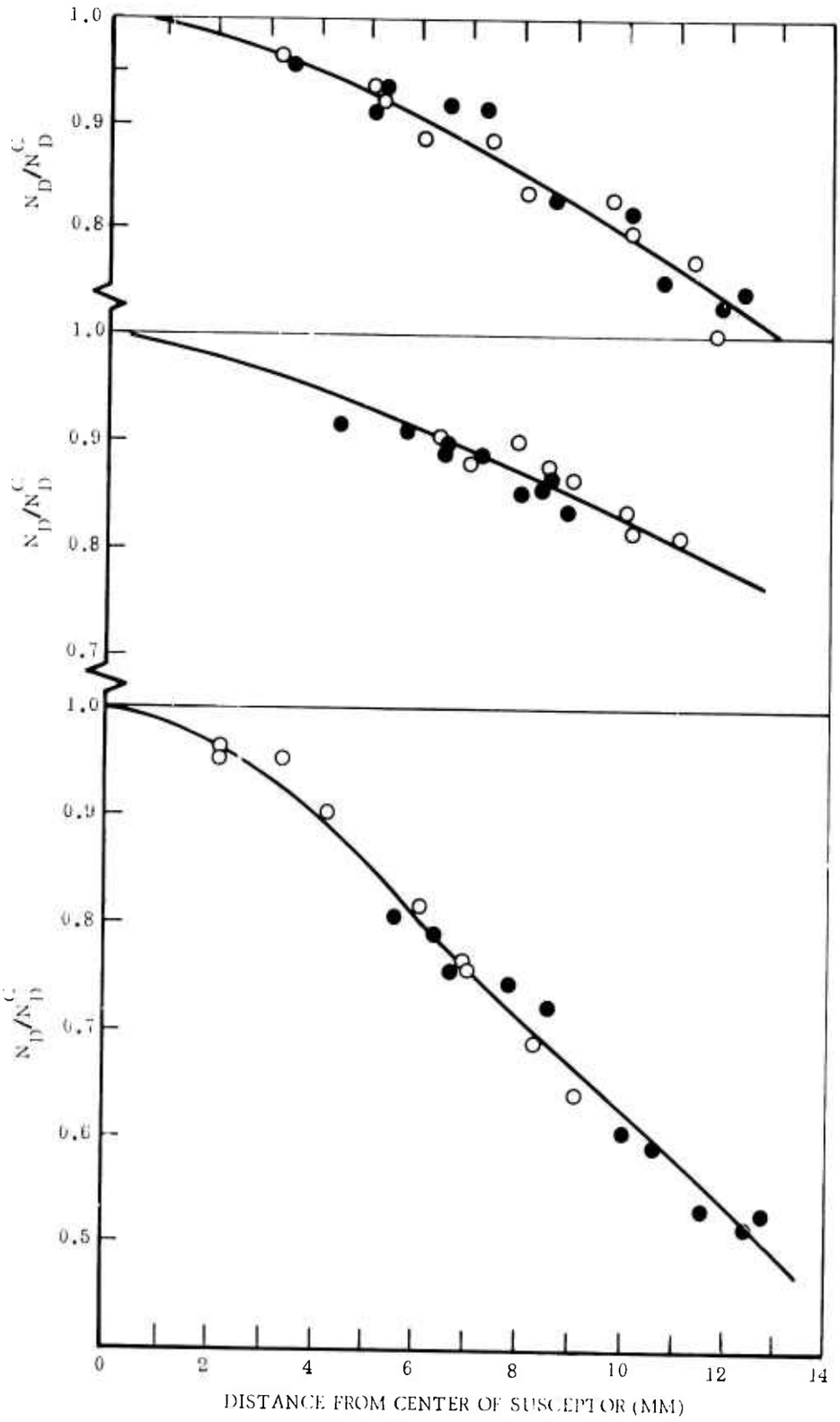

Figure 104. Normalized Carrier Concentration as Function of Distance from Center of Susceptor (Sample Pedestal) for Pairs of Si/Al_2O_3 Samples Grown Simultaneously.

variation in carrier concentration (~10%), one shows a maximum variation (~45%), and one is between the other two. The closeness of the data points to a smooth curve tends to strengthen the validity of the assumption that a radial concentration gradient does indeed exist.

The reasons for the variations are not known, but they could relate to gas flow characteristics in the reactor. This is suggested by the fact that growth in a horizontal reactor (where presumably the gas flow is more laminar in nature) has consistently yielded more homogeneous films. Alternatively, the variation in temperature across the susceptor due to inhomogeneous heating by the rf coils was examined. Measurements of the variation in temperature as a function of position on the susceptor indicated that temperature gradients of as much as 5-20C over a distance of 0.5 in may exist at Si growth temperatures (1000-1100C). Although the exact profiles were not determined, if a temperature gradient of 20C in 0.5 in were assumed it was possible to use previous data to estimate the variation of carrier concentration to be the order of 30%. Such a large temperature gradient could well account for the observed film inhomogeneities.

Subsequent to these considerations an experiment designed to verify the suspected characteristic of the vertical reactor system was undertaken, and it was described in Section 3-5 and the results illustrated in Figure 22. Some attempts to correct the situation by using specially shaped susceptors were undertaken without success, and the problem was finally circumvented - partially - rather than solved directly, as indicated in the earlier discussion.

The degree of uniformity of Si film properties with distance from the Si/Al_2O_3 interface was also evaluated in some detail; those results were described in Section 3-2. It is interesting that profiling measurements such as those mentioned therein indicated that the electrically-active Al in p-type "autodoped" Si/Al_2O_3 samples evidently does not increase in concentration near the interface, as might be expected. Presumably some of the Al nearer the interface forms neutral complexes with the higher concentrations of defects and/or impurities which may be present in the film near the Al_2O_3.

2. VARIATION OF ELECTRICAL PROPERTIES OF Si/Al_2O_3 WITH TEMPERATURE

The development of a computer program for the analysis of low temperature Hall-effect data provided a technique for deducing information about electrically active impurities and defects in Si/Al_2O_3 films. That information, coupled with the knowledge of carrier scattering mechanisms in Si films that could be gained from low-temperature measurements, suggested a study of the feasibility of using low-temperature data as a measure of film quality and as a means to assist in optimizing film growth.

The model used for the computer program was a semiconductor containing a single donor species of concentration N_D (for an n-type sample) and having an energy level E_D, with a number of compensating acceptors of concentration N_A. The equation used to fit the data for the carrier concentration n was

$$\frac{n(n+N_A)}{(N_D-N_A-n)} = 2\beta\left(\frac{2\pi m^* kT}{h^2}\right)^{3/2} \frac{1}{\sum_j (j)^2 \exp(E_D/j^2 kT)}, \qquad (60)$$

where m^*, k, T, h, and β are the effective mass, Boltzmann's constant, absolute temperature, Planck's constant, and a degeneracy factor, respectively.

The summation over j takes into account the excited states of the impurity (hydrogenic model). The iteration program adjusts the parameters N_A, N_D, m^*, and E_D for the best fit for any choice of j. Hall data for p-type films could be fitted to the same equation with appropriate redefinition of terms.

The first phase of this study was the detailed analysis of Hall-effect data on p-type $Si/(01\bar{1}2)Al_2O_3$ films grown at 1050 and 1100C; measurements on two such samples yielded the following results (for $\beta^{-1}=4$, j=1 in the model):

(1) $N_A = 6.2\times10^{15}cm^{-3}$, $N_D = 1.06\times10^{15}cm^{-3}$, $E_D = 0.065$ eV, $m^*=0.225m_o$
(2) $N_A = 2.46\times10^{16}cm^{-3}$, $N_D = 4.27\times10^{15}cm^{-3}$, $E_D= 0.055$ eV, $m^*=0.292m_o$

The energy values agree well with the value of 0.057 eV quoted in the literature for Al in Si and were considered to confirm the presence of Al in nominally undoped films grown at high temperatures. (Autodoping was discussed in some detail in Section 3-3.)

An interesting result of this calculation was the rather high concentration of compensating donor species apparently present in the material. Since the growth of undoped films at lower temperatures yields very low carrier concentrations (probably $<10^{15}cm^{-3}$), the above analysis suggested the presence of a comparatively high concentration of deep donors. The origin of these was unknown, but they may have been due to an unknown impurity (e.g., Fe, Mn, Ag, Pt, or Hg) or, possibly, to lattice defects. The effective masses determined by the analysis appeared to be consistent with each other and represented a hole of rather light mass.

The second phase of this study was the examination of n-type Si/Al_2O_3 films. The electrical properties of two As-doped n-type $Si/(01\bar{1}2)Al_2O_3$ films having thicknesses of 0.7 and 3.9μm were measured between room temperature and ~40K. The growth conditions and substrates were identical for the two samples (with the exception of length of time of growth), so that a meaningful comparison of thin and thick Si films could be made. It was expected that any differences in electrical behavior in the two samples could be attributed to the difference in strain and/or defect structure in the two samples. After growth, both samples were annealed for a total of 1.5 hr in O_2 followed by a 2-hr anneal in N_2 at 1100C. (As determined previously, this annealing sequence assured the electrical deactivation of any Al impurities present in the film.)

The electrical characteristics of the two samples at room temperture are shown in Table 32 along with data on bulk single-crystal Si obtained from the literature (Ref 81). The major differences to be noted are those in the mobilities of the thick samples (~470 cm^2/V-sec), the thin samples (~290 cm^2/V-sec), and bulk Si (~1400 cm^2/V-sec).

Table 32. Electrical Characteristics of Two As-doped Si/$(01\bar{1}2)Al_2O_3$ Films Used for Low-Temperature Measurements

Sample Number and Thickness	Resistivity at 300K (ohm-cm)+	Net Carrier Conc. at 300K (cm^{-3})+	Mobility at 300K (cm^2/V-sec)+	N_D Donor Conc, (cm^{-3})	N_A Acceptor Conc. (cm^{-3})	Effective Mass m^*	E_D Donor Energy Level (eV)	Mobility (77K) / Mobility (300K)
11-4A-71 (LH-130) t = 3.9μm	0.64	2.1×10^{16}	470	2.4×10^{16}	2.6×10^{15}	$0.26m_o$	0.037	2.0
11-2C-71 (LH-20) t = 0.72μm	1.5	1.5×10^{16}	290	1.7×10^{16}	1.3×10^{15}	$0.11m_o$	0.034	0.74
Bulk As-doped Si	-	1.75×10^{16}	~1400	$\sim1.8\times10^{16}$	1.5×10^{15}	$1.2m_o$	0.048	5.7

+Numbers represent single determination of electrical parameter by standard technique.

Although the room-temperature mobilities of the two Si/Al_2O_3 samples were not grossly different there was a marked difference in the variation of mobility with temperature. As can be seen from Figure 105, the thicker sample initially shows an increasing mobility with decreasing temperature and becomes nearly temperature-independent from 100 to 40K. The mobility of the thin sample is nearly constant from 300 to 100K, but decreases with decreasing temperature from 100 down to 40K. These data suggest that the ratio of the low-temperature to the room-temperature mobility of these films may be a good measure of the extent of defect structure. Accordingly, this ratio was computed for 77 and 300K (temperatures easily obtained in the laboratory) and has been included in Table 32.

The variation of net carrier concentration with temperature was slightly different from that obtained for bulk samples; smooth experimental curves are plotted in Figure 106 for the 3.9μm-thick sample and for bulk Si. The difference in shape between the two curves is manifested in the different values for the parameters used to fit the data theoretically by the computer analysis; these parameters are also given in Table 32.

The smaller energy level E_D found for the As donor in the Si/Al_2O_3 samples compared with that for bulk material is primarily a result of the difference in the slopes of the curves in Figure 106 at low temperatures. Another significant difference between the properties of the bulk material and those of the epitaxial samples is in the effective mass, where there is an order of magnitude difference. This suggests that the mass may also be useful as a parameter for characterizing film properties.

It was originally intended that these measurements of carrier concentration would yield a value of minority carrier concentration (N_A for the n-type films) that could be related to defect structure. The slight difference in this parameter for the two films (thick and thin) showed this not to be the case. The negative result here was probably due to one of the following characteristics of the defect centers involved: (1) they do not act as acceptor centers; (2) they can act as both acceptor and donor centers;

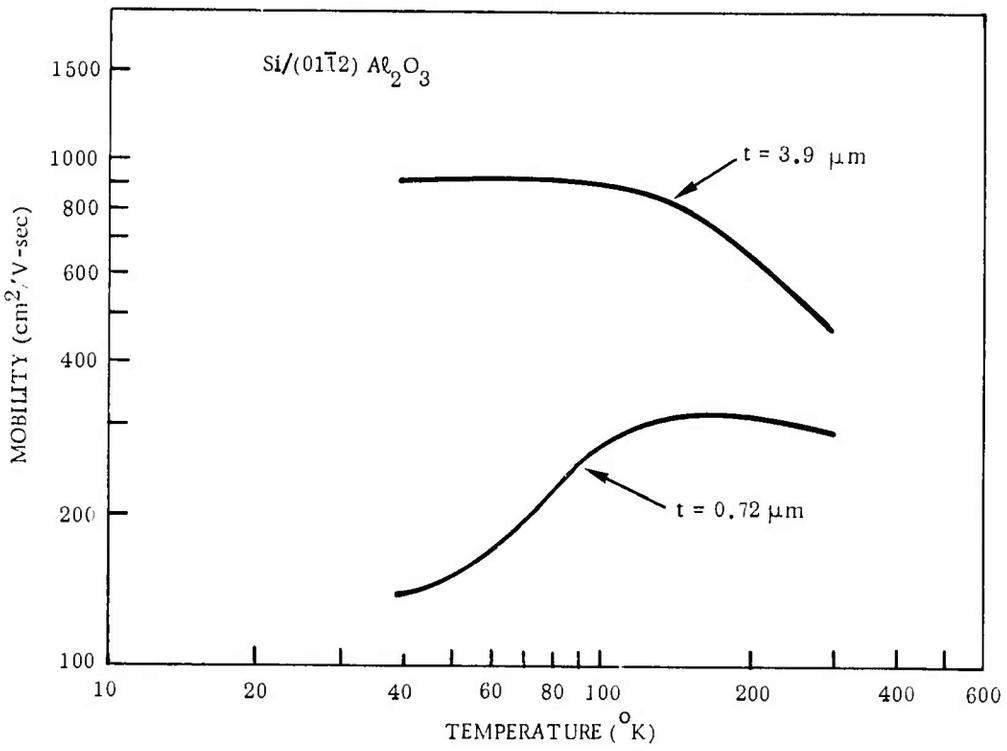

Figure 105. Electron Mobility as Function of Temperature for Two Samples of Arsenic-doped N-type Si/Al_2O_3 Grown under Identical Conditions

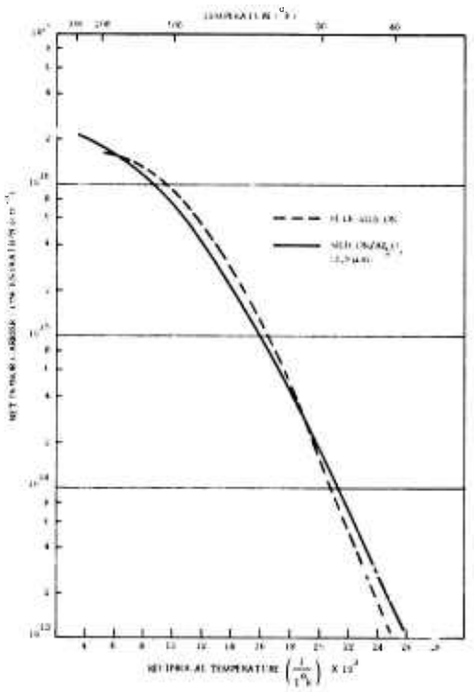

Figure 106. Net Carrier Concentration as Function of Temperature for 3.9μm-thick Si/Al_2O_3 Film and for Bulk Single-crystal Si (Smooth curves drawn through experimental data points)

(3) they act as deep donors; or (4) they are electrically neutral.

Additional measurements on p-type samples should indicate which of the first three is the more likely possibility. The fourth alternative is considered unlikely since defects appear to be too effective as scattering centers. It should be noted that if (2) is the correct explanation then the model used in the analysis of the data was not correct, and the resulting parameters, although possibly useful, would not be physically meaningful.

It is important to consider possible reasons for the discrepancy in the activation energy deduced from the data. It appeared at the time that this result might be a consequence of inhomogeneous strain in the film. It is well known that strain can lower both the conduction-band minimum and the ground-state energy of an impurity. For large homogeneous strains these effects tend to lead to an increase in measured ionization energy; however, if the film has a high locally-inhomogeneous strain field, as might be expected with a large number of defects, the situation would be different. If, for example, the strain "smears out" the donor energy level and "smears out" or lowers the conduction-band minimum, the energy measured might be expected to be lower than in an unstrained crystal or in a homogeneously strained crystal, and it would be approximately equal to the amount the conduction-band minimum is lowered. Estimates of such a shift have been given as ~0.015 eV (Ref 82) and from 0.040 to 0.070 eV (Ref 83), either value of which could easily account for the difference in As level of 0.014 eV that was observed between the bulk Si value and that for the thinner film. Thus, the possibility of stress-related phenomena playing a major part in determining the electrical properties of Si films on Al_2O_3 seemed to be indicated by these preliminary results.

Measurements on n-type Si films of various thicknesses as well as on additional p-type Si films had been planned for these studies, which were carried out during the second year of the contract. However, a detailed examination of the directional variation of the electrical properties in the plane of the Si films on Al_2O_3 was begun at about the same time. The results of those

studies were so significant that the major part of the electrical evaluation work for the remainder of the contract period was devoted to investigations of anisotropy phenomena.

3. ANISOTROPY IN ELECTRICAL PROPERTIES OF HETEROEPITAXIAL Si FILMS

As indicated above, a study of the directional variation of electrical properties of Si films on Al_2O_3 in the plane of the film was undertaken in the second year of the contract. This investigation was begun in an attempt to explain what had been a large amount of scatter in the data for carrier mobility as a function of carrier concentration (impurity doping density) and also a lack of reproducibility in the measurements of electrical properties of Si films on Al_2O_3 prepared under presumably the same growth conditions. (See, e.g., Section 3-2).

These effects had been found most pronounced in (221)Si films grown on $(11\bar{2}2)Al_2O_3$ substrates. Upon systematic examination it was found that these films were highly anisotropic in carrier mobility in the plane of the film; preliminary measurements indicated a difference by a factor of nearly 2 between the minimum mobility, observed for current flow in a specific direction, and the maximum mobility, found in a different direction separated from that of the minimum by approximately 90 deg.

On the basis of an early assertion that the anisotropy could be the result of the large piezoresistance effect in Si coupled with the rather large stresses known to be generated in heteroepitaxial films and the anisotropy in the coefficient of thermal expansion in Al_2O_3, a systematic study of two different Si/Al_2O_3 systems was undertaken. A relatively low-symmetry Si plane was represented by the $(221)Si/(11\bar{2}2)Al_2O_3$ combination, and a high-symmetry plane was represented by the $(001)Si/(01\bar{1}2)Al_2O_3$ system. These two Si planes were initially selected because anisotropy in the (221) plane could be expected for any heteroepitaxial system, whereas anisotropy in the (001)Si plane would be the result of the anisotropic thermal contraction of the Al_2O_3 substrate and might not be present for (001)Si films grown on other sub-

strates (e.g., $MgAl_2O_4$) having isotropic thermal expansion properties.

The mobility anisotropy factor A (in percent) was defined as

$$A = \frac{\mu_{max}-\mu_{min}}{\mu_{max}+\mu_{min}} \times 200, \qquad (61)$$

where μ_{max} and μ_{min} are the maximum and minimum carrier mobilities determined from a least-squares fit of data of Hall mobility vs angular direction in the plane of the film measured with respect to a primary crystallographic direction. The anisotropy factor was found to be about 40% for the (221) plane and about 9% for the (001) plane. Results of calculations (see Section 2-5) based on the piezoresistance effect in Si resulting from the difference in the thermal expansion coefficients for Si and Al_2O_3 agreed well with the experimental data. The calculations and the experimental results also indicated that (221)Si probably exhibits higher electron mobilities than other more commonly used orientations.

Experimental studies of anisotropy in the electrical properties of (111)Si/Al_2O_3 were carried out, using both $(10\bar{1}4)$- and $\sim(11\bar{2}0)$-oriented Al_2O_3 substrates. The observed anisotropies did not agree with the predictions of the piezoresistance model for this Si orientation, for reasons which have not yet been established; anisotropies as high as 50% were observed, with an average of 16 to 30%, while the stress model predicts values of 4 to 10%, depending on the substrate orientation. These discrepancies are still under investigation; the results suggest, however, that there are physical phenomena which are relatively more important for (111)Si growth on Al_2O_3 and which are not yet understood. Because of the importance of the details of the anisotropy in the Si/Al_2O_3 system, these investigations are described further in Section 10 of this report.

The Si/$MgAl_2O_4$ system is one of potentially equal interest in the semiconductor device industry, despite a current emphasis on Si/Al_2O_3. As indicated above, the fact that $MgAl_2O_4$ is cubic and has isotropic thermal expansion coefficients would lead to the expectation that any observed anisotropy would

result strictly from symmetry considerations and the piezoresistance effect in the Si films and not from any direct anisotropic contribution from the $MgAl_2O_4$.

Electrical measurements on a variety of Si films grown on $MgAl_2O_4$ substrates were performed and are described in more detail in Section 3-4 and 3-8. However, the results of measurements of mobility anisotropy on three (111)Si/(111)$MgAl_2O_4$ films are given here. The anisotropy parameters obtained using the analytical procedure employed in the other anisotropy investigations (Section 10) are given in Table 33.

Table 33 . Mobility Anisotropy Parameters for (111)Si/(111)$MgAl_2O_4$ at Room Temperature

Sample No.	μ_{max} (cm^2/V-sec)	μ_{min} (cm^2/V-sec)	A(%)	ER1 (%)	ER2 (%)
MB-24-3	796	760	4.6	1.1	2.0
MJ-2-5	873	833	4.7	1.5	2.2
MB-17-2	861	801	7.3	5.5	6.1

The data indicate that a small anisotropy in mobility may in fact occur for (111)Si/(111)$MgAl_2O_4$. However, the error parameters ER1 and ER2, which provide a measure of the "goodness-of-fit" of the experimental data to the theoretical relationship* between mobility and direction in the plane of the film, are relatively large for these samples. As a consequence, it does not appear justified to conclude that an anisotropy effect was actually detected. Clearly, additional measurements must be made in the Si/$MgAl_2O_4$ system to resolve this and other questions.

*See Section 2-5 for a discussion of the theory of the mobility anisotropy effect and Section 10-3-a-1 for a discussion of the error parameters ER1 and ER2 in this context.

4. MEASUREMENT OF CARRIER LIFETIMES IN HETEROEPITAXIAL SEMICONDUCTOR FILMS*

Minority carrier lifetime is one of the most important device-related parameters of semiconductors, but relatively little work had been done in determination of this property in the heteroepitaxial Si/insulator or GaAs/insulator systems prior to the start of this contract.

Several alternative methods of measuring carrier lifetime in Si and GaAs heteroepitaxial films were carefully evaluated early in the contract and it was determined that the most useful technique for the purpose would be that involving pulsed capacitance-voltage (C-V) measurements in an MOS structure. For such measurements, a semiconductor film (on an insulating substrate which serves simply as a support for the semiconductor) is covered with a deposited oxide film (preferably SiO_2 deposited by means of PVD using an electron-beam-heated evaporation source), over which a thin metal control electrode is deposited. A voltage pulse is applied to the MOS structure to take it from an initial condition of accumulation to a final state of strong inversion or from inversion to very strong inversion. Immediately following the application of the pulse, within a time interval the order of the dielectric relaxation time, a large depletion region (much larger than the maximum depletion-region width under steady-state condition) is formed. The capacitance of the MOS structure decreases, therefore, to a very small value. As carriers are thermally generated in the depletion region, the depletion region starts to decrease in width while the charge in the inversion layer correspondingly increases. Thus, the capacitance recovers to the steady state C_{min} value with a time constant which is related to the carrier lifetime approximately by a factor $\frac{N}{n_i}$, where N is the impurity concentration in the semiconductor and n_i is the intrinsic concentration. Thus, by measuring the time response of the MOS capacitor and appropriately correcting for various factors, the lifetime is determined. The method has the important advantage that the

---

*This work was done in the Department of Electrical Sciences and Engineering of the University of California at Los Angeles by C. R. Viswanathan, D. McGreivy, and T. Takino.

actual lifetime is magnified by the factor $\frac{N}{n_i}$ so that very short lifetimes, such as those typical of heteroepitaxial systems (e.g., $\sim 10^{-9}$ sec), can be measured.

a. Theoretical Considerations

In the MOS structure used in this method an insulating layer of SiO_2 was grown onto a film (or wafer) of Si and a metal contact (gate electrode) was evaporated onto the top of the SiO_2. A metal ohmic contact was then made to the Si film (or bulk wafer). Figure 107 shows the MOS geometry initially used in this study for exploratory measurements on bulk Si wafers and for Si/Al_2O_3 films.

When a negative voltage pulse is applied to the gate electrode of a Si MOS structure, majority carriers (electrons) flow away from the SiO_2-Si interface and into the bulk Si, uncovering immobile ionized donor atoms. A space-charge region will be formed in a time interval the order of the dielectric relaxation time τ_d ($\sim 10^{-12}$ sec for 1 ohm-cm Si). Throughout the semiconductor electron-hole pairs will be thermally generated at a constant rate g, dependent only on temperature and crystal parameters. Within the strong field of the space-charge region thermally generated holes will move toward the SiO_2-Si interface and electrons will move toward the bulk Si. Within a depletion layer of area A and width x(r) there will be $A\,g\,x\,dt$ electrons thermally generated between the times t and (t+dt). These electrons will drift to the edge of the depletion layer, neutralizing the space charge in a region dx containing $AN_d dx$ immobile ionized donor atoms, where N_d is the donor doping concentration.

In a space-charge region the lifetime τ_g of the thermally generated carriers is related to the generation rate g by

$$g = \frac{n_i}{2\tau_g}, \tag{62}$$

where n_i is the intrinsic carrier concentration.

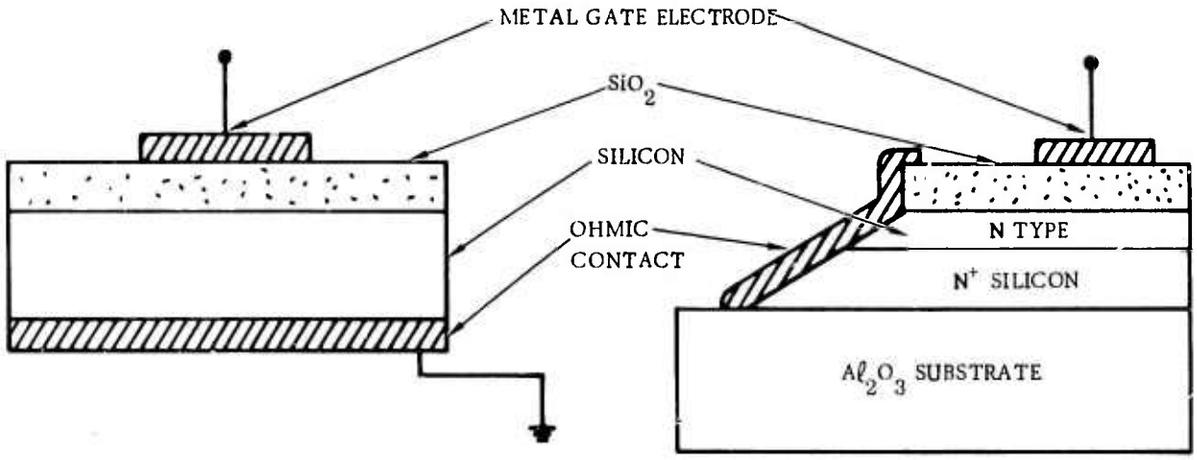

(a) MOS GEOMETRY FOR SILICON WAFERS

(b) MOS GEOMETRY USED FOR SOS SAMPLES

Figure 107. MOS Geometry for Carrier Lifetime Measurements

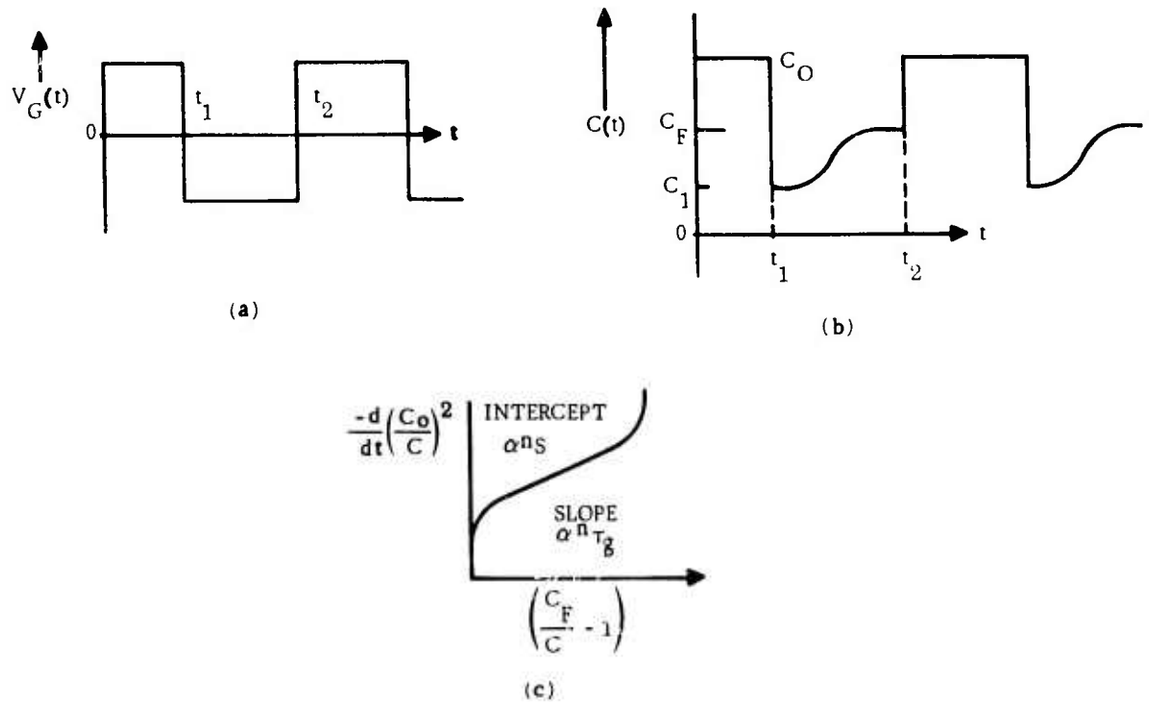

Figure 108. Characteristics of MOS Capacitor in Si/Al_2O_3. (a) Gate Voltage Pulse $V_G(t)$; (b) Resulting MOS Capacitance Transient Response; (c) Zerbst Plot for Capacitor

Then,

$$AN_a\, dx = -A\, g\, x\, dt = -A \frac{n_i}{2\tau_g} x\, dt. \tag{63}$$

Solving for x gives

$$x(t) = x(0)e^{-t/T}, \tag{64}$$

where $T = 2\tau_g (N_d/n_i)$.

At room temperature in Si $n_i \approx 10^{10}cm^{-3}$ and N_d is typically 10^{15} to $10^{18}cm^{-3}$. The MOS capacitor characteristic relaxation time T will be 5 to 8 orders of magnitude larger than the lifetime τ_g. In GaAs, $n_i \sim 10^7 cm^{-3}$ so that T is 8 to 11 orders of magnitude larger than τ_g. If the capacitance C(t) is monitored as a function of time, from the characteristic shown in Figure 108 it appeared that the anticipated lifetime values of 10^{-9}-10^{-10} sec for heteropeitaxial films of Si and GaAs could be measured.

In a more rigorous analysis of the problem, Zerbst (Ref 84) showed that a plot of $-\frac{d}{dt}\left(\frac{C_o}{C}\right)^2$ versus $\left(\frac{C_F}{C} - 1\right)$ yields a straight-line portion whose slope is related to the bulk generation lifetime τ_g and whose intercept on the $-d/dt\ (C_o/C)^2$ axis is related to the surface recombination velocity S. (C_F is the MOS capacitance at time $\tau = \infty$.) This analysis has been improved by a variety of workers to include surface effects more realistically, but always for the case of an ideal MOS device, uniformly doped.

When a Si film or wafer is subjected to a thermal oxidation cycle to create an SiO_2 layer, it has been shown by Grove et al (Ref 85) that in a region the order of 1μm into the Si adjoining the SiO_2-Si interface the doping concentration is redistributed. The surface impurity concentration may differ from that in the interior by a factor of from 2 to 7, depending upon the impurity and the SiO_2 growth conditions (temperature and ambient). An analysis was made to consider the effect of this impurity redistribution on the interpretation of lifetime measurement data obtained by this method.

This measurement technique has been suggested for in-process measurement of τ_g and S during device fabrication, and has been extended (Ref 86) for the case of Schottky-barrier diodes to determine the lifetime, energy level, and density of both deep and shallow impurity levels. In a study of the impurity redistribution in Si near the SiO_2-Si interface that occurs during thermal oxidation, Deal et al (Ref 87) used an "effective" surface doping concentration in examining the C-V characteristic of an MOS capacitor. However, this approach is unsuitable in pulsed measurements to determine lifetime since the depletion layer width W, and hence capacitance, changes with time t.

It is possible to illustrate quantitatively the effect of impurity redistribution on the interpretation of bulk generation lifetime using the pulsed MOS capacitance technique. This was done as follows. Grove et al (Refs 85 and 87) have shown that if a wafer of Si, initially uniformly doped in the bulk with boron to a concentration N_B, is subjected to a thermal oxidation process, the resulting concentration N_S of boron in the Si at the SiO_2-Si interface will be lower than the bulk value by a factor typically from 2 to 7, depending on oxidation conditions. For a phosphorus-doped Si wafer N_S will be larger than N_B by a factor of from 1.1 to 4.

An exponential doping profile of the form

$$N(x) = N_B + (N_S - N_B)e^{-x/x_1} \tag{65}$$

was compared with the exact solution of Grove et al and was found to be in very close agreement (±5 percent). The parameter x_1 is used to fit the exponential doping profile to the exact profile of Grove et al (Ref 85) and is plotted in Figure 109 against $\frac{N_S}{N_B}$ for both boron and phosphorus under various oxidation conditions. Using the exponential doping profile in a double integration of Poisson's equation, an expression for the voltage across the space charge region was obtained.

Following the analysis of Zerbst (Ref 84), it can be shown that the rate

of increase of charge Q_S at the SiO_2-Si interface is related to the MOS capacitance C(t) by

$$\frac{dQ_S}{dt} = \frac{-qN_B\epsilon_S}{2C_o} \frac{d}{dt}\left(\frac{C_o}{C}\right)^2 - \frac{q(N_S-N_B)\ \epsilon_S e^{-W/x_1}}{2C_o} \frac{d}{dt}\left(\frac{C_o}{C}\right)^2 , \qquad (66)$$

where ϵ_S is the permittivity of the Si and q is the electronic charge. It has been assumed that the area A of the metal gate electrode is large enough to neglect surface effects and that the total capacitance may be represented by C_o in series with the depletion layer capacitance $C_d = \epsilon_S A/W$. The first term on the right-hand side of Equation (66) is the result due to Zerbst assuming a uniformly-doped sample, and the second term is the modification due to the exponential doping profile.

Setting Equation (66) equal to the bulk and surface generation current terms gives

$$-\left[\frac{N_B\epsilon_S}{2C_o} \frac{d}{dt}\left(\frac{C_o}{C}\right)\right]^2 B(C) = n_i S + \frac{n_i\epsilon_S}{\tau_g C_F}\left[\frac{C_F}{C} - 1\right], \qquad (67)$$

where the function B(C) is given by

$$B(C) = \left[1 + \left(\frac{N_S}{N_B} - 1\right) \exp\left(\frac{C_1}{C_o} - \frac{C_1}{C}\right)\right] = \left[1 + \left(\frac{N_S}{N_B} - 1\right)\exp\left(-\frac{W}{x_1}\right)\right], \qquad (68)$$

where $C_1 = \dfrac{\epsilon_S A}{x_1}$.

A plot of the left side of Equation (67) as ordinate versus $\left(\frac{C_F}{C} - 1\right)$ yields a straight line whose slope is related to τ_g and whose intercept on the vertical axis is related to S. A Zerbst plot assuming uniform doping yields a lifetime value $\tau_g' \neq \tau_g$, due to the function B(C). If $W \lesssim x_1$ then the entire space-charge region is located within a region of impurity redistribution, and B(C) departs from unity.

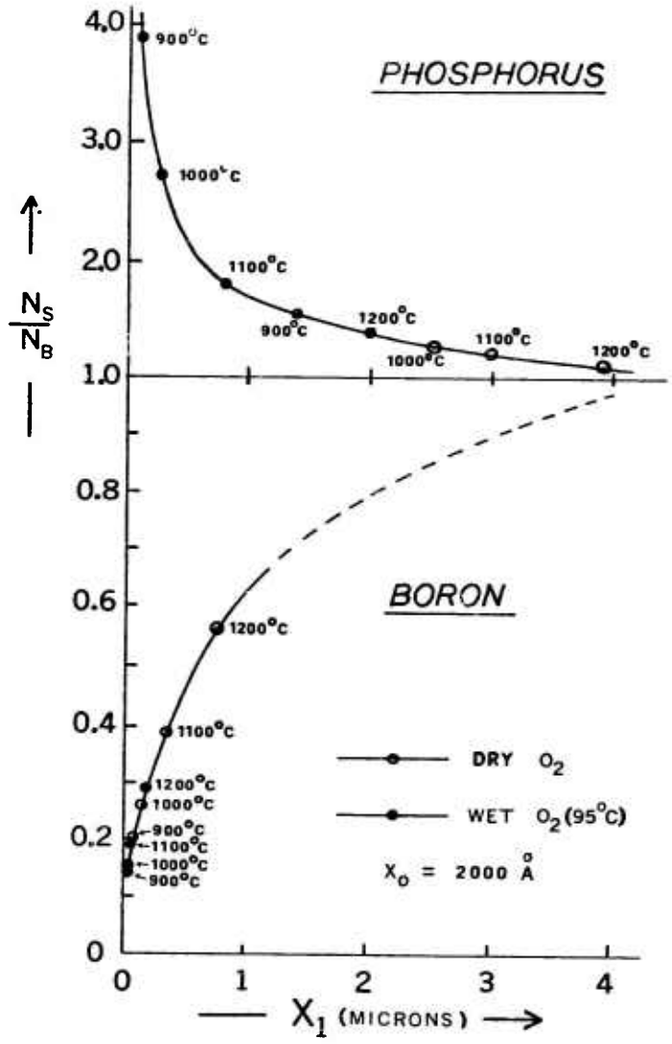

Figure 109. $\frac{N_S}{N_B}$ vs x_1 (in μm) for Phosphorus- and Boron-doped Si under Various Oxidation Conditions (Compiled with the aid of data from Ref 85)

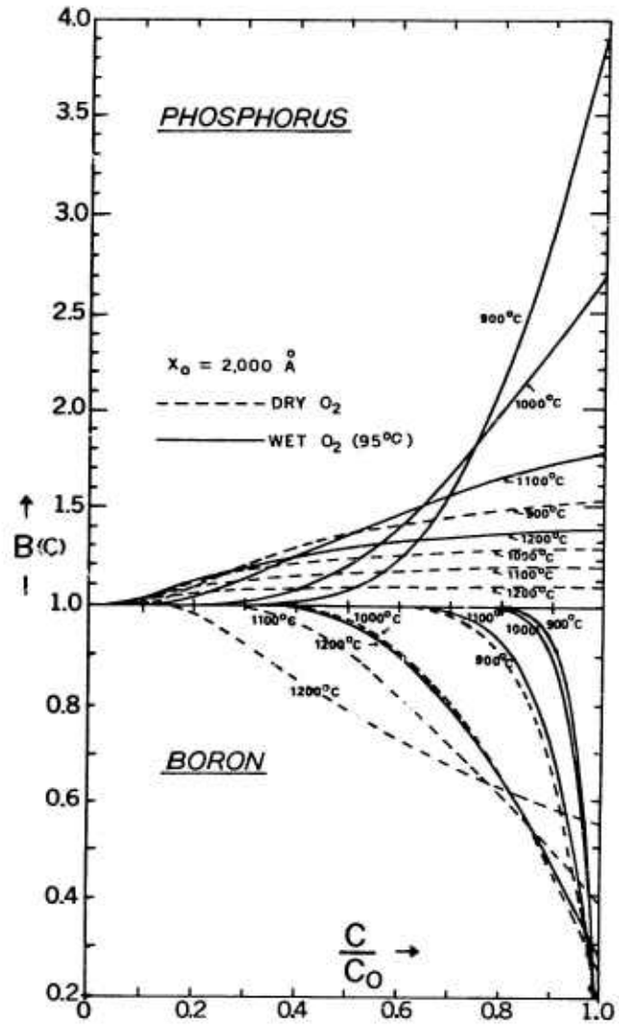

Figure 110. Impurity Redistribution Function B(C) vs Normalized MOS Capacitance C/C_o for Phosphorus- and Borcn-doped Si under Various Oxidation Conditions

Figure 110 shows the variation of B(C) during the capacitance transient for various oxidation conditions. From Equations (67) and (68) and Figures 109 and 110 it can be seen that for boron the function $B(C) < 1$ and $\tau_g > \tau_g'$. For phosphorus the function $B(C) > 1$ and $\tau_g < \tau_g'$.

For $W >> x_1$ then $B(C) \simeq 1.0$ and $\tau_g' \simeq \tau_g$ for the entire transient response.

The exponential doping profile used in the analysis illustrates the effect of impurity redistribution on the interpretation of lifetime measurements from pulsed MOS capacitance experiments. Further high-temperature processing such as annealing, gettering, or a second oxidation step could cause departures in the impurity redistribution profile, thereby leading to apparent changes in lifetime unless the actual doping profile is used in the analysis.

However, the actual doping profile may be obtained from the C-V characteristic (Ref 88). As a computer calculation is usually used to extract the doping profile from the C-V characteristic, it is convenient simply to incorporate this measured doping profile into the computer program analyzing the capacitance-time response, thereby obtaining more precise measurements of τ_g and S. Alternatively, thermal oxide growth conditions may be chosen from Figures 109 and 110 that result in negligible impurity redistribution, thereby allowing the simpler uniform doping approximation to be used in the waveform analysis.

To establish the effects of surface phenomena on the lifetime measurements the following analysis (valid when the diameter D of the gate electrode of the n-type MOS capacitor is $\geq 20\mu m$) was carried out.

When a negative voltage is applied on the gate electrode a space-charge region (SCR) is formed in the semiconductor. The value of the surface recombination velocity S is a maximum immediately after application of the voltage pulse (depleted surface) but decreases rapidly as the minority carrier concentration increases throughout the transient. If the MOS capacitor is prebiased into inversion prior to the depleting voltage step, then the sur-

face recombination velocity in the region of the surface directly beneath the gate electrode will remain at a very low value throughout the transient.

Due to the impurity redistribution effects, the SCR width y_d along the Si surface will differ from the SCR width x_d perpendicular to the gate electrode. For a boron-doped Si sample oxidized in steam at 900C typically $y_d = 2.7\ x_d$. For a phosphorus-doped Si sample oxidized under identical conditions $y_d = 0.5\ x_d$. With the surface generation currents reduced to an edge effect when prebiased into inversion and with impurity redistribution effects being considered, the MOS transient is described by the equation

$$-\frac{d}{dt}\left(\frac{C_o}{C}\right)^2 = \frac{n_i C_o \left(\frac{C_F}{C} - 1\right)}{C_F N_B \left[1+\left(\frac{N_S}{N_B} - 1\right)\exp\left(-\left\{\frac{C_1}{C} - \frac{C_1}{C_o}\right\}\right)\right]} \frac{1}{\tau_{g_{eff}}}, \qquad (69)$$

where C = MOS capacitance, C_o = oxide capacitance, and C_F = MOS capacitance at end of transient.

In the last term $\tau_{g_{eff}}$ is an "effective" thermal generation lifetime given by

$$\frac{1}{\tau_{g_{eff}}} = \frac{1}{\tau_g} + \frac{4aS}{D}, \qquad (70)$$

where τ_g = actual bulk thermal generation lifetime, D = gate diameter and $a = \sqrt{\frac{N_B}{N_S}}$.

The S value in Equation (70) is the value of the surface recombination velocity for the depleted lateral SCR and so should represent the maximum surface recombination velocity of the Si sample. The effect of the surface

on the MOS transient is thus reduced to that of an edge effect. Schroder and Nathanson (Ref 89) first noted this effect on pulsing from accumulation to inversion. With the capacitor prebiased into inversion, however, the surface effects are essentially eliminated.

The maximum possible value of S is given by $S_{max} = \frac{\bar{v}}{2}$, where $\bar{v}$ is the thermal velocity of the minority carriers. For holes with $\bar{v} = 5 \times 10^6$ cm/sec the maximum possible value of the surface term $\frac{4aS}{D}$ is, for a = 0.5 and $D = 5 \times 10^{-2}$ cm, equal to 10^8 sec^{-1}. For bulk thermal generation lifetime values of $\tau_g \leq 10^{-9}$ sec the surface generation term becomes negligible in comparison with the bulk generation term. For many of the Si/Al_2O_3 samples measured $\tau_{g_{eff}}$ was found to be $\leq 5 \times 10^{-10}$ sec, so that it may be concluded that the generation-recombination mechanisms are bulk - rather than surface - dominated in these samples.

A further feature of the above expression for $1/\tau_{g_{eff}}$ is that a plot of $1/\tau_{g_{eff}}$ versus 1/D should yield a straight line whose intercept on the $1/\tau_{g_{eff}}$ axis is proportional to $1/\tau_g$ and whose slope is proportional to S.

b. Preliminary Results

In the first attempts to apply this method to the measurement of carrier lifetime in Si/Al_2O_3 samples the device configuration shown in Figure 107 was used. SiO_2 films typically 1000 to 2000Å thick were grown on bulk Si wafers (for control) and on Si/Al_2O_3 samples using a standard thermal oxidation system. (The system was capable of producing dry, wet or steam-grown oxides at temperatures up to 1200C.) Since the surface recombination velocity for very small geometries can dominate the C-t response of an MOS device, particular attention was given to avoiding contamination of the samples during thermal oxidation. The SiO_2 layers grown on the Si/Al_2O_3 samples were grown at temperatures below the Si film growth temperatures.

Electrical contacts were formed by vacuum-deposited metal films. Al was used

for the gate electrode on both p- and n-type devices. Al deposited onto the back face of Si wafers served as an ohmic contact for p-type samples and Au/Sb deposited contacts served as ohmic contacts to n or n^+ regions. In some cases the Au/Sb contacts were sintered at 500C in a N_2 atmosphere for 20 min to improve their ohmic behavior.

After fabrication of an MOS device the dc electrical conductivity (between gate and ohmic contacts) was checked to ensure that a highly insulating oxide had been grown. The C-V characteristic was then automatically recorded on an x-y recorder. The C-t characteristic was then recorded, using either an x-y recorder for transients of the order of 5 sec or longer (typical for bulk wafers) or a storage oscilloscope and camera for shorter capacitance transients. The test equipment was capable of measuring C-V characteristics from 1 to 10 pf ($\pm$0.2 pf) or $\pm$2 percent from 10 to 3000 pf, and C-t transients of from 10^{-4} to 10^{3} sec. The capacitance monitoring equipment was also capable of displaying dC/dt versus t. This feature decreased the task of data reduction in an exact C-t analysis.

The first successful measurements were made on Si/Al_2O_3 samples with SiO_2 films 1500Å thick grown at 1000C in steam, after some initial difficulties with the oxide growth process. Measurements of C-V and C-t were made on several n-type films about 3μm thick grown on n^+ layers 10-15μm thick. The C-t responses were essentially exponential, and the theory yielded lifetime values in the $1\text{-}2\times10^{-9}$ sec range. As reported previously (Ref 4), many of the samples of n-type Si/Al_2O_3 used in the earlier part of the program for these lifetime measurements exhibited a high incidence of pinholes in the Si film during and after processing; a higher pinhole density was observed in the (111) orientation than in the (100) orientation, and the thinner films were also more subject to this difficulty. Fortunately, this problem disappeared later in the program (the exact cause unidentified) and satisfactory MOS structures were readily fabricated.

c. Recent Experimental Results

In its most recent configuration the experimental arrangement for these carrier lifetime measurements was as shown schematically in Figure 111. Figure 111a shows the general schematic of the entire apparatus and Figure 111b is the diagram of the flip-flop circuit designed to provide a step voltage to the MOS capacitor (shown in the center of Figure 111a). The flip-flop was triggered from a pulse generator which could be manually triggered to provide a pair of pulses each time. The first pulse was used to trigger the sweep of the trace in the oscilloscope and a second delayed pulse was used to trigger the flip-flop. The capacitance of the MOS sample was measured by applying a small-signal high-frequency (3MHz) voltage to the MOS capacitor in series with a small resistance. The amplitude of the high-frequency voltage across the resistor was proportional to the instaneous value of the capacitance of the MOS structure. This voltage was amplified and rectified to provide a dc voltage proportional to the capacitance, and this voltage was applied to Y-input terminals of the oscilloscope such that a capacitance-vs-time response was displayed on the oscilloscope. Figure 111c shows a typical C-vs-t response obtained with this apparatus.

Using the analysis developed by Zerbst (Ref 84) the C-t data were reduced to yield lifetime values as well as the surface recombination velocity, as discussed earlier.

(1) Sample Preparation

All of the samples reported on here were n-type or n/n^+-type Si/Al_2O_3 samples prepared under one of the subtasks of this contract program. For comparison purposes some Si/Al_2O_3 samples prepared by an outside vendor (Inselek, Inc.) were occasionally used in the measurements. These are discussed subsequently.

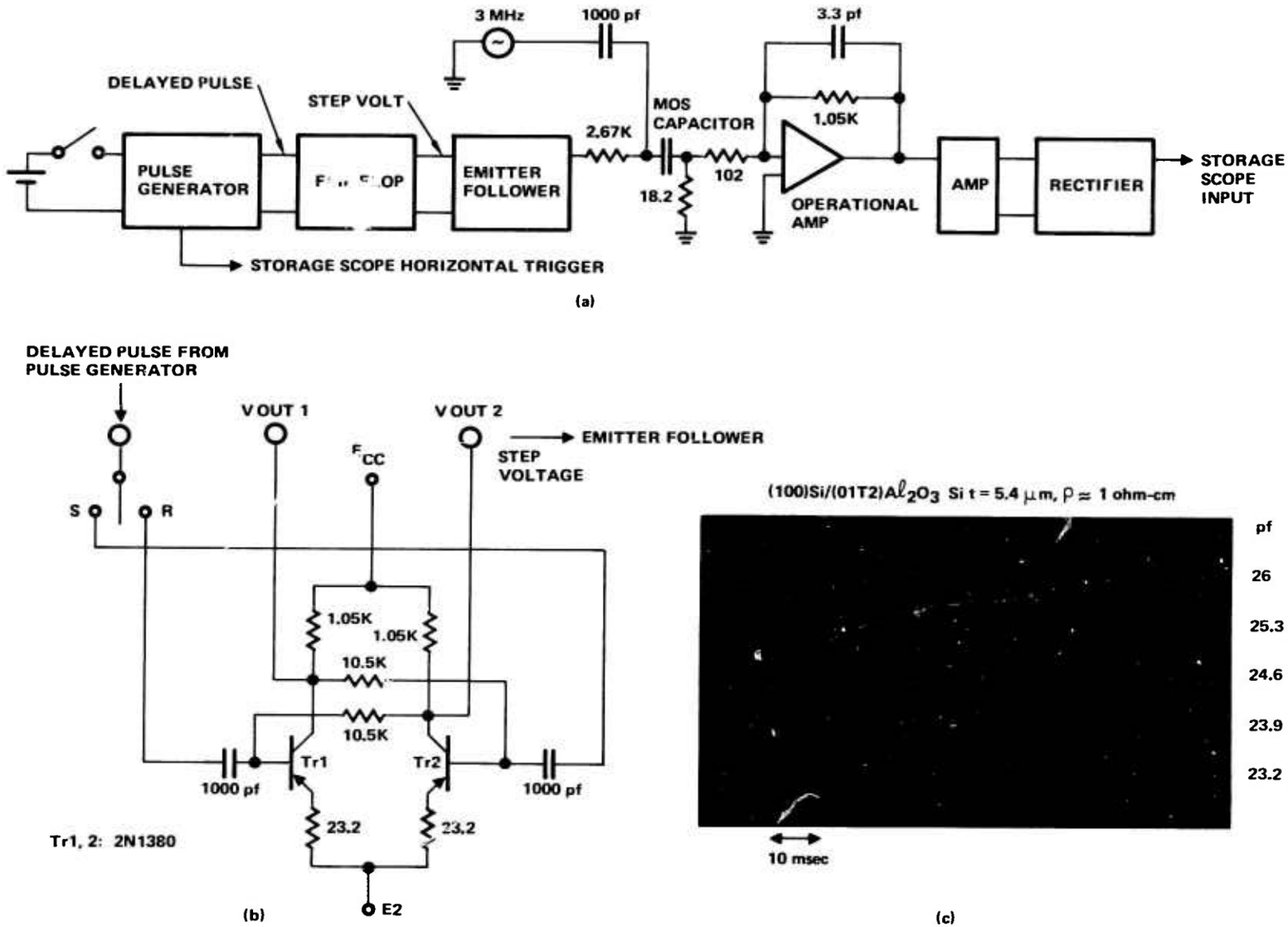

Figure 111. Schematic Diagram of Apparatus for Measuring Carrier Lifetime by Pulsed C-V Technique in MOS Structures. a) Full Apparatus; b) Flip-flop Circuit.

The composite film/substrate samples were cleaned as follows: They first were cleaned in hot trichloroethylene for 10 min and then placed in the ultrasonic cleaner for 5 min, cleaned in hot acetone for 5 min, and then rinsed in D.I. water. They were next immersed in hot H_2SO_4 for 15 min and then rinsed in D.I. water. A rinse in HF was used to remove the thin oxide film on the samples, after which they were rinsed in D.I. water again and dried in a clean N_2 gas stream.

The Si films were oxidized, using a wet oxidation process, at 900C for 3 hr to obtain an oxide film of 6000Å thickness. If the samples had an n^+ or a p^+ layer underneath, this step was replaced by depositing a 6000Å-thick oxide layer by the oxidation of SiH_4 ("silox" process) at 500C. The Si was then coated with a film of KMER and the sample was prebaked for 15 min at 100C. Using a suitable mask (A in Figure 112) the sample was exposed for 30 sec, developed and rinsed, and postbaked for 90 min at 100C. Windows were cut in the oxide with dilute HF and the photoresist stripped in hot H_2SO_4. For n-type samples there was a P predeposition at 950C for 6-8 min.

Without any further processing a coat of KMER was again applied and the process repeated, this time using mask B (Figure 112) to cut windows for gate oxidation. The gate oxidation was carried out using a wet oxidation process at 900C for 50 min to obtain an oxide thickness of 1700Å. Again using the photoresist process and with mask A as contact mask, windows were cut in the oxide. The samples were then metallized by Al deposition, the film being approximately 5000Å thick. Using the photoresist process and mask C, the required MOS capacitors with a guard ring arrangement were then fabricated. After this step, the Al films were sintered in N_2 at 500C for 3 min.

The n-type Si/Al_2O_3 samples used in these measurements were prepared by the standard SiH_4 pyrolysis CVD process in a vertical reactor, as described in Section 3 of this report. They were As-doped during growth at temperatures of typically 1075C at growth rates of ~2μm/min. The Al_2O_3 substrates were prefired in H_2 for 15 min at 1300C before Si deposition, and most of the films were annealed for 1/2 hr in O_2 and 1 hr in N_2 at 1100C after growth.

MOS CAPACITOR MASK (RELATIVE DIMENSIONS)

A. MASK FOR p^+ DIFFUSION AND CONTACT

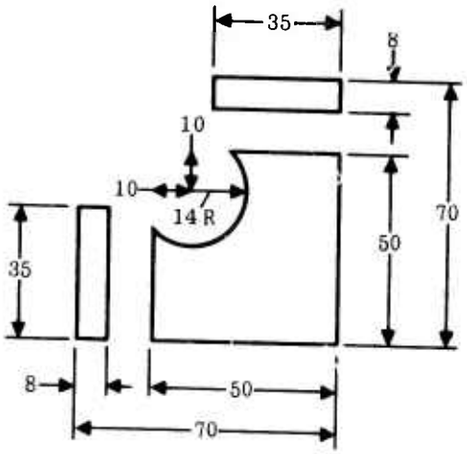

B. MASK FOR GATE OXIDE

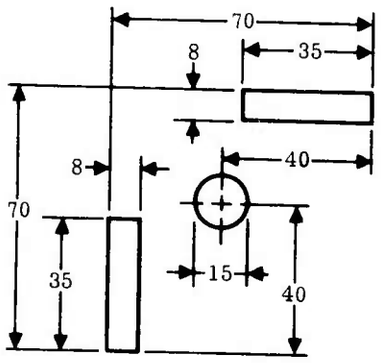

C. MASK FOR METALLIZATION

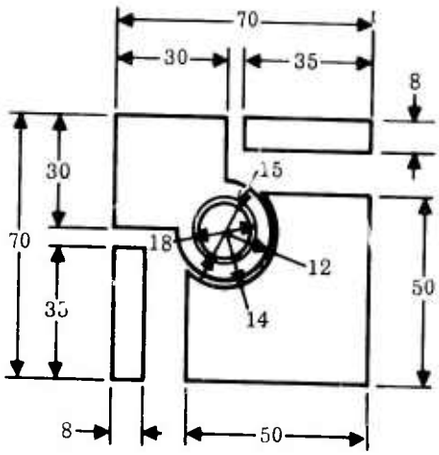

Figure 112. Mask Set Used for Fabricating MOS Capacitor for Carrier Lifetime Measurements

(2) Results of Measurements

Four-point probe resistivity measurements were made on all of the films and Hall-effect measurements on some of them, as well as on companion samples grown simultaneously in the reactor for monitoring purposes. In several instances MOS capacitors were fabricated according to the processing procedures outlined earlier. On capacitors exhibiting a dc resistance of greater than 10^9 ohms both high-frequency C-V and C-t measurements were performed. The value of doping concentration obtained from the C-V curve was in general found to agree with the carrier concentration obtained from Hall-effect measurements performed on the As-doped films grown at Rockwell, but did not agree with the value of doping concentration specified by the vendor for the P-doped films.

At several locations on each sample C-V and c-t characteristics of the MOS capacitors were measured. Values of the bulk thermal generation lifetime τ_g were then obtained for each capacitor from a plot of $-d/dt(C_o/C)^2$ versus $C_F/C - 1)$. The average value of τ_g over at least five devices on each Si film was then computed; the data are plotted in Figure 113 as a function of the Si film thickness for both As-doped and P-doped films. The range of τ_g values measured across a single Si/Al_2O_3 sample is represented in Figure 113 by the vertical bar.

It does not necessarily follow from Figure 113 that in general P-doped Si/Al_2O_3 films yield a higher lifetime than As-doped Al_2O_3 films, since the two batches of films were grown in separate laboratories using slightly different techniques and growth conditions. All of the As-doped films of Figure 113 were grown on a rotating pedestal in a vertical reactor at a temperature of 1075C at a growth rate of 2.0μm/min and had a doping concentration in the range 5×10^{16} to 2×10^{17} cm^{-3}. The P-doped films were all grown on a rotating pedestal in a vertical reactor at a temperature of 1000C and a growth rate of 4μm/min, and were doped to a concentration of 1×10^{15} cm^{-3}. Both the As- and P-doped Si films of Figure 113 were (100)-oriented.

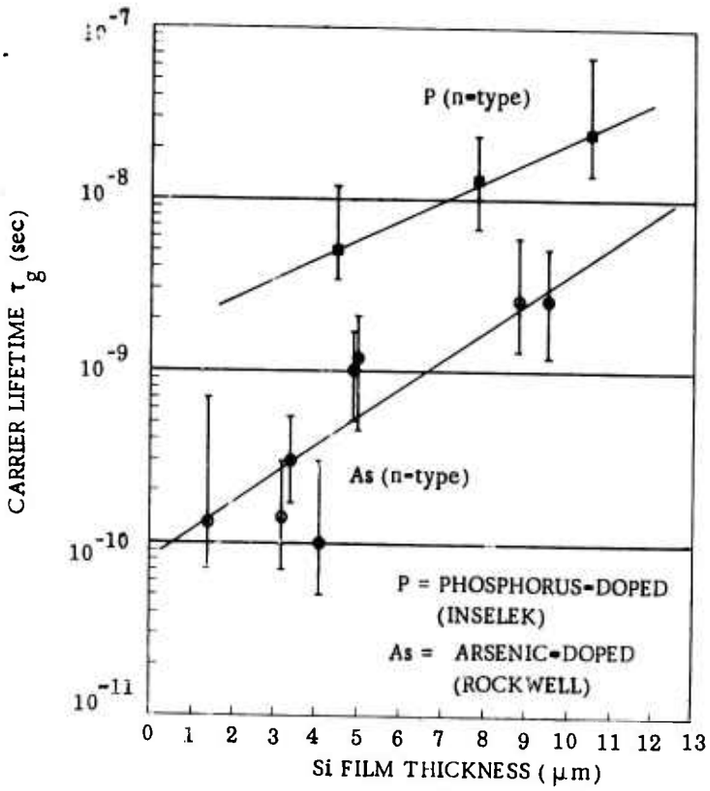

Figure 113. Carrier Lifetime in N-type Si/Al_2O_3 as Function of Film Thickness for As-doped and P-doped Films

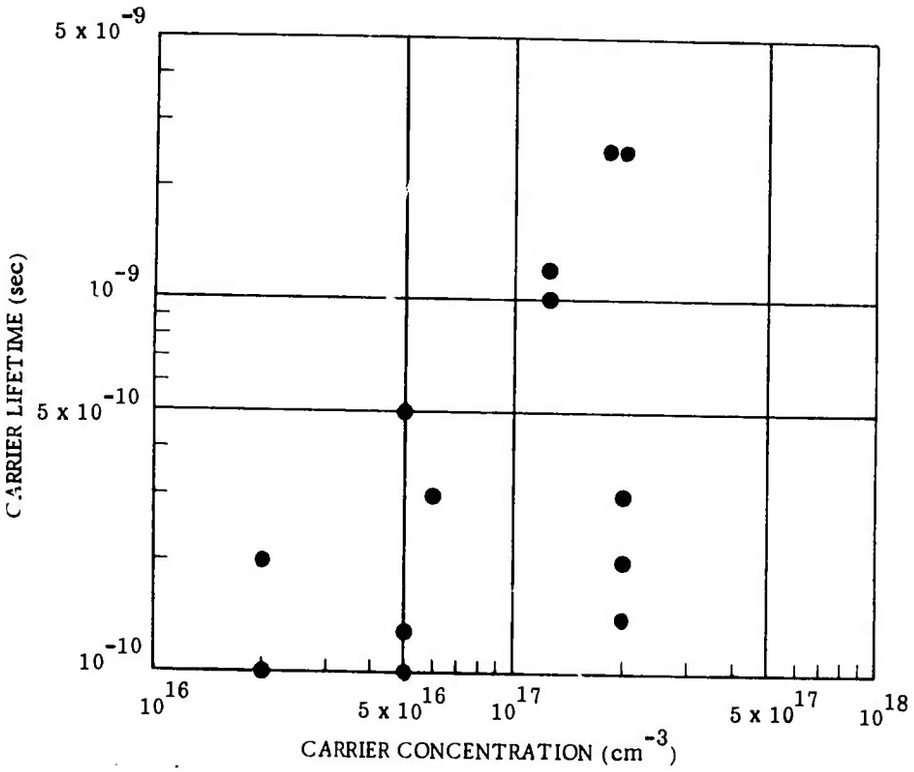

Figure 114. Carrier Lifetime in N-type As-doped Si/Al_2O_3 as Function of Doping Concentration

The C-t characteristics of several MOS capacitors were monitored for various gate-voltage pulse amplitudes. Due to the relatively high doping concentrations in the As-doped films only a very small distance into the Si could be probed by increasing the gate-voltage pulse amplitude. No significant changes in τ_g values were observed when this was done. At pulse amplitudes in excess of 40V the oxide layer suffered dielectric breakdown, destroying the MOS capacitor.

C-V and C-t characteristics were measured on Si film samples doped with As to concentrations from 1×10^{16} to $3 \times 10^{18} cm^{-3}$. Values of bulk thermal generation lifetime τ_g obtained from a plot of $-d/dt\ (C_o/C)^2$ versus $(C_F/C-1)$ for films of similar thickness and grown under similar conditions of growth rate and growth temperature are given in Figure 114 as a function of the doping concentration. The τ_g values plotted in this figure represent the average τ_g determined from the C-t transients of several capacitors at different locations on the same wafer subjected to the same gate-voltage pulse amplitude. No clear dependence of the value of τ_g on As doping concentration can be seen in the data, although the highest lifetime values were obtained on films exhibiting the highest doping concentration.

In order to examine the effect upon carrier lifetime of an underlying heavily-doped layer several composite samples were prepared on $(01\bar{1}2)$-oriented Al_2O_3 substrates. Various thicknesses of n^+ Si (As concentration $\sim 3 \times 10^{18} cm^{-3}$) were grown (at 1075C) first, followed by a 3μm upper layer of n-type Si As-doped to concentrations of $\sim 2 \times 10^{16} cm^{-3}$ (also grown at 1075C).

The average τ_g values measured from at least five capacitors on each film are shown in Figure 115 as a function of the total thickness. For comparison, the results of measurements of τ_g versus film thickness for n-type films, as shown in Figure 113, are reproduced in this figure. The presence of the heavily-doped n^+ sublayer is seen to increase the value of τ_g for a given Si thickness.

The density N_t of the efficient generation-recombination (g-r) centers that are responsible for the low lifetime values in Si/Al_2O_3 films is seen from Figure 113 to decrease with an almost exponential dependence on the distance x

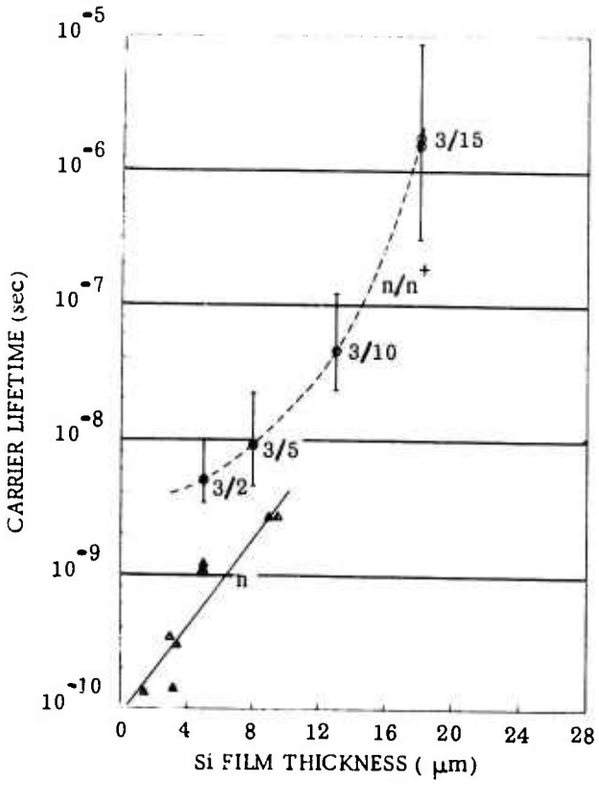

Figure 115. Carrier Lifetime in N-type As-doped Si Film on N^+ Layer on Al_2O_3 Substrate, as Function of Total Si Thickness. (Results for single layer from Figure 113 included for comparison.)

from the Si-Al_2O_3 interface into the Si film. As a first order approximation this dependence can be written as

$$N_t(x) = N_t(o)\exp(-x/h), \tag{71}$$

where h is a constant characterizing the rate of decrease of the trap (or g-r center) density with distance from the Si-Al_2O_3 interface. Since the density of the effective g-r centers in the n-on-n^+ films is essentially an order of magnitude lower than in n-type films of the same thickness and grown under identical conditions, it may be concluded that the n^+ sublayer acts as a "sink" or "gettering" region for the efficient g-r centers. Since the lightly doped 3μm-thick n-type film is grown in a time of only 90 sec at a temperature of 1075C, it is unlikely that the defect centers actually diffuse out of the lightly doped layer and into the n^+ layer. Rather, the As atoms in the n^+ layer appear to "tie up" the efficient g-r centers in such a manner that their propagation through the lattice is dramatically reduced.

Very recently, and independent of this study, Schroder and Rai-Choudhury (Ref 90) have reported that the presence of a heavily P-doped sublayer beneath a lightly doped n-type layer has a similar gettering effect. By using a P concentration in excess of $10^{20}cm^{-3}$ in a 1μm-thick n^+ layer (two orders of magnitude higher concentration than the As concentration in the n^+ layers used in this study), these investigators were able to achieve values of τ_g the order of 1μsec in a 2μm-thick Si/Al_2O_3 film. Unfortunately, P-doped Si/Al_2O_3 films were not available for this study so that no comparison of the effective gettering action of As and P n^+ layers of the same doping concentration and thickness could be made. It should be noted that this is evidently the first report of a gettering action being associated with As doping in Si.

To examine the effect of the Si film orientation on these results, carrier lifetime measurements were made on MOS capacitors fabricated on (100)- and

(111)-oriented As-doped Si films which had been grown simultaneously in the vertical reactor. In general, the (100)Si films exhibited a two to three times heavier doping concentration than (111)Si films grown in the same batch. However, no significant differences in thermal generation lifetime results were observed in the two Si orientations. Table 34 lists the average values of τ_g for a pair of (100) and (111) Si/Al_2O_3 films grown in the same growth cycle and also for a variety of other (100)- and (111)-oriented Si films grown under almost identical conditions but in separate batches.

The carrier lifetime was measured at four different temperatures one one (100)-oriented n-type Si/Al_2O_3 sample which had a thickness of 4-5μm. Figure 116 gives a plot of the lifetime values measured on two different MOS capacitors at different temperatures. The data points marked with x represent the values obtained on a sample which had a gate oxide 600Å thick, while the points marked with circles represent the values obtained on a sample with the oxide layer 1700Å thick. The increase of lifetime values with temperature seems quite strange and is not explained at this time.

Finally, the surface recombination velocities corresponding to the two sets of lifetime determinations of Figure 116 are shown in Figure 117.

It is clear that this lifetime study should be extended to low temperatures in order to obtain a more complete understanding of the recombination - generation process in heteroepitaxial Si films. A systematic study of lifetime dependence on the amplitude of the step voltage in lightly doped samples is also needed. Unfortunately, p-type samples were not included in this study, and a systematic investigation of lifetime in p-type Si film samples and in p on p^+ Si film samples should be undertaken.

Table 34. Thermal Generation Carrier Lifetimes τ_g for Two Orientations of Si/Al_2O_3

Sample Number	Thickness (μm)	As Concentration (cm^{-3})	Si Film Orientation	τ_g ($x10^9$ sec)
As-94*	1.4	5×10^{16}	(111)	0.12
As-11*	1.4	2×10^{16}	(100)	0.10
As-61	8.8	2×10^{17}	(111)	2.6
As-107	9.5	1.2×10^{17}	(100)	2.6
As-66	5.0	1.2×10^{17}	(111)	0.3
As-34	3.4	2×10^{17}	(100)	0.3
As-30	2.0	6×10^{16}	(111)	0.12
As-111	3.2	2×10^{17}	(100)	0.30

*Samples grown simultaneously.

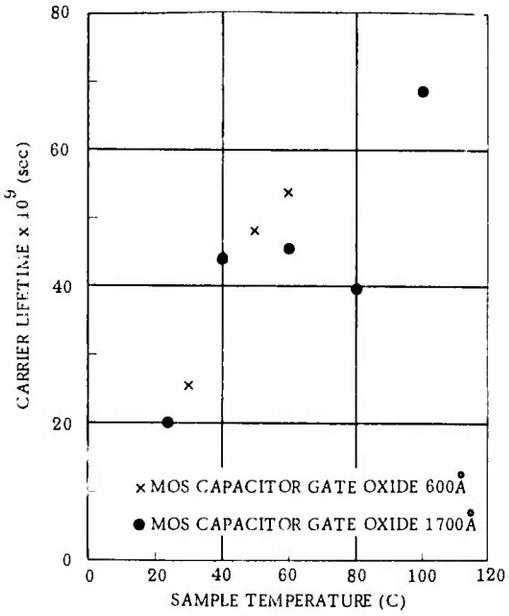

Figure 116. Carrier Lifetime in N-type $(100)Si/(01\bar{1}2)Al_2O_3$ as Function of Temperature

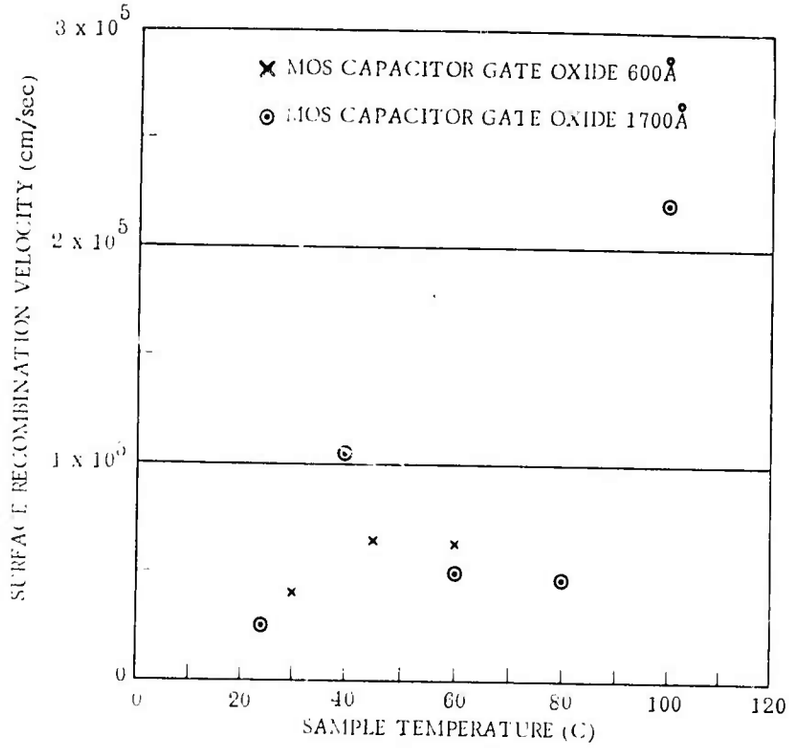

Figure 117. Surface Recombination Velocities as Function of Temperature for Si/Al_2O_3 Samples of Figure 116.

5. DETERMINATION OF SURFACE-STATE DENSITY IN Si/Al_2O_3*

As part of the characterization of the electrical properties of heteroepitaxial Si films on Al_2O_3 the surface-state density of thermally oxidized Si films was determined using the MOS-CV technique employed in the carrier lifetime measurements. This parameter is of use not only in understanding the electrical and physical characteristics of the films but also in evaluating the performance of MOS devices fabricated in Si/Al_2O_3 composites.

Several methods are available for the surface-state density determination using C-V plots obtained with MOS capacitors. In any of the methods there are two steps: The first is to determine the surface potential as a function of the applied voltage, and the second is to determine the surface-state density as a function of the applied voltage and therefore as a function of the surface potential.

---

*This investigation was carried out by C. R. Viswanathan of the University of California at Los Angeles, Department of Electrical Sciences and Engineering.

a. Experimental Procedure

The integration procedure developed by Berglund (Ref 91) was selected to obtain the surface potential as a function of the applied voltage from the low-frequency C-V data. The only requirement for the validity of this method is that the surface states be in equilibrium during the measurement of the capacitance as a function of the applied voltage; this means that the dc bias voltage should be swept very slowly and the measurement frequency should be low enough for the surface states to follow the varying voltage.

A small change in the applied voltage dV can be expressed as

$$dV = dV_o + dV_s, \tag{72}$$

where dV_o is the change in voltage V_o across the oxide and dV_s is the change in the surface potential V_s. Therefore

$$\frac{dV_s}{dV} = 1 - \frac{dV_o}{dV} = 1 - \frac{C}{C_o}, \tag{73}$$

where C is the capacitance of the MOS structure at a given voltage and C_o is the oxide capacitance.

The change in the surface potential between two values of applied voltage V_1 and V_2 is obtained by direct integration:

$$V_s(V_1) - V_s(V_2) = \int_{V_2}^{V_1} (1 - \frac{C}{C_o}) dV. \tag{74}$$

In order to perform the integration the low-frequency C-V data are used.

To determine the exact location in the band gap, a reference point is needed. There are several ways of obtaining this; the flat-band voltage method was used first, as follows. The C-V curve was obtained at a sufficiently high frequency so that the surface states were not able to follow the applied alternating small-signal voltage. The flat-band capacitance was calculated knowing the C_{min}/C_{max} ratio, the area, and the thickness of the gate oxide. From the high frequency C-V curve, the flat-band voltage V_{FB} was then obtained. This provided a reference point, since $V_S = 0$ at the flat-band voltage.

To determine the surface-state density, C-V curves obtained at high and low frequencies were used (Ref 92). The surface-state density is given as

$$N_{ss} = \left[\frac{C_{LF}}{C_o - C_{LF}} - \frac{C_{HF}}{C_o - C_{HF}} \right] \frac{C_o}{qA} , \qquad (75)$$

where C_{LF} is the low-frequency capacitance, C_{HF} is the high-frequency capacitance, A is the area of the gate electrode, and q is the electronic charge. The C-V curve was also measured at intermediate frequencies so that the time constant of the surface states could be obtained.

The circuit to measure the capacitance was similar to that described in the discussion of carrier lifetime measurement (Section 9-4). The samples that were used in this investigation were prepared in the Rockwell laboratories under this contract in exactly the same way as the samples used in the lifetime measurements.

b. Results and Discussion

The C-V curves obtained at the measurement frequencies of 2, 25 and 100 Hz are shown in Figure 118 for an n-type (100) $Si/(01\bar{1}2)Al_2O_3$ sample of 1 ohm-cm resistivity. From the low-frequency C-V curve, the surface potential was determined using the integration procedure, and the plot of the surface

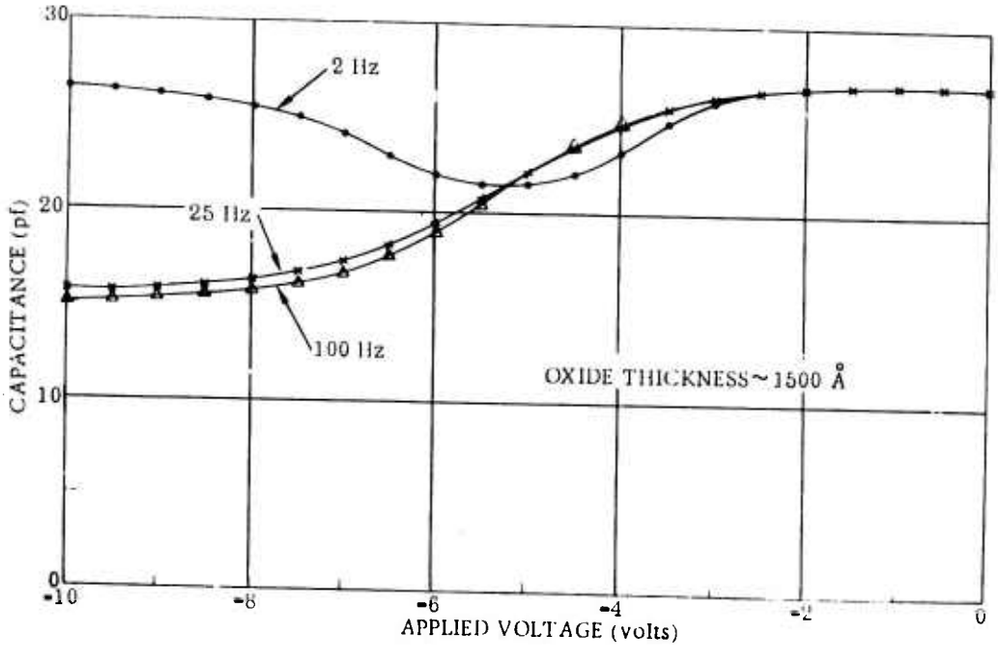

Figure 118. C-V Characteristics for N-type (100)Si/(01$\bar{1}$2)Al_2O_3 at Various Frequencies

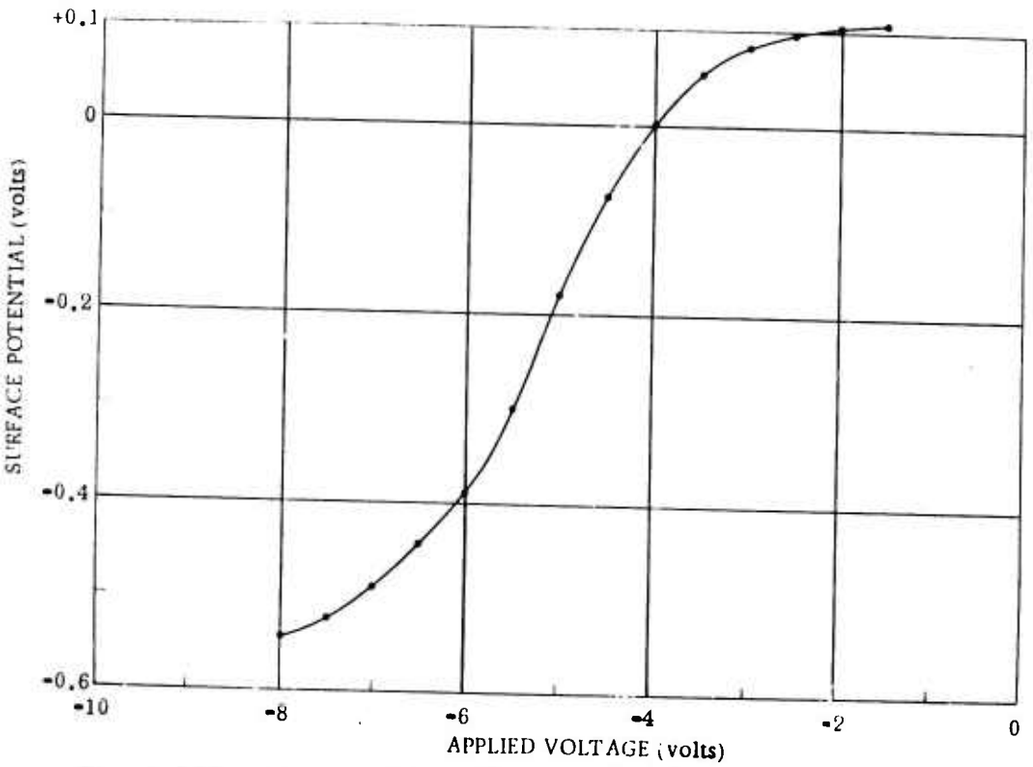

Figure 119. Surface Potentials for Si/Al_2O_3 as Function of Applied Voltage, Obtained from Low-frequency C-V Data

potential as a function of the applied voltage is given in Figure 119. The surface-state density was determined using Equation (75) with the results of the C-V measurement at 2 and 100 Hz.

Evidence of the presence of both donor- and acceptor-type surface-states was obtained. The distribution of these two types of states is shown in Figure 120. The bulk-potential of the Si film was calculated to be 0.34V. A peak in the acceptor-state density at approximately 0.16eV below the conduction band can be seen. The donor-state density appears to increase with surface potential at least up to -0.55V. The exact location of the peak in the donor-state distribution was not determined because the measurements were restricted to a surface potential of -0.55V (-8.2V applied). At more negative values of applied voltage the method introduces inaccuracies due to the onset of strong inversion.

Comparison of the C-V curves obtained at 25 and at 100 Hz permitted determination of the density of surface states having a time constant less than 6 msec, and their distribution is shown by the lower curve in Figure 120.

For comparison purposes the surface-state density of one MOS sample fabricated in (100)Si/Al_2O_3 obtained from a commercial supplier (Inselek, Inc.) was determined. The film thickness was 1μm, and the oxide thickness was grown to 600Å. The C-V curves obtained at 100 and at 1000 Hz are shown in Figure 121. The surface-state density was found to vary from a low value of $1\text{-}6\times10^{10}\,cm^{-2}eV^{-1}$ in the middle of the gap to $10^{12}\,cm^{-2}eV^{-1}$ in the neighborhood of the surface voltage corresponding to the onset of strong inversion.

It is also interesting to note that this sample produced a low-frequency C-V curve at the frequency of 100 Hz, while the sample prepared under the contract and used to obtain the data of Figures 118-120 gave the low-frequency characteristic at a much lower frequency (viz, 2Hz). This suggests that the carrier lifetime in the latter sample is at least 50 times larger than the commercial sample.

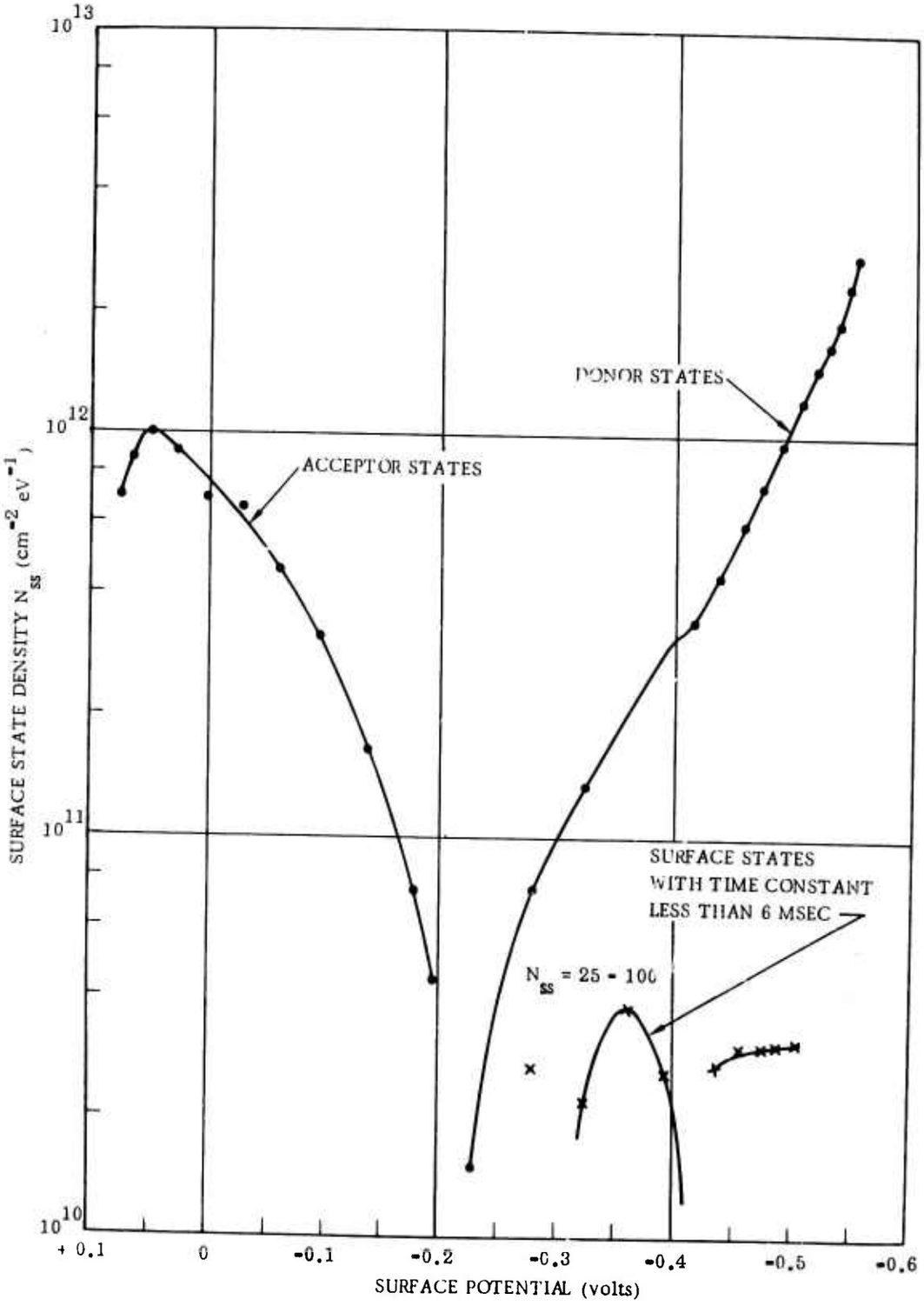

Figure 120. Density Distribution of Donor- and Acceptor-type Surface States in Si Film on Al_2O_3 Substrate; Distribution of States with Time Constant <6msec Included

The results of these brief investigations were sufficiently encouraging, in terms of supplying useful information about the heteroepitaxial films prepared on this contract, to warrant a recommendation for further studies. The surface-state density distribution and associated time constants for various n- and p-type Si/Al_2O_3 films should be measured at several different temperatures. Similar determinations should also be made in the $GaAs/Al_2O_3$ system.

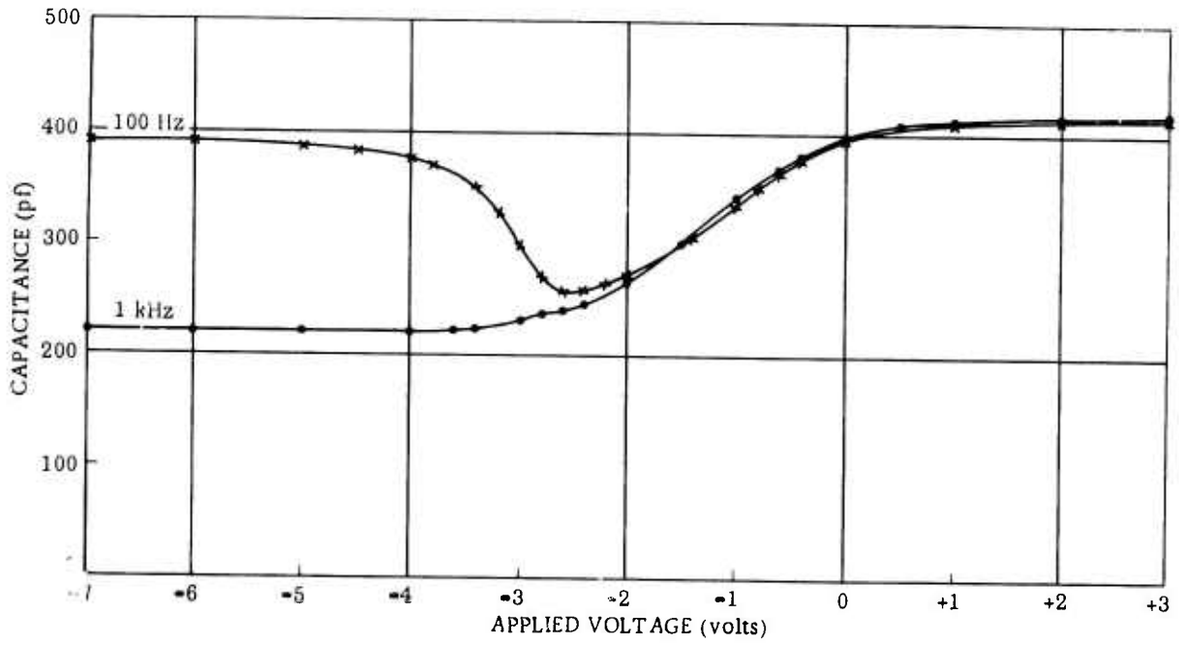

Figure 121. C-V Characteristics at Two Frequencies for N-type Si/Al_2O_3 Sample Obtained form Commercial Supplier

6. MEASUREMENT OF HIGH-FIELD TRANSPORT PROPERTIES OF HETEROEPITAXIAL FILMS*

Investigations of the high-field transport properties of both Si and GaAs films on Al_2O_3 substrates were performed as part of the contract film evaluation procedures.

Measurements of high-field transport properties provide drift mobility data as a function of applied electric field. As is well known, Hall and drift mobilities can differ in semiconductor films, with the drift mobilities being the more sensitive to defects and trapping phenomena. Measurements yielding drift mobilities in heteroepitaxial films are thus complementary to and augment the Hall mobility measurements employed extensively on this contract program.

Drift mobility measurements were made on several heteroepitaxial films as a function of electric field using the simple relationship between measured current and applied field ξ, i.e., $I = nq\mu\xi$. However, since the sample was heated by the current flow and the temperature was no longer constant, a pulse technique was subsequently used, in which the voltage was applied in the form of a narrow pulse at a low repetition frequency and the current pulses were measured on an oscilloscope. A simple calculation indicated that a pulse width of 0.1μsec at a repetition rate of less than 100 sec^{-1} was sufficient to keep the temperature rise negligibly small. A schematic diagram of the experimental arrangement is shown in Figure 122.

Using this apparatus, mobility measurements were made on both n- and p-type Si/Al_2O_3 samples. A typical (111)-oriented n-type sample had a resistivity of approximately 0.3 ohm-cm and dimensions of 11.1μm x 0.03 cm x 0.25 cm. Typical p-type samples had similar resistivities and dimensions. Figures 123 and 124 are plots of the measured values of current density as a function of field strength for two such samples. High-field effects were not detected for these particular samples because of limitations in the sample geometry.

---

*The high-field measurements were carried out in the Department of Electrical Sciences and Engineering of the University of California at Los Angeles by C. R. Viswanathan and T. Takino.

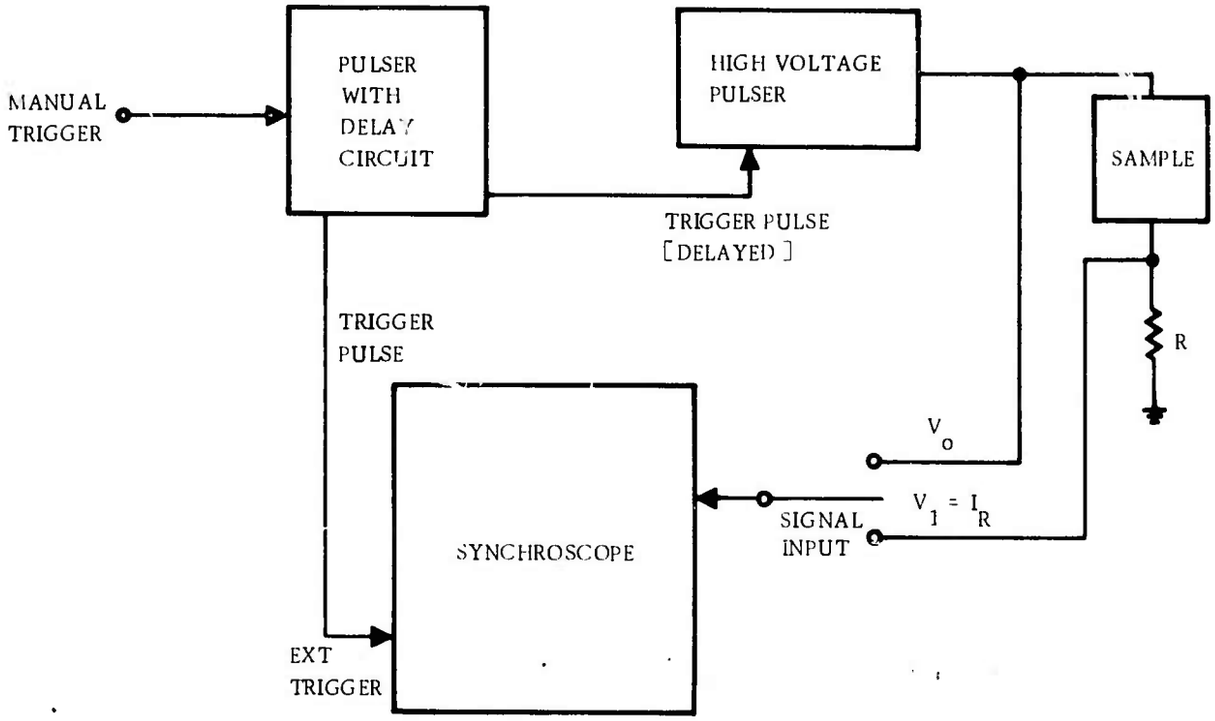

Figure 122. Experimental Arrangement for Film Mobility Measurements at High Fields

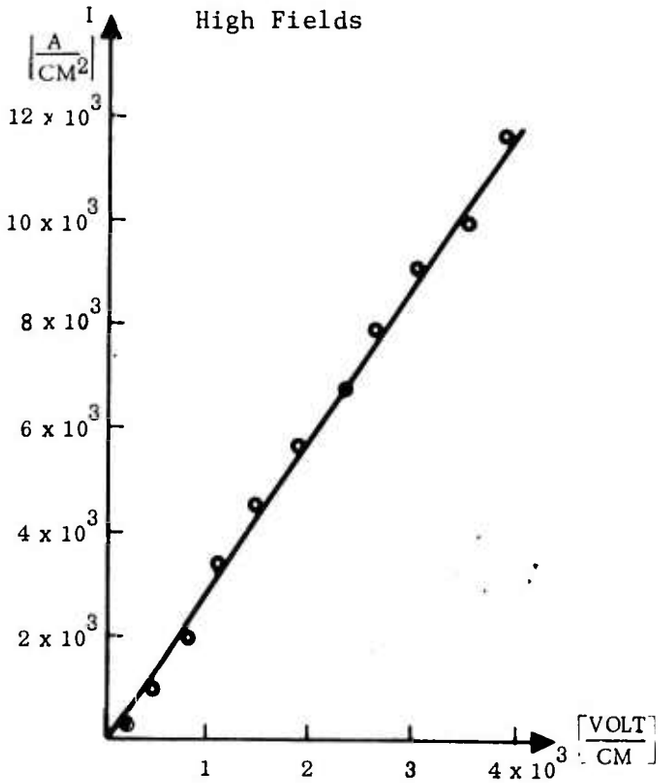

Figure 123. Current Density as Function of Electric Field for N-type Si/Al_2O_3 Film

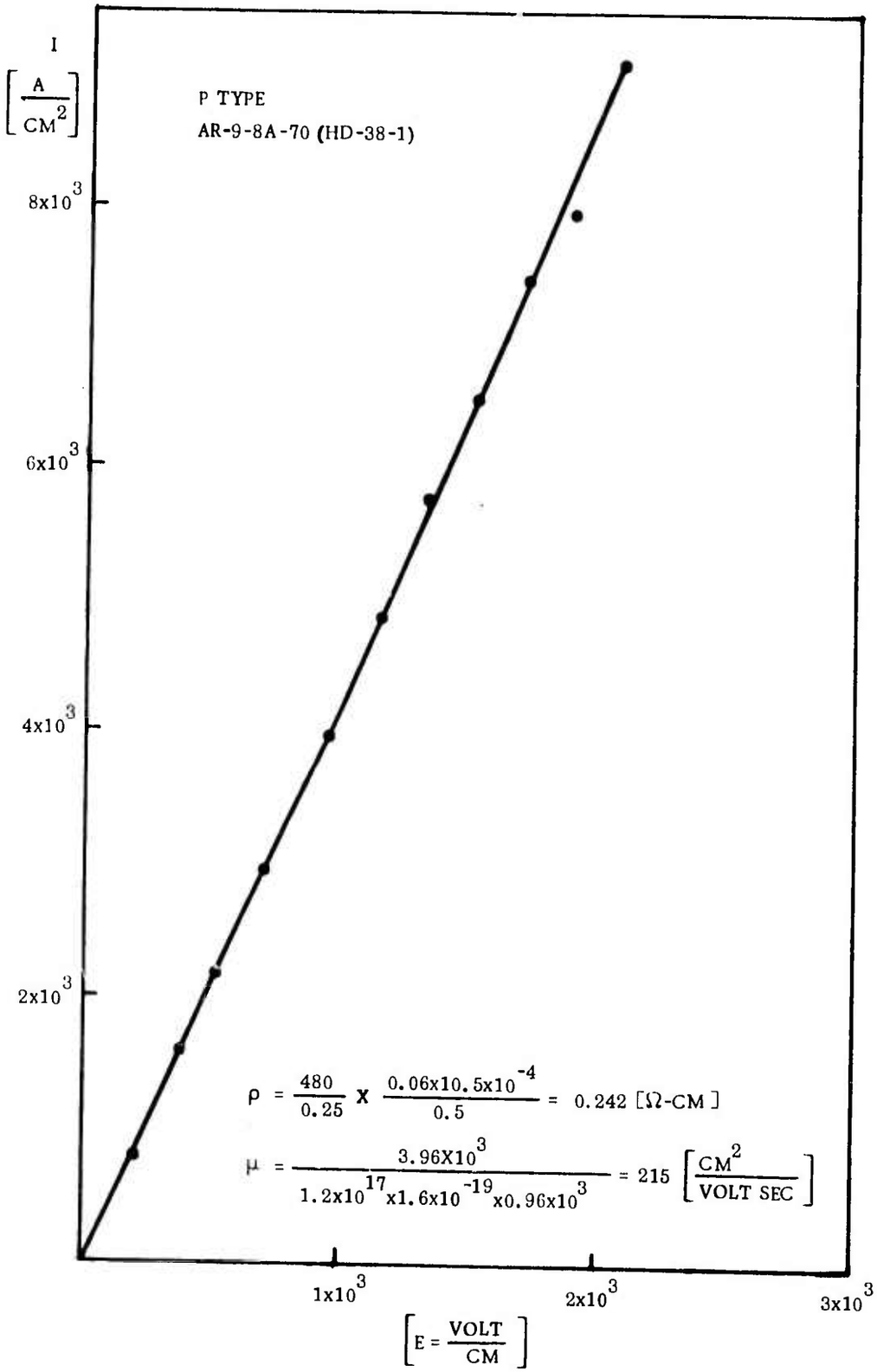

Figure 124. Current Density as Function of Electric Field for P-type Si/Al_2O_3 Film

Thus, the mobilities were constant over the range of fields investigated and were equal to 754 and 215 cm^2/V-sec for the n- and p-type samples, respectively.

Considerable difficulty was experienced initially in fabricating the device structure required for these measurements. It was found that the metal pads initially deposited on the Si and GaAs films did not provide good ohmic contacts. Considerable experimentation was directed toward obtaining satisfactory ohmic contacts for high-field measurements on these films.

The following procedure was successful in obtaining ohmic contacts on n-type Si samples. A 5000Å-thick SiO_2 layer was deposited on the n-type Si wafer using the "silox" process. Windows were then cut in the oxide, using a photolithographic technique, in the region where the ohmic contact was required. Phosphorus was next deposited in the window at 950C for 5 to 10 min. Al was evaporated over the entire sample, and then the excess was removed by photolithography. The Al remaining on the contact window was sintered at 530C for 3 min, resulting in ohmic contact to the n-type Si. For GaAs samples it was found that good ohmic contacts were obtained by evaporating an alloy of Ag, In and Ge (90:5:5) onto the GaAs film and heating the sample for two min at 700C in a He gas ambient.

Results of measurements on a GaAs film sample and three different regions of a Si film sample, both on Al_2O_3 substrates, are shown in Figures 125 and 126, respectively. Both films were n-type. The data for GaAs show a deviation from linear behavior for fields beyond about 1.7kV/cm and a "peak" at about 3kV/cm, and with a subsequent current increase at higher fields due to specimen heating. The data for Si were similar and showed deviations from linearity for high fields. However, there was no evidence of heating effects as there was no current increase at higher fields.

Supplementary measurements on these samples as a function of temperature were then carried out. For that purpose two sample chambers - one for low-temperature

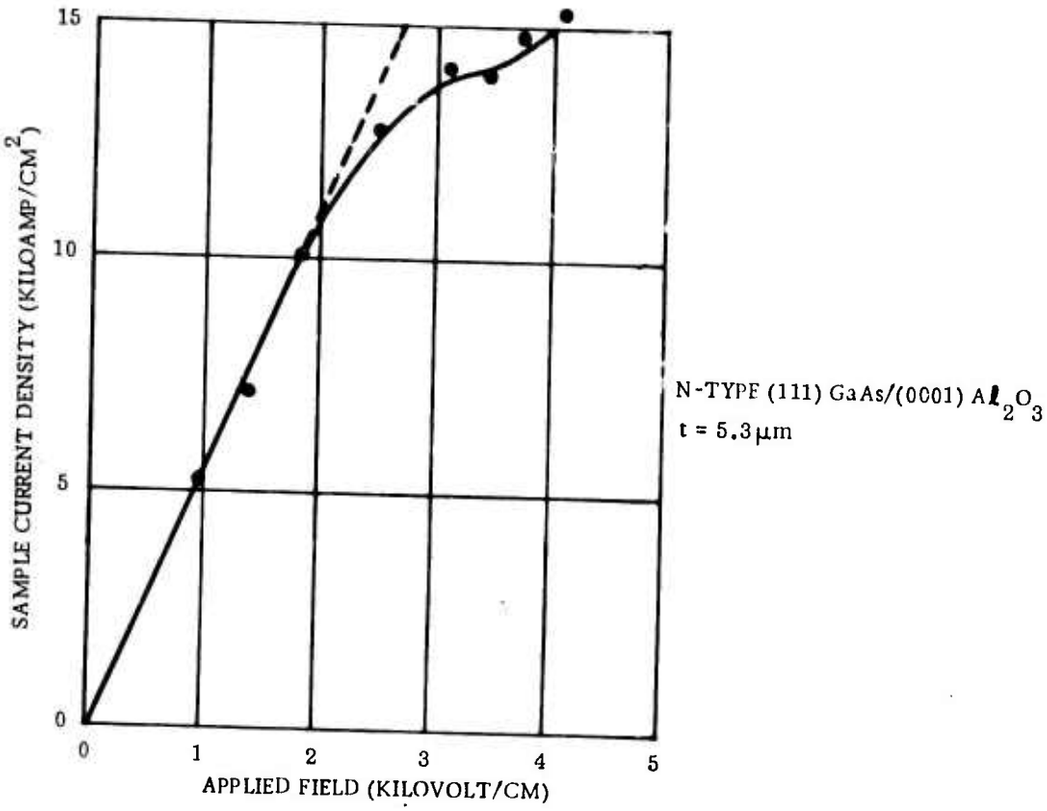

Figure 125. High-field i-$\mathcal{E}$ Characteristic of N-type (111)GaAs/(0001)Al_2O_3

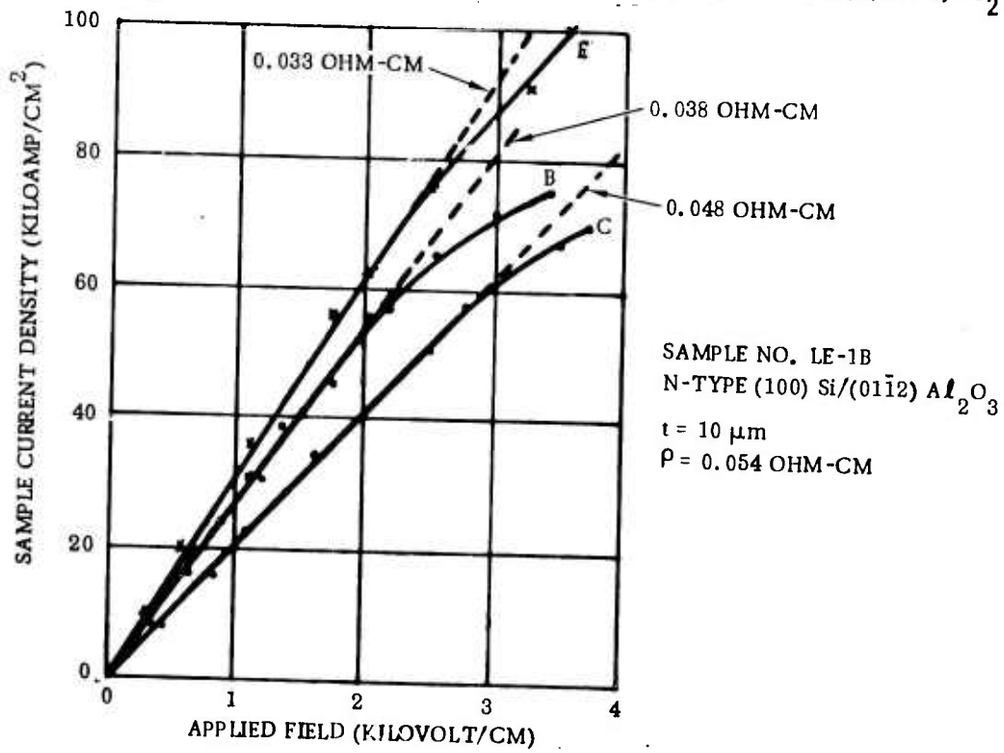

Figure 126. High-field i-$\mathcal{E}$ Characteristic of N-type (100)Si/(01$\bar{1}$2)Al_2O_3

measurements and one for use at elevated temperatures - were fabricated so that measurements could be made throughout a wide range of temperatures. Figure 127 shows the i-$\mathcal{E}$ data for the n-type Si sample of Figure 126, taken at three different temperatures. The functional dependence is seen to remain linear for fields up to nearly 5kV/cm at 77K, with evidence of increased resistivity in the vicinity of room temperature, as expected for Si.

These results for Si at various temperatures indicated that most of the technical problems of making the high-field measurements had been solved, but this occurred near the end of the contract program and the effort required on other aspects of the contract work did not permit further experimentation.

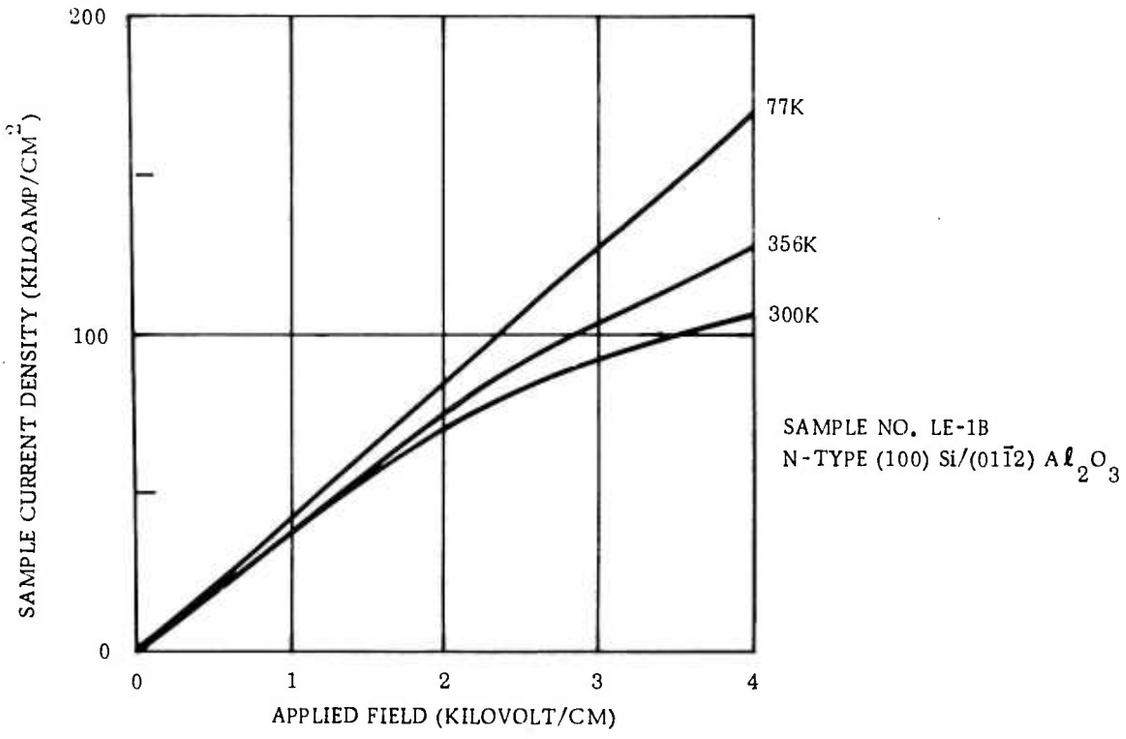

Figure 127. High-field i-$\mathcal{E}$ Characteristic of Si/Al_2O_3 Sample of Figure 126 at Several Temperatures

SECTION 10

ANISOTROPY IN ELECTRICAL PROPERTIES OF Si FILMS ON Al_2O_3

The Hall mobility in epitaxial semiconductor films is usually considered to be a good criterion of film quality. It has been used extensively in guiding the optimization of film growth processes. It is therefore important that the properties of a film be homogeneous and uniform over the plane of the film if a realistic and significant electrical parameter is to be deduced from a particular measurement. It has usually been tacitly assumed that the carrier mobility is isotropic in the plane of the film and does not depend upon the direction in which the measurement is made.

Essentially all Si/Al_2O_3 films evaluated early in this contract program (and before) were found to exhibit some scatter and apparent nonuniformity in measured Hall mobilities as a function of position in the film. Consequently, considerable effort has been devoted in this contract to the question of carrier mobility variation as a function of position in Si films on Al_2O_3 in order to identify the possible causes of the variations.

During the last half of the second contract year, the possibility of a directional dependence in the mobility was explored experimentally. A double Hall-effect bridge pattern, consisting of two ordinary "square" Hall-effect bridges of the type used early in the program and previously described (Ref 1) but oriented with the arms of one bridge rotated 45 deg with respect to the other, was fabricated on a number of $(001)Si/(01\bar{1}2)Al_2O_3$ films. Measurements of the mobility, although exhibiting appreciable scatter in the data, appeared to indicate a systematic variation of mobility with angular orientation in the plane of the film.

An extensive study of the anisotropy of the electrical properties of Si films on Al_2O_3 involving both theoretical and experimental investigations was then initiated and became a major effort of this contract. The results obtained from these investigations are believed to be significant to the entire technology of heteroepitaxial semiconductor devices.

Three different Si film orientations on Al_2O_3 have been explored in detail and include (221)Si/(11$\bar{2}$2)Al_2O_3, (001)Si/(01$\bar{1}$2)Al_2O_3, (111)Si/(11$\bar{2}$0)Al_2O_3 and (111)Si/(10$\bar{1}$4)Al_2O_3. These four film-substrate systems represent the four major modes of Si/Al_2O_3 epitaxy and include the film and substrate orientations of most interest for device applications.

The (221)Si, (001)Si, and (111)Si film orientations are rather different in terms of the origin of the anisotropy. For (001)Si and (111)Si the anisotropy is due solely to the anisotropic thermal-expansion strains induced by the Al_2O_3 substrate, and is therefore extrinsic to the Si film. For (221)Si the anisotropy in mobility derives from the anisotropies in Si piezoresistance coefficients, in Si elastic constants, and in the Al_2O_3 expansion coefficients. The (221)Si anisotropy in origin is thus partially intrinsic and partially extrinsic to the Si film. In general, no anisotropy would be expected for (001)Si and (111)Si on cubic-crystal substrates such as $MgAl_2O_4$, in contrast to the (221)Si case where anisotropic effects would be expected on $MgAl_2O_4$ substrates.

The theoretical studies, discussed at length in Section 2, have been in terms of a thermal-stress and piezoresistance-effect model. Two piezoresistance effects lead to physical quantities which can be measured for the Si/Al_2O_3 films; these effects have been emphasized experimentally. The longitudinal piezoresistance effect deals with the change in resistivity in the direction of current flow. This change in resistivity is exhibited as a change in mobility. The theory indicates that, in general, the mobility variation with current flow angle Θ in the plane of the Si film will be of the form

$$\mu/\mu_o = [a + b \cos 2\Theta]^{-1}, \tag{76}$$

where μ_o is the carrier mobility in the Si film in the absence of stress and Θ is angular direction measured with respect to a suitably determined reference for the particular crystallographic orientation in question. The theo-

retical equation gives two directions in the plane yielding a maximum mobility μ_{max} and two yielding a minimum mobility μ_{min}. Each maximum is separated by 90 deg from the adjacent minima.

The zero-stress mobility μ_o cannot be directly measured experimentally. Comparison of theory and experiment therefore has been based upon equations of the form

$$\mu = [a'+b'\cos 2\theta]^{-1} , \tag{77}$$

where μ_o is incorporated in a' and b'. The experimental mobility data has been computer-fitted to this equation using the least squares technique, and the parameters a' and b' have been determined.

The angular orientations in the Si film plane yielding the maximum and minimum mobilities are independent of μ_o, and direct comparisons between theory and experiment can be made. Similarly, the anisotropy factor A, defined as

$$A = 100(\mu_{max}-\mu_{min})/\mu_A, \tag{78}$$

where μ_A is an average mobility $(\mu_{max}+\mu_{min})/2$ and is independent of μ_o and equal to $200b/a$ and $200b'/a'$. Direct comparisons between theoretical and experimental anisotropies A can therefore be made.

The transverse piezoresistance effect has also been investigated experimentally and theoretically. This effect produces a transverse electric field E_T which is in the plane of the Si film but is perpendicular to the current direction. This field is given theoretically by

$$E_T/j\rho_o = -b\sin 2\theta, \tag{79}$$

where j is the current density and ρ_o the zero-stress resistivity. This

transverse field E_T is measured across the same bridge terminals used to measure the Hall voltage, but it is independent of the magnetic field and should not be confused in its origin with the Hall transverse electric field or voltage. The angular orientations yielding the maximum and minimum experimental values of the transverse field E_T can be compared directly with theory. The overall magnitude of the effect, however, depends upon the zero-stress resistivity ρ_o, which must be estimated or determined by other means.

The results of experimental studies on (221)Si/$(11\bar{2}2)Al_2O_3$ and (001)Si/$(01\bar{1}2)Al_2O_3$ films are described in recent publications (Refs 35, 36). Since both of these papers are included in this report as Appendices, only brief accounts of the work will be given here. Some experimental studies on (221)Si/$(11\bar{2}2)Al_2O_3$ not described in Ref 36 will be discussed, and extensive work done with (111)Si/Al_2O_3 will also be described.

1. ANISOTROPY IN (221)Si/$(11\bar{2}2)Al_2O_3$

The data reported below are from measurements taken on (221)Si grown on an Al_2O_3 orientation ~3 deg from the $(11\bar{2}2)$ plane. Previous orientation studies have shown that (221)Si//$(11\bar{2}2)Al_2O_3$ and the $[\bar{1}10]$Si//$[1\bar{1}00]Al_2O_3$ in the plane of the film. For these experiments, As-doped films having thicknesses from 1.9 to 2.5μm and net donor concentrations of $2\text{-}7\times10^{16}$ cm^{-3} were grown at 1100C at a growth rate of approximately 2μm/min. After growth, the samples were annealed in O_2 for 30 min followed by a N_2 anneal for 2 hr in order to stabilize film properties and electrically neutralize any Al impurities present in the film.

Electrical measurements were carried out on a new specially designed double Hall-bridge pattern etched in the Si film using photolithographic techniques. This bridge pattern is shown in Figure 128. The legs in each bridge are spaced 72 deg apart and the two bridges are rotated with respect to each other by 18 deg. The bridge thus allows an independent measurement of Hall mobility every 18 deg in the plane of the film.

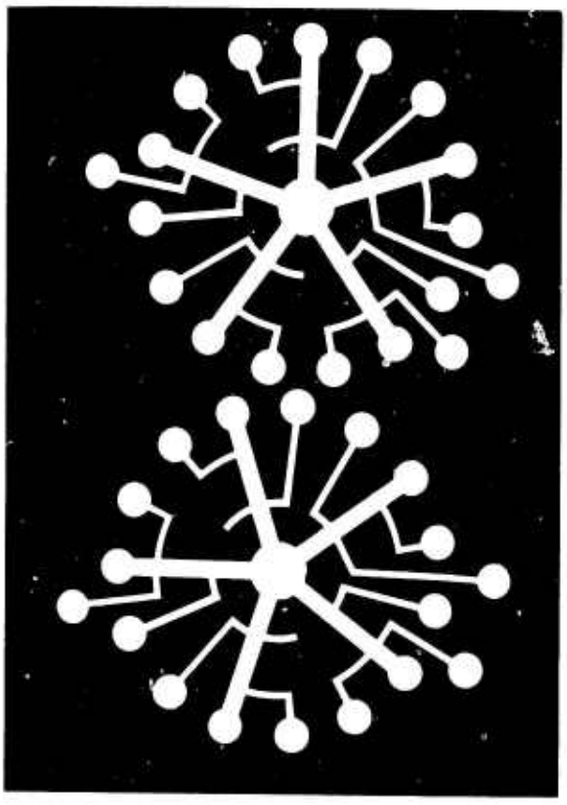

Figure 128. Double Hall-bridge Pattern for Measuring Anisotropic Electrical Parameters

Plots of Hall mobility μ vs angle Θ measured from the $[1\bar{1}0]$Si direction are shown for representative samples in Figure 129. For each sample the data were computer-fitted to the Equation (77) and the parameters A, μ_{max} and μ_{min} were determined. Table 35 shows the values of these parameters for a number of samples. The observed anisotropy is seen to be appreciable, as is evidenced by an average room-temperature anisotropy factor A of approximately 39 percent.

The theory for $(221)Si/(11\bar{2}2)Al_2O_3$ yields the equation $(\mu/\mu_o)^{-1} = 1.06 - 0.212\cos 2\Theta$, where μ_o is the zero-stress mobility and the angle θ is measured from the $[1\bar{1}0]$Si direction in the plane of the film. The theoretical anisotropy A is 41 percent, in good agreement with the experimental values given in Table 35. The maximum mobility direction predicted by the theory, along the $[1\bar{1}0]$Si direction, is also in agreement with the experiment.

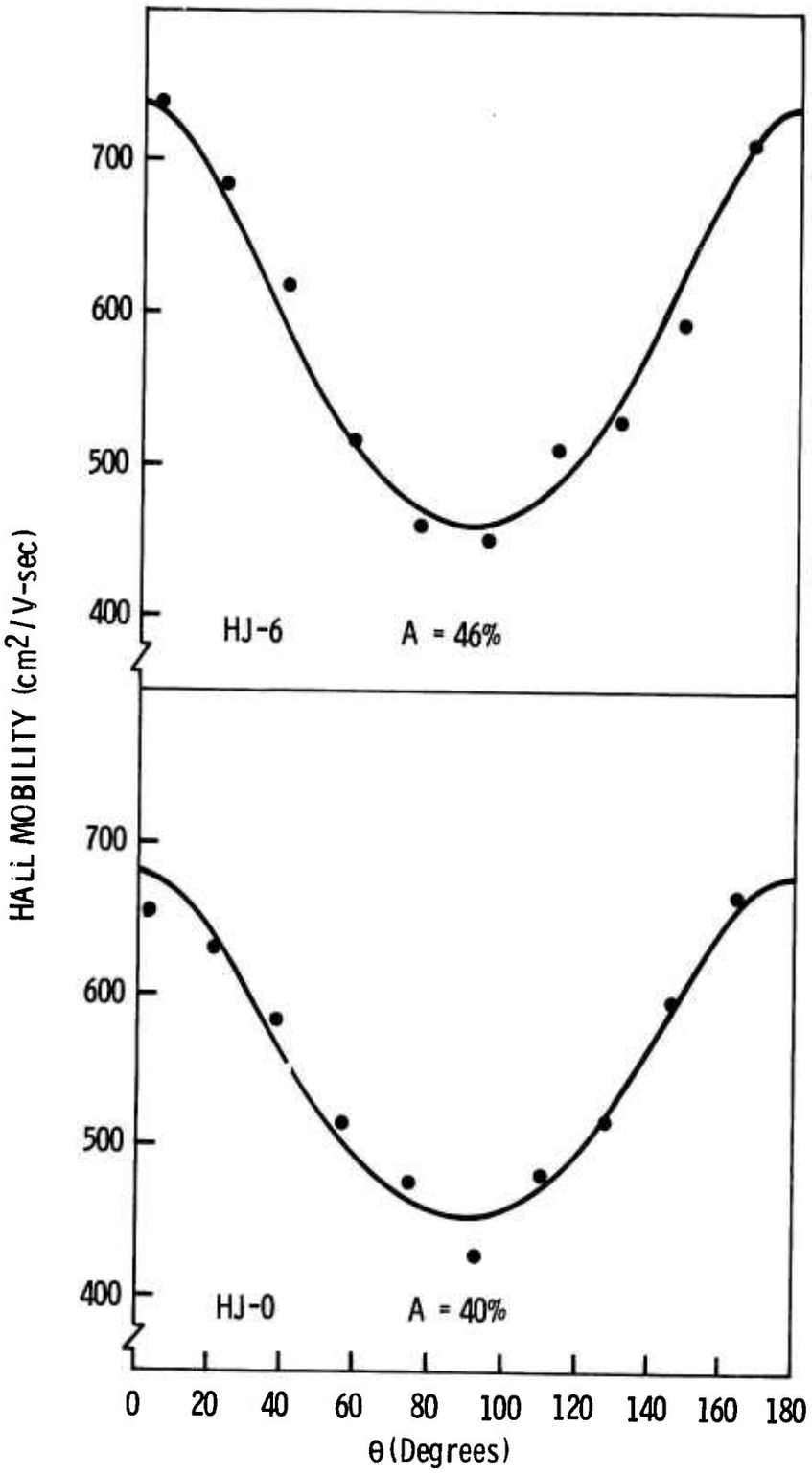

Figure 129. Variation in Hall Mobility as Function of Direction in (221)Si/(11$\bar{2}$2)Al_2O_3

An interesting feature of the piezoresistance in this plane is that the mobility is predicted to be larger than the unstressed mobility for 0 deg $\leq \Theta \leq$ 37 deg (if only the first quadrant is considered). At 37 deg, theory predicts that the mobility reduction due to thermal stress is zero, so that μ(37 deg) = μ_o. At this angle the experimental value of mobility can thus be used to estimate the mobility degradation due to causes other than thermally induced stress.

Table 35. Anisotropy Parameters of Several (221)Si/(11$\bar{2}$2)Al_2O_3 Films

Sample No.	Temp (K)	A (%)	μ_{max} (cm^2/V-sec)	μ_{min} (cm^2/V-sec)	μ_o (cm^2/V-sec)	RMS Error (%)
HJ-1	300	30.4	671	494	597	2.7
HJ-58	300	32.2	700	506	615	3.3
HJ-58	77	84.9	1900	769	1250	3.8
HJ-16	300	35.5	690	483	600	2.3
HJ-15	300	39.5	686	46[illegible]	585	2.8
HJ-0	300	40.1	679	452	575	2.6
HJ-6	300	46.3	737	460	607	3.4
HJ-25	300	48.6	708	431	575	3.5
HJ-25	77	108.6	1680	497	900	6.0

Consequently, if it is assumed that the film mobility at 37 deg (i.e., $\mu_o \simeq 600$ cm^2/V-sec for the films used in this study) is given by $(1/\mu_o) = (1/\mu_B) + (1/\mu_D)$, where μ_B is the bulk mobility ($\simeq 1000$ cm^2/V-sec), then $\mu_D \simeq 1500$ cm^2/V-sec represents the limiting value of mobility due to all mechanisms other than thermally induced stress. However, μ_D probably is related almost entirely to defect structure in the film. The fact that the value of the mobility μ_o is much smaller than the bulk mobility strongly suggests that thermally induced stress is not the dominant mechanism in lowering the mobility in these films.

Measurements pertaining to the transverse piezoresistance effect were also made; the transverse field E_T was measured on the above samples. The theory predicts that the transverse field E_T for the (221)Si films is given by $E_T/j\rho_o = 0.212\sin 2\theta$, where j is the current density and ρ_o the zero-stress resistivity.

The quantity $E_T/j\rho_o$ is shown plotted for two samples in Figure 130. The quantity ρ_o is found from $\mu_o = R_H/\rho_o$, where R_H is the Hall constant and μ_o, as before, is the mobility at θ=37 deg. A least-squares fit of the data to the predicted equation yields an average value for the coefficient of sin θ of 0.2, in good agreement with theory.

The temperature dependence of the anisotropy was not examined in detail, although measurements on selected samples at 77K showed a much larger anisotropy, as evidenced by the data in Table 35. Such an increase is consistent with what might be expected for the variation of piezoresistance with temperature. Although detailed measurements of all of the piezoresistance coefficients are not available in the literature, π_{11} appears to be the order of three times greater at 77K than at 300K. If it is assumed that all of the coefficients vary by the same amount, it can be shown that the anisotropy factor A would be expected to be the order of 2.7 times greater at 77K. The data on two samples show an average increase of a factor of 2.4, consistent with that predicted.

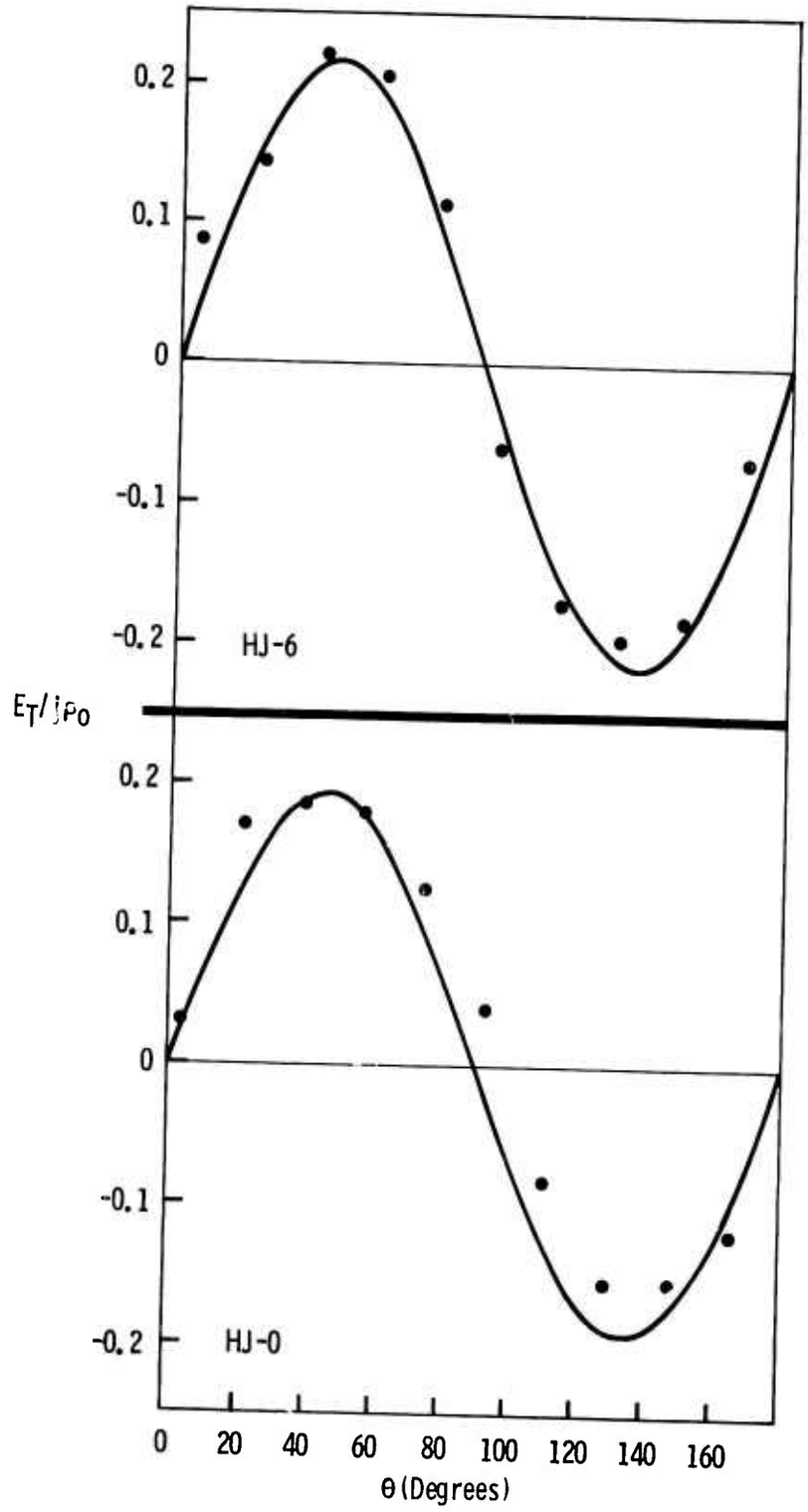

Figure 130. Transverse Electric Field Associated with Piezoresistance Effect and Thermally Induced Stress in (221)Si/(11$\bar{2}$2)Al_2O_3

The enhanced mobility predicted for some current directions suggests that the (221) plane of Si/Al_2O_3 may yield superior electron mobilities. In comparison with (100)Si and (111)Si grown at this laboratory, the (221) plane has indeed yielded higher mobilities. It would be expected that some types of devices would show improved performance if oriented in such a way as to take advantage of this improved mobility.

Since the mobility is unaffected by thermal stress for one current direction in the (221) plane, insight may be gained into the scattering mechanisms in Si/Al_2O_3 by studies of the mobility versus temperature. For example, the comparison of such data at various angles may make it possible to separate the contributions of various scattering mechanisms to the reduction in the mobility.

Attempts were made to examine the variation of the anisotropy factor A in $(221)Si/(11\bar{2}2)Al_2O_3$ films as a function of film thickness. Such data, if interpreted solely in terms of the stress-piezoresistance model, would provide information on the variation of stress in heteroepitaxial films with film thickness. The results of this brief study are shown in Figure 131, where the measured anisotropy factor A and the transverse-effect coefficient D in $E_T/j\rho_o = D\sin 2\theta$ are plotted versus film thickness. Although there is considerable scatter in the data, there does appear to be a trend for the anisotropy effects to increase for thinner films.

However, this trend may not be a direct thickness-dependent effect but one related to the quality of the films and thus only indirectly to the film thickness. For example, the measured anisotropy of the (221)Si films in Table 35 plotted versus average mobility suggests that the anisotropy is a function of average mobility - specifically, that the anisotropy depends inversely upon mobility. Such a dependence of anisotropy upon mobility would also lead to the results shown in Figure 131, since mobility decreases with decreasing film thickness. The general question of the relation between

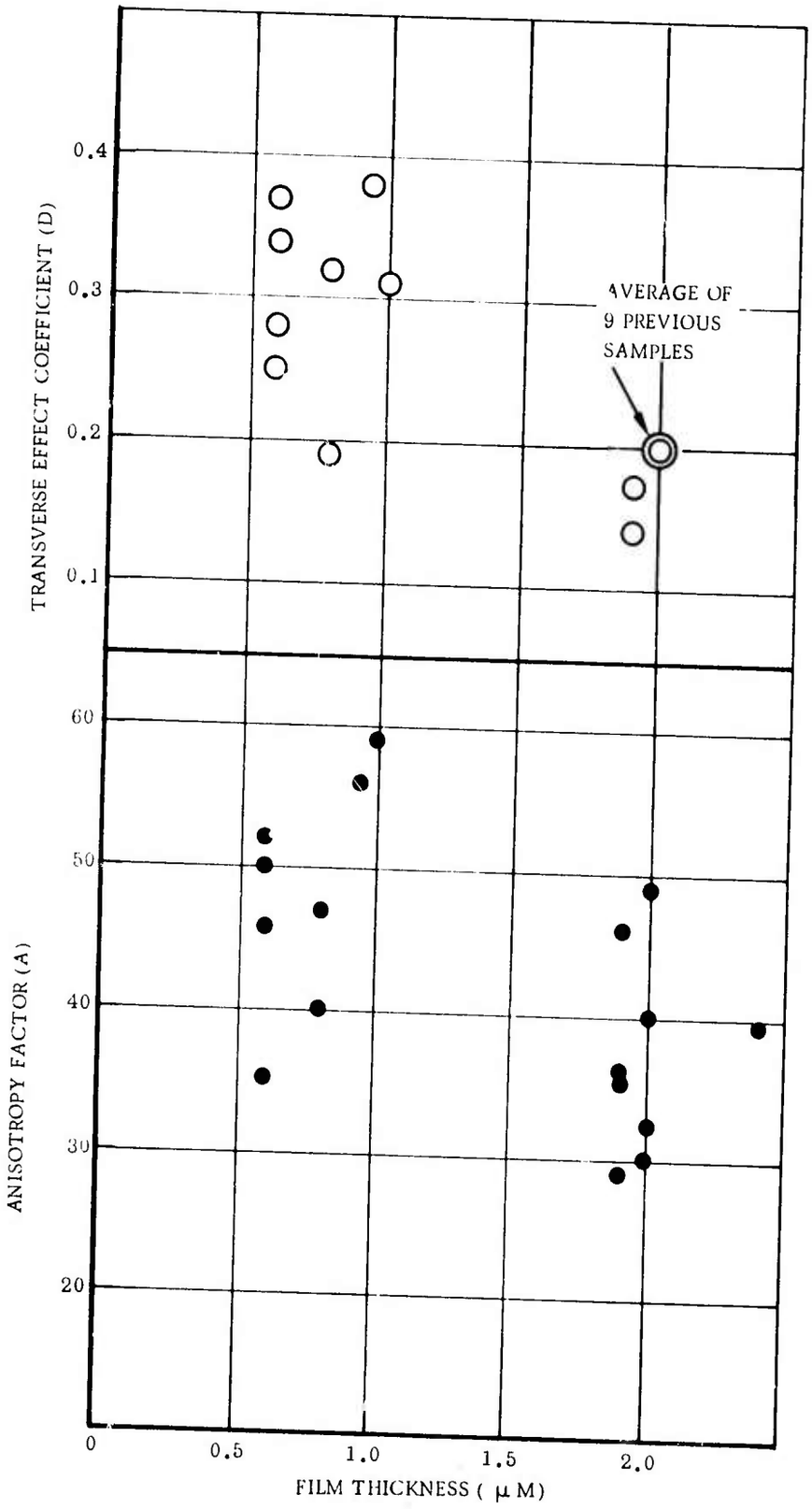

Figure 131. Anisotropy and Transverse-effect Coefficient for Various Film Thicknesses for (221)Si/(11$\bar{2}$2)Al_2O_3 Samples

anisotropy and mobility is discussed later in more detail in connection with (111)Si films which appear to display the same characteristic as indicated here.

2. ANISOTROPY IN (001)Si/(01$\bar{1}$2)Al_2O_3

The films used for the study of the (001)Si/(0112)Al_2O_3 system were grown in two different reactor systems. One of these was the vertical system normally used in this program, and the other was a horizontal system of a type used for commercial preparation of epitaxial Si. As in the (221)Si study described above, the films were formed by thermal decomposition of SiH_4, with H_2 used as a carrier gas. Intentional doping to concentrations from 1 to $6x10^{16}cm^{-3}$ was achieved with the use of AsH_3 as the dopant gas. Growth temperatures ranged from 995C in the horizontal system to 1075C in the vertical system, and film thicknesses varied from 1.5 to 1.8μm.

Detailed electrical data were taken on eight samples of (001)Si/(01$\bar{1}$2)Al_2O_3. For every sample, the orientation of each leg of the Hall pattern was determined with respect to the ⟨100⟩ Si direction which is parallel to the [2$\bar{1}\bar{1}$0]Al_2O_3 direction in the plane of the substrate. The mobility in each leg could then be plotted vs the angle θ between the current direction and the ⟨100⟩Si axis. Typical mobility data are shown plotted in Figure 132 for two samples. The mobility can be seen to vary with angle and appears to approach a maximum at 0 deg.

As in the case of (221)Si, the experimental mobility data has been fitted to an equation of the form $\mu = [a'+b'\cos 2\theta]^{-1}$. The calculated parameters A, μ_{max} and μ_{min} are tabulated in Table 36. It can be seen that the anisotropy varies between approximately 8 and 12%; the average value is 9.5%. The RMS error (the actual RMS error in the mobility divided by the average mobility) between the experimental points and the theoretical fitted curve for each sample is also shown.

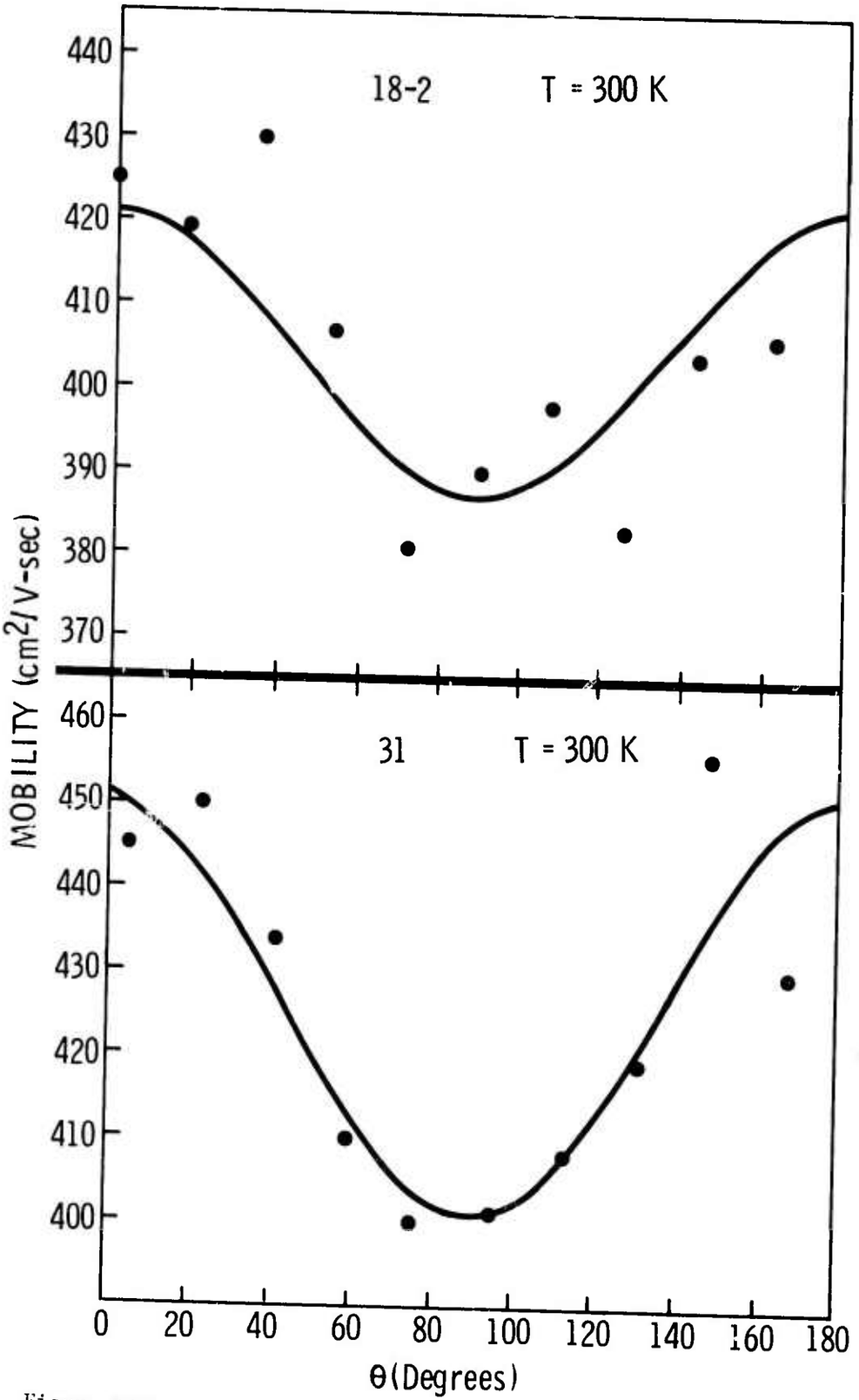

Figure 132. Variation of Hall Mobility with Direction in (001)Si/(01$\bar{1}$2)Al_2O_3

Table 36. Anisotropy Data for (001)Si/(01$\bar{1}$2)Al_2O_3

Sample No.	μ_{max} (cm^2/V-sec)	μ_{min} (cm^2/V-sec)	μ_A (cm^2/V-sec)	A (%)	RMS Error (%)	μ_o (cm^2/V-sec)
			Room Temperature Data			
102	446	408	427	8.9	1.6	615
18-1	432	397	415	8.6	1.4	598
15	472	425	449	10.5	2.5	648
3412-3	513	472	493	8.2	1.9	711
3411-1	516	478	497	7.6	2.1	717
18-2	422	387	405	8.6	2.5	584
31	451	401	426	11.6	2.2	614
13	443	394	419	11.7	2.9	604
(average)	(462)	(420)	(441)	(9.5)		(636)
			77K Data			
18-1	1014	797	906	24	5.7	1305
31	1063	832	948	24	7.0	1367

Since the data display the type of scatter normally encountered in Si/Al_2O_3 films, and since the anisotropies are small for this Si orientation, the RMS error comparison with the anisotropy has been used to judge the statistical significance of the fit. Because of the definition of the anisotropy A, the comparison is made between A/2 and the RMS error. In all cases the relative magnitude of the two percentages suggests that the fit is statistically significant.

The theoretical equation, using the values of thermal expansion coefficient believed most accurate, yields $\mu/\mu_o = [1.437-0.0667\cos 2\Theta]^{-1}$ for Θ measured from the [100]Si direction. The theoretical anisotropy is therefore 9.3%, in good agreement with experiment, and the mobility maxima and minima are correctly located.

The zero-stress mobility μ_o has been calculated from the theoretical equation in conjunction with the computer-fitted curves, and these values are also given in Table 36. Comparison with Table 35 shows that the values of μ_o are very similar for both the (001) and the (221)Si planes.

Measurements were made at 77K on several selected samples, and representative data for one sample are shown in Figure 133; the parameters deduced from the curve fitting procedure are also shown in Table 36. The anisotropy is found to increase in going from room temperature to 77K by roughly a factor of three for those samples measured. This is consistent with the variation of the piezoresistance coefficients in Si with temperature.

The theory also predicts a transverse electric field effect in the (001)Si plane, given by $E_T/j\rho_o = 0.06673 \sin 2\theta$. Attempts were made to measure this voltage; however, the small voltage involved made the determination extremely difficult. Representative data on one sample are shown in Figure 134. A least-squares fit to the data gave a coefficient of ~0.08, which is somewhat larger than predicted; however, the data fit was not good. The value of μ_o used in this expression was found from the value of μ_o determined from the longitudinal mobility measurements described above. This transverse voltage also increases at 77K and is also shown in Figure 134. The magnitude of the increase is a factor of between 2 and 3, similar to that for the longitudinal effect. Note that the fit to theory is much better at 77K, due to the larger signal.

Comparison of theory and experiment for (001) and (221)Si films on Al_2O_3 thus conclusively indicates that the amount of anisotropy and the location of mobility maxima and minima have been substantially accounted for in terms of the thermal stress model applied to these two orientations. The (111)Si case is considered in the next section.

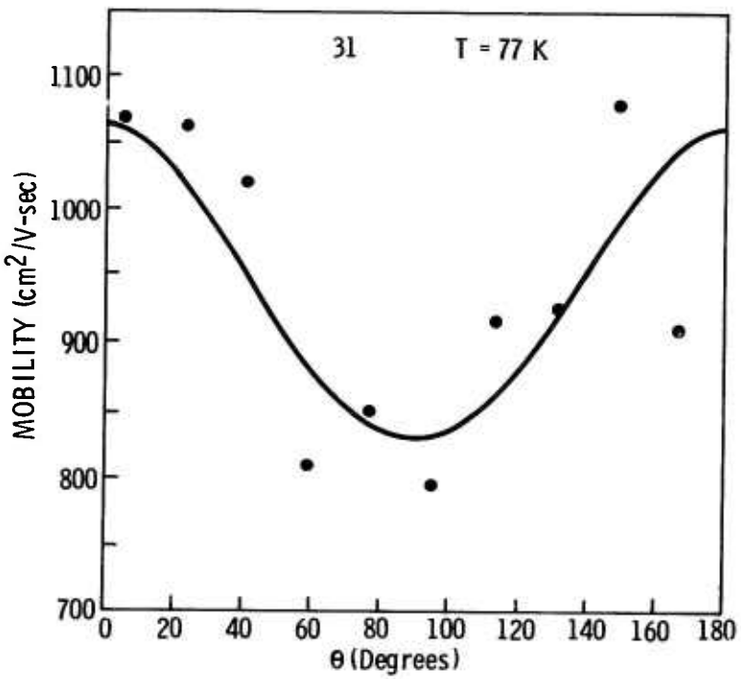

Figure 133. Variation in Hall Mobility with Direction at 77K in (001)Si/(01$\bar{1}$2)Al_2O_3

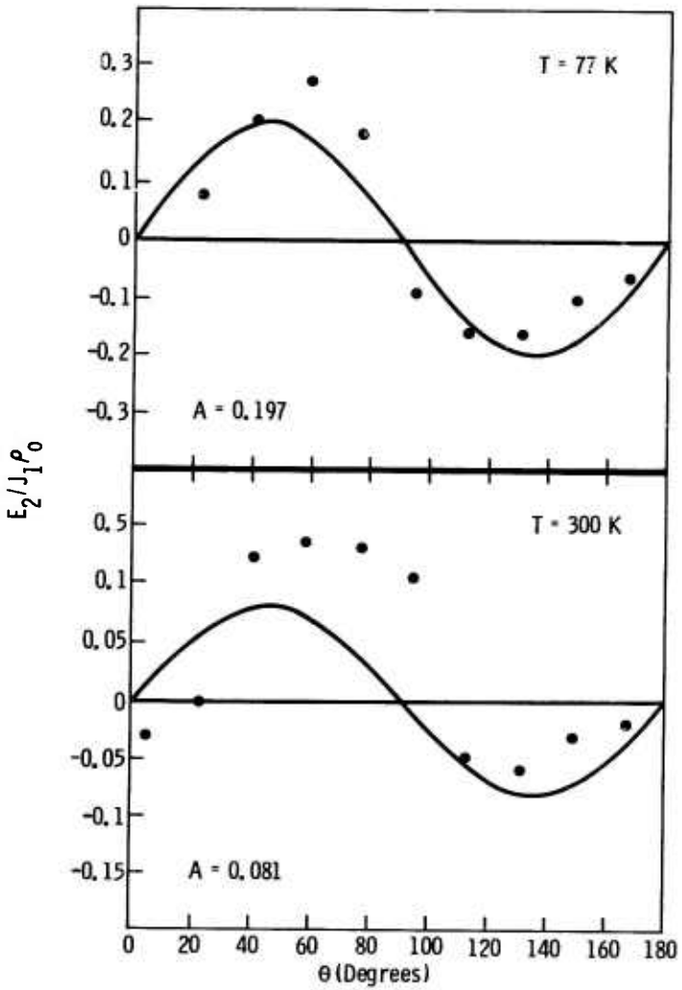

Figure 134. Transverse Electric Field Associated with Thermally Induced Stress and Piezoresistance Effect in (001)Si/(01$\bar{1}$2)Al_2O_3

3. ANISOTROPY IN (111)Si ON Al_2O_3

Extensive experimental studies of anisotropy in the electrical properties of (111)Si/Al_2O_3 films were carried out using both ~$(11\bar{2}0)$- and $(10\bar{1}4)$-oriented Al_2O_3 substrates. For both (111)Si/$(11\bar{2}0)Al_2O_3$ and (111)Si/$(10\bar{1}4)$ Al_2O_3 the experimental anisotropies were substantially larger than predicted on the basis of thermal stresses, suggesting that other phenomena play an important role in determining the anisotropy for (111)Si. The measurements indicated that the anisotropy in (111)Si is a sensitive function of growth conditions and may provide a means for film characterization that is more closely related to nucleation and growth processes than ordinary measurements of mobility employed in the past.

a. (111)Si/$(11\bar{2}0)Al_2O_3$

The properties of ~(111)Si/$(11\bar{2}0)Al_2O_3$ were explored in detail during the final year of the contract. High quality nominally (111)-oriented Si epitaxial films are typically obtained on this Al_2O_3 plane; the specific orientation most used (~6 deg from the $(11\bar{2}0)$ plane)was found to produce a Si film whose orientation was 4 deg off the (111)Si plane.

(1) Experimental Results

Data were obtained on the variation of electrical properties with angular orientation in the plane of the film for seven ~(111)Si/$(11\bar{2}0)Al_2O_3$ films and are shown in Table 37.

The coordinate systems relating the measurement directions to the crystallography of the Si and Al_2O_3 crystals were the following. Cartesian x and y axes in the film and substrate surface planes were defined consistent with the parallel relations for this mode of epitaxy. In the Si, the x and y axes were the $[1\bar{1}0]$ and $[11\bar{2}]$ directions, respectively, and in the Al_2O_3 they were the $[2\bar{2}01]$ and $[2,\bar{2},0,-1.61]$ directions, respectively. Angular rotations from the x axes toward the y axes were taken as positive. The resulting angular

Table 37. Room Temperature Anisotropy Parameters for N-type (111)Si/(11$\bar{2}$0)Al_2O_3

Sample No.	Bridge No.	N_A (cm^{-3})	ΔN (%)	δN (%)	μ_{max}	μ_{min}	μ_A	A (%)	ER1 (%)	ER2 (%)	$\Phi_{\mu_{max}}$ [2$\bar{2}$01]	$\Phi_{\mu_{max}}$ [1$\bar{1}$00]	D	Φ_D [1$\bar{1}$00]	Comments
LM-71	1 & 2	4.14×10^{16}	9.41	2.19	568	410	489	32.5	2.1	12.3	-10.8	-49.1	0.158	-49	Horiz. Reactor
	1	4.24×10^{16}	2.36	1.02	565	405	485	33.1	2.5	12.6	-10.6	-48.9			
	2	4.05×10^{16}	4.93	1.66	572	415	493	31.9	1.2	11.9	-11.1	-49.3			
LM-67	1 & 2	1.35×10^{16}	23.0	7.10	621	536	578	14.6	3.3	6.3	-16.5	-54.8	0.153	-53	Vertical Reactor
	1	1.40×10^{16}	15.7	4.75	623	523	573	17.4	3.3	7.2	-12.8	-51.0			
	2	1.30×10^{16}	23.1	7.47	620	549	584	12.2	2.8	5.2	-22.0	-60.3			
LM-83	1 & 2	4.71×10^{16}	22.9	5.32	576	538	557	6.9	2.5	3.5	-20.7	-58.9	0.091	-55	Vertical Reactor
	1	4.78×10^{16}	20.3	5.70	567	532	549	6.3	1.9	3.0	-20.5	-58.7			
	2	4.64×10^{16}	18.7	4.77	587	542	564	8.1	1.9	3.4	-13.7	-52.0			
LM-91	1 & 2	4.96×10^{16}	14.9	3.25	620	555	587	11.0	2.5	4.7	-35.4	-73.6	0.046	-82	Vertical Reactor
	1	5.03×10^{16}	14.7	3.29	628	560	594	11.5	0.4	4.1	-42.7	-80.4			
	2	4.88×10^{16}	5.7	2.14	614	549	581	11.2	2.9	5.1	-28.6	-66.8			
LM-105	1 & 2	4.46×10^{16}	30.3	6.39	615	524	570	15.8	2.8	6.5	-21.8	-60.0	0.077	-60	Vertical Reactor
	1	4.33×10^{16}	26.5	6.89	615	522	569	16.4	1.7	6.0	-25.6	-63.8			
	2	4.59×10^{16}	16.1	5.58	615	526	571	15.5	3.5	6.9	-17.7	-56.0			
LM-109	1 & 2	3.67×10^{16}	22.3	5.58	583	470	527	21.5	3.9	8.7	-6.7	-45.0	0.13	-49	Vertical Reactor
	1	3.82×10^{16}	17.5	10.20	594	458	526	25.8	3.6	9.7	-7.1	-45.0			
	2	3.52×10^{16}	11.9	4.20	573	482	528	17.3	3.9	7.7	-6.0	-44.3			
LM-110	1 & 2	3.13×10^{16}	29.9	9.95	626	562	594	10.8	2.6	4.8	-10.5	-48.8	0.17	-53	Vertical Reactor
	1	3.38×10^{16}	23.7	6.56	620	567	594	8.8	2.5	4.1	-13.4	-51.7			
	2	2.89×10^{16}	27.3	7.20	633	556	594	12.9	2.4	5.3	-8.5	-46.8			
Averages								16.3			-16.4	-54.7	0.12	-59	

positions of some principal directions in Si are $[1\bar{1}0]$ at 0 deg, $[10\bar{1}]$ at +60 deg, $[11\bar{2}]$ at +90 deg, $[1\bar{2}1]$ at -30 deg, and $[0\bar{1}1]$ at -60 deg. Angular positions of some principal directions in the Al_2O_3 substrate plane are $[2\bar{2}01]$ at 0 deg, $[2\bar{2}00]$ at +38.24 deg, $[2\bar{2}0\bar{1}]$ at +76.48 deg, $[2\bar{2}0\bar{2}]$ at +95.91 deg, $[2\bar{2}02]$ at -19.36 deg, and [0001] at -51.76 deg.

The experimental data on which Table 37 is based were taken from measurements on a double Hall bridge pattern similar to that shown earlier in Figure 128. Additional contacts were added to permit two Hall measurements and hence two carrier concentration and mobility measurements for eight of the ten legs. In this way a more accurate averaging of spatial inhomogeneities was obtained.

The data were analyzed in terms of both bridges taken together (Bridges 1 and 2), as well as in terms of the separate bridges (Bridge 1 or Bridge 2); thus three sets of data are shown in Table 37 for each sample. N_A is the average carrier concentration in cm^{-3} and ΔN is the range in the carrier concentration over the bridge legs in question divided by the average concentration N_A, and is given in percent. δN is the average deviation (as commonly defined) divided by the average carrier concentration N_A. δN and ΔN thus characterize the inhomogeneity in carrier concentration for the sample bridge legs measured.

The remaining parameters in the table were derived from computer least-squares fitting to the measured data for each of the samples. A more complicated procedure than that used for the (001)Si and (221)Si films was employed here. From the theory it is known that the experimental mobility should be of the form $\mu=[a'+b'\cos2(\theta-\phi)]^{-1}$, where ϕ is the angle in the plane where the extremum occurs. This equation is nonlinear in the parameter ϕ and cannot be directly fitted; consequently, the equation was written in the form $\mu=[a'+b''\cos2\theta+ c''\sin2\theta]^{-1}$, which permitted a linear least-squares technique to be employed.

After a', b", and c" were determined the parameters b' and ϕ were found using trigonometric identies. The derived parameters μ_{max}, μ_{min}, and μ_A (the maximum, minimum, and average mobilities, respectively) were then easily determined and are given in units of cm^2/V-sec in the table. Finally, the anisotropy factor $A = 100(\mu_{max}-\mu_{min})/\mu_A$ (in percent) was calculated.

The significance of the computer fit to the data can be assessed by comparison of various error parameters. The parameter denoted as ER1 in the table is the RMS error, in percent, of the fit of the experimental data to the equation $\mu = [a' + b'\cos 2(\Theta-\phi)]^{-1}$. The data were also fitted to a second equation μ = constant. The percent RMS error obtained in fitting the data to a constant is denoted by ER2 in the table. The criteria adopted for statistical significance are 1) the RMS error ER1 should be smaller than half the anisotropy A and 2) the RMS error ER1 resulting from fitting to the cosine equation must be less than the RMS error ER2 resulting from fitting the data to a constant. On this basis, all of the samples in Table 37 yield computer fits which are statistically significant and exhibit a clear-cut anisotropy.

The parameter $\phi_{\mu_{max}}[2\bar{2}01]$ is the angle in the film plane yielding the maximum mobility in the fitted theoretical equation relative to the $[2\bar{2}01]$ direction in Al_2O_3. $\phi_{\mu_{max}}[1\bar{1}00]$ is the same angle but measured relative to the $[1\bar{1}00]$ direction. The sign convention on the angles is that discussed earlier. The remaining two parameters, D and $\phi_D[1\bar{1}00]$, relate to the transverse piezoresistance effect discussed in the sections on (001)Si and (221)Si films. D measures the magnitude of the transverse field and $\phi_D[1\bar{1}00]$ denotes the angle, from the $[1\bar{1}00]$ direction, at which the transverse field E_T is zero.

Sample LM-71 (Table 37) was grown in a horizontal reactor, while all the other samples listed in the table were grown in a vertical reactor. Based on this sample and others to be discussed later the horizontal reactor appears to yield a more homogeneous carrier concentration but a lower mobility film. The scatter in the mobility data as measured by the RMS

error ER1 is somewhat less for the horizontal reactor sample than for the other samples, indicating that the horizontal reactor yields slightly more homogeneous mobilities, also. However, the relative magnitude of ER1 in the two systems varies much less than does the relative magnitude of ΔN or δN in the two systems; this suggests that the anisotropy is relatively independent of the concentration variation per se.

The transverse-effect parameters D and ϕ_D were derived from a computer fit to an equation of the form $E_T/j\rho_o = D\sin 2(\theta - \phi_D)$, where E_T is the transverse field measured across the bridge Hall terminals at zero magnetic field, j is the current density, and ρ_o the zero-stress resistivity. The transverse-field data typically contain much more scatter than the longitudinal-effect (mobility) data, for a number of reasons. The transverse measurements for these $(111)Si/(11\bar{2}0)Al_2O_3$ samples have thus not been emphasized. Qualitatively, the magnitudes and the angles were consistent with the longitudinal effect data, and the locations of the zero-field directions in the Si film plane were generally close to those determined from the mobility measurements.

Comparison between theory and experiment has shown for this case that the experimental average anisotropy A was about a factor of four larger than the theoretical thermal stress anisotropy, and the experimental and theoretical angles $\phi_{\mu_{max}}$ differed substantially. The anisotropy factor A, derived from computer fitting and given in the table, ranged from a low of 6.3% to a high of 33.1%, with an average of 16.3%. The highest anisotropies were found for the horizontal reactor sample LM-71, which also has the lowest mobility in the table.

The data suggest that the anisotropy depends upon and is inversely related to the average mobility. Based on the double-bridge data, the samples were ranked in order of decreasing anisotropy, and for six of the seven samples this ordering produced a ranking that was also in order of increasing average mobility μ_A.

Similar treatment of the (001)Si and (221)Si mobility data also suggests an inverse relation between anisotropy and average carrier mobility, although the evidence is not as clear for (001)Si as for (221)Si and (111)Si. It is concluded that an inverse relation between anisotropy and mobility is probably a general characteristic of all orientations of Si/Al_2O_3 epitaxial films.

Attempts were made to extract more detailed information from the mobility-anisotropy data for the (111)Si samples. The stress-piezoresistance model leads to an equation of the form $\mu/\mu_o=[a+b\cos 2\theta]^{-1}$, where the angle θ is measured with respect to a suitably chosen reference. The anisotropy is then $A=2b/a$, and the mobility parameters μ_{max}, μ_{min} and μ_A are given by $\mu_o/a(1-A/2)$, $\mu_o/a(1+A/2)$ and $\mu_o/a(1-A^2/4)$, respectively. The linear dependence of μ_{max} and μ_{min} on A suggested that these mobilities might be explored in terms of the anisotropy. For definiteness, the μ_{min} mobility was chosen and $1/\mu_{min}$ was examined as a function of A.

It is known that electrical properties of Si/Al_2O_3 films vary with position within a given sample and also vary from sample to sample. The data in the above table, although actually representing 126 different measurements of carrier concentration and Hall mobility, are inadequate to address the electrical property variation in any detail. However, the following procedure was employed to extract the maximum amount of information from the available data. The ten-leg double-bridge pattern (see Figure 128) was divided into three bridges of three legs each. Bridge A was comprised of the three outermost legs of Bridge #1, Bridge B was comprised of three legs from the interior of the double-bridge pattern (two legs from Bridge #1 and one leg from Bridge #2). Bridge C was comprised of the three outermost legs of Bridge #2. The Bridges A, B, and C then constituted a linear progression from one end of the sample to the other.

The experimental mobility data for the twenty-one three-leg bridges were then computer-fitted, and the corresponding anisotropy parameters μ_{max}, μ_{min}, μ_A and A determined. The relation between μ_{min} and A was examined by plotting

$1/\mu_{min}$ versus A. This data indicated a clear tendency for higher anisotropies to be associated with lower minimum mobilities μ_{min}. However, the data exhibited considerable scatter, suggesting a variation in properties from sample to sample, so no attempt was made to derive a $1/\mu_{min}$-versus-A curve representative of all the data.

Attention was then turned to the variation of $1/\mu_{min}$ versus A for the seven individual samples. The three data points for each sample were plotted and connected with a smooth curve. For two of the samples straight lines resulted, but for most of the remaining samples the curves were quasi-linear with the main dependence of A upon $1/\mu_{min}$ approximately described by straight lines.

One aspect of this triple-bridge analysis should be understood. The equation being fitted has three parameters and thus fits the three-leg bridge data exactly. There is thus no least-squares smoothing of the data or any error criterion. For about half of the samples the spread in anisotropies among the three bridges was greater than for the previous two-bridge analysis. This was consistent with a possible variation from one end of the sample to the other, but it may also be a statistical artifact. Because of considerations of this nature, the subsequent discussion is restricted to only qualitative conclusions which the analyses suggest.

The double- and triple-bridge data analyses suggest that 1) on a given sample, $1/\mu_{min}$ is linearly related to the anisotropy measured at different positions on the sample, 2) in comparing properties of different samples, the higher anisotropies are generally associated with lower average and lower minimum mobilities; and 3) there is considerable scatter in the detailed relation of anisotropy and mobility among different samples.

These conclusions can be described on the basis of the general stress-piezoresistance model and suggest interpretations in terms of the zero-stress mobility and the two principal stresses, T_1 and T_2, in the plane of the Si film. As noted earlier, the theory leads to a minimum mobility of the form

$$\mu_{min} = \frac{\mu_o}{a(1+\frac{A}{2})} = [\frac{a}{\mu_o}(1+\frac{A}{2})]^{-1} = [\frac{a}{\mu_o}(1+|\frac{b}{a}|)]^{-1}. \quad (80)$$

μ_o is the zero-stress mobility and is a function of the various growth process parameters and would be expected to vary from sample to sample. The parameter a for (111)Si consists of combinations of the Si piezoresistance coefficients multiplied by the average stress $(T_1+T_2)/2$ in the Si film, and the parameter b is equal to different combinations of piezoresistance coefficients multiplied by the stress anisotropy (T_1-T_2) in the Si plane.

The linearity of $1/\mu_{min}$ versus A on individual samples would suggest that μ_o/a is a constant for a given film. The quantities μ_o and a may be weakly interrelated through some phenomena but they do depend upon other different physical phenomena. There is thus no evident reason for μ_o and a to vary in such a way as to make their ratio constant. This suggests that μ_o and a separately are approximately constant for a given film, and this seems physically reasonable. The average stress is primarily thermal stress and should be constant for a given film, leading to constant a. The zero-stress mobility μ_o depends upon growth parameters. Different portions of a given film should represent the limiting case of different films grown under identical conditions. On this basis μ_o should be constant for a given film. Spatial variations in growth parameters, such as a temperature variation across the sample (see Sections 3-5 and 9-3), would tend to counter the validity of this argument and may be responsible for the deviations from linearity seen on some of the samples.

Assuming that μ_o and a are substantially constant for a given film, variations in anisotropy across the film then represent variations in b and hence variations in the stress anisotropy (T_1-T_2). (T_1-T_2) is small compared with the average stress $(T_1+T_2)/2$, and thus a moderate percentage change in (T_1-T_2) could occur without changing $(T_1+T_2)/2$ very much, particularly if the increments in T_1 and T_2 were of opposite sign. Thus, a spatial variation in stress anisotropy (T_1-T_2) across the sample is not unreasonable as the proximate cause of variation in the mobility anisotropy across the sample.

The second conclusion, that a higher anisotropy is usually associated with a lower minimum mobility and a lower average mobility among different samples, is based on the relationship of Equation (80). This tendency is built into the model and would occur unless sample-to-sample variations of μ_o/a were strong enough to counterbalance the tendency.

The third observation concerns the fact that, while the above association is generally observed, a plot of μ_A or μ_{min} versus A^{-1} shows appreciable scatter. This is interpreted as a variation in μ_o/a from one sample to another, with most of the variation probably occurring in the zero-stress mobility μ_o.

The angular directions of the experimentally observed mobility maxima are also specified in Table 37. $\phi_{\mu_{max}}$ ranges from -6.0 deg to -42.7 deg, for an average of -16.4 deg, with respect to the $[2\bar{2}01]$ direction in Al_2O_3 for the seven samples included in the table. The mobility minima are located at +90 deg and -90 deg from the direction of the mobility maximum at $\phi_{\mu_{max}}$. With the exception of sample LM-91, for which the data fall outside the general range of the other samples, the angles of μ_{max} are all quite similar and suggest a consistent systematic dependence upon orientation. As will be discussed later, however, the experimental angles $\phi_{\mu_{max}}$ are not in agreement with that predicted on the basis of thermal stress theory.

Electrical properties of samples LM-71 and LM-105 were also measured at 77K. For the horizontal reactor sample LM-71 the carrier concentration decreased by a factor of 5.7 (from 4.14×10^{16} to 7.24×10^{15} cm^{-3}) between room temperature and 77K. The mobilities μ_{max}, μ_{min} and μ_A were 1096, 484 and 790, respectively, and increased by factors of 1.9, 1.2 and 1.6, respectively, from the room-temperature values. The 77K anisotropy was 77%, which is ~2.4 times the room-temperature value.

LM-105 was grown in a vertical reactor. The carrier concentration decreased by a factor of 9.5 (from 4.46×10^{16} to 4.70×10^{15} cm^{-3}) between room temperature and 77K. The mobilities μ_{max}, μ_{min} and μ_A were 1376, 852 and 1114, respectively, and increased by factors of 2.2, 1.6 and 2.0, respectively,

from the room-temperature values. The 77K anisotropy was 47%, which is ~3.0 times the room-temperature value.

The increase in anisotropy by factors of 2.4 and 3.0 associated with the temperature reduction is similar to that observed for (001)Si and (221)Si, and is roughly consistent with that predicted from the increase in the piezoresistance effect in cooling from room temperature to 77K.

The temperature dependence of carrier mobility has been studied in some detail by various authors for both bulk Si and Si/Al_2O_3 (Ref 93). By comparing experimental mobility data with the known temperature dependences of lattice scattering, dislocation scattering, charged impurity scattering and neutral impurity scattering, the relative influence of these phenomena can be estimated. For the films in question rather different conclusions about the temperature dependence of mobility would be reached if mobility measurements were to be taken in the μ_{max} direction rather than in the μ_{min} direction, for example. This indicates that previous studies of the temperature dependence of mobility for Si/Al_2O_3, since the stress-piezoresistance effect and the mobility anisotropy were not incorporated into the measurement and analysis, are quite likely to be in error and thus of diminished significance in understanding fundamental physical phenomena in the Si/Al_2O_3 system.

(2) Comparison of Experimental Data with Theoretical Predictions

Theoretical calculations have been performed for both on-axis $(11\bar{2}0)Al_2O_3$ and +5 deg off-axis $(11\bar{2}0)Al_2O_3$ substrate orientations. The off-axis orientation approximates the substrate orientation used in the experimental investigations. Comparisons between calculations for these two slightly different orientations are of considerable interest in indicating the sensitivity of the anisotropy to small changes in substrate orientation.

The off-axis theoretical calculation yields an anisotropy of 3.95% and a maximum mobility located at approximately +80 deg from the $[2\bar{2}01]$ direction. The experimental average anisotropy of 16.3% is thus about four times larger than the theoretical value. The experimental direction of maximum mobility at about -16 deg is displaced approximately 96 deg from the theoretical direction.

Qualitatively similar results were obtained for the much simpler on-axis $(11\bar{2}0)$ Al_2O_3 orientation. An anisotropy of 9.6% and a maximum mobility direction of approximately +38 deg are predicted. Compared with these calculations, the experimental anisotropy is about 1.7 times too large and the maximum mobility direction is displaced about 55 deg from the predicted direction.

The differences in the theoretical data for the two orientations indicate that the anisotropy and maximum mobility directions are fairly sensitive to the exact substrate orientation. The reason for this is that intrinsic and extrinsic anisotropy effects compete at the particular off-axis orientation employed and tend to cancel one another.

The general conclusion is the same for both substrate orientations: The thermal stress model predicts anisotropies which are 1.7-4.1 times too small and maximum mobility directions which are displaced by 55-96 deg from the experimental values, so it appears that phenomena other than thermal stress are important for (111)Si films on Al_2O_3 substrates. However, anisotropic models are not presently available for the other physical phenomena which could influence (111)Si film mobilities. Thus, a definitive explanation for the substantial observed anisotropy in this case cannot be given at this time.

However, if it is assumed that the experimental results can be completely described solely within the framework of the stress-piezoresistance model, then these stresses can be determined by fitting the theory to the experimental data. For thin Si films the stress is described totally in terms of the normal components of stress T_1 and T_2 and the shear stress component T_6 (Ref 35). On the assumption that the average stress $(T_1+T_2)/2$ in the film is correctly given by the thermal stress model, $(T_1-T_2)/2$ and T_6 have been determined by fitting the experimental average anisotropy and the maximum mobility direction. For the off-axis $(11\bar{2}0)$ substrate orientation the stresses required to yield the experimental results are $(T_1+T_2)/2 = -1.20\text{x}10^{10}$ dyn/cm^2, $(T_1-T_2)/2 = +2.09\text{x}10^{9}$ dyn/cm^2, and $T_6 = -0.0429\text{x}10^{9}$ dyn/cm^2, compared with the thermal stresses for this orientation which are $(T_1+T_2)/2 = -1.20\text{x}10^{10}$, $(T_1-T_2)/2 = 0.313\text{x}10^{9}$ and $T_6 = +0.940\text{x}10^{9}$ dyn/cm^2.

For the on-axis substrate orientation the derived stresses are $(T_1+T_2)/2 = -1.20\text{x}10^{10}$ dyn/cm^2, $(T_1-T_2)/2 = +1.13\text{x}10^{9}$ dyn/cm^2, $T_6 = -0.726\text{x}10^{9}$ dyn/cm^2, while the thermal stresses are $(T_1+T_2)/2 = -1.20\text{x}10^{10}$ dyn/cm^2, $(T_1-T_2)/2 = +0.185\text{x}10^{9}$ dyn/cm^2, and $T_6 = +0.770\text{x}10^{9}$ dyn/cm^2.

The stresses obtained in the two substrate orientations relate to two coordinate systems which are mutually rotated by 5 deg and thus cannot be compared in detail. However, the same qualitative conclusion follows in the two cases: A substantial additional positive stress anisotropy $(T_1-T_2)/2$ and a substantial additional negative shear stress T_6 are required, in addition to the thermal stresses, to explain the experimentally observed mobility anisotropy using the stress-piezoresistance model.

It has long been recognized that lattice-constant mismatch between dissimilar materials such as Si and Al_2O_3 can, in principle, lead to residual growth stresses. At present there is apparently no way of determining if such growth stresses do in fact exist in Si films in the (111) orientation and - if they are important - why such stresses do not appear to be required in the theoretical explanation for the (001)Si and (221)Si anisotropy cases. However, the possibility of a residual growth stress explanation appears plausible. Such an explanation would, if found to be correct, represent a major step forward in understanding some of the basic physics of heteroepitaxial Si films.

b. $(111)Si/(10\bar{1}4)Al_2O_3$

The electrical properties of $(111)Si(10\bar{1}4)Al_2O_3$ were also investigated in some detail. Experimental data on ten films grown in a vertical reactor and three films grown in a horizontal reactor were obtained and are described here.

The coordinate systems relating the measurement directions to the crystallography of the Si and Al_2O_3 crystals in this case were the following. In the Si, the Cartesian x and y axes were the $[1\bar{1}0]$ and $[11\bar{2}]$ directions, respectively, and in the Al_2O_3 were the $[1\bar{2}10]$ and $[20\bar{2}\bar{1}]$ directions, respectively. Again, angular rotations from the x-axes toward the y-axes were taken as positive. The coordinate system for the Si is thus identical to that given earlier for $(111)Si/(11\bar{2}0)Al_2O_3$ and the various principal directions are the same. Angular positions of some principal directions in the Al_2O_3 substrate plane are $[1\bar{2}10]$ at 0 deg, $[4\bar{4}0\bar{1}]$ at +36.3 deg, $[20\bar{2}\bar{1}]$ at +90 deg and $[0\bar{4}41]$ at -36.3 deg.

(1) Experimental Results

The experimental data for the $(111)Si/(10\bar{1}4)Al_2O_3$ samples are given in Tables 38 and 39. Table 38 lists data at room temperature for 13 n-type samples while Table 39 lists data obtained at ~77K on six n-type samples. The notation used for the various parameters in these tables is identical to that employed in the table for the $(111)Si/(11\bar{2}0)Al_2O_3$ data with the exception that the angular position of the maximum mobility direction is measured with respect to the $[1\bar{2}10]$ direction for $(111)Si/(10\bar{1}4)Al_2O_3$. The procedures employed in fitting the experimental mobility data to theoretical curves and the significance criteria employed here are all identical to those used earlier.

Samples LG-105, LG-111 and LG-109 were grown in a horizontal reactor, while all the other samples were grown in a vertical reactor. As was the case for the $(111)Si/(11\bar{2}0)Al_2O_3$ films, the horizontal reactor appears to yield a more homogeneous carrier concentration but a lower mobility film. The scatter in the mobility data, as measured by the RMS error ER1, is generally less for the horizontal reactor samples than for the other samples, indicating that the horizontal reactor also yields slightly more homogeneous mobilities.

Table 38. Room Temperature Anisotropy Parameters for N-type (111)Si/(10$\bar{1}$4)Al_2O_3

Sample No.	Bridge No.	Thickness (μm)	N_A (cm^{-3})	ΔN (%)	δN (%)	μ_{max}	μ_{min}	μ_A	A (%)	ER1 (%)	ER2 (%)	$\Phi_{\mu_{max}}$ [1$\bar{2}$10]	D	Comments
LG-105	1 & 2	2.05	5.71×10^{16}	12.8	3.31	384	249	317	42.6	2.5	16.2	93.5	0.271	Horiz. Reactor
	1		5.52×10^{16}	5.4	1.84	381	244	312	43.7	1.9	17.0	96.5		
	2		5.89×10^{16}	5.8	1.41	389	254	321	42.0	1.2	15.3	90.3		
LG-111	1 & 2	2.08	5.57×10^{16}	7.0	1.96	392	256	324	42.2	1.6	16.3	93.6	0.220	Horiz. Reactor
	1		5.60×10^{16}	7.0	2.14	390	254	322	42.2	1.3	16.2	93.7		
	2		5.54×10^{16}	9.8	1.56	394	257	325	42.3	1.7	16.3	93.5		
LG-109	1 & 2	1.99	4.99×10^{16}	8.0	1.64	323	236	280	31.0	7.0	13.9	85.1	0.270	Horiz. Reactor
	1		4.97×10^{16}	4.2	1.01	352	232	292	41.0	0.4	15.3	89.0		
	2		5.02×10^{16}	8.0	2.07	301	240	271	22.4	7.1	11.6	78.4		
JP-48	1 & 2	1.68	2.39×10^{16}	23.4	8.05	524	365	445	35.6	4.2	14.0	96.6	0.199	Vertical Reactor
	1		2.19×10^{16}	12.8	4.23	535	375	455	35.2	1.7	13.0	91.3		
	2		2.58×10^{16}	3.9	1.64	516	355	435	37.1	4.0	14.5	101.5		
LG-98	1 & 2	2.01	3.86×10^{16}	17.1	3.94	504	401	452	22.8	4.8	9.8	94.5	0.170	Vertical Reactor
	1		3.82×10^{16}	17.3	4.44	518	424	471	19.9	3.0	8.2	93.2		
	2		3.90×10^{16}	9.2	3.34	490	380	435	25.4	1.9	9.5	95.4		
LG-92	1 & 2	1.95	3.54×10^{16}	26.5	7.00	502	407	455	20.8	7.2	10.2	95.9	0.120	Vertical Reactor
	1		3.78×10^{16}	14.3	4.15	485	371	428	26.5	2.3	9.9	93.2		
	2		3.31×10^{16}	13.0	4.33	521	449	485	14.8	1.8	5.4	101.5		
LG-77	1 & 2	1.84	4.08×10^{16}	17.6	4.61	487	393	440	21.2	4.4	9.3	90.6	0.103	Vertical Reactor
	1		4.21×10^{16}	13.5	4.60	478	394	436	19.2	5.1	9.2	84.2		
	2		3.95×10^{16}	8.3	2.47	498	391	445	24.1	3.1	9.4	84.3		
LG-79	1 & 2	1.82	3.84×10^{16}	16.2	3.82	520	426	473	20.0	2.7	7.5	87.3	0.078	Vertical Reactor
	1		3.83×10^{16}	15.6	4.72	511	444	478	14.1	0.3	4.9	86.0		
	2		3.84×10^{16}	9.4	2.80	528	403	465	26.8	1.3	9.9	85.4		
LG-100	1 & 2	1.83	3.81×10^{16}	26.8	7.07	493	415	454	17.2	5.7	8.1	89.1	0.127	Vertical Reactor
	1		4.00×10^{16}	11.0	2.86	491	385	438	24.3	3.8	9.1	88.9		
	2		3.59×10^{16}	24.8	7.30	496	451	473	9.5	2.6	4.3	89.7		
LG-103	1 & 2	1.95	1.18×10^{17}	13.5	3.35	322	196	259	48.4	3.2	18.5	95.0		Vertical Reactor
	1		1.19×10^{17}	13.4	3.44	335	195	265	52.8	3.7	19.5	94.9		
	2		1.17×10^{17}	11.1	2.90	311	197	254	44.6	1.6	17.3	95.0		
LG-49	1 & 2	2.05	1.51×10^{17}	31.8	7.74	392	285	339	31.4	7.1	13.8	86.6		Vertical Reactor
	1		1.64×10^{17}	17.1	5.56	399	286	342	33.0	6.5	12.6	79.6		
	2		1.30×10^{17}	28.5	11.26	389	283	336	31.7	7.1	14.9	93.7		
LG-81	1 & 2	1.93	1.19×10^{17}	17.6	3.86	382	293	337	26.5	5.8	10.9	94.8		Vertical Reactor
	1		1.22×10^{17}	14.8	3.47	362	281	322	25.4	0.5	9.1	94.1		
	2		1.17×10^{17}	15.4	3.48	404	305	354	27.9	4.4	10.1	95.5		
LG-34	1 & 2	2.10	1.57×10^{17}	20.4	4.35	437	353	395	21.5	7.5	10.6	88.3		Vertical Reactor
	1		1.54×10^{17}	16.2	4.43	447	334	391	29.1	7.7	11.9	93.5		
	2		1.60×10^{17}	16.9	4.27	431	371	4[illegible]	15.1	6.9	8.8	77.5		(Poor fit)
Averages									29.6			90.7		

A detailed correlation between ΔN or δN and the RMS error ER1 is not obvious, and there are exceptions to the general statement given above. Bridge #2 of sample LG-109 shows a relatively large RMS error, so the data may be spurious. On the other hand, sample LG-79 shows values of ER1 which are comparable with the horizontal reactor sample errors even though its ΔN and δN are substantially larger. In general, however, larger RMS errors ER1 are associated with larger ΔN or δN to a greater degree than was found for the $(111)Si/(11\bar{2}0)Al_2O_3$ films.

The relation between mobility and anisotropy for these samples was explored by plotting the anisotropy A versus μ_{min} in Figure 135 (A similar plot would be obtained for A versus μ_A.) Although the data show considerable scatter, there is a definite inverse relation between anisotropy A and the minimum mobility μ_{min}, with lower mobility (μ_{min} or μ_A) samples yielding higher anisotropies. The data also suggest that the horizontal reactor samples exhibited lower mobilities and higher anisotropies compared with the vertical reactor samples.

The mobility and anisotropy would, on general grounds, be expected to depend upon film thickness and carrier concentration in these heteroepitaxial systems. The range of thicknesses of the Si films is not large and no definite relation between mobility or anisotropy and the thickness is evident. The thinnest sample (JP-48) does, however, exhibit a rather large anisotropy and a somewhat reduced μ_{min}. The general effect of mobility variation with carrier concentration is that to be expected, with the mid-10^{16} cm^{-3} samples yielding higher mobilities than the low-10^{17} cm^{-3} samples. A more detailed correlation does not appear warranted by the limited data.

(2) Other Experimental Results and Theoretical Predictions

The anisotropies in Table 38 range from a low of 9.5% to a high of 52.8%, with an average for the individual bridges of 29.6%. The angles $\phi_{\mu_{max}}$ denoting the angular positions of maximum mobility in the Si film plane range from +77.5 deg to +101.5 deg, with an individual bridge average of +90.7 deg. The majority of the samples have values within ± 5 deg of the average value.

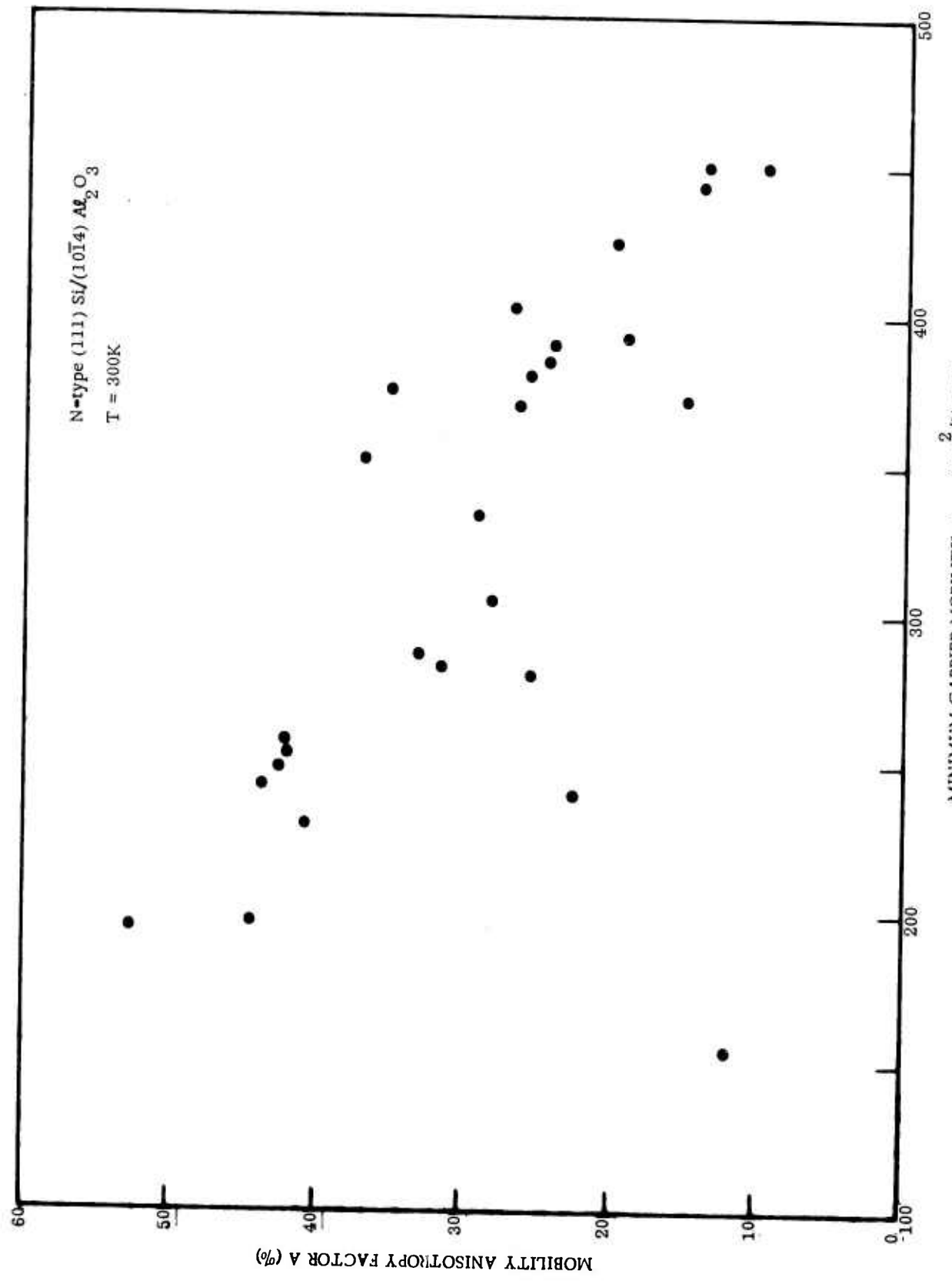

Figure 135. Plot of Anisotropy Factor A vs μ_{min} for 13 N-type (111)Si/(10$\bar{1}$4)Al_2O_3 Films

The thermal stress model predicts an anisotropy of 3.69% and a maximum mobility at ϕ = 0 deg, which is along the $[1\bar{2}10]$ direction in Al_2O_3. The theoretical anisotropy is thus about 8 times smaller than the experimental average and the theoretical and experimental maximum mobility directions are displaced by approximately 91 deg. The transverse-effect magnitude given by the coefficient D in the table varies from 0.078 to a high of 0.27, with an average of 0.17. The thermal stress model predicts a value of 0.019, which is about 9 times smaller than the experimental average.

The calculated effects of thermal stress on the mobility are therefore inadequate as an explanation for the experimental anisotropies found in these $(111)Si/(10\bar{1}4)Al_2O_3$ films, as was also the case for the $(111)Si/(11\bar{2}0)Al_2O_3$ films.

The role of surface conduction on the Si films was explored as a possible explanation for the large anisotropies. The films would not generally be expected to have appreciable surface conduction since the relatively high carrier concentrations would tend to mask surface effects. In addition, in the above measurements there was no intentionally grown oxide and no applied perpendicular electric field.

In order to more adequately assess possible surface effects, four of the $(111)Si/(10\bar{1}4)Al_2O_3$ films were reprocessed, and an oxide layer and Al gate electrode were deposited over the conduction paths in the bridge. The Hall bridges are considerably larger in physical size than the MOS device structures usually fabricated; yield problems were encountered, with poor quality oxide being obtained on many of the legs of the bridges. Complete anisotropy measurements were not possible. Instead, measurements of mobility versus gate voltage, below and above flat-band, were performed on individual legs of samples exhibiting good quality oxides.

These samples had carrier concentrations in the $1 \times 10^{17} cm^{-3}$ range. The bridge legs showed very little modulation of Hall mobility with voltage. Comparisons of measured mobilities, before and after fabrication of the MOS structures, indicated the mobilities to be identical within experimental error. Thus, surface

conduction apparently did not play a role in the samples investigated. Based on the limited data, it was concluded that surface effects were not responsible for the large anisotropies measured in (111)Si/Al_2O_3 films.

Effort was next directed toward a three-bridge analysis of the (111)Si/(10$\bar{1}$4)Al_2O_3 samples identical to that performed for the (111)Si/(11$\bar{2}$0)Al_2O_3 samples. Three samples were selected at random and triple-bridge computer fits to the mobility data were obtained. The anisotropy parameters derived from these three-arm bridges showed appreciably more scatter than for the previous samples. This is consistent with the larger RMS error ER1 on the (111)Si/(10$\bar{1}$4)Al_2O_3 samples as compared with the (111)Si/(11$\bar{2}$0)Al_2O_3 samples. The former samples apparently are less homogeneous and of poorer quality. In general, the (111)Si/(10$\bar{1}$4)Al_2O_3 mobilities are lower than those for the (111)Si/(11$\bar{2}$0)Al_2O_3 samples. This suggests that growth on (10$\bar{1}$4)Al_2O_3 substrates might be further optimized by additional work in the future.

The residual stress that would be required to explain the experimental mobility anisotropies of about 30% has been determined for (111)Si/(10$\bar{1}$4)Al_2O_3. Assuming the average stress to be a constant, the anisotropic stress $(T_1-T_2)/2$ would have to change from the thermal stress value of $+0.303\times10^9$ dyn/cm^2 to a large negative value of -2.46×10^9 dyn/cm^2. Thus an anisotropic stress ratio $(T_1-T_2)/\frac{1}{2}(T_1+T_2)$ of about 43% would be required to explain the experimental mobility anisotropy. This represents a large stress anisotropy; the existence of such stresses in the films and an explanation solely in terms of a stress model remain to be established.

Experimental mobility measurements at 77K have been made on six (111)Si/(10$\bar{1}$4)Al_2O_3 samples, and the anisotropy parameters determined are shown in Table 39. The anisotropies are almost exactly a factor of two greater than the corresponding room-temperature values and thus increase somewhat less in this regard than do the (111)Si/(11$\bar{2}$0)Al_2O_3, (001)Si/(01$\bar{1}$2)Al_2O_3, or (221)Si/(11$\bar{2}$2)Al_2O_3 samples at 77K.

Table 39. Anisotropy Parameters for N-type (111)Si/(10$\bar{1}$4)Al_2O_3 at Liquid Nitrogen Temperature

Sample No.	Bridge No.	N_A (cm^{-3})	ΔN (%)	δN (%)	μ_{max}	μ_{min}	μ_A	A (%)	ER1 (%)	ER2 (%)	$\Phi_{\mu_{max}}$ [1$\bar{2}$10]	$\frac{\mu_{max}(LN_2)}{\mu_{max}(RT)}$	$\frac{\mu_{min}(LN_2)}{\mu_{min}(RT)}$
LG-105	1 & 2	8.19×10^{15}	11.1	2.99	418	171	295	83.7	2.8	35.9	93.7	1.09	0.68
	1	7.95×10^{15}	3.3	1.17	411	167	289	84.4	0.7	37.3	95.6	1.08	0.68
	2	8.44×10^{15}	6.2	1.93	427	176	301	83.5	2.3	34.4	91.6	1.10	0.69
LG-111	1 & 2	7.80×10^{15}	6.4	1.54	429	184	306	80.2	2.1	35.0	91.2	1.09	0.72
	1	7.82×10^{15}	6.4	1.84	429	182	305	80.8	1.8	36.0	92.4	1.10	0.72
	2	7.78×10^{15}	3.86	1.34	430	185	308	79.5	2.1	34.0	91.0	1.09	0.72
LG-109	1 & 2	7.17×10^{15}	7.8	1.65	292	142	217	68.7	11.8	32.5	87.7	0.90	0.60
	1	7.09×10^{15}	7.0	2.10	338	146	242	79.1	0.7	33.7	88.7	0.96	0.63
	2	7.24×10^{15}	2.7	0.88	257	139	198	59.6	11.3	27.7	86.5	0.85	0.58
LG-77	1 & 2	5.39×10^{15}	14.8	4.82	692	456	574	41.0	11.6	21.7	93.1	1.42	1.16
	1	5.52×10^{15}	12.7	5.36	689	444	566	43.3	11.5	23.4	87.5	1.44	1.12
	2	5.25×10^{15}	10.5	2.95	700	468	584	39.8	11.7	19.9	97.3	1.40	1.20
LG-79	1 & 2	4.88×10^{15}	18.4	4.07	838	543	690	42.8	7.1	16.6	89.4	1.61	1.27
	1	4.90×10^{15}	18.4	4.90	805	597	701	29.7	1.3	9.8	88.6	1.57	1.34
	2	4.85×10^{15}	8.2	2.67	870	481	675	57.5	3.3	23.0	83.2	1.65	1.19
LG-100	1 & 2	4.96×10^{15}	21.8	5.94	716	491	604	37.3	13.3	19.2	85.1	1.45	1.18
	1	5.15×10^{15}	15.0	4.41	728	415	572	54.8	11.2	21.9	89.4	1.48	1.07
	2	4.72×10^{15}	14.8	3.97	723	596	660	19.3	5.7	9.9	73.6	1.46	1.32

Table 39 also lists the ratios of μ_{max} at 77K and 300K and μ_{min} at 77K and 300K. Comparing these ratios with those given for the two (111)Si/(11$\bar{2}$0)Al_2O_3 samples that were also measured at both temperatures indicates carrier compensation and/or poorer quality films for the (10$\bar{1}$4) orientation. As was the case for (111)Si/(11$\bar{2}$0)Al_2O_3 films, any analysis of mobility versus temperature which does not explicitly take the anisotropy into account would lead to inaccurate estimates of the various scattering mechanisms in these films. Clearly, this is an area needing further study in order to understand more of the important fundamentals.

c. Summary

Studies of mobility anisotropy in (111)Si films on ~(11$\bar{2}$0) and (10$\bar{1}$4)Al_2O_3 substrates revealed substantial anisotropies which were larger by factors of approximately 4 and 8, respectively, than the theoretical anisotropies predicted on the basis of thermal stress. The same theoretical model gives good agreement for (001)Si/(01$\bar{1}$2)Al_2O_3 and (221)Si/(11$\bar{2}$2)Al_2O_3 films. The results suggest that there are physical phenomena which are relatively more important for (111)Si film growth on Al_2O_3 and which are not understood at present.

The substantial variation in anisotropy from sample to sample and to a much smaller degree from point to point on a given sample in the (111)Si films studied suggests that the anisotropy is a sensitive function of the various growth parameters and experimental conditions. Thus, anisotropy studies potentially can provide a more thorough understanding of the phenomena important in the Si/Al_2O_3 system than has been possible in the past.

An apparent inverse relation between anisotropy and the minimum and average mobilities was established empirically for Si/Al_2O_3. For the (111)Si/Al_2O_3 systems this relationship makes it tempting to assume that, as further optimization and increases in mobilities are obtained, the experimentally observed anisotropies will decrease and come closer to the much smaller values predicted by theory on the basis of thermal stress alone.

A recent result may indicate such a trend. Mobility measurements on a $(111)Si/(10\bar{1}4)Al_2O_3$ film grown very recently with a 9:1 He-H_2 mixture indicated a carrier concentration of $2.08 \times 10^{16} cm^{-3}$ and mobilities $\mu_{max} = 737$ and $\mu_{min} = 706$ $cm^2/V\text{-sec}$. These mobilities are notably higher than those obtained earlier on substrates of this orientation. The anisotropy determined by least squares fitting was 4.2%. However, since the RMS error ER1 was 3.0% and the RMS error ER2 was 3.4%, the anisotropy was evidently too small to measure. In any case, the very small anisotropy exhibited by the sample is in agreement with the theoretical thermal stress model value of 3.69% for this substrate orientation.

These results are for only one sample, and until further work is done and the electrical properties are shown to be reproducible, they must be considered as tentative. Nonetheless, the results further confirm that the anisotropy is a very sensitive function of growth conditions and film quality and is a powerful new fundamental tool for better understanding and optimizing Si films on Al_2O_3 substrates.

using ion-thinned Al_2O_3 substrates (see Section 6-3) and techniques of transmission electron microscopy.

Finally, although the experiments were not carried out as a part of this contract program, a series of very recent investigations by Ushioda et al (Ref 94) using samples of heteroepitaxial (111)GaAs on (0001)Al_2O_3 prepared on this contract and loaned for the experiments has resulted in the first definite observations of surface polaritons in GaAs films.* A strongly dispersive mode in a very thin (~¼μm)GaAs film on a polished Al_2O_3 substrate was observed by means of Raman scattering of the 4880Å line from an Ar ion laser and identified to be the surface polaritons of the layered structure air(vacuum)/GaAs/Al_2O_3. The investigators have suggested that the presence of the dielectric substrate in contact with the semiconductor is the principal distinction between these experiments and earlier unsuccessful attempts to observe surface polaritons in GaAs using the surface-reflection Raman scattering method. The fact that the observed line widths were comparable with those of bulk modes was taken to indicate a high degree of uniformity of the film thickness and abruptness (perfection) of the interface.

A theoretical explanation of these experimental observations of surface polaritons by Ushioda et al has recently been given by Mills and Maradudin (Ref. 95). These investigators also propose that the many previous unsuccessful attempts to observe surface polaritons by the Raman technique have suffered primarily from the lack of a rear interface between the GaAs and a material of relatively high dielectric constant. They suggest that the details of the dispersion relation and line width of the surface polariton as seen in the Raman spectrum may be quite useful in providing information about the quality of the interface in a composite system such as GaAs/Al_2O_3.

---

*These experiments were carried out in the Department of Physics of the University of California at Irvine by S. Ushioda, J. D. McMullen and D. J. Evans.

1. POST-GROWTH ELECTRON MICROSCOPY OF Si FILMS ON Al_2O_3

Additional information on the early growth stages of Si on Al_2O_3 was obtained by conventional transmission electron microscopy of Si films grown on ion-thinned Al_2O_3 substrates in a conventional atmospheric-pressure vertical-flow reactor (see Section 3-1).

The substrates were $(01\bar{1}2)$-oriented Al_2O_3 0.050 in in diameter which had been ion-thinned to produce a central electron-transparent region. They were heated (at 1 atm) in a H_2 flow of 1.5 lpm to which SiH_4 at a flow rate of 10 cc/min was added. Deposition time and temperature data for several samples are given in Table 40.

The sequence of samples FE3, FE4, and FE1 provides a good representation of the stages of early growth of Si on Al_2O_3, as shown in Figure 136. Allowing for the possibility of an incubation period, the Si island size and density in samples FE4 and FE1 are as expected based on the deposition times. Sample FE4, grown for 1 sec (Figure 136) has smaller islands of ~500Å diameter, with a density of 2.4×10^5 islands/cm^2. The 3-sec sample FE1 (Figure 137) has larger islands of ~3000Å diameter, with a lower density of 1.5×10^4 islands/cm^2, indicative of additional growth plus coalescence.

Examination of sample FE3, grown for 1/2 sec, did not reveal the presence of any Si nuclei, suggesting that an incubation period is required for growth of stable islands sufficiently large to detect in the electron microscope. Such an induction period has been reported by Joyce et al (Ref 96) for the growth of Si on Si by SiH_4 pyrolysis, but the explanation for its existence in that work is not likely to be applicable to Al_2O_3 substrates. The question of an induction period was not pursued further in this program because of the difficulty in accurately controlling the short deposition times required. It should be noted, however, that the time required to establish an equilibrium gas flow around the substrate in Si CVD by SiH_4 pyrolysis may possibly be large compared with the total experiment time, which would give an apparent incubation period for Si islands to appear.

Table 40. Deposition Conditions for CVD Si Grown on Ion-thinned $(01\bar{1}2)Al_2O_3$

Sample No.	Deposition Temperature (C)	Growth Time (sec)	Results
FE3	1045	1/2	No observable nucleation
FE4	1030	1	See Figure 136
FE1	1030	3	See Figure 137
FE5	1200	3	See Figure 138

Several observations are common to the two samples grown at 1030C, the first being the large amount of strain present in the Si islands as revealed by the extinction contours visible. Extinction contours are the irregular, curved light and dark bands faintly visible in the Si nuclei,* typified by location A in Figures 136a and b. They are caused by electron diffraction from various regions in the Si which are mutually misoriented by fractions of a degree as a result of lattice strain. The presence of extinction contours from the highly strained Si islands makes the observation of other defects, e.g., grain boundaries, twins, and stacking faults, more difficult. (The broad light and dark bands in Figure 136 are extinction contours present in the Al_2O_3 substrate.

A second observation common to Figures 136 and 137 is that many twins are present in the Si islands. Location B in Figure 136a and especially location A in Figure 137a illustrate the presence of twins. The twins are perhaps more visible in the dark-field micrograph, Figure 136b. Only the grains which are oriented such that they contribute to the circled region of the (111) ring in Figure 136c appear bright in Figure 136b. The origin of the twins is likely to be coalescence of individual Si crystals separately nucleated in the twin orientation as a result of double positioning on the substrate

*These features are much more clearly visible in the original negatives; considerable detail is lost in reproduction.

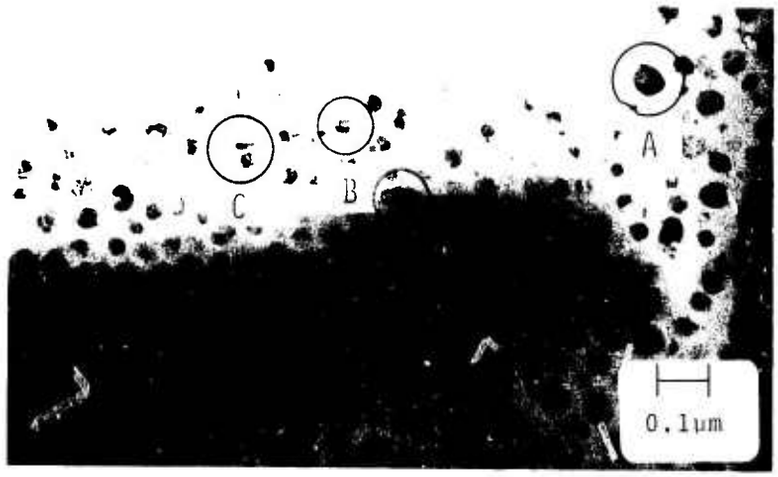

(a)

(b)

(c)

Figure 136. Electron Micrograph of Si Grown on $(01\bar{1}2)Al_2O_3$ (Sample FE4) at 1030C for 1 sec; (a) Bright Field, (b) Dark Field, (c) Diffraction Pattern.

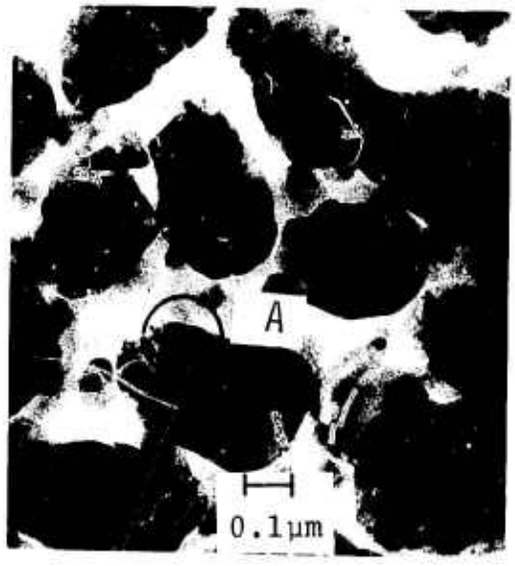

(a)

(b)

Figure 137. Electron Micrograph of Si Grown on $(01\bar{1}2)Al_2O_3$ (Sample FE1) at 1030C for 3 sec; (a) Bright Field, (b) Diffraction Pattern.

surface. The possibility of twin nucleation at the periphery of the growing Si-Al_2O_3 composite is also reasonable, but neither mechanism can be uniquely identified in these limited experiments.

Figures 136 and 137 indicate that considerable coalescence has occurred in the relatively early stages of growth shown by these figures. It is especially visible in Figure 137, which shows that each grain is composed of from 4 to 20 subcrystals, each originally from separate nuclei. Even in Figure 136 a significant amount of coalescence has taken place, as shown in location C and the nearby area. Note that in Figure 137 and presumably in Figure 136 considerable nucleation has occurred on the underside of the substrate, which makes the visual examination and interpretation of the micrographs somewhat more difficult. In Figure 137a the large islands are all on the top surface and the smaller islands are on the bottom surface, which in this case received less SiH_4 flux.

There is a significant orientation change as coalescence takes place in the early growth stages, as may be seen by comparing the diffraction patterns taken after 1 and 3 sec growth, Figures 136c and 137b, respectively. In Figure 136c the Si is almost entirely polycrystalline (the spots are from the Al_2O_3 substrate). In Figure 137b there is some polycrystalline Si present, but in addition there is a large single-crystal component, indicated by the four spots lying on the innermost Si ring (spots not lying on the Si rings are from the Al_2O_3). A large amount of twinning is also indicated by the two-fold symmetry of the Si spots.

The results of these experiments are significant, for they indicate the achievement of a single-crystal Si film is the result of coalescence processes in the early growth stages and not of nucleation phenomena alone. The individual nuclei are probably randomly oriented and it is only through coalescence that islands (or grains) with the desirable orientation prevail, while the more randomly oriented grains are consumed in the process. The change in orientation represented by the deposts of Figure 136 and 137 is significant, but additional change must take place to result in a continuous single-crystal film. These micrographs clearly demonstrate that single-crystal Si growth on $(01\bar{1}2)Al_2O_3$ is not the result of preferred (100)Si

nucleation; if this had been the case it would have been detectable in Figures 136c and 137b.

Formation of a single-crystal film by a coalescence mechanism rather than as a result of initial nucleation is further significant because more defects are likely to be present in such films. During coalescence, there will always be some misoriented nuclei or islands which are not completely eliminated, leaving a defect in the film which ultimately acts as a charge-carrier scattering center. Likewise, stacking faults, twins, and dislocation arrays are certain to be more prevalent in a film which has developed by coalescence from randomly oriented nuclei. The net result would be a lower carrier mobility in such films.

It should be possible, then, to produce (100)Si films with better electrical properties by increasing the nucleation rate of the (100)-oriented nuclei, hence minimizing the dominant role coalescence tends to play in the formation of a single-crystal film.

In view of the small number of (100)-oriented nuclei formed at 1030C, one sample (FE5) was grown at 1200C. A transmission electron micrograph is shown in Figure 138a and the corresponding diffraction pattern in Figure 138b. The Si nuclei formed were mostly (100) oriented, as indicated by the four-fold symmetrical Si spot pattern superimposed over the Al_2O_3 Kikuchi-line pattern. The (100) orientation was confirmed by dark field electron microscopy using the displaced aperture technique. On the basis of growth at 1030C versus growth at 1200C, it is concluded that increasing growth temperature results in more favorably oriented nuclei. This results in a more perfect film structurally, but unfortunately autodoping from the Al_2O_3 becomes more of a problem at these temperatures.

As may be seen in Figure 138a, there has been considerable attack of the Al_2O_3 by the Si. Many areas at the originally thin, wedge shaped edge of the sample have been completely eroded away. The etching of Al_2O_3 by SiH_4 or Si at elevated temperatures has previously been reported (Refs 97, 98). The

(a)

(b)

Figure 138. Electron Micrograph of Si Grown on $(01\bar{1}2)Al_2O_3$ (Sample FE5) at 1200C for 3 sec; (a) Bright Field, (b) Diffraction Pattern.

appearance of such etching phenomena presents additional complications in Si growth which clearly dictate the use of lower temperatures for device quality material.

2. RUTHERFORD BACKSCATTERING AND CHANNELING ANALYSES OF HETEROEPITAXIAL SEMICONDUCTOR FILMS ON Al_2O_3

The combination of Rutherford backscattering and channeling effects of H^+ and He^+ ions has been used by various investigators to study the lattice perfection (Refs 99,100) and chemical composition of thin (<2μm) solid films (Ref 101). Most of the earlier work was done in connection with ion implantation; however, this technique is now being applied in other areas.

Early in the contract program (Ref 1) it was suggested that it might be possible to characterize heteroepitaxial film perfection and obtain defect density distributions as a function of depth in the interfacial region by means of observations of the energy spectrum of backscattered ions injected into the film. This method was investigated experimentally in the first year of the program; exploratory measurements were carried out on both Si and GaAs films on Al_2O_3 substrates.* After these experiments were performed and described there were reports in the literature of other similar applications of the technique to heteroepitaxial semiconductor systems (Refs 102, 103).

The major advantages of the technique are that it provides a profile of the lattice perfection or chemical composition vs depth and it is nondestructive. Thus, profiles can be obtained on the same area before and after annealing under various conditions of temperature, ambient atmosphere, and quenching. The major disadvantage of the technique is a lack of sensitivity; the minimum detectable number of atoms off normal lattice sites is ~1%.

The backscattering measurement utilizes a monoenergetic H^+ or He^+ ion beam which is incident on the desired target. The backscattered particles are

---

*The backscattering measurements and calculations were carried out by J. S. Harris,Jr., and B. Welch at the Rockwell International Science Center in Thousand Oaks, CA.

detected with a solid-state detector and energy-analyzed with a multichannel analyzer.

The proton backscattering spectrum for randomly-oriented GaAs is shown in Figure 139. The spectrum is a continuum from zero energy to $E_{max} = k^2 E_i$, where E_i is the incident energy and k is a scattering parameter (Ref 104) ($k<1$) which is dependent upon the scattering angle and the atomic masses of the projectile and target atoms.

If the target is a single crystal with a major crystallographic axis aligned with the incident proton beam, then the incident ions will be steered or channeled between the open planes of the lattice, and the probability of a large-angle backscattering collision is greatly reduced. A spectrum for an aligned (111)GaAs single-crystal sample is also shown in Figure 139. When the incident beam is aligned with a crystal in which atoms are off normal lattice sites, the scatterint probability increases and the spectrum is intermediate between the aligned and the random spectra of Figure 139.

The density of scattering centers (atoms off lattice sites) can be calculated from the channeling measurements, following the work of Bogh (Ref 104) and Eisen (Refs 105, 106). The scattering density is

$$N(E) = N_o \frac{X_A(E) - X_R(E)}{1 - X_R(E)} , \qquad (81)$$

where N_o is the atomic density of the target, X_A is the normalized aligned yield, and X_R is the random fraction of the analyzing beam. X_R is calculated using the plural scattering theory of Kiel et al (Ref 107). (A complete description of this disorder calculation is presented in the Appendix of Ref 106.) For Ge, Si, GaAs and some other materials the energy loss dE/dX is known. With this information and the backscattering geometry, the energy scale of the spectra can be converted into a depth scale, thus yielding a profile of disorder density vs depth.

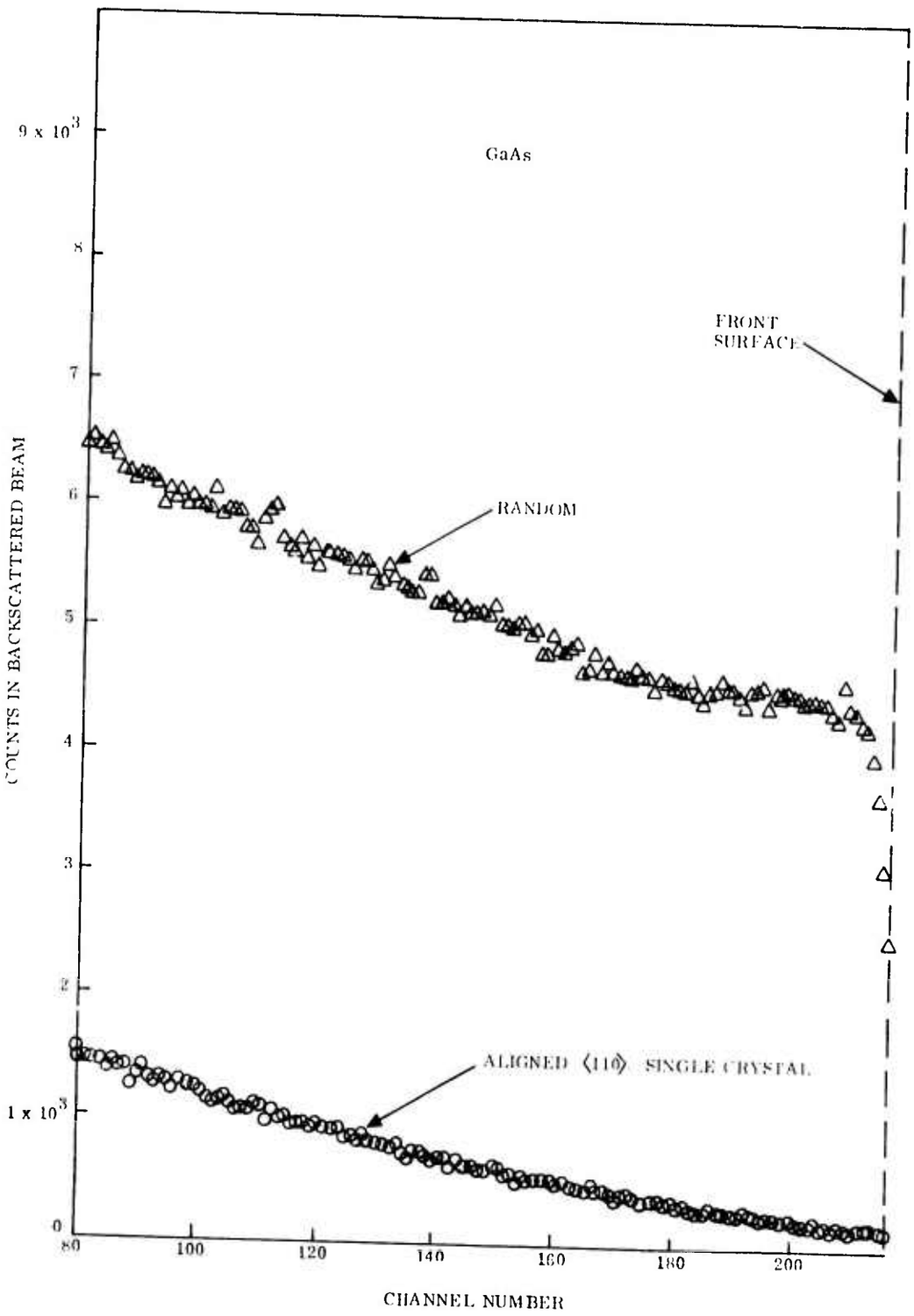

Figure 139. Backscattered Proton Energy Spectra for Randomly Oriented and Aligned (111) Single-crystal GaAs

Aligned and random backscattering spectra for a Si film on Al_2O_3 are shown in Figure 140. The reduction in scattering below channel 110 was due to protons which scattered from the Al_2O_3 substrate. Some typical results of the computer calculation of disorder density for Si and GaAs on Al_2O_3 are shown in Figures 141 through 145. Figures 141 and 142 are for (111)Si layers grown on the $(10\bar{1}4)$ and $\sim(11\bar{2}0)$ surfaces, respectively. The disorder density at the surface was approximately the same for both films; however, the Si-Al_2O_3 interface region (peak of the disorder) was much better (about half as many scattering centers) for the layer grown on the $\sim(11\bar{2}0)$ surface. Figure 143 shows a twinned region of the same film as is shown in Figure 142, which exhibited considerably higher disorder at both the interface (peak of the disorder) and the front surface.

Figure 144 shows the profile for a (100) Si film on a $(01\bar{1}2)Al_2O_3$ substrate which appeared to be about the same as the best (111) profile in Figure 141. Thus, the backscattering measurements revealed the best Si films to be (100) grown on $(01\bar{1}2)$ substrates and (111) grown on the $\sim(11\bar{2}0)$ plane of Al_2O_3.

Figure 145 shows a profile for a (111) GaAs film grown on Al_2O_3. The disorder density at the GaAs-Al_2O_3 interface (peak of the disorder) was very nearly equal to the atomic density of GaAs. Better interfaces were observed for other GaAs films; however, those other films were all very thin ($t \sim 1500\text{Å}$), and the spectrum obtained from proton backscattering is limited by the energy resolution of the detector and the available proton energy. He^+-scattering spectra provided greater depth resolution, and the density of scattering centers obtained in that manner appeared to be approximately one-fourth the value shown in Figure 145. However, the scattering calculation had not been modified to handle He^+ injected into GaAs at the time these measurements were made.

These preliminary results indicated that the Rutherford backscattering-channeling technique is a useful tool to study the crystal perfection of thin heteroepitaxial films on insulating substrates. The number of lattice atoms off lattice sites is well within the sensitivity of this measurement and the effects of annealing, substrate orientation, and perfection should be detectable. However, because

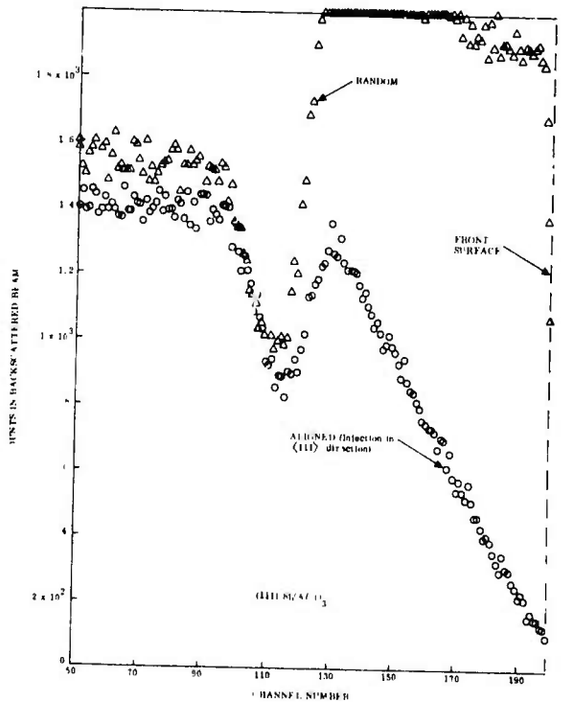

Figure 140. Backscattered Proton Energy Spectra for Heteroepitaxial (111)Si Film on $(10\bar{1}4)Al_2O_3$ for both Randomly Oriented and [111] Injections

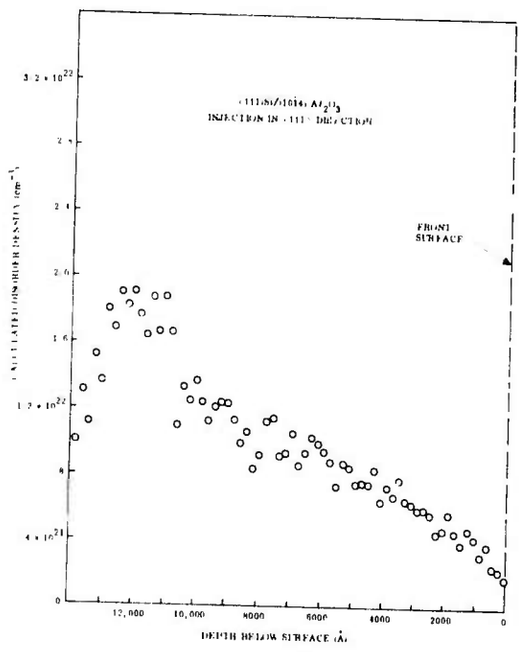

Figure 141. Calculated Disorder Density as Function of Depth below Surface of (111)Si Film on $(10\bar{1}4)Al_2O_3$ Substrate. (Peak disorder is at interface)

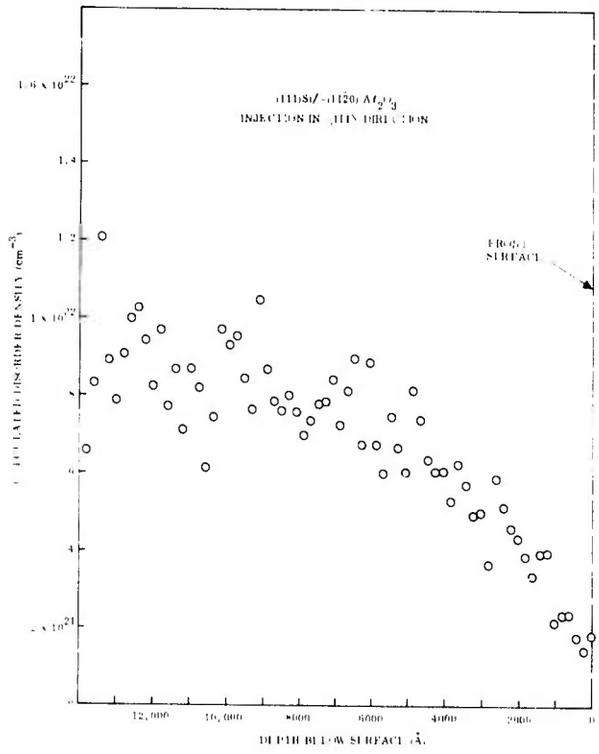

Figure 142. Calculated Disorder Density as Function of Depth below Surface of (111)Si Film on ~$(11\bar{2}0)Al_2O_3$ Substrate. (Peak disorder is at interface.)

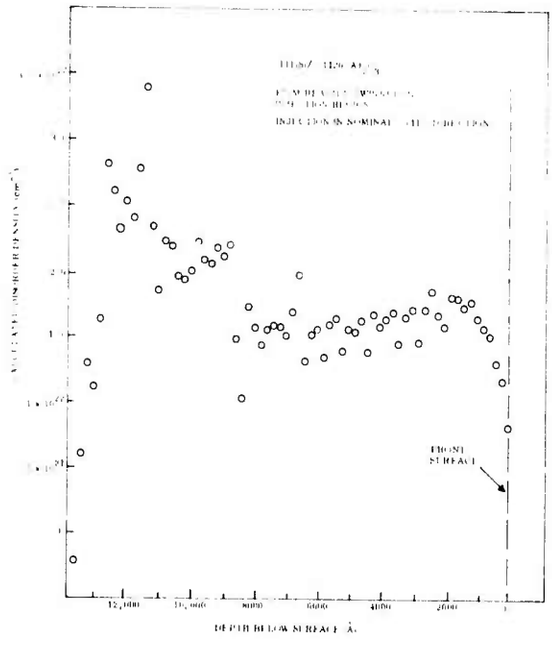

Figure 143. Calculated Disorder Density as Function of Depth below Surface of Sample of Figure 142, but in Twinned Region of Film. (Note higher disorder density throughout.)

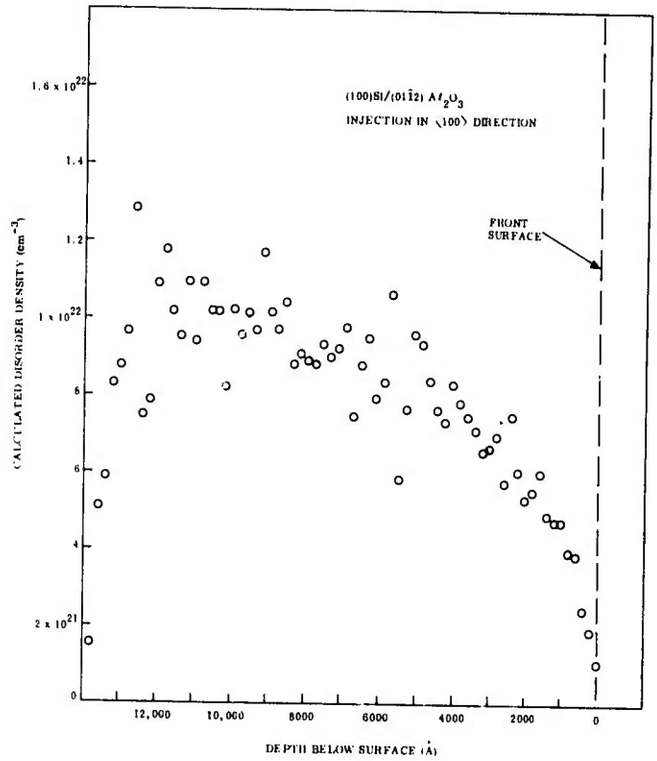

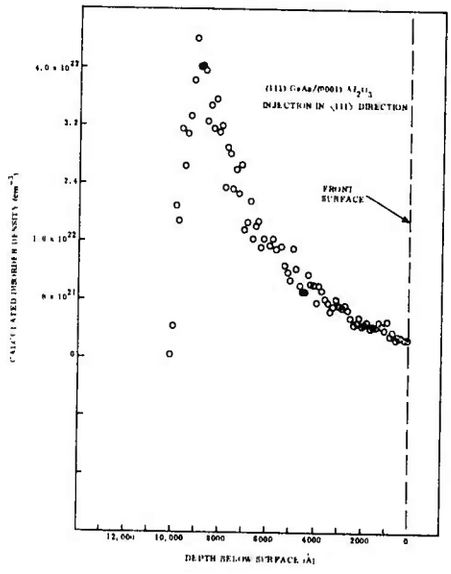

Figure 145. Calculated Disorder Density as Function of Depth below Surface of (111)GaAs Film on (0001)Al_2O_3 Substrate. (Peak disorder is at interface.)

of the difficulties of obtaining machine time on the ion accelerating equipment used for these measurements and the involvement of contract personnel in other program tasks, these investigations were not pursued further under this contract.

3. MEASUREMENT OF PHOTOELECTRIC EFFECTS AT THE Si/Al_2O_3 INTERFACE*

Photoelectric effects in heteroepitaxial semiconductor films on Al_2O_3 substrates using a metal-insulator-semiconductor (MIS) device configuration, as well as in Al_2O_3 substrates using a metal-insulator-metal (MIM) device configuration, were measured under the contract program as a means of characterizing the properties of the materials interfaces. The experimental study characterizing the Al_2O_3 substrate by means of the MIM device configuration has already been discussed in Section 7.

Here the experimental studies of Si and GaAs heteroepitaxial films on Al_2O_3 by means of photoelectric measurements using the MIS device configuration are described along with those aspects of the MIM measurement needed to interpret the MIS measurements. The results of these two types of experimental photoelectric studies have been described in several publications (Refs 61, 62, 63); more detail can be obtained from those references.

The technique of utilizing the photoelectric process in the MIS structure has been used by a number of workers (Refs57, 58, 59) to study the interface between a semiconductor and an insulator. Usually a thin insulating layer (~2000Å) is grown on a polished semiconductor and a semitransparent metal film is deposited on top of the insulating layer to form the MIS structure. Monochromatic light is directed onto the semitransparent electrode and is partially absorbed in the metal layer. The remainder of the light is absorbed in the semiconductor close to the semiconductor-insulator interface. (The insulator is transparent to light for the photon energies used.)

---

*The photoelectric effect measurements were carried out at the Department of Electrical Sciences and Engineering of the University of California at Los Angeles by C. R. Viswanathan and R. Y. Loo.

Electrons are excited both in the metal layer and in the semiconductor by the absorbed photons. With a bias voltage applied across the MIS structure, with the metal layer positive with respect to the semiconductor, electrons excited in the semiconductor near the interface will then flow through the insulator and into the metal electrode, provided the electrons have sufficient energy to overcome the barrier at the interface. This photoelectric current is measured by a meter in the external circuit, as shown in Figure 146. When the metal electrode is biased negative with respect to the semiconductor, a current due to photoelectric emission of electrons from the metal will flow through the insulator to the semiconductor.

By studying the photoelectric yield as a function of photon energy, it is possible to obtain information about the interface barrier height (location of the conduction band of the insulator at its two interfaces), the electron affinity of the insulator, and the amount of band bending in the semiconductor, as mentioned in Section 7. Photoelectrons emitted from the region of the semiconductor adjoining the insulator provide a type of electric "probe" to characterize the interfacial region of the semiconductor.

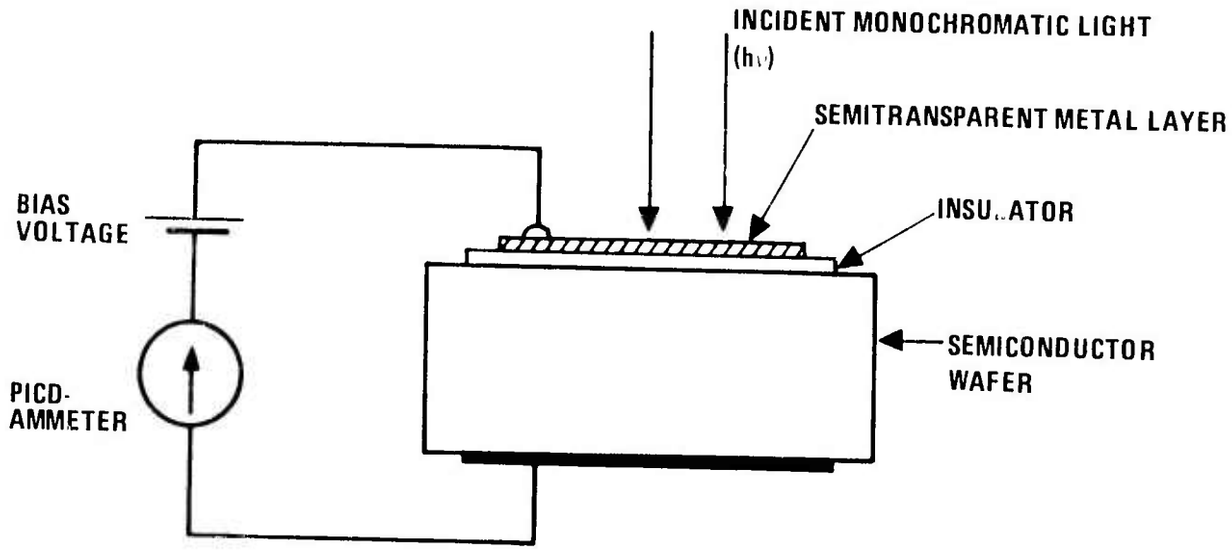

Figure 146. Schematic of Experimental Arrangement for Photoelectric Current Measurement in MIS Structures

Heteroepitaxial films of both Si and GaAs grown on Al_2O_3 were examined in this MIS configuration by means of the photoelectric technique. The Al_2O_3 substrate layer served as the insulator, and an Al film deposited on the "back" side of the substrate (opposite the semiconductor film) served as the metal electrode.

In addition to yielding information on the interface barrier height and the amount of band bending in the semiconductor near the interface, these experiments demonstrated that electrons excited either in the semiconductor film or in the metal layer can be transported through single-crystal Al_2O_3 substrates whose thickness is the order of several mils (Section 7). The fact that photoelectrons excited on one side of the thick transparent substrate can flow completely through it is a very significant result and may suggest novel photodevice applications using heteroepitaxial thin-film semiconductors, although it must be recognized that the achievable photocurrents are quite small.

The Si films used in these measurements were grown on polished $(01\bar{1}2)$ and $(10\bar{1}4)Al_2O_3$ substrates; the GaAs films were grown on $(0001)Al_2O_3$. Thickness of the substrates ranged from 0.014 to 0.019 in. The metal layer was vacuum-deposited on the side of the substrate opposite that on which the epitaxial film was grown.

Originally, it was expected that the Al_2O_3 substrates were too thick to permit the transport of photoelectrons. Attempts were made to reduce the substrate thickness after the heteroepitaxial films were grown but proved impractical. An experiment was then performed to determine if electrons could penetrate substrates of several mils thickness. A thick Al film (~5000Å thick) was deposited by PVD on one side of a clean, polished Al_2O_3 substrate; on the other side, a thinner Al film (~400Å) was deposited.

This metal-insulator-metal sample was then used in the photoelectric measurement, with a bias voltage of 150 V and incident light of photon energy equal

to 5.4 eV. The current flowing through the sample with light incident on either the thick or the thin Al layer was measured, giving the results shown in Table 41.

From the table it can be seen that the measured current was not due to electrons photoexcited in the Al_2O_3 layer, since the current depended upon the polarity of the bias voltage. The fact that light incident on the negatively-biased electrode produced photocurrent, while light incident on the positively-biased electrode did not produce photo-current, showed that the current was due to electrons excited in whichever electrode the light was incident upon.

Table 41. Relationship between Relative Polarity of Bias Voltage and Illuminated Metal Layer

Side with Incident Light	Bias Voltage*	Magnitude of Current
Thick Al layer	-150 V	Large
Thick Al layer	+150 V	Negligible
Thin Al layer	-150 V	Negligible
Thin Al layer	+150 V	Large

*Polarity of bias voltage is that of thick Al layer with respect to thin layer.

This demonstrated clearly that electrons were easily transported across a thick single-crystal Al_2O_3 layer. The results also showed that most of the incident light was absorbed even when the thickness of the Al layer was as low as 400 Å, in agreement with earlier results (Ref 108), and that photoelectric yield could be obtained even when the thickness of the Al layer was as much as 5000 Å.

Batt and Mee (Ref 108) reported that the photoelectric yield as a function of thickness of Al films rises to a maximum value at a thickness of about 50 Å and then falls to a constant value about 0.2 of the maximum; their observations extended to film thicknesses of up to about 500 Å. The experiments described here showed that even beyond 500 Å the photoelectric yield seems either to be constant or to drop very slowly with thickness. These observations showed that the MIS structure consisting of the Al_2O_3 substrate as the insulator, a heteroepitaxial semiconductor film as the semiconductor, and a PVD metal layer as the metal electrode could be used in a photoelectric investigation of the properties of the interfaces.

Although from the experimental results shown in Table 41 indicated that the measured photocurrent was not caused by electrons photoexcited in the Al_2O_3 layer, one further experiment was carried out to ensure that the current observed in the photoelectric measurements was indeed due to photoinjection of electrons into Al_2O_3. In that experiment, six Al film stripes, each ~300Å thick and 1 mm wide, were deposited on one side of a substrate, with a spacing of approximately 1 mm between adjacent stripes (Figure 147). A Au film was deposited uniformly on the other side of the substrate. A sharply

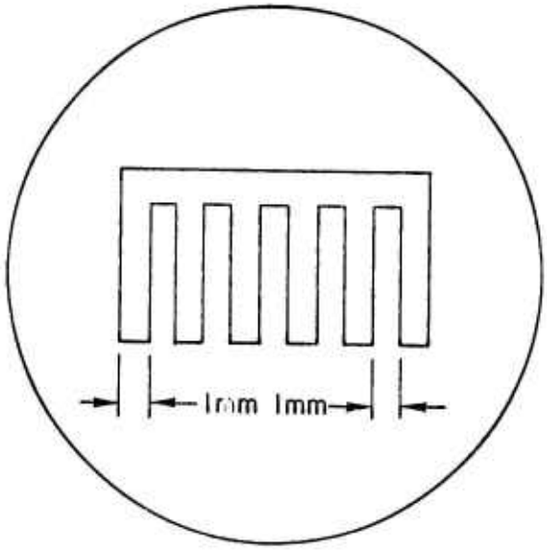

Figure 147. Configuration of Semitransparent Al Stripes Deposited on Al_2O_3 Substrates

focused light beam was scanned at a slow rate across the surface of the substrate having the semitransparent Al stripes, and the photoelectric current was recorded by an X-Y recorder as a function of the position of the light beam.

Six peaks, with well-defined minima between, were observed in the photoelectric current for both polarities of the bias voltage, as shown in Figures 148 and 149. The peaks correspond to incidence of light on a stripe and the minima correspond to incidence of light in the spaces between stripes. Observation of the six peaks even when the Al films were biased positive again demonstrated that (1) electrons were injected into Al_2O_3 from the Au film, and (2) such injection occurred only in those regions of Al_2O_3 where an electric field existed, viz, the regions under the Al stripes.

For a given bias voltage, as soon as the light beam was directed onto the metal electrode the photocurrent reached a peak value in a time interval the order of a few msec and then decayed as a function of time, reaching a steady-state value after several minutes, thereby indicating that traps were being filled. The higher the bias voltage, the larger was the number of traps that were filled.

On the basis of these two experiments, device configurations suited to detailed measurements of the properties of these photocurrents were then fabricated. By means of photolithographic techniques the heteroepitaxial semiconductor film was selectively etched to leave circular mesas of the semiconductor on the substrate. An Al film was then deposited on the opposite side of the substrate. Another metallization process formed an ohmic contact to the semiconductor mesas, while leaving most of the semiconductor surface open to the incident light.

Photoelectric emission from the semiconductor into Al_2O_3, as well as from the Al electrode into Al_2O_3, was then studied as a function of photon energy. The photoelectric response was measured with a Bausch and Lomb 1/4-meter monohhromator using a 1000-watt Hg-Xe light source and suitable instrumentation. The measured photoelectric currents were in the 10^{-11} to 10^{-12} a range. The dark currents were lower than a fraction of a picoampere.

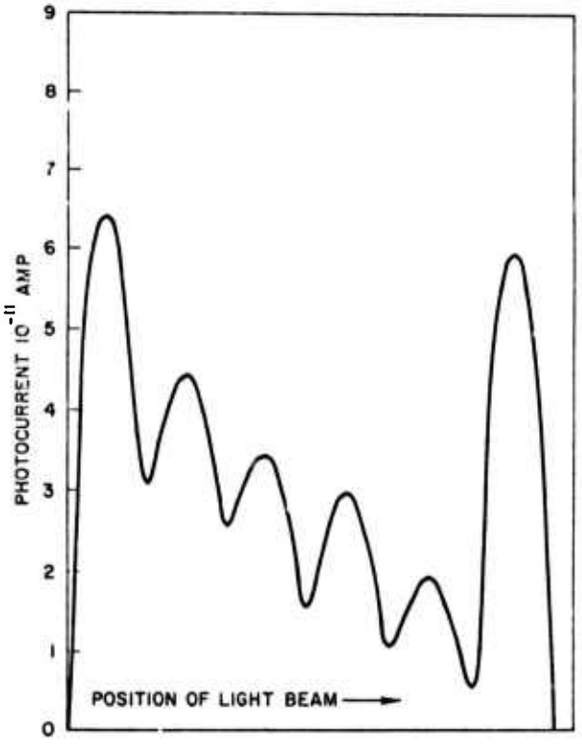

Figure 148. Photocurrent as Function of Position of Scanning Light Beam, with Al Biased Negative

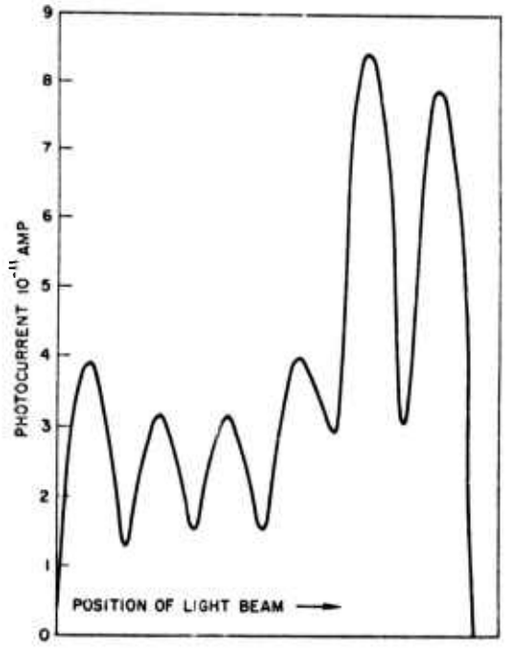

Figure 149. Photocurrent as Function of Position of Light Beam, with Al Biased Positive

For the case of electron emission from the Al electrode into the Al_2O_3, the steady-state current values were measured for various photon energies with the bias voltage kept constant. The square root of the photoelectric current was then plotted as a function of the photon energy to obtain a Fowler plot, as shown in Figure 150. Two linear regions corresponding to two threshold energy values of 3.15 and 4.3 eV, respectively, were observed. Taking the lower value as that corresponding to the height of the interface barrier between Al and Al_2O_3, the energy-band diagram shown in Figure 151 was constructed. The work function of Al was taken to be 4.1 eV (Ref 109) and this gives a value of 1.0 eV for the electron affinity of Al_2O_3, which agrees well with the value quoted by Pong (Ref 60) for amorphous Al_2O_3. The value of 3.15 eV for the interface barrier height agrees with the value 3.05 eV measured by Szydlo and Poirier (Ref 110) for the polycrystalline Al_2O_3-Al interface.

When the photoelectric current corresponding to emission of electrons from other metals, such as Au, Ag, and Cu, was measured as a function of photon energy, the resulting Fowler plots were again characterized by two linear regions. The lower threshold energy values, again taken as the interface barrier heights, when combined with the value of 1.0 eV for the electron affinity of Al_2O_3 gave work function values (Ref 111) agreeing with previously published values for the metals involved.

In all these cases, the threshold energy value corresponding to the second linear region was 1 to 1.1 eV higher than the interface barrier height. This suggests the possibility that the higher threshold energy might correspond to vacuum emission of electrons from the metal into pinholes in the metal film. Further experiment would be needed to verify this.

The fact that a photoelectric current was observed in Al_2O_3 layers several mils thick clearly established that the range of photoinjected electrons is much larger than the value of 130 Å reported for amorphous Al_2O_3 layers

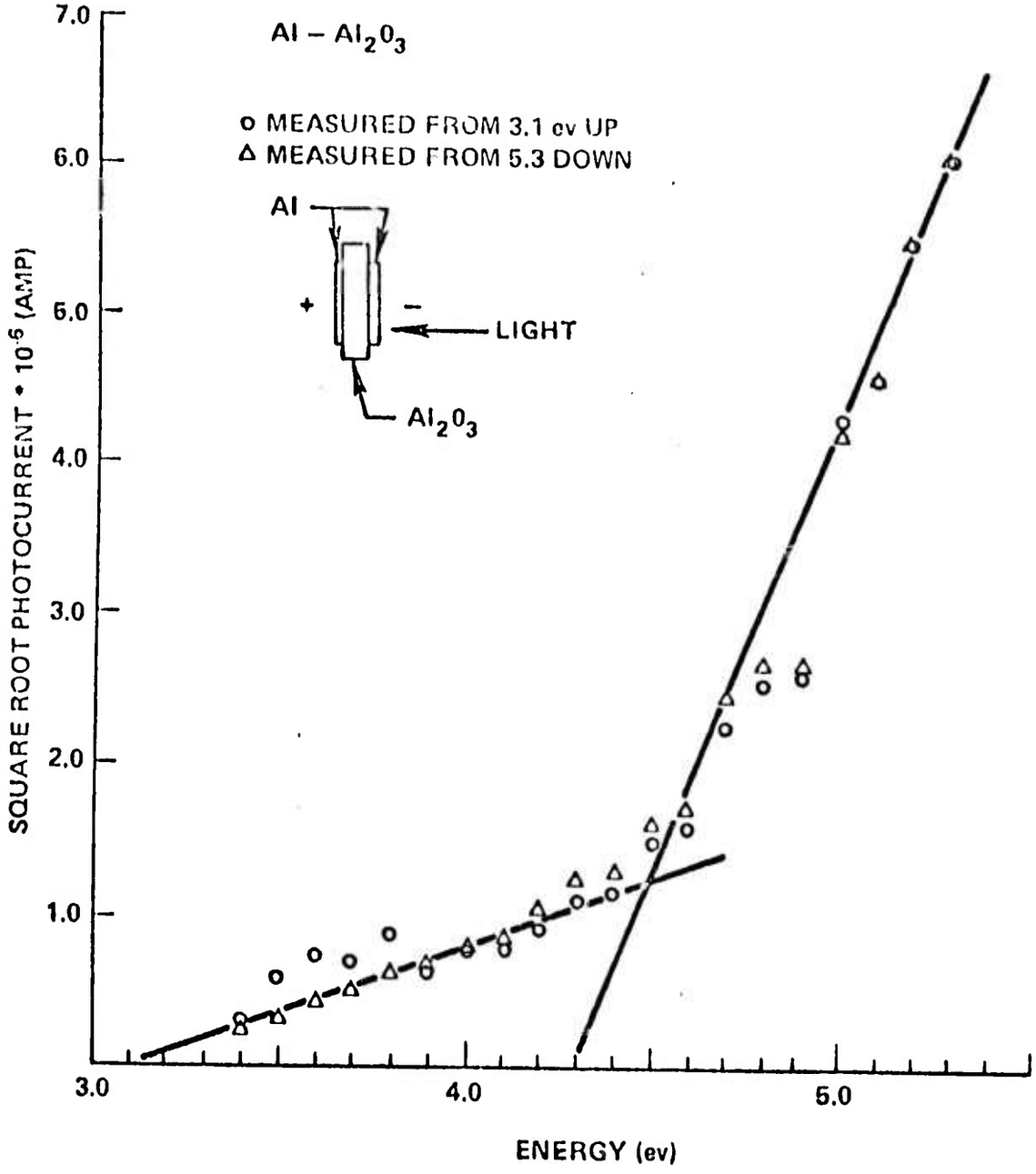

Figure 150. Fowler Plot of Room-temperature Photocurrent as Function of Photon Energy for Al-Al_2O_3 Interface

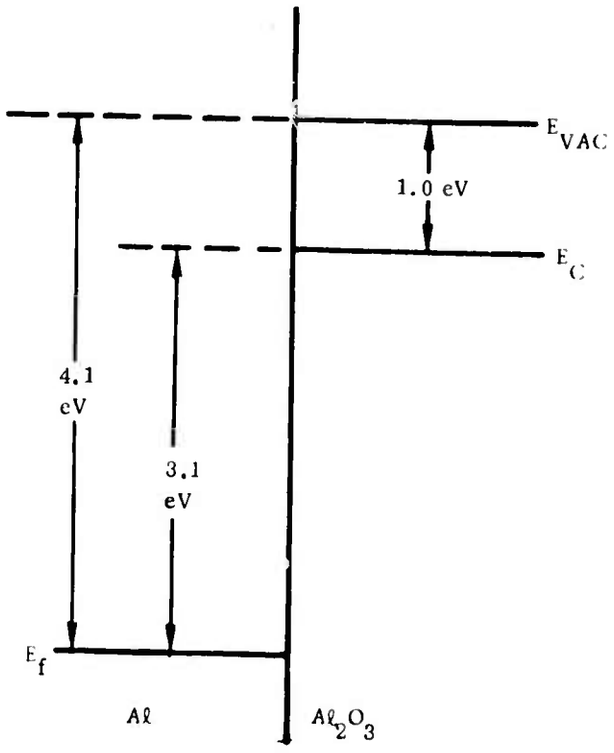

Figure 151. Energy-band Diagram for Al-Al_2O_3 Interface

(Ref 60). It would thus be possible to measure the range of the injected electrons by carrying out measurements with Al_2O_3 substrates of several different thicknesses.

The magnitude of the current as a function of the thickness of Al films deposited on the same Al_2O_3 substrate was also measured, with the light incident on the Al films. A peak was observed around 2500 Å thickness, and the current was found to be an appreciable fraction of the peak even when the thickness of the Al layer was as large as 5000 Å. This result is in contrast to the mean range for electrons in Al as measured by other workers (Ref 112).

The photoemission current from Si has been observed to follow a cubic law (Ref 113). Figure 152 shows a plot of the cube-root of the photoelectric current as a function of photon energy for a heteroepitaxial Si film of thickness 12.5μm. The intercept of the linear portion of this curve gives the interface barrier height at the Si-Al_2O_3 interface to be 4.50 ± 0.05eV.

The photoelectrons are due to excitation of electrons mainly in regions beyond that near the interface in which the energy bands may be bent. Combining the photoelectric threshold of 4.5eV with an electron affinity in Al_2O_3 of 1.0eV and subtracting the energy difference between the vacuum level and the valence band in Si (5.17eV) yields an estimate of 0.37eV for the amount of band bending in Si near the interface.

The results obtained with a heteroepitaxial GaAs film of 23.5μm thickness on Al_2O_3 are also plotted in Figure 152 to give a photoelectric threshold energy of 4.4eV. Since the electron affinity and bandgap in GaAs are 4.07eV and 1.43eV, respectively (Ref 114), band bending the order of 0.10eV is indicated for GaAs films in this configuration.

It is noteworthy that the band bending in Si and GaAs films at the semiconductor-Al_2O_3 interface probably cannot be measured by any technique other than that employed here. Thus, the photoelectric technique offers a unique characterization of this aspect of the interface.

With both Si and GaAs samples the light was incident directly on the semiconductor surface. Since a significant amount of photocurrent due to emission from the other side of the semiconductor surface into the Al_2O_3 was observed, it is suggested that the mean free path (escape length) of excited electrons is at least the order of or larger than the thickness of the heteroepitaxial films studied. This indicates an escape length at least the order of 12.5μm in Si, and the order of 23.5μm in GaAs. This is a surprising result which is in sharp disagreement with the very low escape length values quoted for bulk Si (Ref 113).

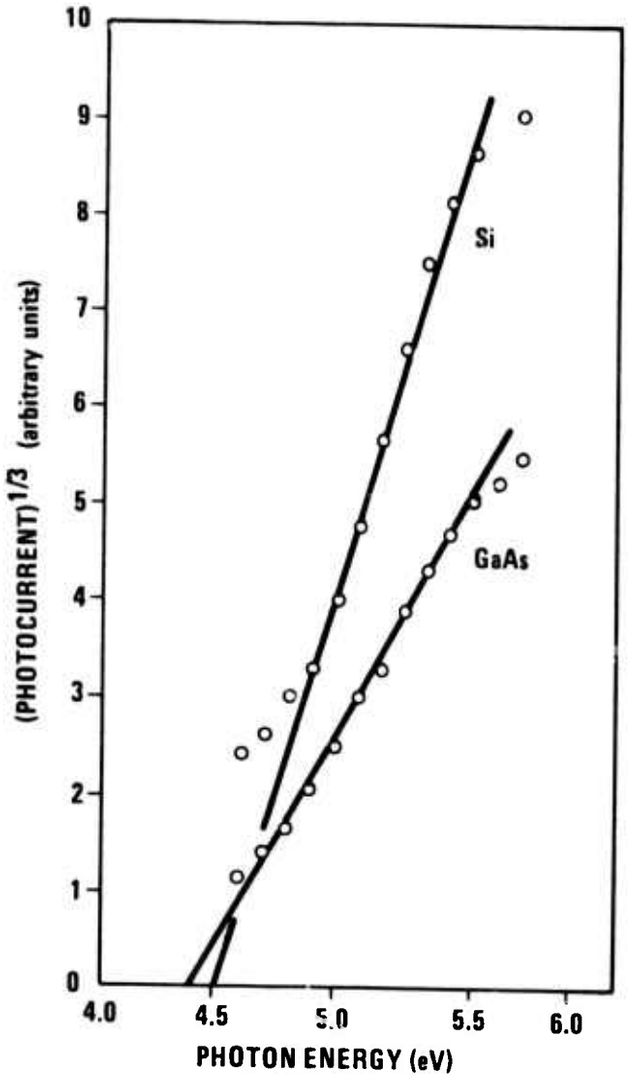

Figure 152. Plot of Cube Root of Room-temperature Photoelectric Current Due to Emission of Electrons from Si and from GaAs into Al_2O_3, as Function of Photon Energy

SECTION 12

DESIGN AND FABRICATION OF SPECIAL DEVICES*

In the first year of the contract apparatus for determining minority carrier lifetime by pulsed C-V measurement in MOS structures was designed and constructed and tests were begun. A special MOS structure was designed for measurement of channel conductance, high- and low-field transport properties, and various interface characteristics of heteroepitaxial films.

Initial attempts to fabricate Schottky-barrier diodes in Si/Al_2O_3 films as a means of evaluating their electrical properties were not successful and were not pursued further. In the second year the design of a Schottky-barrier type of FET was completed for use in fabricating experimental FET structures in GaAs/insulator films for operation at 1 GHz. Most of the device-oriented effort centered about the determination of carrier lifetimes using the MOS pulsed C-V technique (see Section 9-4) and attempts to fabricate Schottky-barrier FET's in $GaAs/Al_2O_3$.

More recent device efforts produced Schottky-barrier diodes (in n-type Si/Al_2O_3 samples) having good reverse but unsatisfactory forward characteristics. The Schottky-barrier FET structures were still not satisfactory. Preliminary work on fabricating and evaluating Schottky-barrier photovoltaic cells was begun, and charge-coupled devices in Si/Al_2O_3 composites were successfully designed, fabricated, and tested. The latter two device investigations will be described further in the following sections.

1. CHARGE-COUPLED DEVICES IN Si/Al_2O_3

In the final year of this contract the fabrication of charge-coupled devices in Si films grown on Al_2O_3 substrates was undertaken. Charge-coupled devices (CCD's) had been previously fabricated in bulk Si and showed good charge transfer. Heteroepitaxial Si surface devices of other types on Al_2O_3 substrates had exhibited good high-frequency and radiation-resistance characteristics, so it appeared logical to attempt to fabricate CCD's in the Si/Al_2O_3 composites.

---

*Other work with various device structures is described in Sections 7, 9, 10, and 11.

The goal of the investigation was to obtain preliminary characteristics of CCD's in Si/Al_2O_3; there was concern about the possible properties that would be achieved because of the short carrier lifetimes common to heteroepitaxial Si films and because of the geometry problems that might be encountered. However, the devices were successful, with good transfer efficiency at high frequencies. Four-phase 8-mil-per-cell devices were operated at 2 MHz with 0.99 efficiency. Low-frequency operation was found to be limited by the carrier lifetime, which allows charge-up of the potential well.

The properties of the Si/Al_2O_3 samples used for these investigations are given in Table 42. The films were (100) oriented, on $(01\bar{1}2)Al_2O_3$ substrates. Initially, an MOS capacitor structure was fabricated in one of the samples;* and

Table 42. Properties of Si/Al_2O_3 Composites Used for Fabrication of Charge-coupled Devices

Sample Number	Si Film Thickness (μm)	Electrical Properties of Si Film**		
		ρ(ohm-cm)	$n(cm^{-3})$	$\mu(cm^2/V\text{-}sec)$
AR2-26B-73	4.7	0.56	2.7×10^{16}	418
AR2-26C-73	4.4	~13.	4.9×10^{15}	147
AR2-21A-73	4.5	8.0	3.4×10^{15}	230
AR2-21B-73	5.9	5.7	2.1×10^{15}	513

**Determined by van der Pauw method.

C-V measurements were carried out to establish charge-up times for a rapid determination of the feasibility of making CCD's in these samples. Figure 153 shows the results; the charge-up time was found to be about 2 msec, indicating that a CCD fabricated in such material would have to be operated at a frequency higher than $2N/T=1KHz$, where N is the integral length of the CCD (i.e., the number of cells) and t is the charge-up time in sec.

*Sample No. AR2-26B-73

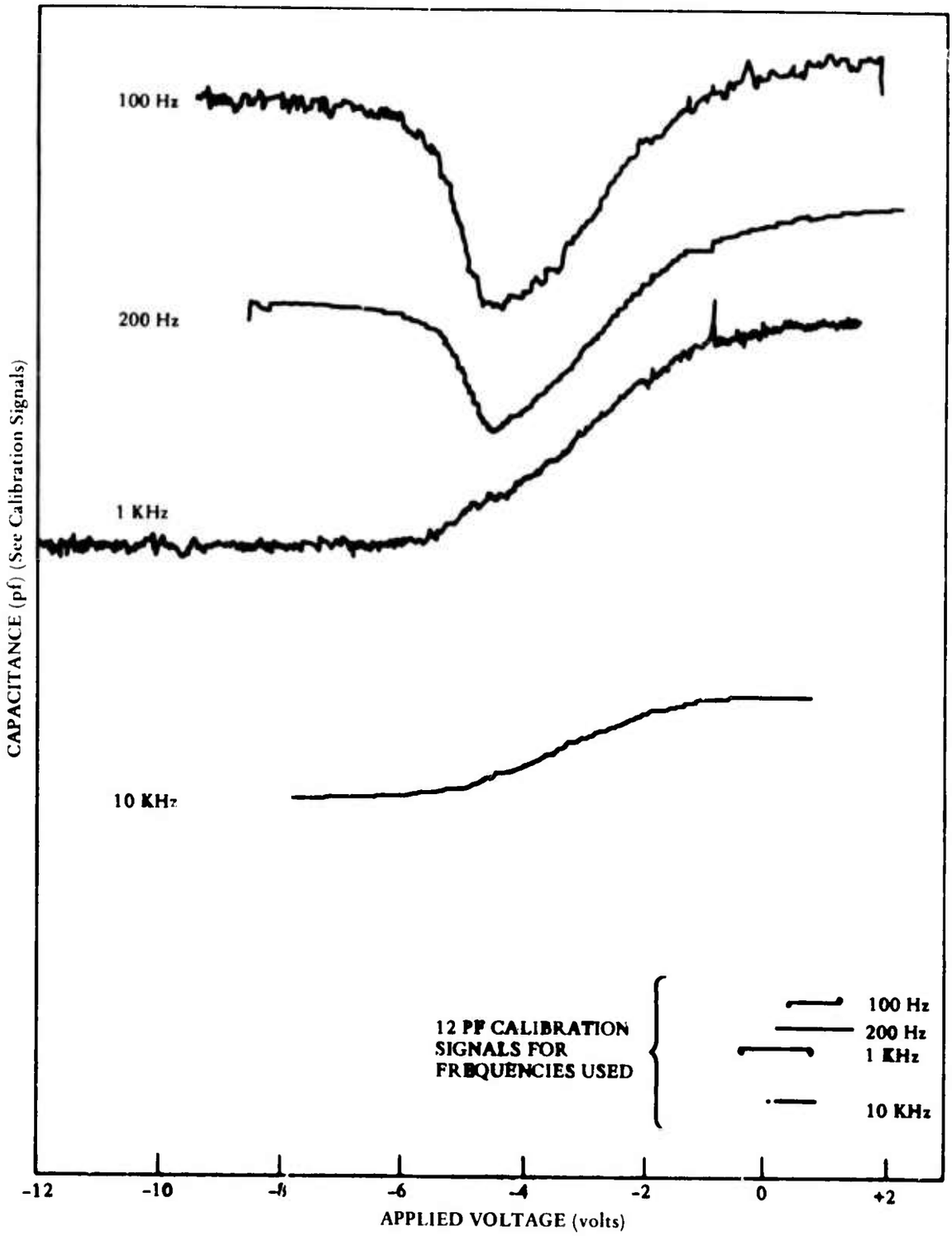

Figure 153. Exploratory C-V Measurements on Si/Al_2O_3 Sample to Determine Charge-up Times

A set of masks was prepared for forming a 10-bit and a 2-bit CCD and an MOS structure, and was used to fabricate CCD's in the other three n-type Si films on Al_2O_3. The CCD structure is shown in Figure 154.

One of the samples (the one with highest ρ) resulted in no device yield whatever, due to some processing difficulties. The other two exhibited a yield of about 20% before scribing and dicing; most of the failures were gate shorts to the Si "substrate." Breaking the wafers after scribing was difficult because the Al_2O_3 substrates were ~20 mils thick. Dice edges chipped severely, penetrating the device area in many places; the 10-bit devices were essentially completely damaged by this procedure. These devices were then used to make contact to the Si layer with conducting paint.

A typical processed CCD is shown in the photograph in Figure 155; this is a 2-bit CCD with Al gates and p-type polycrystalline Si over the oxide layer, as shown in Figure 154. The "I-bar" shown in the center of the array is the change transfer channel of the device. Input and output diodes can be seen at the left and right ends of the I-bar, respectively. The outside portion of the I-bar was diffused with P to form an n^+-type layer to prevent field inversion. The Al gates, 1 mil wide with a 1 mil spacing, were slightly misaligned off the I-bar.

In operation, the first gate on the left in Figure 155 is an input transfer gate which was biased at -4V. The second and sixth gates, the third and seventh gates, the fourth and eighth gates, and the fifth and ninth gates were connected to a 15V sine wave having 0 deg, -90 deg, -180 deg, and -270 deg phases, respectively. The sinusoidal voltages were offset by -10V. The 0 deg phase voltage is represented by the lower trace in Figure 156. The last gate is the output transfer gate, biased at -11V.

The input diode was connected to a pulse generator. The diode voltage is represented by the middle trace in Figure 156. During testing of the device

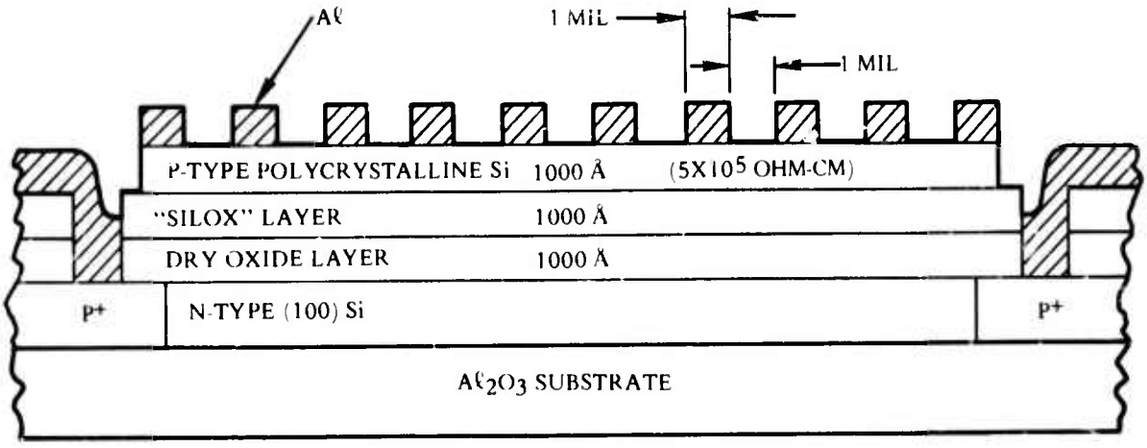

Figure 154. Schematic Diagram of CCD Structure in Si/Al_2O_3.

Figure 155. Typical Processed 2-bit CCD Structure in Si/Al_2O_3.

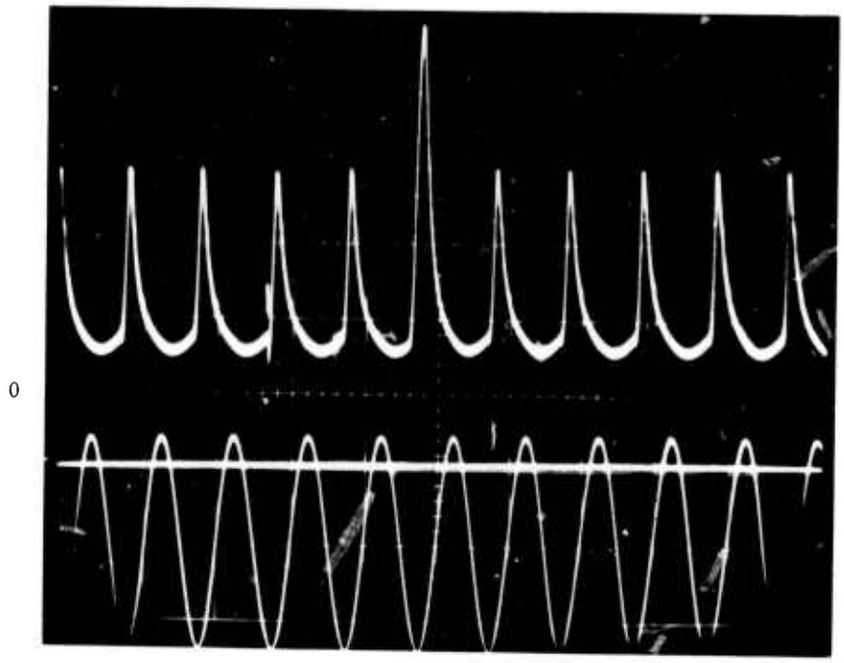

200 μsec/div
Freq = 5 kHz R = 1Mohm

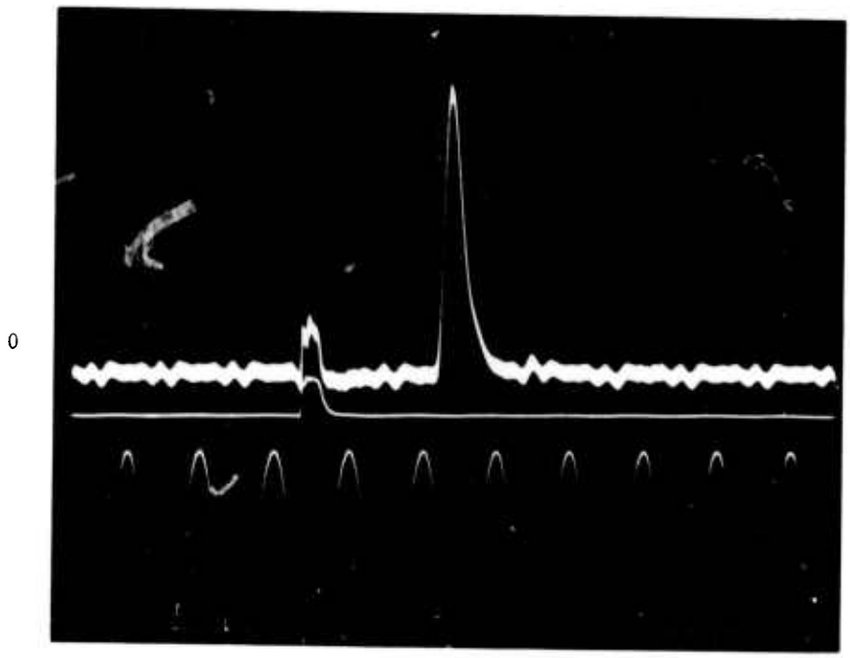

0.5 μsec/div
Freq = 2 MHz R = 3.6 Kohm

Figure 156. Characteristics of CCD in Si/Al_2O_3 at 5 KHz and 2 MHz. Top Trace: CCD Output. Middle Trace: Input Diode Voltage. Bottom Trace: 0 Deg Phase Gate Voltage

the base line was moved up and down to verify that "fat zero" was not provided. The output diode was connected to a -11V source through a resistor, and its value was changed for various operating frequencies; the voltage across the resistor was observed with an oscilloscope. The output is shown by the top trace of Figure 156.

Outputs at other operating frequencies are shown in Figures 157 and 158. The transfer efficiency at 2MHz was approximately 0.99, although the value could not be precisely determined since the device was only 2-bits in length. The CCD had a 1-mil gate width and, according to Kim (Ref 115), the diffusion discharge time constant of such a device would be approximately 0.7μsec, assuming the hole mobility to be 130 cm^2/V-sec. However, the device was operated with an efficiency of 0.998 per gate at 2MHz. This indicates that 1) the device did not operate in the diffusion discharge mode, even though the mobility at the surface might have been higher than average; 2) the small amount of leakage involved assisted the charge transfer at the so-called "fat zero"; and 3) the fast states in the device were either low in density or filled up rapidly due to the short carrier lifetime in the Si film.

The successful achievement of CCD's that exhibited good transfer efficiency at high frequencies in Si/Al_2O_3 composites provides considerable encouragement for further development of this type of device in heteroepitaxial semiconductor systems.

2. SCHOTTKY-BARRIER SOLAR CELL IN Si/Al_2O_3*

Heteroepitaxial semiconductor films grown on Al_2O_3 substrates are good candidates for use in the fabrication of solar cells because of the inherent advantage of

---

*These studies were performed in the Department of Electrical Sciences and Engineering of the University of California at Los Angeles by C. R. Viswanathan and C. Huang.

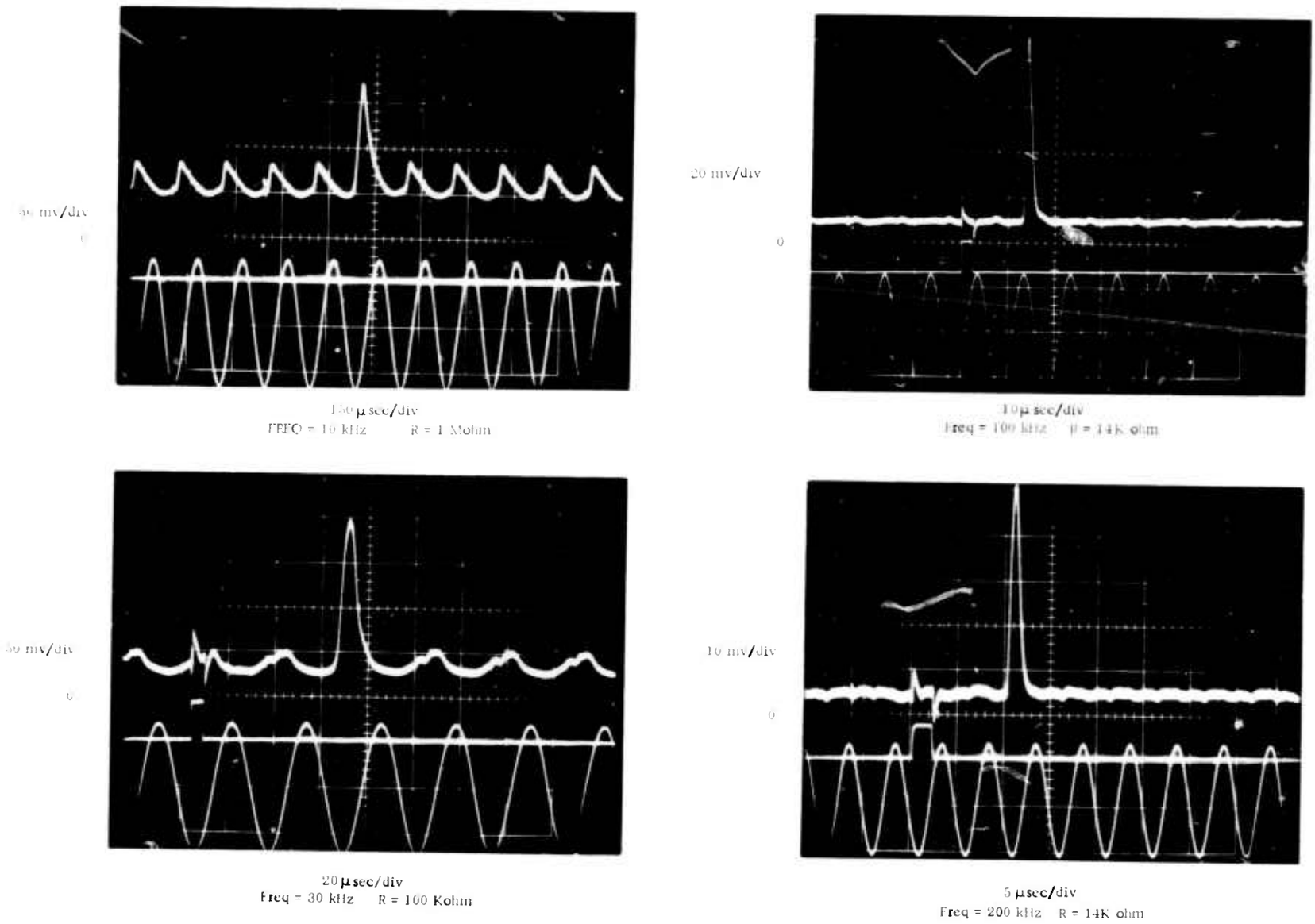

Figure 157. Characteristics of CCD in Si/Al_2O_3 at Several Operating Frequencies. Top Trace: CCD Output. Middle Trace: CCD Input

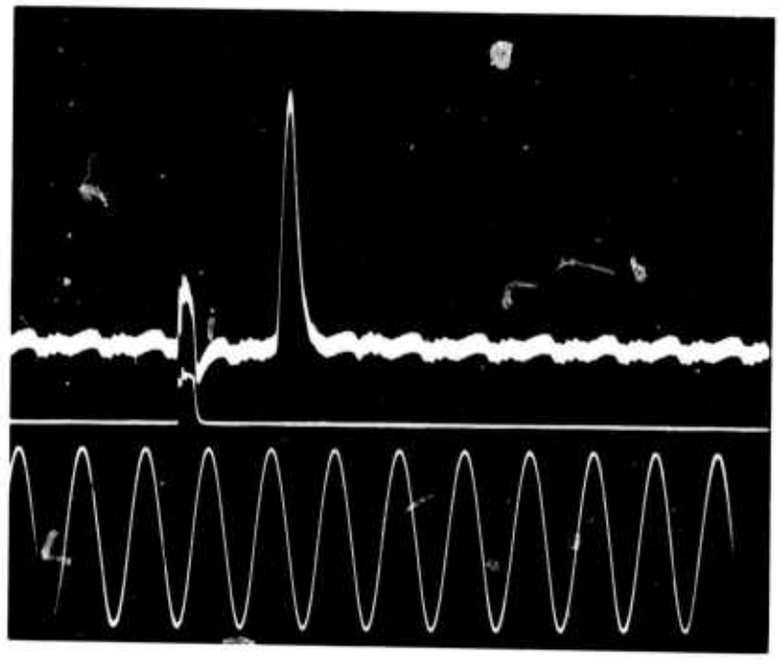

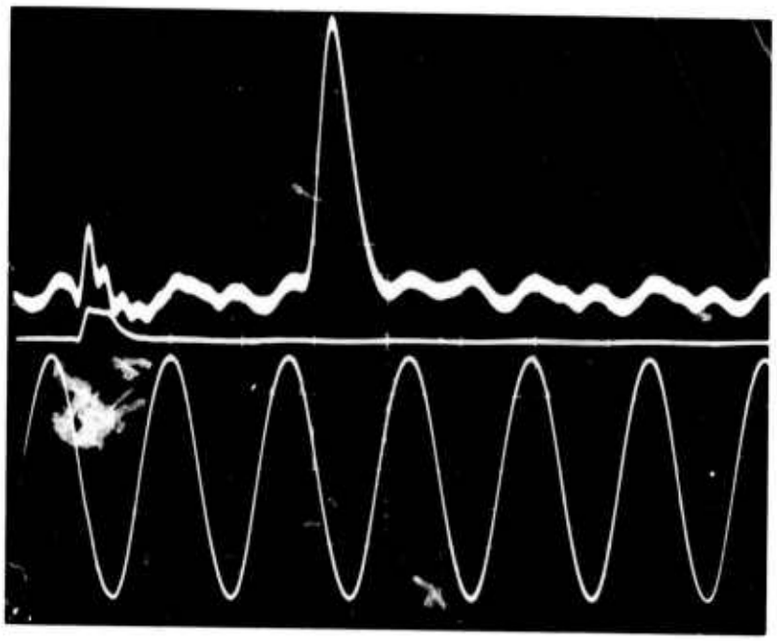

Figure 158. Characteristics of CCD in Si/Al_2O_3 at Higher Operating Frequencies. Top Trace: CCD Output. Middle Trace: CCD Input Pulse. Bottom Trace: 0 Deg Phase Gate Voltage

the optically transparent substrate which permits the illumination to be made from the backside. In conventional solar cells using bulk semiconductors and illumination from the front surface the overall efficiency is reduced because of reflection and absorption of light by the front-surface metal contact.

Accordingly, a Schottky-barrier photovoltaic cell structure was fabricated in p-type Si on Al_2O_3. The geometry of the structure is shown in Figure 159. In order to reduce the series resistance of the solar cell, the heteroepitaxial Si film was grown in the form of a p-type layer on top of a p^+ layer. The ohmic contact to the p-type Si was made through the Al contact, while the Au electrode deposited on the Si layer provided the Schottky barrier. Light was incident on the Al_2O_3 on the side opposite to that on which the Si film was grown.

Electron-hole pairs created in the Si film in or near the Schottky-barrier depletion region, due to the absorption of the photon energy, are acted on by the electric field in the depletion region; the holes move toward the Si layer while the electrons move toward the Au electrode, producing a photocurrent.

The dark-current characteristics of a typical Schottky-barrier diode fabricated in one of these samples is shown in Figure 160. The reverse current was relatively large, presumably due to surface leakage. Light from a 5mw He-Ne laser was focused on the cell; the total photon flux incident on the cell was determined (using a thermopile) to be 3.5×10^{15} photons/sec.

Table 43 gives the photocurrent as a function of the reverse bias on the cell, and from the photocurrent and the photon flux values the quantum efficiency was determined; this is also given in the table. It can be seen that the quantum efficiency increased with reverse bias. The increase in reverse bias voltage widens the Schottky-barrier depletion region and therefore the number of electron-hole pairs created in the depletion region increases.

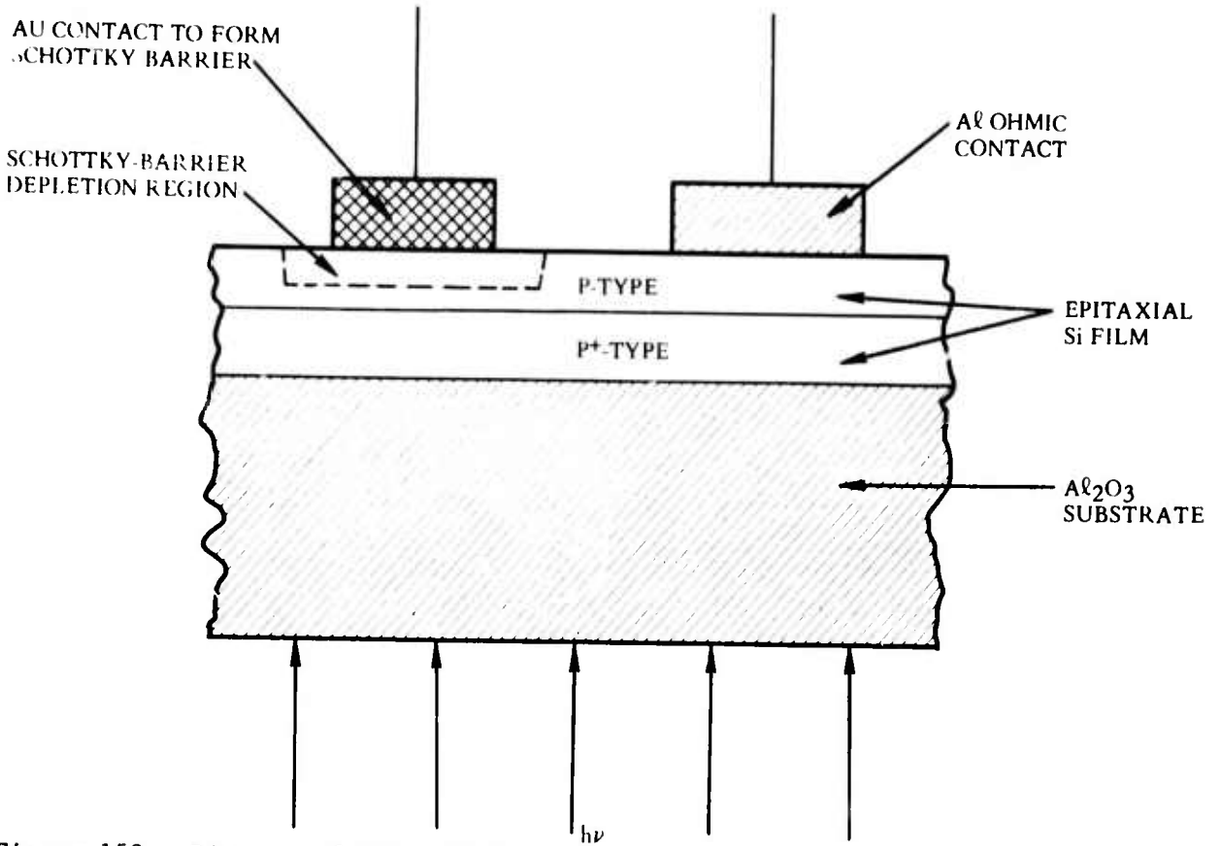

Figure 159. Diagram of Schottky-barrier Photovoltaic Cell Structure in Si/Al_2O_3

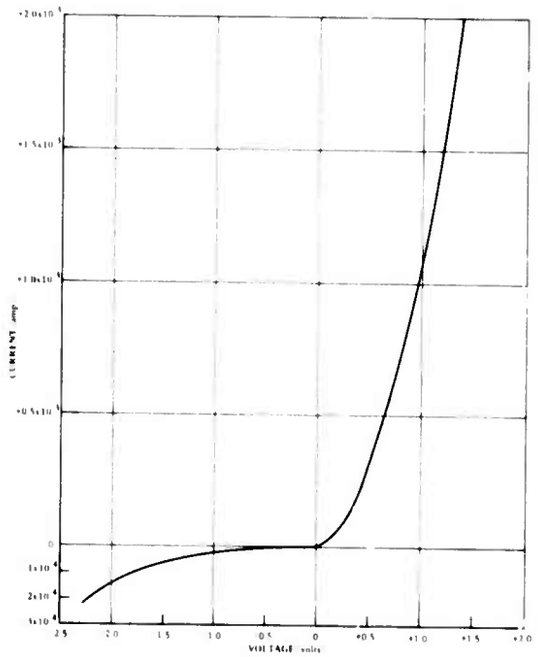

Figure 160. Dark-current Characteristics of Schottky-barrier Diode in Si/Al_2O_3

Table 43. Photocurrent and Quantum Efficiency as Function of Reverse Bias Voltage in Schottky-barrier Photovoltaic Cell.

Reverse Bias (volts)	Photocurrent (amp)	Quantum Efficiency η $\left(\frac{\text{No. measured electrons}}{\text{No. incident photons}}\right)$
0.1	2×10^{-6}	9.16×10^{-3}
0.2	3.8×10^{-6}	1.74×10^{-2}
0.3	5×10^{-6}	2.29×10^{-2}
0.4	5×10^{-6}	2.29×10^{-2}
0.5	5.5×10^{-6}	2.52×10^{-2}
0.6	6×10^{-6}	2.75×10^{-2}
0.7	5.5×10^{-6}	2.52×10^{-2}
0.8	6×10^{-6}	2.75×10^{-2}
0.9	5×10^{-6}	2.29×10^{-2}
1.0	4×10^{-6}	1.83×10^{-2}
1.1	5×10^{-6}	2.29×10^{-2}
1.2	6×10^{-6}	2.75×10^{-2}
1.3	6×10^{-6}	2.75×10^{-2}
1.4	7×10^{-6}	3.21×10^{-2}
1.5	7×10^{-6}	3.21×10^{-2}
1.6	9×10^{-6}	4.12×10^{-2}
1.7	1×10^{-5}	4.58×10^{-2}
1.8	1×10^{-5}	4.58×10^{-2}

However, the total photocarrent is comprised of the sum of the component due to the electron-hole pairs created in the depletion region and the component due to the electron-hole pairs created outside the depletion region within a diffusion length. The semiconductor sample used for these measurements consisted of a 2.8μm-thick p-type region grown on top of a 5-6μm-thick p^+ region. If it is assumed that the diffusion length was much larger than the combined thickness (8.4μm) of the p and p^+ regions, then the photocurrent should have been practically independent of the reverse bias voltage. From the fact that the photocurrent increased with the width of the depletion region, it appears that the diffusion length was, in fact, extremely small.

It is clear that additional work is required to find the most suitable geometrical structure to minimize the series resistance of the sample. Also, the diffusion length of the carriers in the Si film should be measured to determine the internal dimensions and electrical properties required. Heteroepitaxial films on transparent substrates have the potential to become efficient solar cells, although in these preliminary studies the quantum efficiency was two orders of magnitude lower than that reported (Ref 116) for bulk material.

REFERENCES

1. R. P. Ruth, "Fundamental Studies of Semiconductor Heteroepitaxy," First Semiannual Report, 28 January 1971, ARPA Order No. 1585, Contract No. DAAH01-70-C-1311. Prepared by North American Rockwell, Autonetics Division, Anaheim, CA, for USAMICOM, Redstone Arsenal, AL.

2. R. P. Ruth, "Fundamental Studies of Semiconductor Heteroepitaxy," Second Semiannual Report, July 1971, ARPA Order No. 1585, Contract No. DAAH01-70-C-1311. Prepared by North American Rockwell, Autonetics Division, Anaheim, CA, for USAMICOM, Redstone Arsenal, AL.

3. R. P. Ruth, "Fundamental Studies of Semiconductor Heteroepitaxy, "Third Semiannual Report, January 1972, ARPA Order No. 1585, Contract No. DAAH01-70-C-1311. Prepared by North American Rockwell Electronics Group, Research and Technology Division, Anaheim, CA, for USAMICOM, Redstone Arsenal, AL.

4. R. P. Ruth, A. J. Hughes, J. L. Kenty, H. M. Manasevit, and A. C. Thorsen, "Fundamental Studies of Semiconductor Heteroepitaxy," Fourth Semiannual Report, July 1972, ARPA Order No. 1585, Contract No. DAAH01-70-C-1311. Prepared by North American Rockwell Electronics Group, Research and Technology Division, Anaheim, CA, for USAMICOM, Redstone Arsenal, AL.

5. R. P. Ruth, A. J. Hughes, J. L. Kenty, H. M. Manasevit, A. C. Thorsen, C. R. Viswanathan, and M. A. Ring, "Fundamental Studies of Semiconductor Heteroepitaxy," Fifth Semiannual Report, January 1973, ARPA Order No. 1585, Contract No. DAAH01-70-C-1311. Prepared by North American Rockwell Electronics Group, Research and Technology Division, Anaheim, CA, for USAMICOM, Redstone Arsenal, AL.

6. H. Reiss, J. Appl. Phys. 39, 5045 (1968).

7. E. Hückel, Z. Physik 70, 204 (1931); 72, 310 (1931); 76, 628 (1932).

8. a. H. Kuhn, Helv. Chim. Acta 31, 1441 (1948); 34, 1308 (1951); J. Chem. Phys. 17, 1198 (1949).
   b. K. Rudenberg and C. W. Scherr, J. Chem. Phys. 21, 1565 (1953).

9. E. W. Montroll, J. Math. Phys. 11, 635 (1970); with R. G. J. Mills, 2525 (1970).

10. P. K. Rawlings and H. Reiss, Surface Sci. 36, 580 (1973).

11. See, e.g., Appendix A in "GaAs on Beryllia Substrates for Application to Microwave Ceneration," Second Quarterly Report, 8 September 1970, Contract No. N00019-70-C-0080. Prepared by Autonetics, Anaheim, CA, for Naval Air Systems Command, Washington, D.C.

12. B. Lewis, Thin Solid Films 7, 179 (1971).

13. H. Sato and S. Shinozaki, Surface Sci. 22, 229 (1970).

14. M. Bettman, in Single Crystal Films, ed. by M. H. Francombe and H. Sato (Pergamon Press, Oxford, 1964), p. 177.

15. D. W. Pashley, Advan. Phys. 14, 327 (1965).

16. J. W. Matthews, in Physics of Thin Films, Vol. 4, ed. by G. Hass and R. E. Thun (Academic Press, New York, 1967), p. 137.

17. J. H. van der Merwe, in Single Crystal Films, ed. by M. H. Francombe and H. Sato (Pergamon Press, Oxford, 1964), p. 137

18. J. H. van der Merwe, J. Appl. Phys. 34, 117, 123 (1967); 41, 4725 (1970).

19. N. H. Fletcher, J. Appl. Phys. 35, 234 (1964); Phil. Mag. 16, 159 (1967).

20. N. H. Fletcher and P. L. Adamson, Phil. Mag. 14, 99 (1966).

21. C. C. Chang, J. Vac. Sci. and Tech. 8, 500 (1971); J. Appl. Phys. 39, 5570 (1968).

22. J. Callaway and A. J. Hughes, Phys. Rev. 156, 860 (1967); 164,1043 (1967).

23. M. D. Feit and H. B. Huntington, Phys. Rev. 172, 580 (1968).

24. R. A. Johnson, Phys. Rev. 145, 423 (1966).

25. P. Wynblatt, Phys. Stat. Sol. 36, 797 (1969).

26. P. A. Tick and A. F. Witt, Surface Sci. 26, 165 (1971).

27. R. A. Swalin, J. Phys. Chem. Solids 18, 290 (1961).

28. A. Scholz and A. Seegar, Phys. Stat. Sol. 3, 1480 (1963).

29. E. B. Moore, Jr. and C. M. Carlson, Solid State Commun. 4, 47 (1966); A. J. Bennett, B. McCarroll and R. P. Messmer, Surface Sci. 24, 191 (1971); G. D. Watkins, R. P. Messmer, C. Weigal, D. Peak and J. W. Corbett, Phys. Rev. Lett. 27, 1573 (1971).

30. B. McCarroll and R. P. Messmer, Surface Sci. 27, 451 (1971).

31. J. H. Gieske and G. R. Barsch, Phys. Stat. Sol. 29, 121 (1968).

32. O. L. Anderson, in Physical Acoustics, ed. by W. P. Mason, Vol. III, Part B (Academic Press, Inc., New York, 1965), p. 43.

33. D. J. Dumin, J. Appl. Phys. 36, 2700 (1965); A. C. Ipri and J. N. Zemel, J. Appl. Phys. 44, 744 (1973).

34. J. B. Austin, J. Am. Ceram. Soc, 14, 795 (1931).

35. A. J. Hughes and A. C. Thorsen, J. Appl. Phys. 44, 2304 (1973).

36. A C. Thorsen and A. J. Hughes, Appl. Phys. Lett. 21, 579 (1972).

37. A. J. Hughes, to be published.

38. H. M. Manasevit, R. L. Nolder, and L. A. Moudy, Trans. TMS-AIME 242, 465 (1968).

39. D. J. Dumin and P. H. Robinson, J. Appl. Phys. 39, 2759 (1968).

40. W. E. Ham, Appl. Phys. Lett. 21, 440 (1972).

41. L. J. van der Pauw, Philips Res. Repts. 13, 1 (1958).

42. D. J. Dumin and E. C. Ross, J. Appl. Phys. 41, 3139 (1970).

43. R. F. C. Farrow and J. D. Filby, J. Electrochem. Soc. 118, 149 (1971).

44. D. J. Dumin, Solid State Electron. 13, 415 (1970).

45. H. M. Manasevit and W. I. Simpson, J. Electrochem. Soc. 116, 1725 (1969).

46. A. C. Thorsen and H. M. Manasevit, J. Appl. Phys. 42, 2519 (1971).

47. K. Borer and C. S. G. Phillips, Proc. Chem. Soc. 1959, 189.

48. G. S. G. Phillips and P. L. Timms, Anal. Chem. 35, 505 (1963).

49. G. R. Seely, J. P. Oliver and D. M. Ritter, Anal. Chem. 31, 1993 (1959).

50. K. Borer, A. B. Littlewood and C. S. G. Phillips, J. Inorg. Nucl. Chem. 15, 316 (1960).

51. H. W. Myers and R. F. Putnam, Anal. Chem. 34, 664 (1962).

52. A. B. Littlewood, Gas Chromatography (Academic Press, New York, 1970), p. 225.

53. H. M. Manasevit and F. L. Morritz, J. Electrochem. Soc. 114, 204 (1967).

54. H. M. Manasevit, J. Electrochem. Soc. 115, 434 (1968).

55. J. W. Faust, Jr., Electrochem. Tech. 2, 339 (1964).

56. A. Reisman, M. Berkenblit, J. Cuomo, and S. A. Chan, J. Electrochem. Soc. 118, 1653 (1971).

57. R. Williams, Phys. Rev. 140A, 569 (1965).

58. A. M. Goodman, Phys. Rev. 144, 588 (1966).

59. C. R. Viswanathan and S. Ogura, Proc. IEEE 57, 1552 (1969).

60. W. Pong, J. Appl. Phys. 40, 1733 (1969).

61. C. R. Viswanathan, R. Loo and S. Ogura, J. Vac. Sci. Technol. 9, 230 (1971).

62. C. R. Viswanathan and R. Y. Loo, Appl. Phys. Lett. 21, 370 (1972).

63. C. R. Viswanathan and R. Y. Loo, Thin Solid Films 13, 87 (1972).

64. C. N. Berglund and R. J. Powell, J. Appl. Phys. 42, 573 (1971).

65. M. Ieda, G. Sawa, and S. Kato, J. Appl. Phys. 42, 3737 (1971).

66. W. S. Wong, M. S. Thesis, UCLA (1973).

67. C. R. Crowell, W. G. Spitzer, L. E. Howarth, and E. E. Bate, Phys. Rev. 127, 2006 (1962).

68. U. Valdre, E. A. Robinson, D. W. Pashley, M. J. Stowell, and T. J. Law, J. Phys. 3E, 501 (1970).

69. D. W. Pashley, M. J. Stowell, E. A. Robinson, T. J. Law, and U. Valdre, in Electron Microscopy (Proceedings of Fourth European Regional Conf., Rome, 1968), ed. by D. A. Bocciarelli (Tipografia Poliglotta Vaticana, Rome, 1968), p. 387.

70. U. Valdre, D. W. Pashley, E. A. Robinson, M. J. Stowell, K. J. Routledge, and R. Vincent, in Electron Microscopy 1966 (Sixth International Congress for Electron Microscopy, Kyoto, 1966), ed. by R. Uyeda (Maruzen Co., Tokyo, 1966), Vol. 1, Physics, p. 155.

71. H. Hashimoto, A. Kumao, T. Etc, and K. Fujiwara, J. Crystal Growth 7, 113 (1970).

72. T. Gabor and J. M. Blocher, J. Appl. Phys. 40, 2696 (1969).

73. R. K. Hart and J. K. Maurin, in Electron Microscopy 1966 (Sixth International Congress for Electron Microscopy, Kyoto, 1966), ed. by R. Uyeda (Maruzen Co., Tokyo, 1966), Vol. 1, Physics, p. 539.

74. J. Escaig and C. Sella, in Electron Microscopy (proceedings of the Fourth European Regional Conference, Rome, 1968), ed. by D. A. Bocciarelli (Tipografia Poliglotta Vaticana, Rome, 1968), p. 241.

75. E. I. Givargizov, Sov. Phys.-Solid State 6, 1415 (1964).

76. J. L. Kenty, in 30th Ann. Proc. Electron Microscopy Soc. Amer., C. J. Arceneaux, ed. (Los Angeles, CA, 1972), p. 624.

77. D. H. Kay, Techniques for Electron Microscopy (F. A. Davis Co., Philadelphia, PA, 1965), p. 58.

78. F. S. Feates, P. S. Harris, and R. T. K. Baker, Seventh International Congress on Electron Microscopy (Societe Francaise de Microscopie Electronique, Paris, 1970), p. 357.

79. D. W. Pashley, M. J. Stowell, M. H. Jacobs, and T. J. Law, Phil. Mag. 10, 127 (1964). See also references in Appendix 5.

80. H. M. Manasevit and A. C. Thorsen, "Heteroepitaxy of III-V Compound Semiconductors on Insulating Substrates," Final Report, January 1970, p.9, NASA Contract No. NAS 12-2010. Prepared by North American Rockwell, Autonetics Division, Anaheim, CA, for NASA/ERC, Boston, MA.

81. F. J. Morin and J. P. Maita, Phys. Rev. 96, 28 (1954).

82. H. F. Mataré, private communication.

83. H. Schlötterer, Sol. St. Electronics 11, 947 (1968).

84. M. Zerbst, Z. angew. Phys. 22, 30 (1966).

85. A. S. Grove, O. Leistiko, Jr., and C. T. Sah, J. Appl. Phys. 35, 2695 (1964).

86. G. H. Glover, IEEE Trans. ED-19, 138 (1972).

87. B. E. Deal, A. S. Grove, E. H. Snow, and C. T. Sah, J. Electrochem. Soc. 112, 308 (1965).

88. W. Van Gelder and E. H. Nicollian, J. Electrochem. Soc. 118, 138 (1971).

89. D. K. Schroder and H. C. Nathanson, Sol. St. Electronics 13, 577 (1970).

90. D. K. Schroder and P. Rai-Choudhury, Appl. Phys. Lett. 22, 455 (1973).

91. C. N. Berglund, IEEE Trans. Electron Dev. ED-13, 701 (1966).

92. R. Castagne, Compt. rend., (Paris) 267, 866 (1968).

93. a) T. H. Geballe, in Semiconductors, ed. by N. B. Hannay (Reinhold Pub. Corp., New York, 1959), p. 313.

    b) A. C. Ipri and J. N. Zemel, J. Appl. Phys. 44, 744 (1973).

94. D. J. Evans, S. Ushioda, and J. D. McMullen, submitted for publication.

95. D. L. Mills and A. A. Maradudin, submitted for publication.

96. B. A. Joyce, R. R. Bradley, and G. R. Booker, Phil. Mag. 15, 1167 (1967); also 19, 403 (1969).

97. H. M. Manasevit, A. Miller, F. L. Morritz, and R. Nolder, Trans. AIME 233, 540 (1965).

98. R. W. Bicknell, B. A. Joyce, J. H. Neave, and G. V. Smith, Phil. Mag. 14, 31 (1966).

99. R. S. Nelson, The Observation of Atomic Collisions in Crystalline Solids (North Holland, Amsterdam, 1968).

100. J. W. Mayer, L. Erickson and J. A. Davies, Ion Implantation in Semiconductors (Academic Press, New York, 1970).

101. O. Meyer, J. Gyulai, and J. W. Mayer, Surface Sci. 22, 263 (1970).

102. S. T. Picraux, Appl. Phys. Lett. 20, 91 (1972); J. Appl. Phys. 44, 587 (1973).

103. S. T. Picraux and G. J. Thomas, J. Appl. Phys. 44, 594 (1973).

104. E. Bogh, Can. J. Phys. 46, 653 (1968).

105. F. H. Eisen, B. Welch, J. E. Westmoreland and J. W. Mayer, in Atomic Collision Phenomena in Solids, ed. by D. W. Palmer, M. W. Thompson and P. D. Townsend (North Holland, Amsterdam, 1970), p 111.

106. J. E. Westmoreland, J. W. Mayer, F. H. Eisen and B. Welch, Rad. Effects 6, 161 (1970).

107. E. Keil, E. Zeitler and W. Zinn, Z. für Naturforsch. 15a, 1031 (1960).

108. R. J. Batt and C. H. B. Mee, J. Vac. Sci. Tech. 6, 737 (1969).

109. S. M. Sze, Physics of Semiconductor Devices (John Wiley & Sons, New York, 1969), p. 469.

110. N. Szydlo and R. Poirier, J. Appl. Phys. 42, 4880 (1971).

111. C. R. Viswanathan and R. Y. Loo, Int. Conf. on Thin Films, Venice, May 15-19, 1972.

112. J. Antula, J. Appl. Phys. 43, 1830 (1972).

113. F. G. Allen and G. W. Gobeli, Phys. Rev. 127, 150 (1962).

114. S. M. Sze, Physics of Semiconductor Devices (John Wiley & Sons, New York, 1969), p. 57.

115. C. K. Kim, International Solid State Circuits Conference, Philadelphia, PA, Feb. 17-19, 1971, (p. 158 of Digest Vol. XIV).

116. S. S. Li, F. A. Lindholm, and C. T. Wang, J. Appl. Phys. 43, 4123 (1972).